DTU Library

Computational Modelling and Optimization of Electric Fields Generated by Transcranial Brain Stimulation

Bicalho Saturnino, Guilherme

Publication date:
2020

Document Version
Publisher's PDF, also known as Version of record

[Link back to DTU Orbit](#)

Technical University of Denmark

Department of Health Technology

Computational Modelling and Optimization of Electric Fields Generated by Transcranial Brain Stimulation

Guilherme Bicalho Saturnino

Supervisors

Assoc. Prof. Axel Thielscher, DTU Health Technology

Assoc. Prof. Kristoffer Hougaard Madsen, DTU Compute

Prof. Lars Kai Hansen, DTU Compute

August 2020

All models are wrong but some are useful

George Box

Preface

This thesis was submitted in partial fulfillment of the requirements for the degree of Doctor of Philosophy at the Department of Health Technology of the Technical University of Denmark (DTU). The work was carried out at DTU and the Danish Research Centre for Magnetic Resonance (DRCMR), Copenhagen University Hospital Hvidovre, Hvidovre, Denmark. It was funded by the Lundbeck foundation (R244-2017-196 and R186-2015-2138) and the Novonordisk foundation (NNF14OC0011413).

The PhD was part of a special joint PhD and MSc program, with a total duration of 5 years. The corresponding MSc Thesis, called *Efficient Calculations of Transcranially Generated Electric Fields in the Human Brain Using Realistic Head Models*, was submitted and accepted in 2018, and contains a significant amount of the work carried out during the program.

Acknowledgments

I would like to thank my supervisors Axel Thielscher and Kristoffer Hougaard Madsen for their guidance and their trust, and my co-supervisor Prof. Lars Kai Hansen for helping get the project started.

I also would like to thank my colleagues at DRCMR and DTU for their friendship and support though all these five years and my external collaborators for introducing me to many new and exciting ideas.

This work would not be possible without the love and patience from my family and especially my wife, Larissa, who gave me all support I could possibly ask for.

<div align="right">

Guilherme Bicalho Saturnino, Kongens Lyngby, August 2020.

</div>

For my wife Larissa

Abstract

A range of neurostimulation technologies seek to modulate brain activity using electric fields. These methods have several research and clinical applications, for example in the treatment of Parkinson's disease and major depressive disorder. Transcranial brain stimulation (TBS) are types of neurostimulation methods where the electric fields are applied from outside the body, using either scalp electrodes or a magnetic coil positioned over head, and therefore do not require surgical interventions. Over recent years, TBS methods have attracted attention for their potential in human neuroscience research and in the treatment of various neuropsychiatric disorders with minimal side effects. However, as the stimulation sources, located outside the head, are far from the stimulation targets, located in the brain, the electric fields generated by TBS are influenced by individual anatomical features such as skull thickness and brain gyrification patterns. These effects are in part responsible for the large variability observed in the outcomes of TBS interventions.

To gain a better understanding of how TBS affects the brain, practitioners are turning to computational methods for simulating electric fields in individualized head models. In the first part of this thesis, we attempt to validate and compare tools for automatically creating head models from magnetic resonance (MR) images using intracranial electric field measurements. We will see that, while there is considerable variability between electric field estimates provided by the different modelling tools, the intracranial measurements did not clearly indicate which tool provides the greatest accuracy. In the following chapter, we develop novel algorithms for optimizing electrode positions for transcranial electric stimulation (TES) in order to obtain focal electric fields around given targets. Our optimization methods proved to be reliable and efficient, and we were able to apply them to map the accessibility of thousands of brain regions to focal TES as well as the effects of stimulation parameters. Finally, we describe our implementation of computational modelling and optimization tools for TBS into free and open source software, making our research accessible for practitioners.

Resumé

Ved elektromagnetisk hjernestimulation anvendes elektriske felter til at modulere hjerneaktivitet, disse metoder bliver benyttet både indenfor hjerneforskning og flere kliniske anvendelser, for eksempel til behandling af Parkinsons sygdom og depression, er under udvikling. Ved transkraniel hjernestimulation (TBS) er stimulerings kilden placeret uden for hovedet, og der stimuleres typisk ved hjælp af elektroder med elektrisk forbindelse til hovedbunden eller via en magnetisk spole. Dermed er TBS som udgangspunkt ikke invasivt og kræver ikke kirurgiske indgreb. På grund af et betydeligt potentiale indenfor neurovidenskabelig forskning, samt mulige anvendelser i forbindelse med behandling af neuropsykiatriske lidelser med minimale bivirkninger, har TBS tiltrukket betydelig interesse i de seneste år. Da stimulationskilderne er placeret udenfor hovedet, relativt langt fra de områder som ønskes stimuleret (indeni hovedet) har individuelle anatomiske forskelle såsom tykkelsen af kraniet og gyrificeringen betydning for hvorledes det elektriske felt distribueres. Disse effekter kan til dels forklare den store individuelle variabilitet som forekommer i forbindelse med TBS.

Individ-specifikke computer simuleringer af de elektriske felter som opstår ved TBS kan anvendes for at opnå en bedre forståelse af hvordan TBS påvirker hjernen. I den første del af denne afhandling forsøger vi at validere og sammenligne værktøjer som automatisk kan generere realistiske hovedmodeller udfra magnetisk resonans (MR) -billeder af hovedet, på baggrund af intrakraniel måling af det elektriske potential. På trods af at der er betydelige variationer mellem de forskellige modelleringsværktøjer, gjorde de forhåndenværende målinger det ikke muligt med sikkerhed at konkludere hvilket modelleringsværktøj der var mest nøjagtigt. Herefter fokuserer afhandlingen på udvikling af nye algoritmer for optimering af elektrode positioner for transkraniel elektrisk stimulation (TES). De udviklede optimeringsmetoder viser sig at være både pålidelige og effektive i forbindelse med at opnå fokale elektriske felter omkring de ønskede stimulerings områder i hjernen. Ved hjælp af de udviklede optimeringsmetoder var vi stand til at kortlægge i hvor stor grad tusindvis af hjerneområder kan stimuleres med TES samt hvilken indflydelse stimulerings parametre har. Endelig beskriver afhandlingen implementationen af disse værktøjer som frit tilgæn-

geligt computer software hvilket gør forskningen umiddelbar tilgængelig for alle som arbejder med TBS.

Contents

List of Publications

Jornal Articles

First Authorships

- **G. B. Saturnino**, K. H. Madsen, H. R. Siebner, and A. Thielscher, "How to target inter-regional phase synchronization with dual-site transcranial alternating current stimulation," *Neuroimage*, vol. 163, pp. 68–80, 2017.

- †**G. B. Saturnino**, A. Thielscher, K. H. Madsen, T. R. Knösche, and K. Weise, "A principled approach to conductivity uncertainty analysis in electric field calculations," *Neuroimage*, vol. 188, pp. 821–834, 2019.

- †**G. B. Saturnino**, K. H. Madsen, and A. Thielscher, "Electric field simulations for transcranial brain stimulation using fem: an efficient implementation and error analysis," *Journal of neural engineering*, vol. 16,no. 6, p. 066032, 2019.

- ¶**G. B. Saturnino**, H. R. Siebner, K. H. Madsen, and A. Thielscher "Accessibility of cortical regions to focal TES: Dependence on spatial position, safety, and practical constraints," *NeuroImage*, vol. 203,p. 116183, 2019.

- ¶O. Puonti*, **G. B. Saturnino***, K. H. Madsen, and A. Thielscher, "Value and limitations of intracranial recordings for validating electric field modeling for transcranial brain stimulation," *NeuroImage*, vol. 208,p. 116431, 2020.

- ¶**G. B. Saturnino**, K. H. Madsen, and A. Thielscher, "Optimizing the electric field strength in multiple targets for multichannel transcranial electric stimulation," *Journal of neural engineering*, Accepted.

Co-authorships

- A. R. Korshoej, **G. B. Saturnino**, L. K. Rasmussen, G. Von Oettingen,J. C. H. Sørensen, and A. Thielscher, "Enhancing predicted efficacy oftumor treating fields

therapy of glioblastoma using targeted surgical craniectomy: A computer modeling study," *PloS one*, vol. 11, no. 10,2016

- K.-F. Heise, N. Kortzorg, **G. B. Saturnino**, H. Fujiyama, K. Cuypers, A. Thielscher, and S. P. Swinnen, "Evaluation of a modified high-definition electrode montage for transcranial alternating current stimulation (tacs) of pre-central areas," *Brain stimulation*, vol. 9, no. 5,pp. 700–704, 2016

- S. Minjoli, **G. B. Saturnino**, J. U. Blicher, C. J. Stagg, H. R. Siebner, A. Antunes, and A. Thielscher, "The impact of large structural brain changes in chronic stroke patients on the electric field caused by transcranial brain stimulation," *NeuroImage: Clinical*, vol. 15, pp. 106–117,2017

- J. D. Nielsen, K. H. Madsen, O. Puonti, H. R. Siebner, C. Bauer, C. G.Madsen, **G. B. Saturnino**, and A. Thielscher, "Automatic skull segmentation from mr images for realistic volume conductor models of the head: Assessment of the state-of-the-art," *Neuroimage*, vol. 174, pp. 587–598,2018.

- V. Conde, L. Tomasevic, I. Akopian, K. Stanek, **G. B. Saturnino**, A. Thielscher, T. O. Bergmann, and H. R. Siebner, "The non-transcranial tms-evoked potential is an inherent source of ambiguity in tms-eeg studies," *Neuroimage*, vol. 185, pp. 300–312, 2019.

- A. T. Htet, **G. B. Saturnino**, E. H. Burnham, G. Noetscher, A. Nummenmaa, and S. N. Makarov, "Comparative performance of the finite element method and the boundary element fast multipole method for problems mimicking transcranial magnetic stimulation (tms)," *Journal of neural engineering*, 2019.

- H. Siebner, V. Conde, A. Thielscher, T. Bergmann, **G. Saturnino**, and L. Tomasevic, "Frontoparietal tms-eeg: Transcranially versus peripherally induced brain responses," *Brain Stimulation*, vol. 12, no. 2, p. 429, 2019.

- A. N. Karabanov, **G. B. Saturnino**, A. Thielscher, and H. R. Siebner,"Can transcranial electrical stimulation localize brain function?," *Frontiers in psychology*, vol. 10, p. 213, 2019.

- D. Antonenko, A. Thielscher, **G. B. Saturnino**, S. Aydin, B. Ittermann, U. Grittner, and A. Flöel, "Towards precise brain stimulation: Is electric field simulation related to neuromodulation?," *Brain stimulation*,vol. 12, no. 5, pp. 1159–1168, 2019.

- S. Tashiro, H. R. Siebner, A. Charalampaki, C. Göksu, **G. B. Saturnino**, A. Thielscher, and L. Tomasevic, "Probing eeg activity in the targeted cortex after focal transcranial electrical stimulation," *Brain Stimulation*, vol. 13, no. 3, pp. 815–818, 2020.

- H. Yazdanian, **G. B. Saturnino**, A. Thielscher, and K. Knudsen, "Fast evaluation of the biot-savart integral using fft for electrical conductivity imaging," *Journal of Computational Physics*, p. 109408, 2020.

- O. Puonti, K. Van Leemput, **G. B. Saturnino**, H. R. Siebner, K. H. Madsen, and A. Thielscher "Accurate and robust whole-head segmentation from magnetic resonance images for individualized head modeling". *NeuroImage*, 117044, 2020.

Book Chapters

- ¶**G. B. Saturnino***, O. Puonti*, J. D. Nielsen, D. Antonenko, K. H. Madsen,and A. Thielscher, "Simnibs 2.1: a comprehensive pipeline for individualized electric field modelling for transcranial brain stimulation," in *Brain and Human Body Modeling*, pp. 3–25, Springer, Cham, 2019.

Conference Contributions (Posters)

- **G.B. Saturnino**, H. R. Siebner, K. H. Madsen, and A. Thielscher, "Feasibility of focused multichannel transcranial current stimulation", *10th FENS Forum of Neuroscience*, pp. 3274-3274, 2016.

- K. H. Madsen, A. Thielscher, **G. B. Saturnino**, and J. D. Nielsen. "Computationally Efficient and Geometrically Accurate Head Models for eeg Based on fem", *10th FENS Forum of Neuroscience*, pp. 3281-3281, 2016.

- **G. B. Saturnino**, A. Thielscher, K. H. Madsen, T. R. Knösche, and K. Weise, "Assessing the impact of conductivity uncertainties on the accuracy of tes electric field calculation," *24th Annual Meeting of the Organization for Human Brain Mapping*, 2018.

- O. Puonti, K. Van Leemput, **G. B. Saturnino**, J. D. Nielsen, H. R. Siebner, K. H. Madsen, and A. Thielscher, "Robust and accurate modeling of whole-head anatomy for individualized non-invasive brain stimulation," in *25th Annual Meeting of the Organization for Human Brain Mapping*, 2019.

- S. Tashiro, H. R. Siebner, A. Charalampaki, **G. B. Saturnino**, A. Thielscher, and L. Tomasevic, "A hybrid electrode for evaluating brain activity directly after transcranial electrical stimulation," in *25th Annual Meeting of the Organization for Human Brain Mapping*, 2019.

- **G. B. Saturnino**, O. Puonti, K. H. Madsen, A. Thielscher, "SimNIBS 3: Simulation, optimization and uncertainty quantification for transcranial brain stimulation," in *25th Annual Meeting of the Organization for Human Brain Mapping*, 2019.

Conference Contributions (Oral)

- **G.B. Saturnino**, H. R. Siebner, K. H. Madsen, and A. Thielscher, "Fundamental limitations of focal transcranial weak current stimulation", *6th International Conference on Transcranial Brain Stimulation*, pp. 131-132, 2016

- **G.B. Saturnino**, O. Puonti, A. Antunes, J. D. Nielsen, K. H. Madsen, and A. Thielscher, "Reporting the Dose of Non-Invasive Brain Stimulation using SimNIBS 2", in *2018 40st Annual International Conference of the IEEE Engineering in Medicine and Biology Society (EMBC),IEEE*, 2018.

- **G.B. Saturnino**, A. Antunes, J. D. Nielsen, O. Puonti, K. H. Madsen, and A. Thielscher, "SimNIBS 2: A Comprehensive Pipeline for Individualized Electric Field Modeling for Transcranial Brain Stimulation", in *2018 40st Annual International Conference of the IEEE Engineering in Medicine and Biology Society (EMBC),IEEE*, 2018.

- S. Farcito, O. Puonti, H. Montanaro, **G. B. Saturnino**, J. D. Nielsen,C. G. Madsen, H. R. Siebner, E. Neufeld, N. Kuster, B. A. Lloyd,et al.,"Accurate anatomical head segmentations: a data set for biomedical simulations," in *2019 41st Annual International Conference of the IEEE Engineering in Medicine and Biology Society (EMBC)*, pp. 6118–6123, 2019.

- A. R. Korshoej, N. Mikic, F. L. Hansen, **G. B. Saturnino**, A. Thielscher, and Z. Bomzon, "Enhancing tumor treating fields therapy with skull-remodeling surgery. the role of finite element methods in surgery planning," in *2019 41st Annual International Conference of the IEEE Engineering in Medicine and Biology Society (EMBC)*, pp. 6995–6997, 2019.

- **G. B. Saturnino**, W. Wartman, S. Makarov, and A. Thielscher, "Accurate TMS Head Modeling: Interfacing SimNIBS and BEM-FMM in a MATLAB-Based Module"

in *2020 42st Annual International Conference of the IEEE Engineering in Medicine and Biology Society (EMBC)*,2020.

¶ Included in the current thesis

† Included in MSc Thesis

* Equal contribution status

List of Figures

List of Abbreviations

BEM	Boundary Element Method
CCP	Convex Concave Program
CSF	Cerebrospinal Fluid
EEG	Electroencephalography
FEM	Finite Element Method
FMM	Fast Multipole Method
GM	Gray Matter
MEG	Magnetoencephalography
MR	Magnetic Resonance
PDE	Partial Differential Equation
QP	Quadratic Program
SNR	Signal to Noise Ratio
TACS	Transcranial Alternating Current Stimulation
TBS	Transcranial Brain Stimulation
TDCS	Transcranial Direct Current Stimulation
TES	Transcranial Electrical Stimulation
TMS	Transcranial Magnetic Stimulation
UQ	Uncertainty Quantification
WM	White Matter

Chapter 1

Introduction

Neuromodulation methods are indispensable for investigating brain function and treating several neurological and psychiatric conditions [4]. These methods intervene directly with neural activity through a wide array of mechanisms, such as electromagnetic fields, acoustic waves and optics [4], and have applications varying from treatment of Parkinson's disease with implanted deep brain stimulation devices, to in-depth investigations of microscopic brain regions using optogenetics. However, most neuromodulation methods are highly invasive, requiring complex surgical interventions. To overcome these restrictions, transcranial brain stimulation (TBS) has gained a lot of attention in the past decades, as these methods show promising results in modulating brain activity without the need of surgery and with minimal side-effects.

1.1   Transcranial Brain Stimulation

Interest in using electric currents to change brain activity goes back to ancient Rome, where it was noted that using a torpedo fish to deliver a strong current through the head could cure headaches [5]. Usage of electric currents in treating psychiatric conditions became widespread with the introduction of electroconvulsive therapy (ECT) in the 1940s. ECT delivers high-amplitude electric current pulses through scalp electrodes in order to induce a seizure [5]. Although highly efficient in treating psychiatric conditions such as depression, ECT has severe side effects such as memory loss [6], which limits its adoption.

Modern Transcranial Brain Stimulation (TBS) methods allow for modulating brain activity in a non-invasive fashion and with minimal side effects, without inducing seizures. There are two main types of TBS: transcranial electric stimulation (TES), which uses electrodes placed in the scalp to create an electric field in the brain, and transcranial magnetic

stimulation (TMS) which uses a magnetic coil that creates an electric field in the brain via electromagnetic induction. TBS methods have been widely adopted for human neuroscience research, and show promising results in clinical applications.

1.1.1 Transcranial Electric Stimulation

Transcranial electric stimlation (TES) passes small electric currents, typically < 4mA, through the head using electrodes placed in the scalp [7], as shown in Figure 1.1a. These low intensity currents do not induce seizures and do not cause any of the severe side effects observed in ECT. The electric current can be direct, in the case of trancranial direct current stimulation (TDCS) [8], or alternating, in the case of transcranial alternating current stimulation (TACS) [9].

The effect of low intensity, topically applied, electric currents in altering neuron firing rates in the rodent brain has been know the 1960s [10], and of high intensity electric stimulation in humans since the 1980s [11]. However, direct evidence of the effect of low intensity TDCS in humans first became apparent around 2000, when experiments combining TDCS, TMS and electrophysiological recordings became possible [8]. Typically, the small electric fields caused by TDCS in humans are not able to generate spiking activity. However, invasive measurements in non-human primates [12] have show that these fields can induce low-frequency oscillations in the underlying tissue, which correlate with behavioral effects. TACS uses currents in the same range as TDCS, but applies them in an oscillatory fashion, with frequencies compatible with endogenous brain oscillations. It is currently thought that TACS works by entraining and augmenting such oscillations [7].

Since its discovery, interest in TES research grew rapidly [13], and was quickly adopted as a research tool [14] and as a possible treatment for several phsychiatric conditions such as depression, schizophrenia, and substance abuse [15]. However, experimental outcomes are highly variable [16] which has led to a debate about the reproducibility of the findings reported in the TES literature [17]. There are many causes for this high variability, including neurochemestry, neurophysiology, and individual anatomy [18]. Based on simulation studies, we know that electric fields in the brain are highly influenced by anatomical features such as skull and cerebrospinal fluid (CSF) thickness [19, 20], and recently variability in electric fields caused by TES were shown to partially explain the variability in experimental outcomes [21, 22, 23].

1.1.2 Transcranial Magnetic Stimulation

Transcranial magnetic stimulation (TMS) uses a large, time-varying electric current, passing through a coil placed close to the head (Figure 1.1b). This current creates a magnetic field, which by induction creates an electric field in the brain. It was first introduced in the 1980s [24, 25], and has since then became a widely used method to study human electrophysiology and cognition, as well as a possible treatment for various psychiatric disorders [26].

The electric fields created by TMS are much larger than the ones created by TES, and TMS can directly induce neural firing. For example, TMS stimulation over the motor cortex can elicit visible muscular twitch, called a motor evoked potential [27]. TMS has been approved by the United Stated Food and Drug Administration (FDA) as a treatment for drug resistant depression [28] and is being investigated as a treatment for various other neurophsyiatric conditions. However, outcomes of TMS interventions across individuals are variable [29], and managing this variability in order to obtain reliable outcomes remains a challenging. As for TES, the electric field induced by TMS depends on subject-specific anatomical factors such as gyrification [30, 31], and variations in induced electric field can partially explain variability in outcomes [32, 33, 34].
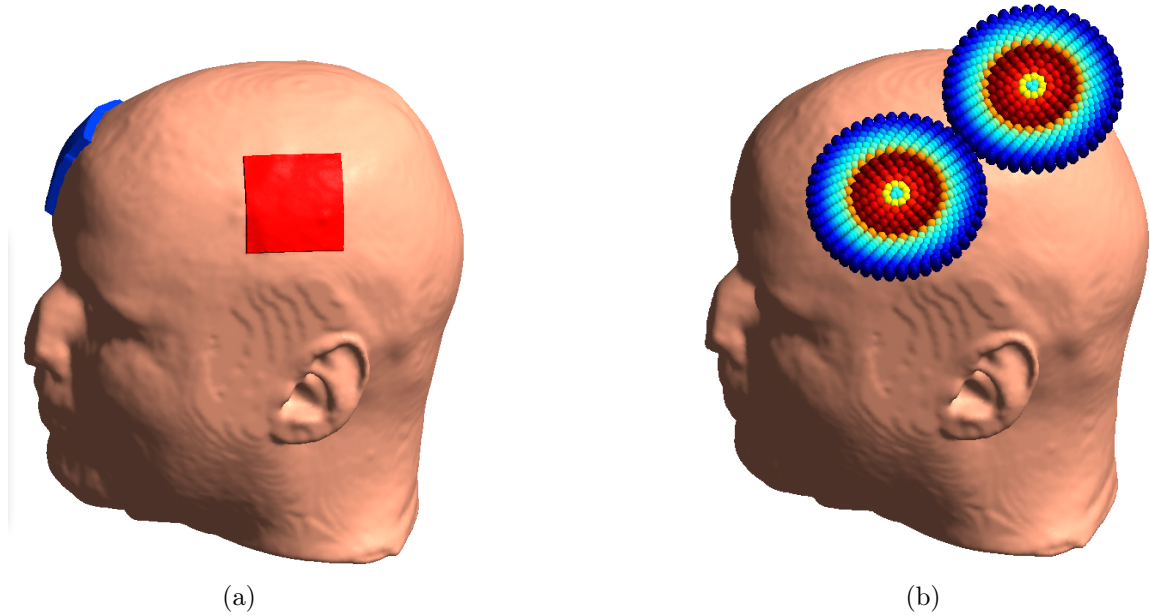

(a)   (b)

Figure 1.1: Computational models of (a) TES and (b) TMS

1.2 Computational Dosimetry

Direct measurement of electromagnetic fields within tissue is a highly invasive and labor intensive endeavour [2]. Because of these difficulties computational dosimetry methods have

been developed since the 1990s to estimate how electromagnetic fields spread in the human body [35]. These methods allow for example to plan of radiotherapy interventions [36], and for preliminary safety evaluation of various medical devices such as magnetic resonance (MR) imaging coils [37]. In this thesis, we will discuss, validate and use computational dosimetry approaches for TBS.

In 1969, Rush and Driscoll [38] developed an analytic solution for the electric field inside a three-layered sphere caused by small electrodes placed in the scalp, and found it to be in good agreement with phantom measurements. Unfortunately, in more complex geometries such as the human head, no analytical solution exists and we must resort to numerical methods such as the finite element method (FEM). Pioneer work in applying FEM to TES simulations was done by Miranda et al. [39], using realistic electrode models and a spherical head model. Anatomical head models were introduced shortly afterwards [40, 41], in order to explore how features such as gyrification affect the electric fields.

Application of computational dosimetry to TMS also started with spherical models, where analytic solutions can be obtained [42, 43]. Interestingly, in this type of model the electric field is invariant to the any radially symmetric conductivity distribution. The first studies using numerical methods such to simulate TMS electric fields relied on simplified models, such as slabs half-spheres [44, 45], and only in the late 2000s, realistic head models began to be introduced together with both FEM [46, 47, 30] as well as the boundary element method (BEM) [48]. More recently, advanced simulation methods such as boundary element method with fast multipole method acceleration (BEM-FMM) were introduced to the field [49, 50], increasing the numerical accuracy of TMS simulations.

There are however key aspects of TBS computational dosimetry that need to be addressed. First, the calculations rely on having an accurate individualized head models. Several pipelines to automatically create head models from magnetic resonance images have been proposed [51, 52, 1], but validation of the electric field estimates produced from individualized head models is challenging [2, 53]. In this thesis, we will use an openly available dataset with intracranial electric field measurements to try to validate some of these modelling tools. Second, there is a great opportunity to leverage computational models to automatically optimize TBS intervention protocols, such as electrode positions in TES [54]. We will improve some of those methods and do a comprehensive analysis of their limitations. Finally, computational dosimetry models need to be easily accessible to TBS practitioners in the form of easy-to-use, free and open source software supporting all steps of the computational dosimetry pipeline, shown in Figure 1.2. In the last part of the thesis, we will

describe our efforts to develop such software, called SimNIBS.
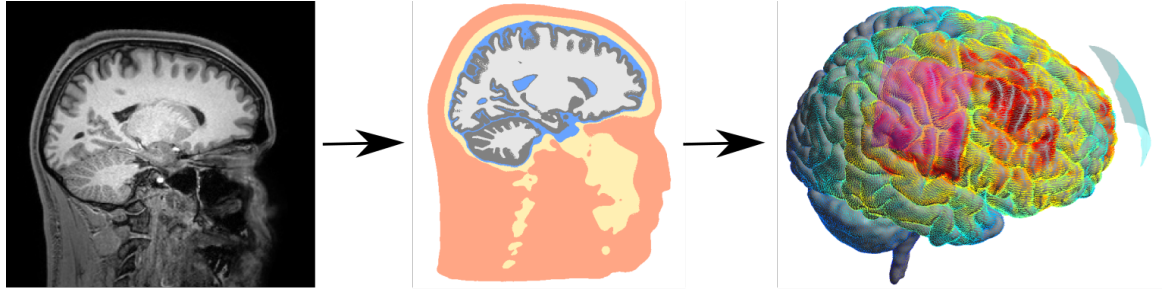
Figure 1.2: Simplified pipeline for transcranial brain stimulation dosimetry. MR images are automatically segmented and meshed to create a volume conductor model of the head. This volume conductor model can be used to perform TES and TMS simulations

1.3 Structure of the Thesis

Chapter 2 will describe the physics behind TES and TMS on a macroscopic level, as well as our numerical method of choice for solving electric field equations: the finite element method (FEM).

In **chapter 3**, we will describe approaches to build individualized head models from MR images and our efforts to validate existing modelling tools using measurement data.

Chapter 4 introduces algorithms for optimizing electrode montages for transcranial electric stimulation. We will develop novel algorithms, validate them, and present insights about their limitations.

In **chapter 5**, we will describe the implementation of electric field simulation and optimization algorithms in the open source software, SimNIBS (`www.simnibs.org`).

Finally, in **chapter 6** we will conclude by summarizing the main results of the project and future work.

Chapter 2

TBS Physics and the Finite Element Method

The behaviour of electric fields inside a volume conductor such as the human head is governed by partial differential equations (PDEs) [55, 56]. In this chapter, we will introduce the PDEs used for modelling electric fields caused by TES and TMS, as well as the finite element method (FEM), which we will use to solve these equations numerically. A more complete description of these equations and methods can be found in [57].

2.1 Physics of Transcranial Brain Stimulation

2.1.1 Transcranial Electric Stimulation

Measurements in both humans and non-human primates [58, 59] suggest that the head acts as an ohmic volume conductor at the low frequencies commonly used in TES. This means that the electric potential ϕ caused by surface electrodes inside the head domain Ω is governed by the Laplace equation [51]

$$\nabla \cdot (\sigma \nabla \phi) = 0, \tag{2.1}$$

where σ are electric conductivity values. In the current work, we will consider σ to be piecewise-constant. That is, each tissue compartment in the head model will be assigned a constant conductivity value, depending on which tissue it represents. There are alternative approaches, for example using data from MR diffusion tensor imaging (DTI) in order to try to reconstruct electric conductivity tensor maps [60, 61, 31]. However, as these methods have not been thoroughly validated thus far, we adopted the simpler approach considering isotropic, piecewise-constant conductivities.

Considering that two electrodes, whose surfaces are denoted Γ_1 and Γ_2, are used for stimulation, we have the boundary conditions

$$\phi = 0 \quad \text{on } \Gamma_1, \tag{2.2}$$

$$\phi = \phi_1 \quad \text{on } \Gamma_2, \tag{2.3}$$

$$\frac{\partial \phi}{\partial \hat{\boldsymbol{n}}} = 0 \quad \text{on } \partial\Omega \setminus (\Gamma_1 \cup \Gamma_2), \tag{2.4}$$

where $\hat{\boldsymbol{n}}$ denotes the direction normal to the surface. In multichannel TES, N electrodes are attached to the head simultaneously. In this case, we add more electrodes surfaces $\Gamma_3, \ldots, \Gamma_N$ and their corresponding electric potential values. As in TES protocols electric current values, and not the electric potentials values, are specified, we first solve the equations using $\phi_1 = 1\text{V}$, measure the current flow, and scale the results in order to obtain the specified current flow value and direction.

After calculating the electric potential ϕ, we can readily obtain the electric field $\boldsymbol{E}$ and the current density $\boldsymbol{J}$

$$\boldsymbol{E} = -\nabla\phi, \tag{2.5}$$

$$\boldsymbol{J} = \sigma\boldsymbol{E}. \tag{2.6}$$

If electrode currents vary in time, such as in tACS, we can use the linearity of the Laplace equation to decompose the electric field into a spatial component, which only depends on spatial position $\boldsymbol{p}$, and a temporal component, which only depends on time t

$$\boldsymbol{E}(\boldsymbol{p}, t) = \boldsymbol{E}(\boldsymbol{p})I(t). \tag{2.7}$$

2.1.2 Transcranial Magnetic Stimulation

At the typical frequencies used in TMS (≈ 10 kHz), electric fields can be well described using a quasi-static approximation, which leads to a Poisson equation [44]

$$\nabla \cdot (\sigma\nabla\phi) = -\nabla \cdot \sigma\frac{\partial \boldsymbol{A}}{\partial t} \tag{2.8}$$

with the Neumann boundary conditions

$$\frac{\partial \phi}{\partial \hat{\boldsymbol{n}}} = -\hat{\boldsymbol{n}} \cdot \frac{\partial \boldsymbol{A}}{\partial t} \quad \text{on } \partial\Omega. \tag{2.9}$$

Here, $\boldsymbol{A}$ is a magnetic vector potential. This quantity is defined such that $\boldsymbol{B} = \nabla \times \boldsymbol{A}$, where $\boldsymbol{B}$ is the magnetic field produced by the coil. The spatial distribution of a coil magnetic field $\boldsymbol{B}(\boldsymbol{p})$ depends on its geometric properties such as shape, number of turns and radii.

The electric field $\boldsymbol{E}$ produced by TMS has two components, one that is produced directly by the coil, commonly called *primary electric field*, and another that is produced by charge dispersion in the volume conductor, called *secondary electric field*

$$\boldsymbol{E} = -\frac{\partial \boldsymbol{A}}{\partial t} - \nabla \phi. \tag{2.10}$$

2.2   Finite Element Method

The finite element method (FEM) is a general method for solving partial differential equations (PDEs) in complex geometries. It was introduced in the 1960s and 1970s, in the domain of structural analysis [62], and generalized to other domains such as thermodynamics and electromagnetism shortly afterwards [63].

The basic concept of the FEM is to *discretize* the space into a large number simple elements, such as triangles or tetrahedra, which form a structure called a *mesh*, shown in Figure 2.1. We then use these elements to define a set of simple basis functions with local support. When summed together, these basis functions can represent complex functions spanning the entire domain. Basis functions are usually differentiable (but not necessarily smooth), which allows for the definition of numerical gradient operators, that play a fundamental role in solving PDEs.

The FEM formulations and implementations used to calculate TES and TMS electric fields in this thesis were thoroughly described and validated in a recent publication [57] as well as in the Master's thesis published after the first part of the PhD program [64]. Namely, we used the Galerkin method with first order tetrahedral elements. Here, we will summarize it briefly.

2.2.1   Mathematical Formulation

We begin by considering a Poisson equation in the form

$$\nabla \cdot (\sigma \nabla \phi) = f. \tag{2.11}$$
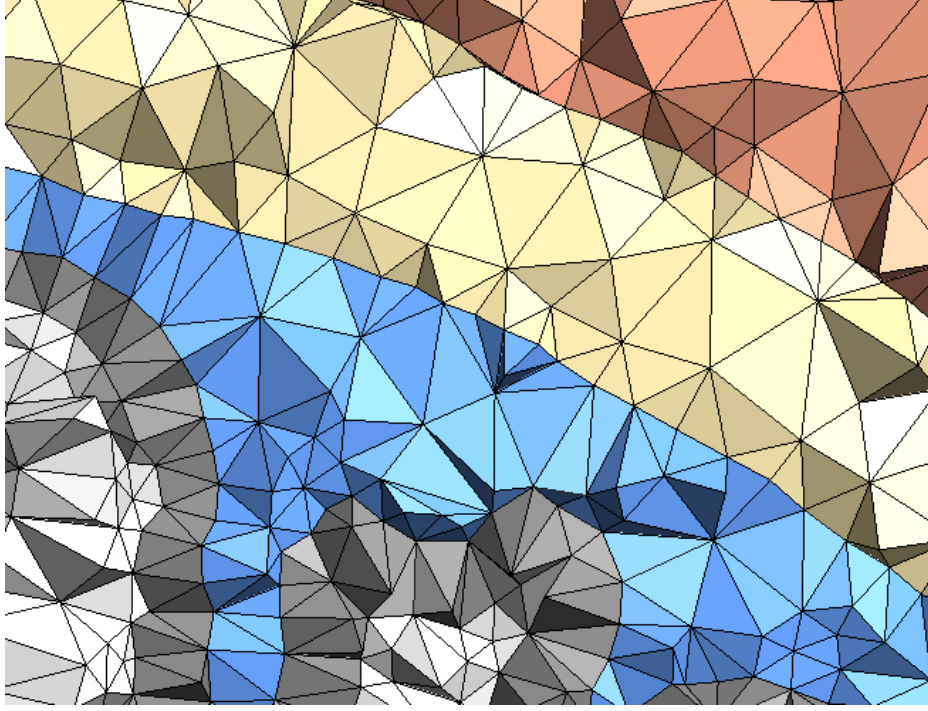
Figure 2.1: Close-up of multi-material tetrahedral head mesh with white matter (white), gray matter (gray), cerebrospinal fluid (blue), skull (beige) and skin (pink)

In TES, we have $f = 0$, while in TMS $f = -\nabla \cdot \sigma \partial \boldsymbol{A}/\partial t$. We then define a residual $r(\phi)$

$$\nabla \cdot (\sigma \nabla \phi) - f = r(\phi), \tag{2.12}$$

and introduce a test function ν, which belongs to an appropriate functional space $\mathcal{V}$ (please see [57] for more details). It can be shown that any function ϕ for which the residual $r(\phi)$ is orthogonal to all test functions $\nu \in \mathcal{V}$ [63]

$$\int_\Omega r(\phi)\nu dV = 0, \quad \forall \nu \in \mathcal{V}, \tag{2.13}$$

is also a solution to Equation 2.11. Substituting Equation 2.13 into Equation 2.12, applying Green's identities and the boundary conditions, we obtain the *weak form* of the Poisson equation [65, 57]

$$\int_\Omega \nabla \nu \cdot (\sigma \nabla \phi) \, dV = \int_\Omega f\nu dV, \quad \forall \nu \in \mathcal{V}. \tag{2.14}$$

Substituting the infinite-dimensional ϕ by a finite-dimensional ϕ^h using a set of basis

functions $\{\psi_i(\boldsymbol{p}) | i = 1, \ldots, N\}$

$$\phi^h = \sum_{i=1}^{N} \phi_i \psi_i(\boldsymbol{p}) \tag{2.15}$$

and $\mathcal{V}$ with the space spanned by the basis functions, $\mathcal{V}^h$, in Equation 2.14, we obtain

$$a^h(\phi^h, \nu^h) = l^h(\nu^h), \quad \forall \nu^h \in \mathcal{V}^h, \tag{2.16}$$

$$a^h(\phi^h, \nu^h) = \sum_{i=1}^{N} \phi_i \int_{\Omega} (\sigma \nabla \psi_i(\boldsymbol{p})) \cdot \nabla \nu^h dV, \tag{2.17}$$

$$l^h(\nu^h) = \int_{\Omega} f \nu^h dV. \tag{2.18}$$

By substituting $\nu^h = \psi_1, \ldots, \psi_N$ and numerically evaluating the integrals in Equation 2.17 and Equation 2.18, we obtain a linear system

$$\boldsymbol{S}\boldsymbol{u} = \boldsymbol{b}. \tag{2.19}$$

Which has to be solved in order to obtain the electric potential $\boldsymbol{\phi}^h$ (corresponding to entries in the vector $\boldsymbol{u}$). The matrix $\boldsymbol{S}$, called *stiffness matrix*, is large, of size $> 10^5 \times 10^5$ in our applications. However, because the basis functions have compact support, the matrix is sparse and can therefore be stored in computer memory. Additionally, because of the formulation of the problem, the matrix $\boldsymbol{S}$ is symmetric and positive (semi)definite, allowing for the use of a wide range of numerical iterative and direct methods in order to solve Equation 2.19 [66].

2.2.2   Implementation

There are many software implementations of FEM. In the current work, we used versions 2 and 3 of SimNIBS (`www.simnibs.org`), developed in-house. Version 2 of SimNIBS uses the open-source software GetDP [67] in order to assemble the FEM system, which in turns calls the PETSc library [68] to solve it using the conjugate gradient method with an incomplete Cholesky preconditioner. Version 3 of SimNIBS implements its own code to assemble the FEM system, described, validated, and shown to be much faster than SimNIBS 2 in [57]. It uses the PETSc and the hypre [69] libraries to solve the FEM system using the conjugate gradient method with an algebraic multigrid preconditioner [69], or the MKL PARDISO [70] direct solver.

Chapter 3

Validation of Computational Models for TBS

While the equations governing electric fields in volume conductors are well known, the spatial distribution of electrical properties such as conductivity in any individual's head is uncertain. And as electric conductivity values varying widely across tissues, from ≈ 0.01 S/m in skull to ≈ 1.5 S/m in cerebrospinal fluid (CSF) [71], accurately determining tissue borders are a key factor for obtaining reliable electric field simulations [71, 57, 72]. Furthermore, the electric conductivity values themselves are not well known, with a wide range of values being reported in the literature [71], and by combining simulations and measurements we might be able to obtain more information about tissue conductivity values and therefore more accurate electric field estimates [73]. In the current chapter, we will describe current approaches for automatically creating head models for TBS simulations and our efforts to validate computational models based on intracranial electric field measurements, summarizing an article published in the journal *NeuroImage* [53], reproduced in Appendix A.

3.1   Head Modelling

In order to accurately capture volume conduction effects, we need to have individualized head models with the major tissues such as brain white matter (WM), brain gray matter (GM), CSF, skull, and scalp segmented [72]. These segmentations are usually done based on MR images, as MR scans do not use ionizing radiation, do not require contrast agents, and offer a good contrast between soft tissues [1], as shown in Figure 3.1. However, manual segmentation of MR images is a very time-demanding task, with a single subject taking dozens of hours of labour. In order to automate this process, several head modelling tools have been proposed

over the years for TBS, electro- and magnetoencephalography (EEG/MEG) applications [74, 75, 51, 76, 1, 77].
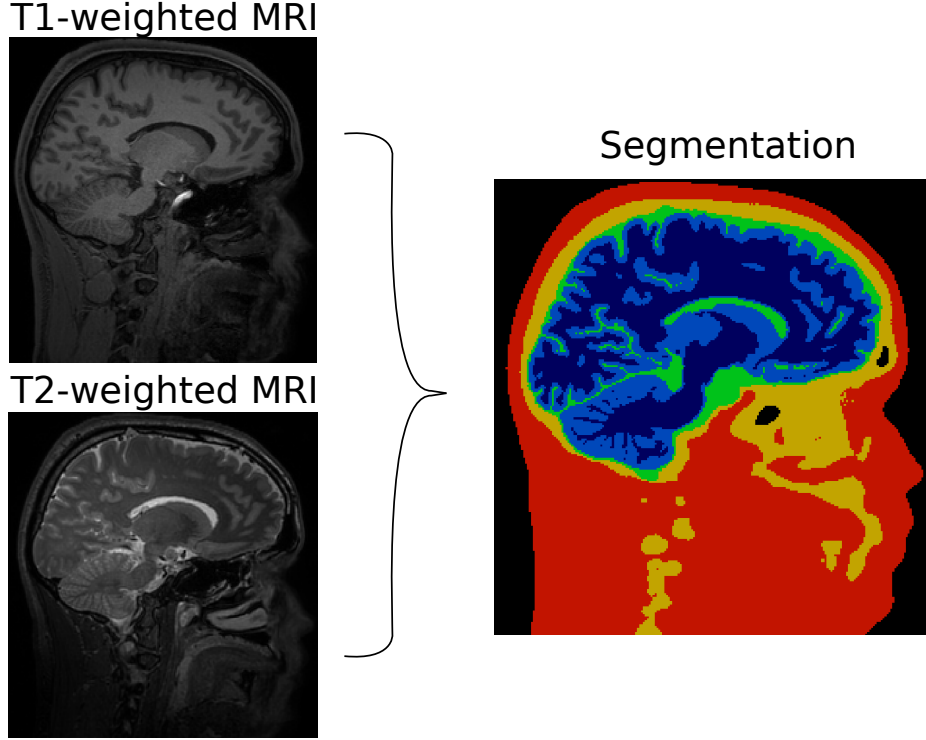
Figure 3.1: Automatic segmentation of T1- and T2-weighted MR images into white matter (dark blue) gray matter (light blue), CSF (green), skull (yellow) and scalp (red) using *headreco* [1].

One of these tools, called *mri2mesh* [51], is part of the SimNIBS package (`www.simnibs.org`) and leverages the brain segmentation approaches implemented by FreeSurfer (`https://surfer.nmr.mgh.harvard.edu/`) [78], which uses a volume segmentation of the cortical white matter compartment and local image gradients to segment cortical gray matter. CSF, skull and scalp are segmented with FSL (`https://fsl.fmrib.ox.ac.uk/fsl/fslwiki`) BET and BETSURF [79], which uses local image thresholds. In the other hand, ROAST (`https://www.parralab.org/roast/`) [76], and *headreco* (also part of the SimNIBS package) [1] use the atlas-based segmentation implemented in SPM (`https://www.fil.ion.ucl.ac.uk/spm/`) [80]. In this approach, the MR images are registered to a template in a non-linear fashion. This template is combined with local MR image intensities to yield the probability for each voxel to belong to each tissue.

A direct comparison using computational tomography scans, which give a sharp contrast between skull and soft tissue, showed that the atlas-based approach implemented in SPM provide more accurate skull segmentations than FSL BET and BETSURF [1]. However, more in-depth comparisons of these tools are still lacking, especially when considering their

effect in the final outcome: electric field simulations.

3.2   Electric Field Measurements

In-vivo intracranial measurements of electric fields are a challenging procedure, usually involving surgical implantation of electrodes. Therefore, these measurements are done either in non-human primates [59], postmortem [81], or in epilepsy patients which have EEG electrodes implanted in order to help localize epileptic foci [2].

However, these electrodes measure electric potentials, and not electric fields, are susceptible to measurement noise, and are spatially limited to a few dozen points for in-vivo studies or a few hundred in postmortem studies. Thus, one can only obtain a sparse, low-resolution, and uni-directional picture of the electric field through these measurements. Furthermore, the segmentation tools proposed are not designed for non-human primates, which means that accuracy estimates obtained in these animals do not necessarily translate to humans, and death results in profound changes in electric conductivity [82], which limits the usability of postmortem data for model validations.

3.3   Validation of TBS Computational Dosimetry Using Intracranial Recordings

Our analysis, reproduced in full in Appendix A, evaluated four head segmentation pipelines: *mri2mesh* [51], *headreco* [1], *headreco + CAT* [1] and *ROAST* [76], using an an openly available dataset with T1-weighted MR scans and intracranial EEG measurements taken during TES [2]. The dataset comes from a study with 14 epileptic patients which had EEG electrodes implanted to monitor seizure activity (see Figure 3.2). The dataset contained, for each subject a T1-weighted MR image acquired before the surgery, a segmented MR image with manual corrections, and a table of intracranial EEG electrode positions and processed electric potentials recorded during TES.

Stimulation electrodes were positioned mostly in a frontal-occipital setup, with some variations between subjects, as shown in Figure 3.2. One particular subject had recordings done with four different stimulation electrode setups.

3.3.1   Methods

Our analysis began by evaluating the quality of the head segmentations. However, because there were visible mistakes in the manually corrected segmentations (see for example Figure
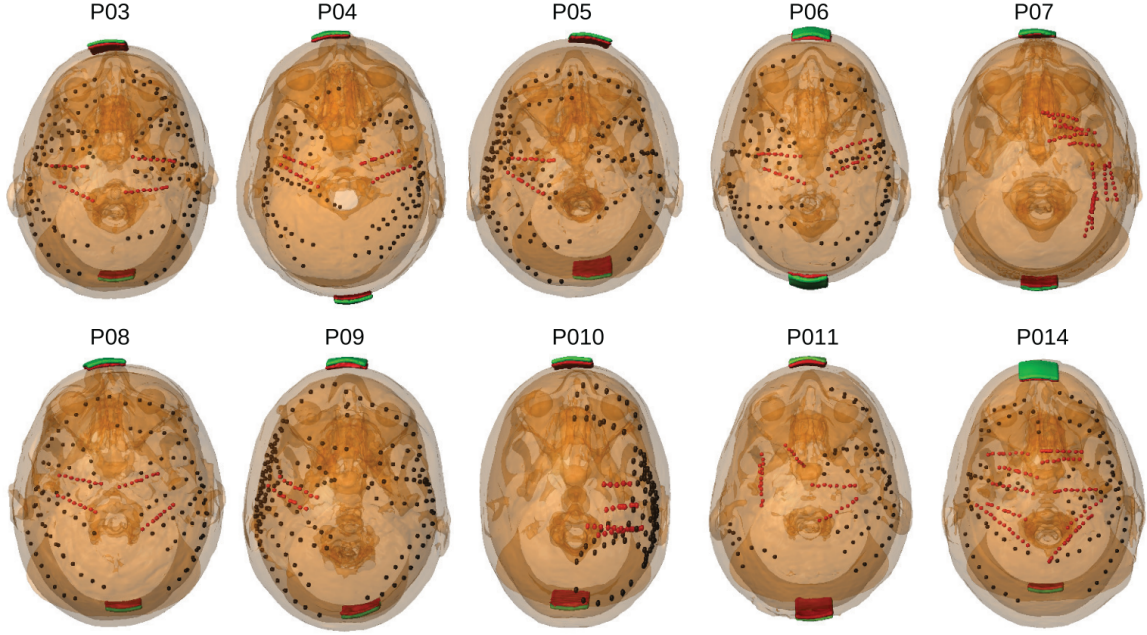
Figure 3.2: Electrode locations in 10 of of the 14 subjects in the dataset from [2]. Copyright: Huang et al., distributed under a CC-BY-4.0 License without modifications

3 of Appendix A, where the gray matter is clearly over-segmented), and those were based on ROAST segmentations, which could induce biases, we used a consensus segmentation as the ground truth. The consensus was formed from majority voting, where each segmentation method, plus the manually corrected segmentation, cast a vote for the label of each voxel, and the label with the most votes wins.

Afterwards, to to have an overview in the amount of variability in the electric fields simulated with each pipeline, we simulated electric fields using the electrodes montages described in the dataset and interpolated results into the middle gray matter model obtained from CAT12 (`http://www.neuro.uni-jena.de/cat/`) [83]. This allowed us to compare electric fields in the entire brain, an not only where the EEG electrodes were placed.

Finally, we compared the simulated electric fields with the intracranial measurements. This process began by producing electric field estimates taking differences between electric potentials obtained both from measurements and simulations at consecutive electrode contacts. After running a simple regression analysis, as done by [2, 76], we found significant biases in the results, as slope estimates were correlated with electric field strengths (see Figure 8 in Appendix A). This bias likely arises because there are errors in the simulations, caused by segmentation errors due to low image quality and erroneous conductivity values, as well as noise in the measurements. As the signal to noise ratio (SNR) in both simulations and measures decrease, a large bias sets in which reduces slope estimates [84]. This led us to propose a new analysis, based on a Bayesian hierarchical errors-in-variable regression [85].

In this setting, we assume that the electric field recordings $\boldsymbol{y}_s$ and each subject s and simulations $\boldsymbol{x}_{s,m}$ calculated for each subject s and segmentation method m have a joint Gaussian distribution

$$(\boldsymbol{y}_s, \boldsymbol{x}_{s,m}) \sim \mathcal{N}(\boldsymbol{\mu}_{s,m}, \boldsymbol{\Sigma}_{s,m}), \tag{3.1}$$

with a mean vector and a noise covariance matrix

$$\boldsymbol{\mu}_{s,m} = \boldsymbol{x}_{s,m}^* \left[\beta_{s,m}, 1\right], \tag{3.2}$$

$$\boldsymbol{\Sigma}_{s,m} = \begin{bmatrix} \sigma_{y,s}^2 & 0 \\ 0 & \sigma_{x,s,m}^2 \end{bmatrix}, \tag{3.3}$$

where $\beta_{s,m}$ is a scalar slope value, $\boldsymbol{x}_{s,m}^*$ are unobserved error-free simulated values, $\sigma_{y,s}^2$ and $\sigma_{x,sm}^2$ are noise terms for the measurements and simulations, respectively. Now we define prior probability distributions

$$x_{s,m}^* \sim \mathcal{N}(0, \sigma_{t,s,m}^2,) \tag{3.4}$$

$$\beta_{s,m} \sim \mathcal{N}(\beta_m, \sigma_{\beta,m}^2), \tag{3.5}$$

where $\sigma_{t,s,m}^2$ is the variance of the unobserved error-free simulation, β_m is a hyperparameter representing the slope for method m, and $\sigma_{\beta,m}^2$ the slope variation. Distributions for the remaining priors and hyper-priors are detailed in supplementary material 1 from [53]. We sampled posterior values for the model parameters using the No-U-Turn Hamiltonian Monte Carlo sampler [86], implement in the Stan probabilistic programming language [87].

3.3.2 Results

Our analysis of the segmentation pipelines showed that the two *headreco* pipelines, as well as the manually corrected segmentations, are more similar to the consensus segmentation with a mean Dice score > 0.9 (see Results in Appendix A). Unfortunately, the dataset only includes T1-weighted scans, many of which are of low quality. It is therefore inappropriate to draw conclusions about which segmentation method would be more accurate in a high-quality dataset. Moreover, an analysis of the simulated electric fields in the whole middle cortical surface showed large variations between the different methods, up to 49% difference between *ROAST* and *mri2mesh* (Table 4 in Appendix A). Using a median split, we saw that segmentations with lower dice score also tend to have more distinct electric fields, as

expected (Figure 4 in Appendix A).

Despite such large differences in the electric fields in the cortex, the simple regression model showed no statistically significant results when comparing slope (β) or explained variance (r^2) between the methods. Besides, this analysis resulted in a large variability of both β and r^2 values across subjects and methods (Figure 7 in Appendix A). One constant, however, is that simulations tended to overestimate the field values (average $\beta <$ 0.65 for all methods), and none explained the data particularly well (average $r^2 < 0.6$ in all methods). By plotting the slope values β against the measured field magnitudes (Figure 8 in Appendix A), we were able to detect a likely bias: the smaller the field magnitudes, the smaller the slope tends to be. One subject, called P014, gave particularly good insight into this problem. In this subject, four different stimulation electrodes montages were used, instead of only one as for the 13 other subjects. By comparing two different montages, we were able to see this likely bias in effect (Figure 9 in Appendix A), where montages causing smaller electric fields in the electrodes, and therefore lower SNR, also led to smaller slope estimate.

Using the Bayesian errors-in-variables regression, we were able to calculate posterior probability distributions for the regression slopes, taking into account noise sources in both measurements and simulations. We saw that the slopes obtained from the Bayesian analysis tended to be larger than the slopes from the standard analysis, again indicating a risk of bias in the later. We also saw that, as the measured electric field magnitude gets smaller, the posterior distributions for the slope spreads out, indicating less confidence in the fit (see Figure 9 in Appendix A for an example). Finally, calculating the posterior predictive distribution for the slope in each method, $\tilde{\beta}_{s+1,m}$, that is, a probability distribution for the slope we would obtain in a new unbosverved subject with each of the pipelines, we see a large spread of possible slope values and little difference across methods (see Figure 10 and Table 4 in Appendix A). This indicates that, based in this dataset, we are not able to say which of these TBS computational dosimetry pipelines performs better in predicting the electric field as measured by intracranial electrodes.

3.4 Discussion

While several pipelines for individualized head modelling have been developed for TBS, EEG, and MEG applications, their validation is challenging as direct measurements of electric fields in the brain require surgical interventions. In Appendix A, we used the publicly available dataset from [2], containing T1-weighted images, segmentations and intracranial

recordings of various subjects, in order to try to validate and compare four head segmentation pipelines. Despite large differences in the simulated electric fields obtained by the segmentation methods, none of the pipelines performed better in predicting the recorded electric fields. Furthermore, our analysis pointed to possible biases in the original results [2] as well as in a follow-up study [76]. However, due to many data quality problems in the dataset, we do not believe that this should be taken as a final comparison between the given TBS pipelines.

Our results indicate that a lot of care needs to be taken when designing studies to validate TBS computational dosimetry models with intracranial recordings. First of all, the MR scans need to be of high quality and include both T1- and T2-weighted images in order to obtain accurate segmentations of extra-cerebral tissues [1]. Second, as we observed from our analyses of the subject P014, positioning of the stimulation electrodes has a large impact in the measurements. Therefore, the stimulation electrodes should be positioned in such a way as to maximize the electric fields in the recording electrodes for a better SNR and consequently more reliable field estimates.

Finally, the issue of conductivity value assignment was not tackled in the current study. Recently, we have shown that uncertainties in tissue conductivity values can result in large uncertainty in the electric fields [71], which could partially explain the inaccuracies in the electric field simulations. One could try to use intracranial measurements to fit electric conductivity values using the present dataset, such as Huang et al. [2]. However, likely due to the various problems present in the dataset, Huang et al. arrive at physiological implausible values (e.g.: $\approx 1 \mathrm{S/m}$ conductivty for skull) and contradictory values (e.g.: both $\approx 0.15 \mathrm{S/m}$ and $\approx 0.35 \mathrm{S/m}$ for WM in the same subject), which suggests that determining conductivity values from this dataset is unreliable.

Magnetic resonance current density imaging (MRCDI) [88] might offer a good alternative to invasive intracranial measurements for model validation and conductivity calibration. MRCDI can measure one component of the magnetic fields caused by the TES electric currents, and thereby partially reconstruct current flow in a 2D slice. Even though MRCDI has seen significant advances in recent years, the technology has not yet reached the SNR required for validating electric field models.

3.5 Contributions

GBS performed simulations, electric field comparisons, and wrote the Stan code for fitting measurements and simulations. Oula Puonti (OP), performed and compared the segmenta-

Chapter 4

Optimization of TES Electrode Montages

Individual head anatomy shapes the electric fields in complex ways [41, 89, 20]. This makes using rule-of-thumb approaches for TES targeting, such as placing the electrode above the region of interest, unreliable [90]. Additionally, the development of multichannel TES devices opened up many new possibilities for electrode montages and targeting strategies, such as 4x1 montages, which uses a central electrode surrounded by four electrodes of opposite polarity [41]. However, to fully leverage these systems and obtain the best electrode montages to focus the electric field in a target region, such as shown in Figure 4.1, we need to adopt computational strategies. There are many open questions about how to best formulate the TES targeting problem, how to efficiently limit the number of electrodes used by optimized montages, and what are the main factors limiting field focality. In this chapter, we will give a brief introduction to mathematical optimization, describe the previous work on TES optimization, and then introduce our contributions to the topic, which include a novel formulation of the optimization problem which can be solved very efficiently, an extensive evaluation of which factors play an important role in obtaining focal TES fields, and a novel algorithm capable of optimizing electric field focality while controlling electric field strength. These contributions are also described in two articles, one published in the journal *NeuroImage* [3] reproduced in Appendix B, and another accepted for publication in the *Journal of Neural Engineering* [91], reproduced in Appendix C.
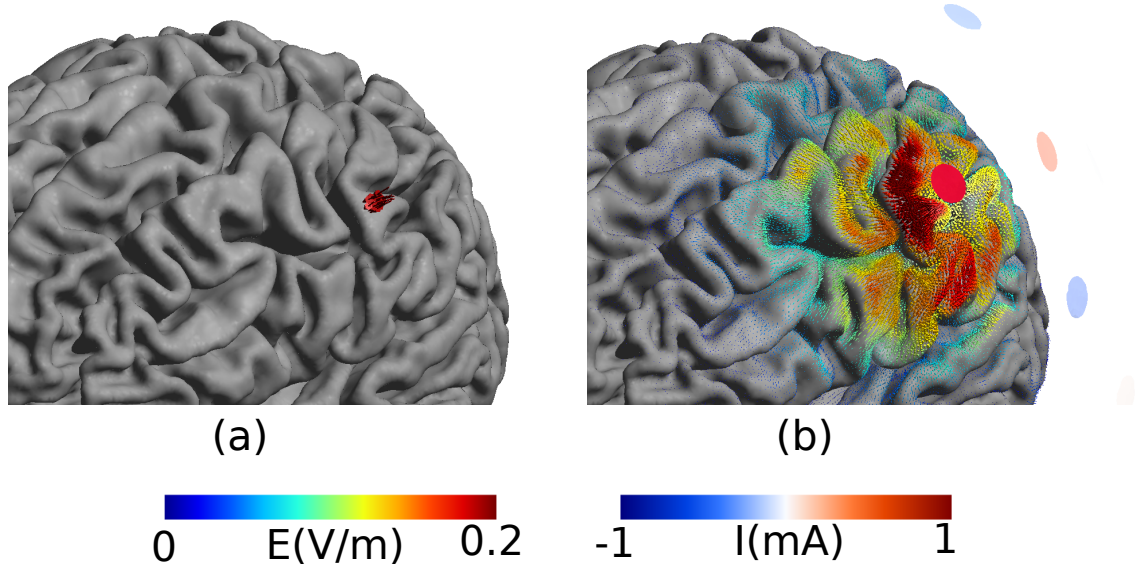
Figure 4.1: Objective of TES targeting procedures: Given a target region (a), find the best electrode configuration to focus the electric field around it (b)

4.1 Mathematical Optimization

Mathematical optimization is a widely used tool with applications ranging from finance to electronic circuit design. A general optimization problem has the form [92]

$$\text{minimize} \quad f_0(x), \tag{4.1}$$

$$\text{subject to} \quad f_i(x) \leq b_i, \quad i = 1, \ldots, m. \tag{4.2}$$

Where x is the *optimization variable*, typically a vector in $\mathbb{R}^n$ which can be changed in order to find the minimum value of the *objective function* $f_0(x) : \mathbb{R}^n \to \mathbb{R}$, while also adhering to the *constraints* $f_i(x) \leq b_i$.

Depending on the functions $f_i(x)$, $i = 0, \ldots, m$, the optimization problem might be categorized into different classes, each with different properties and solution algorithms. Of those classes, the *convex problems* are particularly important. Convex problems have all $f_i(x)$, $i = 0, \ldots, m$ functions convex. This means that they must fulfill for all points x_1 and x_2 in the function domain

$$f(\theta x_1 + (1 - \theta) x_2) \leq \theta f(x_1) + (1 - \theta) f(x_2), \quad \forall \theta \in [0, 1]. \tag{4.3}$$

That is, if we trace a line between any two points $((x_1, f(x_1)), (x_2, f(x_2)))$ in the function graph, this line will be above the graph in the interval $[x_1, x_2]$, as shown in Figure 4.2. Solving convex problems has several theoretical and practical advantages over solving more

complex problems such as general nonlinear problems or combinatorial problems. Convex problems are guaranteed to have a single minimum value, and can be solved reliably and efficiently using interior-point methods [92]. However, not every problem we will address in this chapter will be convex, with combinatorial problems will also playing a major role in TES optimization.
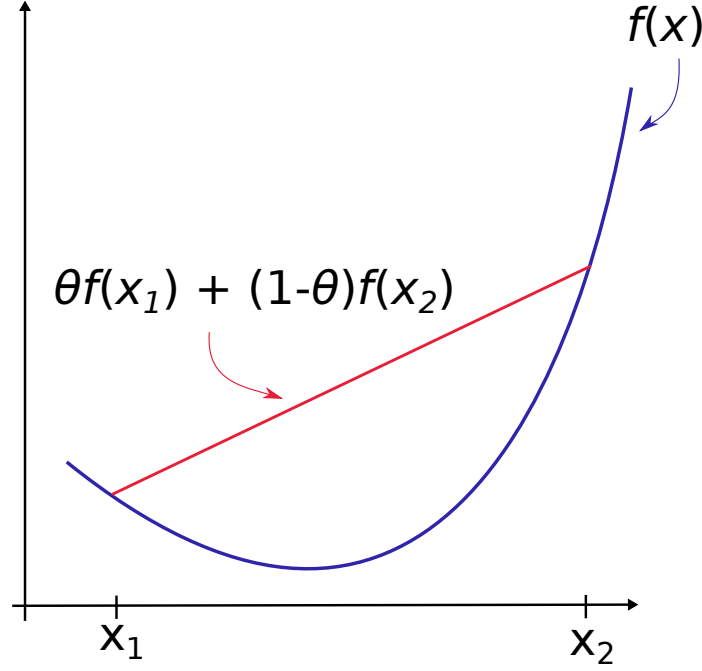
Figure 4.2: The graph of the convex function $f(x)$ must be beneath the line traced between points in the graph

4.2 TES Targeting

The idea of using computational methods for automatically determining electrodes positions in in multichannel TES systems can be traced back to Park et al. [93] and Dmochowski et al. [54]. Park et al. idealized a montage using two large electrodes composed of several patches which can be controlled independently. They then proposed maximizing the current density norm in a target region while controlling the electric potentials in the patches, which is a non-convex problem. In the other hand, Dmochowski et al. proposed using many small (12 mm diameter) electrodes placed all over the head, for example using an EEG cap, such as shown in Figure 4.3. The authors then propose several formulations of the optimization problem: one where the optimization tries to approximate a target field in a least-squares sense, one where the electric field in the target region is tightly controlled at a given value while the field outside the target is minimized, and finally a maximization approach where the electric field at the target region and direction is maximized. All the problems proposed

by Dmochowski et al. are convex.
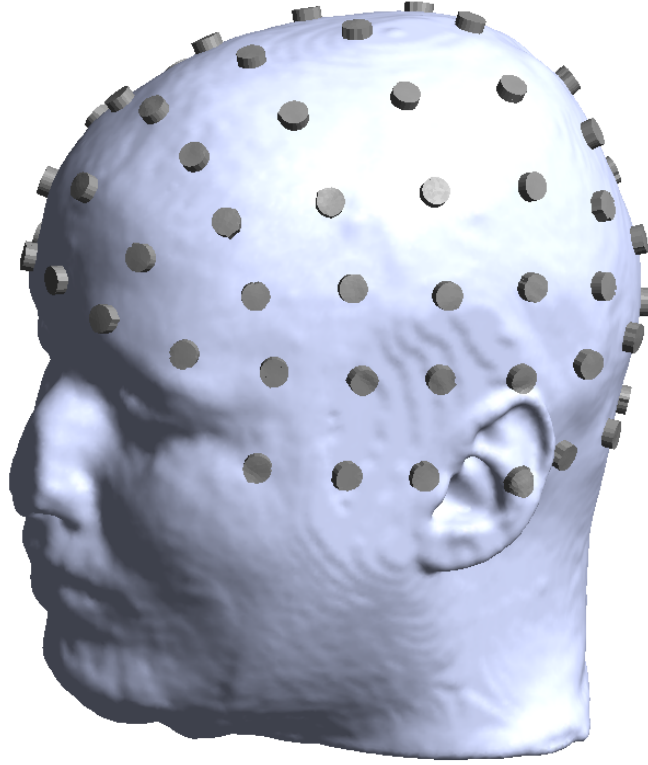
Figure 4.3: Head models with EEG electrodes placed accordingly to the 10/10 international standard

After these initial results, many other formulations and solutions methods for the TES optimization problem where proposed. Most notably, Ruffini et al. [94] proposed using distributed maps obtained from resting state functional MRI as optimization targets, and a genetic algorithm to solve the optimization problem while limiting the number of active electrodes. Wagner et al. [95] proposed an approach where the electric fields outside the target are constrained to a given value, and an optimization algorithm based on the alternating direction method of multipliers. Guler et al. [96] proposed an approach where the electric field energy outside the target region is controlled, while the electric field in the target region and direction is maximized. The authors later expanded their approach in order to limit the number of stimulator channels used with a branch and bound algorithm [97]. Finally, Fernandez-Corazza et al. [98] showed how several of these optimization problems are equivalent.

What most of these approaches have in common is that they keep electrode positions fixed and only change electrode currents or potentials. This allows for using the linearity of the electric field with respect to the injected current, a property arises as the head is an ohmic conductor at low frequencies [58, 59, 2]. Suppose we have an electric field $\boldsymbol{E}(\boldsymbol{p}; I_1, I_2, I_3)$,

which is induced by injecting the currents I_1, I_2, and I_3 through three scalp electrodes, with Kirchhoff's law requiring that $\sum_{i=1}^{3} I_i = 0$. Positive currents designate anodes and negative currents cathodes. Linearity means that we can write

$$\boldsymbol{E}(\boldsymbol{p}; I_1 = a, I_2 = 0, I_3 = -a) = a\boldsymbol{E}(\boldsymbol{p}; I_1 = 1, I_2 = 0, I_3 = -1) \tag{4.4}$$

and

$$\begin{aligned}\boldsymbol{E}(\boldsymbol{p}; I_1 = a, I_2 = b, I_3 = -a - b) &= \boldsymbol{E}(\boldsymbol{p}; I_1 = a, I_2 = 0, I_3 = -a) \\ &+ \boldsymbol{E}(\boldsymbol{p}; I_1 = 0, I_2 = b, I_3 = -b).\end{aligned} \tag{4.5}$$

This allows us to superimpose fields in order to quickly calculate electric fields for new montages. Taking this further, in a discrete setting with m positions and n electrodes, we can calculate electric fields using a matrix-vector multiplication

$$\boldsymbol{e} = \boldsymbol{A}\boldsymbol{x}. \tag{4.6}$$

Where $\boldsymbol{e}$ is a vector with the three electric field components in a set of points, of size $3m$. $\boldsymbol{A}$ is a matrix whose columns are electric field simulation results for each electrode, called *leadfield matrix* of size $3m \times n$. $\boldsymbol{x}$ is a vector of electrode currents, of size n. Typically, we have $m \gg n$, with m in the order of 10^3 to 10^6, and n in the order of 10^1 to 10^2.

In order to make the solutions safe to be used in practice, two constraints are added to the optimization problem:

$$|x_i| < I_{\text{ind}}, \quad \forall i = i, \ldots, m, \tag{4.7}$$

$$\|\boldsymbol{x}\|_1 < 2I_{\text{tot}}. \tag{4.8}$$

Equation 4.7 limits the current that can be injected through each electrode to a value I_{ind}, typically $\leq$ 2mA, while Equation 4.8 limits the total current that can be injected through all electrodes, typically $\leq$ 4mA.

4.3 Determining TES Trade-Offs

Trade-offs are inherit of any multi-objective optimization problem. In optimization of TES montages, the most apparent trade-off happens between field focatity and intensity at the target [54], as many factors that increase the electric field at the target, such as using

electrodes positioned more distant to each other, also cause the electric field to be less focal. There are however many other trade-offs and costs which were so far not extensively mapped, such as how many active electrodes we can make use to create focal fields. In [3], reproduced in full in Appendix B, we set out to answer these questions.

4.3.1 Methods

In order to map the trade-offs, it is important to explicitly control electric field properties such as the value of a given electric field component at the target. Using the leadfield formulation, we can calculate the electric field component along a given direction $\hat{n}$ a target region Ω_τ using a linear form

$$\boldsymbol{l}^\top \boldsymbol{x}, \tag{4.9}$$

developed in detail in Section 2.1.1 of Appendix B as well as in [96]. Furthermore, the potential energy stored the electric field can be calculated using a quadratic form

$$\boldsymbol{x}^\top \boldsymbol{Q} \boldsymbol{x}, \tag{4.10}$$

developed in Section 2.1.2 of Appendix B and in [96].

Using these quantities, we proposed new formulations for the TES optimization, based on the problem:

$$\text{minimize} \quad \boldsymbol{x}^\top \boldsymbol{Q} \boldsymbol{x}, \tag{4.11}$$

$$\text{subject to} \quad \boldsymbol{l}^\top \boldsymbol{x} = t, \tag{4.12}$$

$$\boldsymbol{1}^\top \boldsymbol{x} = 0, \tag{4.13}$$

$$|x_i| < I_{\text{ind}} \quad \forall i = i, \dots, m, \tag{4.14}$$

$$\|\boldsymbol{x}\|_1 < 2I_{\text{tot}}. \tag{4.15}$$

In this optimization problem, the objective (Equation 4.11) is to minimize electric field energy, while keeping the electric field at a given target location and direction at a given value t (Equation 4.12). This explicit control over a given electric field component in the target location allows us to keep this key value constant while varying other parameters of the optimization problem. We also add Kirchhoff's current law (Equation 4.13) and safety constraints (Equations 4.14 and 4.15), in order to make solutions viable for experimental use. This formulation draws heavily from Guler et al. [96], but with the key modification of switching some constraints and objectives.

There are several advantages of using this type of formulation. First of all, it is very explicit, with the electric field at the target position and direction being directly set by the user in physical units (V/m). Electric field values are often reported in the literature, and different ranges of electric field values are thought to have different effects in neurons [7]. Also, it is very flexible, allowing us to define several equality constraints such as Equation 4.12 if many regions are to be targeted simultaneously, and to control other aspects of the field such as field angle at the target (see Section 2.2.3 in Appendix B). Finally, the optimization problem such as defined above is a quadratic programming (QP) problem [92], which can be solved very efficiently. In our study, we implemented an active-set method [99], which was able to solve typical optimization problems in ≈ 0.7 seconds on a laptop computer (see Table 3 in Appendix B).

One very important extension of the optimization problem is to limit the number of electrodes used. This can be done with a constraint of the form

$$\|\boldsymbol{x}\|_0 < N, \tag{4.16}$$

where $\|\cdot\|_0$ is the L0 "norm", which corresponds to the number number of non-zero entries in the vector. By adding this constraint, the optimization problem becomes combinatorial, and we therefore need other strategies to solve it. For this purpose, we designed a branch and bound algorithm [100], described in detail in the supplementary material of [3]. The algorithm provides a global and certified solution for the optimization problem at hand in a small amount of time, typically < 1 minute. With some heuristics, it can be further accelerated to run in < 1.5 seconds (see Table 3 in Appendix B). In comparison, other proposed algorithms to solve this or related problems [94, 97], took a few hours to converge.

By combining the quantities above, we defined ten optimization problems, listed in Table 1 in Appendix B. We used two different objectives: minimize electric field energy or maximize focality, set safety constraints on or off, constrained or not the number of active electrodes and electric field angle at the target, and defined optimization problems with many simultaneous targets.

We used a head model based on existing T1- and T2-weighted images of a healthy volunteer [51], automatically segmented using a version of the *headreco* [1] pipeline that was modified to also include segmentations of compact and spongy bone, and tissue electric conductivity values from [51]. Electric field simulations were done in SimNIBS 2.1 [101]. In order to map the trade-offs between optimal electric fields throughout the cortex, we created a model of the middle gray matter surface containing 20,000 nodes using *FreeSurfer* and

MeshFix [102]. The electric field simulations were interpolated to the nodes of this surface mesh and assembled into a leadfield matrix. We evaluated four different electrode caps, shown in Figure 4.4(a). Unless said otherwise, the electrode cap with $n = 288$ was used.

4.3.2 Results

We began by comparing optimized electric fields to three ad-hoc montages: a bipolar montage and a ring montage targeting the motor cortex as well as a bipolar montage targeting the left cingulate sulcus. We first ran the ad-hoc montages, and used the results to set the normal component of the electric field in the target for the optimizations, as this component in thought to be the most important for TES neuromodulation [7]. In the results, shown in Figure 2 of Appendix B, we see that the optimization results in a much more focal field than the bipolar montage targeting the motor cortex. However, we do not see such pronounced gains when comparing to the ring montage targeting the motor cortex, as this montage already produces relatively focal fields, or with the bipolar montage targeting the left cingulate sulcus, as this region is located deeper inside the cortex which makes it hard to target with superficial electrodes.

We then optimized electric fields for targeting each of the 20,000 positions in the middle gray matter surface model. the target direction was set normal to the cortex surface, with data for tangential targets being shown in the supplementary material of [3]. In order to evaluate the focality of our fields, we used two metrics, *effective area* which is calculated as area of the cortex weighted by the electric field, and *targeting error*, which is the euclidean distance between the target and the electric field maximum. Both are defined in Section 2.5 of Appendix B.

To evaluate a best-case scenario, we began by optimizing the electrode montage without safety constraints, shown in Figure 4.4. We saw a strong dependency between electric field focality and target position, with the targets in gyral crowns having the most focal electric fields. We also used this setting to evaluate the effect of the number of electrodes available in the electrode cap, and saw significant focality gains in using caps with ≥ 190 electrodes, which saturate at around $n = 288$ electrodes. Based on this data, we selected the electrode cap with $n = 288$ electrodes for the rest of the study. As we will later see, this is likely not because we can use more electrodes in the optimized montages, but rather because the algorithm finds electrodes which are better positioned to focally stimulate the targets.

Afterwards, we evaluated the maximal electric field obtainable in each position, considering safety constraints $I_{ind} = 1mA$ and $I_{tot} = 2mA$. This is a slightly different optimization
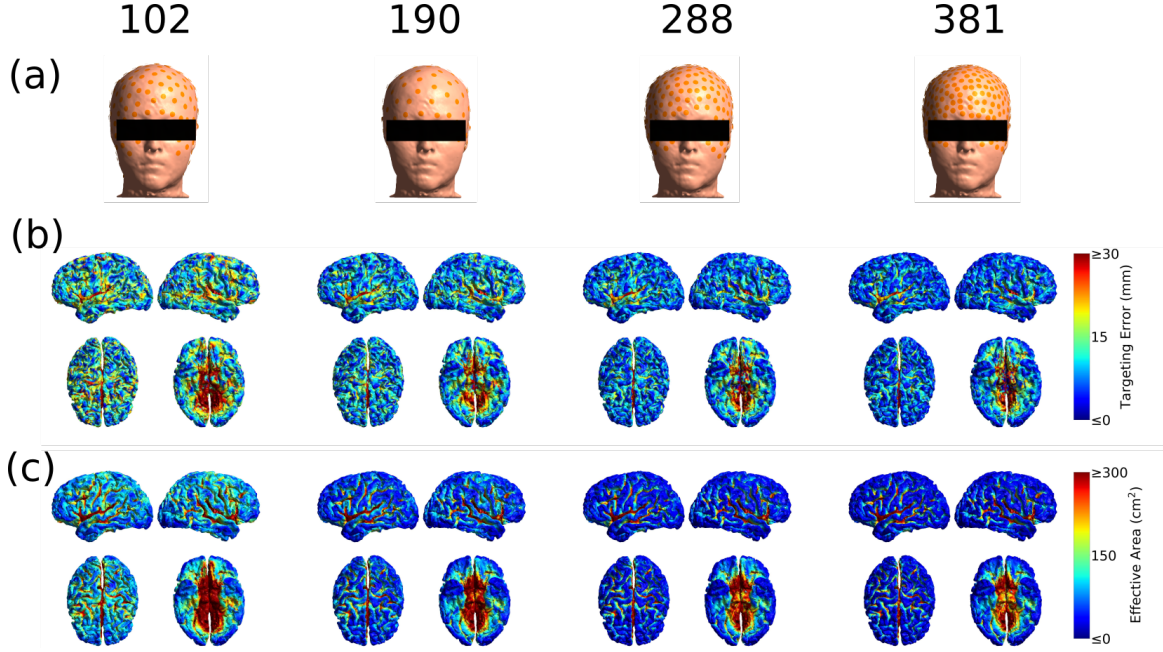
Figure 4.4: Mapping the focality of optimization solutions for different electrode caps. (a) shows the positions of the electrodes, (b) the *targeting error* and (c) the *effective area* focality metrics for optimized montages targeting each position in the cortex, in the normal direction. Reproduced from the supplementary material in [3] with modifications.

problem, which results in a linear program (see Problem 5 in Appendix B). We see in Figure 4 of Appendix B that fields $> 0.3\mathrm{V/m}$ could be reached in majority of cortical positions, and that electric fields were in general larger in the gyri, where electric fields $> 0.6\mathrm{V/m}$ were obtained.

By adding safety constraints to the focatily optimization problem and setting the target electric field normal component $t = 0.2\mathrm{V/m}$, we saw a significant degrading of focality with respect to the optimizations without safety constraints, especially in inferior and medial regions (see Figure 5 in Appendix B).

We then validated our branch and bound algorithm to limit the number of active electrodes and evaluate the effect having a reduced number of available electrodes in optimization results. Figure 6 in Appendix B shows that the branch and bound can give substantially better results than simple approaches, and in Figure 7 of Appendix B, we see that in most positions, using $N > 8$ electrodes results only in small gains to focatily.

We further investigated the effect of controlling the electric field angle at the target, and found it to be relatively small (Figure 8 of Appendix B) and saw the effect of limiting the number of electrodes in an optimization problem targeting both the left and right motor cortices simultaneously (Figure 10 in Appendix B).

4.4 Optimizing Electric Field Strength

In [91], reproduced in full in Appendix C, we extended the optimization problem to use electric field norms or strengths instead of the electric field component along a given direction. While using a preferential direction is the appropriate choice for cortical targets, where it is known that the normal component of the electric field is the most important for neuromodulatory effects [7], a preferential direction is often unclear in subcortical targets.

We begin by noticing that we can approximate the electric field norm in a small area using a quadratic form of the type (see Section 2.3 in Appendix C)

$$\boldsymbol{x}^\top \mathbf{Q}_t \boldsymbol{x} = t^2 \tag{4.17}$$

and formulating the optimization problem to minimize total electric field energy while controlling the electric field at the target

$$\begin{align}
\text{minimize} \quad & \boldsymbol{x}^\top \boldsymbol{Q} \boldsymbol{x}, \tag{4.18}\\
\text{subject to} \quad & \boldsymbol{x}^\top \boldsymbol{Q}_t \boldsymbol{x} = t^2, \tag{4.19}\\
& \mathbf{1}^\top \boldsymbol{x} = 0, \tag{4.20}\\
& |x_i| < I_{\text{ind}} \quad \forall i = i, \dots, m, \tag{4.21}\\
& \|\boldsymbol{x}\|_1 < 2I_{\text{tot}}. \tag{4.22}
\end{align}$$

The problem above is no longer convex, but can be reformulated as a difference of convex programming problem, which can be solved using convex-concave procedures (CCP)[103]. Furthermore, we can add multiple target regions and limit the number of active electrodes using the branch and bound algorithm proposed in [3]. Appendix C describes the CCP algorithm in detail.

We compared the results obtained with the optimization with the best results obtained from searching 25 directions in 1000 randomly selected targets in gray matter, as well as a for searching a combination of 300 directions in 200 pairs of randomly selected gray matter targets. We found that the optimization approach outperforms the search approach in all tested cases for the single target, and in all but one of the cases for the pairs. We also used the novel optimization method in order to obtain focal fields for a target in the amygdala, shown in Figures 1 and 2 of Appendix C.

4.5   Discussion

Computational methods for optimizing multichannel TES can help designing individualized stimulation protocols that generate focal an intense electric fields at a given stimulation target. This is an important tool for TES research, as having a focal field is important in order to clearly establish a causal relationship between stimulation of a given brain region and experimental outcome.

We proposed new formulations of the TES optimization problem, which explicitly controls the electric field at the target and number of active electrodes. We then designed and implemented algorithms to efficiently solve these optimization problems, and used it to map the characteristics and trade-offs of optimal electric fields. We found a large dependency between target location, electrode cap density, and field focality. On the other hand, we did not find many advantages in using > 8 electrodes for obtaining focal electric fields, at least if we want to keep intensity at the target at an effective value (e.g. 0.2 V/m). These results provides an important insight for design of multichannel TES system for focal stimulation, as it indicates that positioning electrodes close together in a precise fashion might be more important to obtaining focal fields than having many (> 8) independent channels.

There are however several aspects of computational optimization of TES were not addressed in our studies. First of all, there are model errors and uncertainties, which were discussed in chapter 3 of this thesis. Scmidt et al. [104] showed that uncertainties in electric conductivity values can also result in large uncertainties in TES montage optimizations, and we also expect gross head segmentation errors to cause large inaccuracies in optimization results. It would therefore be interesting to take these errors and uncertainties into account during the optimization process, in order to obtain more robust montages.

A novel TES method called temporal interference (TI) stimulation [105] uses two overlapping high-frequency electric fields in order to create an interference pattern that can modulate neural activity. As this method uses interference, it is not subject to the same physical constraints as traditional TES, which is why it is able to reach more focal fields albeit at a cost of lower intensity [106]. Even though the method is not yet widely applied for human neuromodulation, algorithms for computational optimization of TI electrode montages are an interesting topic for future research.

4.6 Contributions

GBS formulated the optimization problems, designed the branch and bound algorithm, implemented the optimization algorithms, acquired the data, and wrote the original paper drafts. GBS, Hartwig Siebner, Axel Thielscher and Kristoffer H Madsen conceptualized the study and revised the papers.

Chapter 5

SimNIBS - Open Source Software for TBS Electric Field Simulation

Simulations can give valuable information to TBS practitioners, such as as estimates of electric field in regions of interest. Yet, TBS modelling tools are not widely used in experimental and clinical applications, with most studies relying rather on rule-of-thumb approaches and standardized protocols for TMS coil and TES electrode positioning. However, interest in adopting simulation tools in TBS experimental practice has been increasing, due to studies pointing towards severe reproducibility problems in TBS research [17], mounting evidence that inter-subject variability can be better managed using simulation tools [32, 21, 34], and a push from funding agencies such as the United Stated National Institutes of Health (NIH) [107]. In this chapter, we will describe the development and design of one open source software for individualized TBS electric field simulations called SimNIBS (`www.simnibs.org`). More specifically, we will discuss how it relates to other existing TBS modelling packages, its development history, and the design of versions 2.1, 3.0, 3.1, and 3.2 which were developed during the course of this PhD project together with both internal and external collaborators. Additionally, Version 2.1 was documented in detain in a book chapter reproduced in Appendix D.

5.1 TBS Modelling Tools

The first TBS simulation studies were done using commercial multi-purpose software such as *COMSOL Multiphysics* and ANSYS [45, 39]. However, adoption of this type of software has a large entry barrier due to the high price of software licenses and a steep learning curve. In order to make TBS simulation more easily accessible, several open source software projects

were developed.

- SCIRun [108], (`https://www.sci.utah.edu/cibc-software/scirun/brainstimulator.html`) was released in 2012, supporting TMS and TES simulations.

- SimNIBS (`www.simnibs.org`) [51], was released in 2013 featuring TES, TMS and a head segmentation pipeline called *mri2mesh*. Since then it has been expanded to include TES and TMS optimization and a new head segmentation pipeline called *headreco*.

- Also in 2013, a new SimBIO [109] (`https://www.mrt.uni-jena.de/simbio/`) version [110], supporting simulation of TES electric fields was released.

- ROAST [76] (`https://www.parralab.org/roast/`), a MATLAB library for TES simulations with a head segmentation pipeline was released in 2017.

- in 2019, a new MATLAB library for TMS simulations using BEM-FMM was released [111].

With the exception of the last example, all the software above uses the Finite Element Method (FEM) to numerically solve the TES and TMS PDEs, described in chapter 2.

5.2 SimNIBS Development History

SimNIBS (Simulation of Non Invasive Brain Stimulation) version 1.0 was released in 2013 [51]. This first version was written in BASH and MATLAB, using the GetFEM++ library [112] to form and solve the FEM system. It already provided support for both TES and TMS, as well as the head segmentation tool *mri2mesh*, which relies on the FSL [79] and FreeSurfer [78] neuorimaging packages. SimNIBS 1.0 was fairly slow, with a simulations in a head mesh with 3 million tetrahedra taking $\approx$ 1h [51].

In order to speed up simulations and reduce the dependency in MATLAB, which is proprietary software, SimNIBS 2.0 was developed in the Python programming language, with some time critical operations being implemented in C and compiled as command line utilities for better computational efficiency. The FEM system was assembled and solved using the GetDP [67] software. It also featured for the first time a graphical user interface (GUI), shown in Figure 5.1, allowing users to interactively setup simulations. SimNIBS 2.0 was released in 2015 [101].

SimNIBS version 2.1 was released in 2018, featuring another major refactoring of the simulation code in order to replace many of the C command line utilities with Python

code by leveraging the NumPy (`https://numpy.org/`) and SciPy (`https://www.scipy.org/`) libraries. The refactoring also improved the maintainability and expandability of the software by using an object-oriented design. It also introduced a new head modeling tool, called *headreco* [1], new functionality to transform simulation results to MNI and FsAverage standard spaces, and support for Microsoft Windows. A book chapter describing this version was published in 2019 [113], reproduced in full in Appendix D.

In 2019, SimNIBS 3.0 was released. This version introduced new native code for assembling the FEM matrix, together with direct interfaces for sparse matrix solvers. These improvements reduced times to run TMS simulations in standard head models from ≈ 200s to ≈ 30s, and TES simulations from ≈ 80s to also ≈ 30s [57]. Uncertainty quantification (UQ) functionality was also introduced in this update, allowing users to estimate the effect of tissue conductivity uncertainties in the electric field estimates [71]. In the end of 2019, SimNIBS 3.1 was released bringing support for TES and TMS optimization [3, 34], and in 2020 SimNIBS 3.2 was released supporting TES and electric field strength optimization [91], TES network optimization [94], TMS optimization using the Auxiliary Dipole Method (ADM) [114] and magnetic field calculations for MREIT and MRCDI [115].
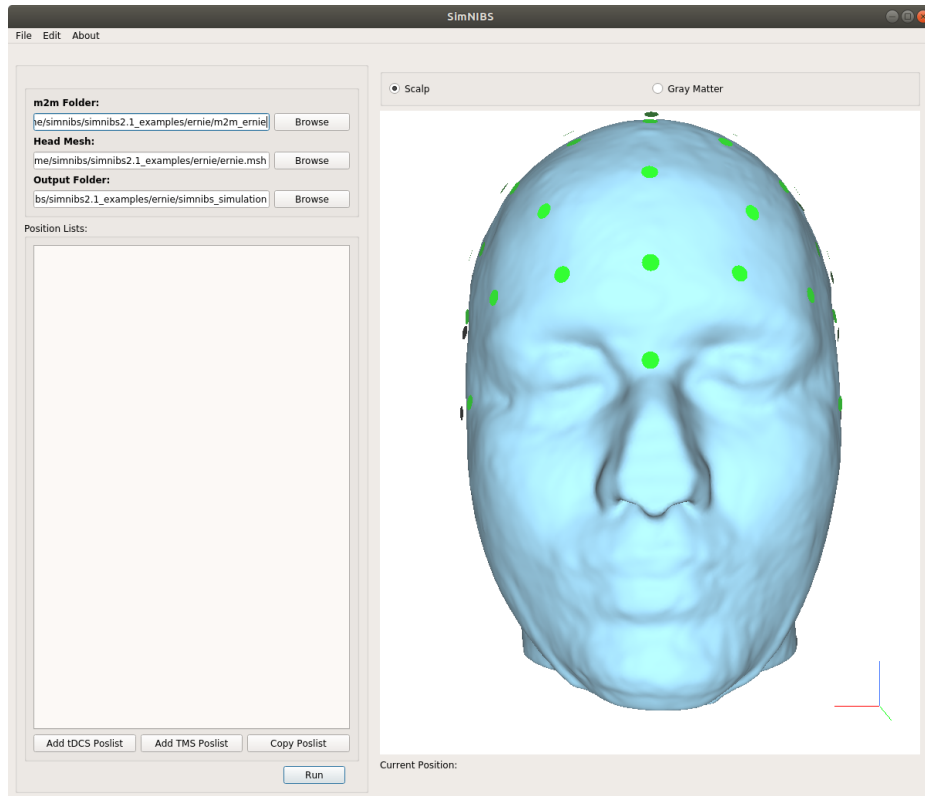
Figure 5.1: *SimNIBS* graphical user interface (GUI)

5.3 Modules
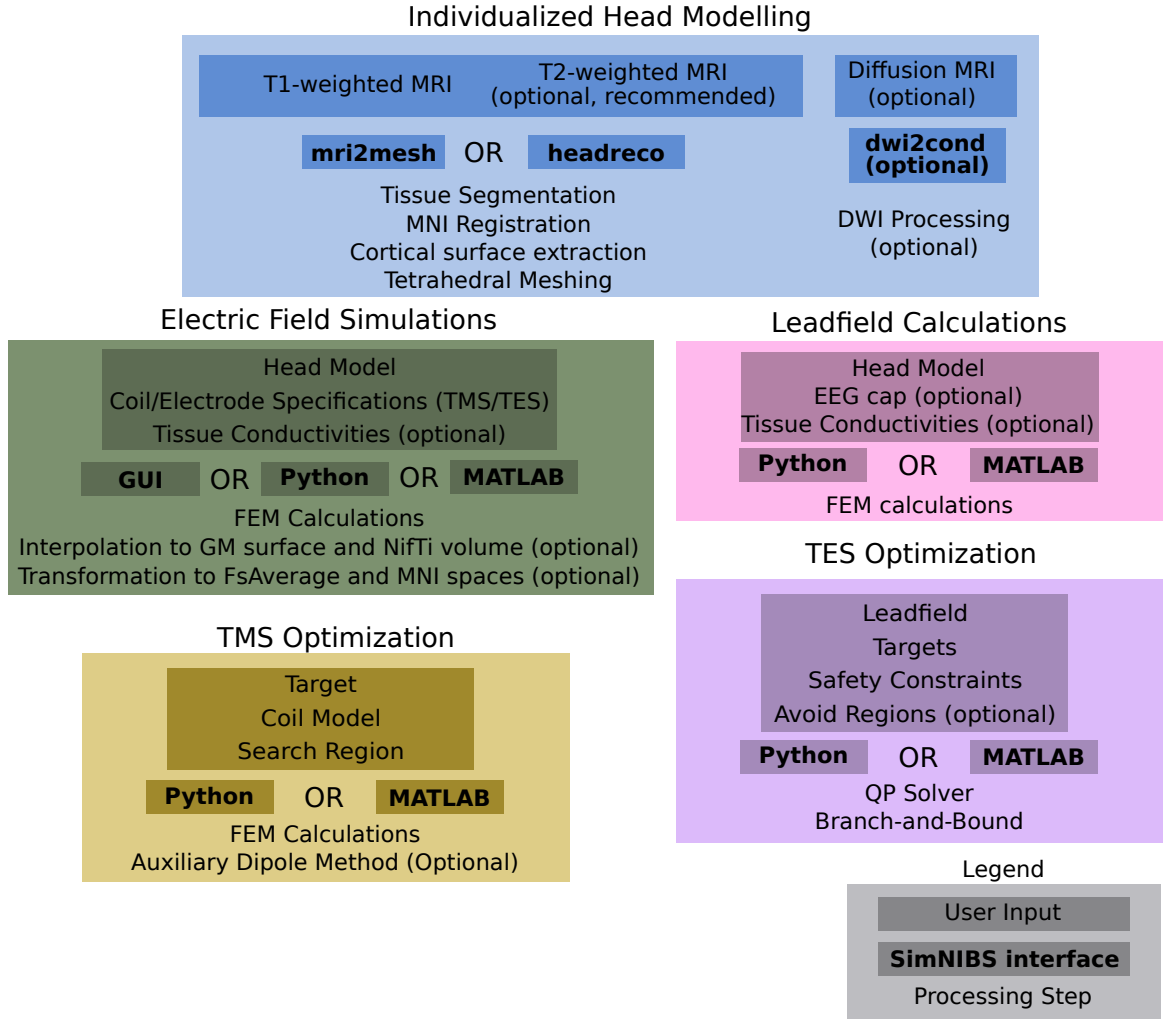
Figure 5.2: SimNIBS modules for individualized electric field simulation and TES optimization

From the user perspective, SimNIBS can be divided into a few major modules, shown in Figure 5.2. Fist of all, there is the individualized head modelling module, whose main function is to create a tetrahedral mesh with segmented tissues from MR images. As of SimNIBS 3.2, there are two head modelling pipelines: *mri2mesh* [51], and *headreco* [1], both summarized in chapter 3. These two pipelines can be accessed by the user through command line utilities as described in Section 1.3.1 of Appendix D, and require a T1-weighted image and optionally a T2-weighted image. It is important to use high-quality images and the optional T2-weighted image is highly recommended as it helps to accurately segment the CSF-Skull border [1]. Additionally, SimNIBS has an utility to estimate electric conductivity tensors from diffusion-weighted MRI, called *dwi2cond*, which implements algorithms proposed by Tuch et al. [60]. However, as these estimates have not been thoroughly validated

thus far and tissue conductivity anisotropy cause relatively minor changes in the cortical electric fields [116, 30], this tool is mostly limited to exploratory use.

With a head model at hand, we can run TES and TMS electric field simulations. The simulations require electrode (TES) or coil (TMS) specifications, such as electrodes positions, shapes and currents, or coil positions, model and stimulation intensity. Optionally, users can also change tissue conductivities. Simulations can be setup using the GUI, shown in Figure 5.1, as well as Python or MATLAB scripts, as described in Section 1.3.2 of Appendix D. In addition to the standard output (a mesh with the electric field as elemental data), SimNIBS can also calculate the electric fields in the middle GM surface or in a NifTi volume, and transform these results to standard spaces such as FsAverage and MNI. Using standard spaces allows for evaluating electric fields in a group level, and therefore perform statistical analyses relating the electric fields in given brain regions against experimental outcomes across subjects [32, 22]. Surface-based analyses are preferred over volume-based analyses, as for the former we can be sure to only consider electric fields in gray matter during the interpolation and subsequent transformation step, while for the later, a voxel which in a subject belongs to for example WM or CSF can be mapped into a GM voxel in the MNI template, which causes artificially high or low electric fields in said voxel, as the electric field is discontinuous across tissue interfaces.

TES electrode montage optimizations were introduced in SimNIBS 3.1, and are divided into two modules: leadfield calculations and TES optimization. Calculating the TES leadfield require only the head model as user input. SimNIBS then chooses a reference electrodes (by default Cz), which is assigned as a cathode, and runs electric field simulations using each other electrode from the 10-10 EEG standard as an anode, one at a time. The user can also define custom electrode caps and electrode shapes. To accelerate simulations, SimNIBS uses Neumann boundary conditions in the anode so that all simulations use the same stiffness matrix. This allows for re-using the preconditioner or direct solver for all simulations, resulting in significant gains in computational efficiency. Simulation results are interpolated to the middle gray matter surface and saved as columns of the leadfield matrix. The TES optimization takes the leadfield as an input, and require that the user sets the target positions and intensities, as well as the safety constraints. SimNIBS then sets it up as a mathematical optimization problem (see Appendix B) and solves it using its native quadratic programming (QP) solver and branch and bound algorithms.

In TMS optimization, first introduced in SimNIBS 3.1, the user inputs a target position where the electric field is to be maximized. SimNIBS then generates a grid of coil positions

and orientations in the scalp, close to the targets, and simulates electric fields with the coil
at each of these grid positions in order to find the position which creates the largest electric
field in the target. SimNIBS can either directly calculate the electric field in the target region
by running a full FEM [34], which can be accelerated using the MKL Pardiso solver [70],
or as of SimNIBS 3.2 leverage the Auxiliary Dipole Method (ADM) [114] for very fast TMS
optimizations.

SimNIBS also has other advanced or experimental options, not shown in the summary
Figure 5.2. One of those is the uncertainty quantification (UQ) functionality, introduced
in the version 3.0. UQ allows for users to set distributions rather than point estimates for
electric conductivity values. SimNIBS then creates a generalized polynomial chaos (gPC)
expansion of the electric field with respect to the uncertain electric conductivity values,
which yields a distribution of possible electric field values at each position [71].

5.4 Development Practices

SimNIBS is available for all major operating systems (Windows, MacOS and Linux), and
can be downloaded for free at `www.simnibs.org`. The website also contains tutorials and
extensive documentation of the software. SimNIBS 3.2 has over 30,000 lines of source code
publicly available in *GitHub* (`https://github.com/simnibs/simnibs`). Most of the code is
implemented in Python, which we chose as the main programming language for the project
due to ease of development, a large ecosystem of numerical and scientific libraries such as
NumPy and SciPy, and accessibility for the final user as Python is distributed under a free
and open source license.

Mri2mesh and *dwi2cond* are implemented in BASH, and require that the user has
FreeSurfer and FSL installed. *Headreco* depends on SPM12 and therefore requires a MAT-
LAB installation. However, the simulation and optimization modules do not require the
installation of any additional software, as all other dependencies such as a Python inter-
preter, Numpy and SciPy libraries are distributed together with SimNIBS. Additionally,
SimNIBS also has an example dataset with the head models of a healthy subject and of the
MNI template, which can be downloaded for free at the website. This allows for users to
experiment with simulations and optimizations without the need of first running the head
segmentation pipelines.

The simulation and optimization modules in SimNIBS were developed in a object-
oriented fashion, and are covered by over 500 unity tests, which aim to validate small
sections of the code, as well as 24 integration tests, which validate large sections of the

code. These tests are configured to run in Linux, MacOS and Windows virtual machines in *Azure Pipelines* (`https://dev.azure.com/simnibs/simnibs/_build`) after each time new code is pushed to the *GitHub* repository. This setting allows for developers and users to quickly detect changes to the code that introduce new bugs. In addition, the virtual machines also create compiled Python packages which are automatically uploaded to *GitHub* for distribution to the final users.

5.5 Discussion

In the past decade, a number of TBS electric field simulation software has emerged, and interest in using simulations to both analyze and plan TBS interventions has been growing. Of these tools, SimNIBS is to the best of our knowledge the most complete, with head modelling, TES and TMS simulation and optimization. It is also highly popular, with over 2500 downloads since the release of SimNIBS 3 in 2019.

Work in SimNIBS is ongoing. At the time of writing version 4.0 is under development. This major release will feature an entirely new head modelling pipeline called *charm* [117], which will replace both *mri2mesh* and *headreco*. We also believe that the graphical user interface can be improved to add support for setting up optimizations and visualization of simulation results.

Furthermore, having SimNBIS in an online platform would improve accessibility. However, in this setting we would likely not be able to provide individualized head models due to ethical and legal constraints to sharing medical data such as MR images.

5.6 Contributions

GBS refactored the simulation code for SimNIBS 2.1, implemented the new FEM code for SimNIBS 3.0 (described in the MSc thesis [64]), the leadfield calculations and TES optimization in SimNIBS 3.1 and 3.2. GBS also wrote most of the documentation in and tutorials in the website. Please see `www.simnibs.org` for detailed credit and bibliography of the different SimNBIS tools. We would like to thank all contributors to SimNIBS, such as Jesper D. Nielsen, Oula Puonti, Luis Gomez, Konstantin Weise, Ole Numssen, Hassan Yazdanian, Kristoffer H. Madsen and Axel Thielscher.

Chapter 6

Conclusion

In chapter 1 of this thesis, we briefly reviewed transcranial brain stimulation (TBS) methods, their applications, and the use of computational dosimetry in TBS. In chapter 2, we introduced the physics behind TMS and TES electric fields as well the finite element method (FEM), which we used extensively in order to simulate these fields in realistic geometries. In chapter 3, we tackled the issue of validating electric field models based on intracranial measurements. Chapter 4 introduced computational methods for optimizing TES electrode setups, and finally chapter 5 described our open source software for TBS simulation and optimization, called SimNIBS.

Computational models for TBS inform practitioners of how electric fields are distributed in a given individual's head, and thus help in planning and analysis of TBS interventions. It is therefore important that these models are reliable and give good estimates of the electric fields. In chapter 3, we described our efforts to validate four different tools for creating individualized head models from MR images, using a publicly available dataset featuring invasive recordings. While there were large differences between the electric fields obtained with each of the modelling tools, none performed better in predicting the recorded electric fields. However, we also saw significant problems with the dataset, and expect that in the future novel methods such MRCDI [88] will be able to provide high-quality experimental data about current flow in the human head in order to validate these models. In addition, recent developments in head segmentation [117], will be implemented in SimNIBS 4.0 to provide much more accurate head models.

We can also use our modelling tools in order to automatically determine the best electrode positions to focally stimulate a given target. These methods, described in chapter 4, were extended to explicitly control the electric field at the target and limit the number of active electrodes in a computational efficient yet optimal fashion. We then used these new

methods to study the inherit trade-offs in TES electrode optimization, and reached important conclusions regarding the design and capabilities of multichannel electrode systems. For example, we saw that positioning electrodes using a dense grid is more important for obtaining focal electric fields than having many stimulation channels. One issue which was not addressed is the resilience of these optimized montages. We know that that electric field estimates are affected by segmentation errors and conductivity uncertainties, which in turn affect optimization results. In the future, it would be interesting to take these errors and uncertainties into account in the optimization algorithm in order to obtain more robust montages.

TBS modelling software has come a long way since their inception around 10 years ago. For example, SimNIBS 3.2 offers tools for automatically creating individualized head models from MR images, simulating TES and TMS electric fields, and optimizing TES electrode montages and TMS coil positions. We are currently developing a new SimNIBS version that will introduce a new and more accurate head modelling tool. Several improvements can also be done to the user experience, such as expanding the SimNIBS graphical user interface in order to support TES optimizations and visualize electric fields.

Errors and inaccuracies are inherit to any model. For TBS field simulations, we know a few different error sources: head segmentation [117], conductivity uncertainties [71], coil and electrode modelling errors [90, 50] and finally numerical errors related to the FEM [50, 57]. Of those, the first two are likely the most difficult to tackle, as it would require more in-depth knowledge about the human head as a volume conductor in a subject-by-subject basis. The electrodes models in SimNIBS are quite simple, and do not model for example material interfaces which could create resistive effects [118]. Also coil models are subject to errors, as actual coil geometry can vary substantially from vendor-specified geometry. Finally, adopting more accurate numerical methods such as higher order FEM or BEM-FMM can improve the numerical accuracy of the simulations [50, 49]. However, even with improved methodology, it is of key importance to critically access the models and their results.

Finally, the relationship between electric fields and the outcomes of TBS interventions is complex. And while electric fields can help explaining experimental outcomes [32, 21, 34], and incorporating realistic neuron models together with electric field simulations [119] gives important new insights into to the effects of TBS in neurons, these models are not enough to fully explain the effect of TBS outcomes, as many other factors such as neurochemistry and brain state play an important role in TBS effects[120]. We believe that, despite all the uncertainties and errors in individualized TBS electric field modelling, it is a valuable tool

allow that allows practitioners to advance TBS applications by improving their efficiency and reliability.

Bibliography

[1] J. D. Nielsen, K. H. Madsen, O. Puonti, H. R. Siebner, C. Bauer, C. G. Madsen, G. B. Saturnino, and A. Thielscher, "Automatic skull segmentation from mr images for realistic volume conductor models of the head: Assessment of the state-of-the-art," *Neuroimage*, vol. 174, pp. 587–598, 2018.

[2] Y. Huang, A. A. Liu, B. Lafon, D. Friedman, M. Dayan, X. Wang, M. Bikson, W. K. Doyle, O. Devinsky, and L. C. Parra, "Measurements and models of electric fields in the in vivo human brain during transcranial electric stimulation," *Elife*, vol. 6, p. e18834, 2017.

[3] G. B. Saturnino, H. R. Siebner, A. Thielscher, and K. H. Madsen, "Accessibility of cortical regions to focal tes: Dependence on spatial position, safety, and practical constraints," *NeuroImage*, vol. 203, p. 116183, 2019.

[4] S. Luan, I. Williams, K. Nikolic, and T. G. Constandinou, "Neuromodulation: present and emerging methods," *Frontiers in neuroengineering*, vol. 7, p. 27, 2014.

[5] A. Priori, "Brain polarization in humans: a reappraisal of an old tool for prolonged non-invasive modulation of brain excitability," *Clinical neurophysiology*, vol. 114, no. 4, pp. 589–595, 2003.

[6] S. H. Lisanby, "Electroconvulsive therapy for depression," *New England Journal of Medicine*, vol. 357, no. 19, pp. 1939–1945, 2007.

[7] A. Liu, M. Vöröslakos, G. Kronberg, S. Henin, M. R. Krause, Y. Huang, A. Opitz, A. Mehta, C. C. Pack, B. Krekelberg, *et al.*, "Immediate neurophysiological effects of transcranial electrical stimulation," *Nature communications*, vol. 9, no. 1, pp. 1–12, 2018.

[8] M. A. Nitsche and W. Paulus, "Excitability changes induced in the human motor cortex

by weak transcranial direct current stimulation," *The Journal of physiology*, vol. 527, no. 3, pp. 633–639, 2000.

[9] A. Antal, K. Boros, C. Poreisz, L. Chaieb, D. Terney, and W. Paulus, "Comparatively weak after-effects of transcranial alternating current stimulation (tacs) on cortical excitability in humans," *Brain stimulation*, vol. 1, no. 2, pp. 97–105, 2008.

[10] L. J. Bindman, O. Lippold, and J. Redfearn, "The action of brief polarizing currents on the cerebral cortex of the rat (1) during current flow and (2) in the production of long-lasting after-effects," *The Journal of physiology*, vol. 172, no. 3, pp. 369–382, 1964.

[11] P. Merton and H. Morton, "Stimulation of the cerebral cortex in the intact human subject," *Nature*, vol. 285, no. 5762, pp. 227–227, 1980.

[12] M. R. Krause, T. P. Zanos, B. A. Csorba, P. K. Pilly, J. Choe, M. E. Phillips, A. Datta, and C. C. Pack, "Transcranial direct current stimulation facilitates associative learning and alters functional connectivity in the primate brain," *Current Biology*, vol. 27, no. 20, pp. 3086–3096, 2017.

[13] M. A. Nitsche, L. G. Cohen, E. M. Wassermann, A. Priori, N. Lang, A. Antal, W. Paulus, F. Hummel, P. S. Boggio, F. Fregni, *et al.*, "Transcranial direct current stimulation: state of the art 2008," *Brain stimulation*, vol. 1, no. 3, pp. 206–223, 2008.

[14] T. O. Bergmann, A. Karabanov, G. Hartwigsen, A. Thielscher, and H. R. Siebner, "Combining non-invasive transcranial brain stimulation with neuroimaging and electrophysiology: current approaches and future perspectives," *Neuroimage*, vol. 140, pp. 4–19, 2016.

[15] M. Kekic, E. Boysen, I. C. Campbell, and U. Schmidt, "A systematic review of the clinical efficacy of transcranial direct current stimulation (tdcs) in psychiatric disorders," *Journal of psychiatric research*, vol. 74, pp. 70–86, 2016.

[16] Y.-Z. Huang, M.-K. Lu, A. Antal, J. Classen, M. Nitsche, U. Ziemann, M. Ridding, M. Hamada, Y. Ugawa, S. Jaberzadeh, *et al.*, "Plasticity induced by non-invasive transcranial brain stimulation: a position paper," *Clinical Neurophysiology*, vol. 128, no. 11, pp. 2318–2329, 2017.

[17] J. C. Horvath, J. D. Forte, and O. Carter, "Evidence that transcranial direct current stimulation (tdcs) generates little-to-no reliable neurophysiologic effect beyond mep

amplitude modulation in healthy human subjects: a systematic review," *Neuropsychologia*, vol. 66, pp. 213–236, 2015.

[18] A. Karabanov, A. Thielscher, and H. R. Siebner, "Transcranial brain stimulation: closing the loop between brain and stimulation," *Current opinion in neurology*, vol. 29, no. 4, p. 397, 2016.

[19] I. Laakso, S. Tanaka, S. Koyama, V. De Santis, and A. Hirata, "Inter-subject variability in electric fields of motor cortical tdcs," *Brain stimulation*, vol. 8, no. 5, pp. 906–913, 2015.

[20] A. Opitz, W. Paulus, S. Will, A. Antunes, and A. Thielscher, "Determinants of the electric field during transcranial direct current stimulation," *Neuroimage*, vol. 109, pp. 140–150, 2015.

[21] I. Laakso, M. Mikkonen, S. Koyama, A. Hirata, and S. Tanaka, "Can electric fields explain inter-individual variability in transcranial direct current stimulation of the motor cortex?," *Scientific reports*, vol. 9, no. 1, pp. 1–10, 2019.

[22] D. Antonenko, A. Thielscher, G. B. Saturnino, S. Aydin, B. Ittermann, U. Grittner, and A. Flöel, "Towards precise brain stimulation: Is electric field simulation related to neuromodulation?," *Brain stimulation*, vol. 12, no. 5, pp. 1159–1168, 2019.

[23] K. A. Caulfield, B. W. Badran, W. H. DeVries, P. M. Summers, E. Kofmehl, X. Li, J. J. Borckardt, M. Bikson, and M. S. George, "Transcranial electrical stimulation motor threshold can estimate individualized tdcs dosage from reverse-calculation electric-field modeling," *Brain Stimulation*, 2020.

[24] A. T. Barker, R. Jalinous, and I. L. Freeston, "Non-invasive magnetic stimulation of human motor cortex," *The Lancet*, vol. 325, no. 8437, pp. 1106–1107, 1985.

[25] P. Merton, H. Morton, D. Hill, and C. Marsden, "Scope of a technique for electrical stimulation of human brain, spinal cord, and muscle," *The Lancet*, vol. 320, no. 8298, pp. 597–600, 1982.

[26] S. Rossi, M. Hallett, P. M. Rossini, A. Pascual-Leone, S. of TMS Consensus Group, *et al.*, "Safety, ethical considerations, and application guidelines for the use of transcranial magnetic stimulation in clinical practice and research," *Clinical neurophysiology*, vol. 120, no. 12, pp. 2008–2039, 2009.

[27] M. Hallett, "Transcranial magnetic stimulation: a primer," *Neuron*, vol. 55, no. 2, pp. 187–199, 2007.

[28] J.-P. Lefaucheur, N. André-Obadia, A. Antal, S. S. Ayache, C. Baeken, D. H. Benninger, R. M. Cantello, M. Cincotta, M. de Carvalho, D. De Ridder, *et al.*, "Evidence-based guidelines on the therapeutic use of repetitive transcranial magnetic stimulation (rtms)," *Clinical Neurophysiology*, vol. 125, no. 11, pp. 2150–2206, 2014.

[29] F. Maeda, J. P. Keenan, J. M. Tormos, H. Topka, and A. Pascual-Leone, "Interindividual variability of the modulatory effects of repetitive transcranial magnetic stimulation on cortical excitability," *Experimental brain research*, vol. 133, no. 4, pp. 425–430, 2000.

[30] A. Thielscher, A. Opitz, and M. Windhoff, "Impact of the gyral geometry on the electric field induced by transcranial magnetic stimulation," *Neuroimage*, vol. 54, no. 1, pp. 234–243, 2011.

[31] A. Opitz, M. Windhoff, R. M. Heidemann, R. Turner, and A. Thielscher, "How the brain tissue shapes the electric field induced by transcranial magnetic stimulation," *Neuroimage*, vol. 58, no. 3, pp. 849–859, 2011.

[32] A. Bungert, A. Antunes, S. Espenhahn, and A. Thielscher, "Where does tms stimulate the motor cortex? combining electrophysiological measurements and realistic field estimates to reveal the affected cortex position," *Cerebral Cortex*, vol. 27, no. 11, pp. 5083–5094, 2017.

[33] I. Laakso, T. Murakami, A. Hirata, and Y. Ugawa, "Where and what tms activates: experiments and modeling," *Brain stimulation*, vol. 11, no. 1, pp. 166–174, 2018.

[34] K. Weise, O. Numssen, A. Thielscher, G. Hartwigsen, and T. R. Knösche, "A novel approach to localize cortical tms effects," *Neuroimage*, vol. 209, p. 116486, 2020.

[35] B. Siebert and R. Thomas, "Computational dosimetry," *Radiation protection dosimetry*, vol. 70, no. 1-4, pp. 371–378, 1997.

[36] G. G. Powathil, D. J. Adamson, and M. A. Chaplain, "Towards predicting the response of a solid tumour to chemotherapy and radiotherapy treatments: clinical insights from a computational model," *PLoS computational biology*, vol. 9, no. 7, 2013.

[37] J. Chen, Z. Feng, and J.-M. Jin, "Numerical simulation of sar and b/sub 1/-field inhomogeneity of shielded rf coils loaded with the human head," *IEEE transactions on biomedical engineering*, vol. 45, no. 5, pp. 650–659, 1998.

[38] S. Rush and D. A. Driscoll, "Eeg electrode sensitivity-an application of reciprocity," *IEEE transactions on biomedical engineering*, no. 1, pp. 15–22, 1969.

[39] P. C. Miranda, M. Lomarev, and M. Hallett, "Modeling the current distribution during transcranial direct current stimulation," *Clinical neurophysiology*, vol. 117, no. 7, pp. 1623–1629, 2006.

[40] T. F. Oostendorp, Y. A. Hengeveld, C. H. Wolters, J. Stinstra, G. van Elswijk, and D. F. Stegeman, "Modeling transcranial dc stimulation," in *2008 30th Annual International Conference of the IEEE Engineering in Medicine and Biology Society*, pp. 4226–4229, IEEE, 2008.

[41] A. Datta, V. Bansal, J. Diaz, J. Patel, D. Reato, and M. Bikson, "Gyri-precise head model of transcranial direct current stimulation: improved spatial focality using a ring electrode versus conventional rectangular pad," *Brain stimulation*, vol. 2, no. 4, pp. 201–207, 2009.

[42] J. Sarvas, "Basic mathematical and electromagnetic concepts of the biomagnetic inverse problem," *Physics in Medicine & Biology*, vol. 32, no. 1, p. 11, 1987.

[43] B. J. Roth, J. M. Saypol, M. Hallett, and L. G. Cohen, "A theoretical calculation of the electric field induced in the cortex during magnetic stimulation," *Electroencephalography and Clinical Neurophysiology/Evoked Potentials Section*, vol. 81, no. 1, pp. 47–56, 1991.

[44] W. Wang and S. R. Eisenberg, "A three-dimensional finite element method for computing magnetically induced currents in tissues," *IEEE Transactions on Magnetics*, vol. 30, no. 6, pp. 5015–5023, 1994.

[45] P. C. Miranda, M. Hallett, and P. J. Basser, "The electric field induced in the brain by magnetic stimulation: a 3-d finite-element analysis of the effect of tissue heterogeneity and anisotropy," *IEEE transactions on biomedical engineering*, vol. 50, no. 9, pp. 1074–1085, 2003.

[46] M. De Lucia, G. J. Parker, K. Embleton, J. Newton, and V. Walsh, "Diffusion tensor mri-based estimation of the influence of brain tissue anisotropy on the effects of transcranial magnetic stimulation," *Neuroimage*, vol. 36, no. 4, pp. 1159–1170, 2007.

[47] M. Chen and D. J. Mogul, "A structurally detailed finite element human head model

for simulation of transcranial magnetic stimulation," *Journal of neuroscience methods*, vol. 179, no. 1, pp. 111–120, 2009.

[48] F. Salinas, J. L. Lancaster, and P. T. Fox, "3d modeling of the total electric field induced by transcranial magnetic stimulation using the boundary element method," *Physics in Medicine & Biology*, vol. 54, no. 12, p. 3631, 2009.

[49] S. N. Makarov, G. M. Noetscher, T. Raij, and A. Nummenmaa, "A quasi-static boundary element approach with fast multipole acceleration for high-resolution bioelectromagnetic models," *IEEE transactions on biomedical engineering*, vol. 65, no. 12, pp. 2675–2683, 2018.

[50] L. J. Gomez, M. Dannhauer, L. M. Koponen, and A. V. Peterchev, "Conditions for numerically accurate tms electric field simulation," *Brain stimulation*, vol. 13, no. 1, pp. 157–166, 2020.

[51] M. Windhoff, A. Opitz, and A. Thielscher, "Electric field calculations in brain stimulation based on finite elements: an optimized processing pipeline for the generation and usage of accurate individual head models," *Human brain mapping*, vol. 34, no. 4, pp. 923–935, 2013.

[52] Y. Huang, J. P. Dmochowski, Y. Su, A. Datta, C. Rorden, and L. C. Parra, "Automated mri segmentation for individualized modeling of current flow in the human head," *Journal of neural engineering*, vol. 10, no. 6, p. 066004, 2013.

[53] O. Puonti, G. B. Saturnino, K. H. Madsen, and A. Thielscher, "Value and limitations of intracranial recordings for validating electric field modeling for transcranial brain stimulation," *NeuroImage*, vol. 208, p. 116431, 2020.

[54] J. P. Dmochowski, A. Datta, M. Bikson, Y. Su, and L. C. Parra, "Optimized multi-electrode stimulation increases focality and intensity at target," *Journal of neural engineering*, vol. 8, no. 4, p. 046011, 2011.

[55] H. v. Helmholtz, "Ueber einige gesetze der vertheilung elektrischer ströme in körperlichen leitern, mit anwendung auf die thierisch-elektrischen versuche (schluss.)," *Annalen der Physik*, vol. 165, no. 7, pp. 353–377, 1853.

[56] D. B. Geselowitz, "On bioelectric potentials in an inhomogeneous volume conductor," *Biophysical journal*, vol. 7, no. 1, pp. 1–11, 1967.

[57] G. B. Saturnino, K. H. Madsen, and A. Thielscher, "Electric field simulations for transcranial brain stimulation using fem: an efficient implementation and error analysis," *Journal of neural engineering*, vol. 16, no. 6, p. 066032, 2019.

[58] N. K. Logothetis, C. Kayser, and A. Oeltermann, "In vivo measurement of cortical impedance spectrum in monkeys: implications for signal propagation," *Neuron*, vol. 55, no. 5, pp. 809–823, 2007.

[59] A. Opitz, A. Falchier, C.-G. Yan, E. M. Yeagle, G. S. Linn, P. Megevand, A. Thielscher, M. P. Milham, A. D. Mehta, C. E. Schroeder, *et al.*, "Spatiotemporal structure of intracranial electric fields induced by transcranial electric stimulation in humans and nonhuman primates," *Scientific reports*, vol. 6, no. 1, pp. 1–11, 2016.

[60] D. S. Tuch, V. J. Wedeen, A. M. Dale, J. S. George, and J. W. Belliveau, "Conductivity tensor mapping of the human brain using diffusion tensor mri," *Proceedings of the National Academy of Sciences*, vol. 98, no. 20, pp. 11697–11701, 2001.

[61] J. Haueisen, D. S. Tuch, C. Ramon, P. Schimpf, V. Wedeen, J. George, and J. Belliveau, "The influence of brain tissue anisotropy on human eeg and meg," *Neuroimage*, vol. 15, no. 1, pp. 159–166, 2002.

[62] K. Gupta and J. Meek, "A brief history of the beginning of the finite element method," *International journal for numerical methods in engineering*, vol. 39, no. 22, pp. 3761–3774, 1996.

[63] O. C. Zienkiewicz, R. L. Taylor, and J. Z. Zhu, *The finite element method: its basis and fundamentals*. Elsevier, 2005.

[64] G. B. Saturnino, "Efficient calculations of transcranially generated electric fields in the human brain using realistic head models," 2018.

[65] H. P. Langtangen and K.-A. Mardal, *Introduction to Numerical Methods for Variational Problems*, vol. 21. Springer Nature, 2019.

[66] Y. Saad, *Iterative methods for sparse linear systems*, vol. 82. siam, 2003.

[67] C. Geuzaine, "Getdp: a general finite-element solver for the de rham complex," in *PAMM: Proceedings in Applied Mathematics and Mechanics*, vol. 7, pp. 1010603–1010604, Wiley Online Library, 2007.

[68] S. Balay, S. Abhyankar, M. F. Adams, J. Brown, P. Brune, K. Buschelman, L. Dalcin, A. Dener, V. Eijkhout, W. D. Gropp, D. Karpeyev, D. Kaushik, M. G. Knepley, D. A. May, L. C. McInnes, R. T. Mills, T. Munson, K. Rupp, P. Sanan, B. F. Smith, S. Zampini, H. Zhang, and H. Zhang, "PETSc Web page." `https://www.mcs.anl.gov/petsc`, 2019.

[69] R. D. Falgout and U. M. Yang, "hypre: A library of high performance preconditioners," in *International Conference on Computational Science*, pp. 632–641, Springer, 2002.

[70] Intel, "Intel mkl pardiso - parallel direct sparse solver interface." `https://software.intel.com/content/www/us/en/develop/documentation/mkl-developer-reference-fortran/top/sparse-solver-routines/intel-mkl-pardiso-parallel-direct-sparse-solver-interface.html`, 2020.

[71] G. B. Saturnino, A. Thielscher, K. H. Madsen, T. R. Knösche, and K. Weise, "A principled approach to conductivity uncertainty analysis in electric field calculations," *Neuroimage*, vol. 188, pp. 821–834, 2019.

[72] J. Vorwerk, J.-H. Cho, S. Rampp, H. Hamer, T. R. Knösche, and C. H. Wolters, "A guideline for head volume conductor modeling in eeg and meg," *NeuroImage*, vol. 100, pp. 590–607, 2014.

[73] V. Rimpiläinen, A. Koulouri, F. Lucka, J. P. Kaipio, and C. H. Wolters, "Improved eeg source localization with bayesian uncertainty modelling of unknown skull conductivity," *NeuroImage*, vol. 188, pp. 252–260, 2019.

[74] F. Tadel, S. Baillet, J. C. Mosher, D. Pantazis, and R. M. Leahy, "Brainstorm: a user-friendly application for meg/eeg analysis," *Computational intelligence and neuroscience*, vol. 2011, 2011.

[75] R. Oostenveld, P. Fries, E. Maris, and J.-M. Schoffelen, "Fieldtrip: open source software for advanced analysis of meg, eeg, and invasive electrophysiological data," *Computational intelligence and neuroscience*, vol. 2011, 2011.

[76] Y. Huang, A. Datta, M. Bikson, and L. C. Parra, "Realistic volumetric-approach to simulate transcranial electric stimulation—roast—a fully automated open-source pipeline," *Journal of neural engineering*, vol. 16, no. 5, p. 056006, 2019.

[77] E. A. Rashed, J. Gomez-Tames, and A. Hirata, "Development of accurate human head

models for personalized electromagnetic dosimetry using deep learning," *NeuroImage*, vol. 202, p. 116132, 2019.

[78] A. M. Dale, B. Fischl, and M. I. Sereno, "Cortical surface-based analysis: I. segmentation and surface reconstruction," *Neuroimage*, vol. 9, no. 2, pp. 179–194, 1999.

[79] S. M. Smith, "Fast robust automated brain extraction," *Human brain mapping*, vol. 17, no. 3, pp. 143–155, 2002.

[80] J. Ashburner and K. J. Friston, "Unified segmentation," *Neuroimage*, vol. 26, no. 3, pp. 839–851, 2005.

[81] M. Vöröslakos, Y. Takeuchi, K. Brinyiczki, T. Zombori, A. Oliva, A. Fernández-Ruiz, G. Kozák, Z. T. Kincses, B. Iványi, G. Buzsáki, *et al.*, "Direct effects of transcranial electric stimulation on brain circuits in rats and humans," *Nature communications*, vol. 9, no. 1, pp. 1–17, 2018.

[82] A. Opitz, A. Falchier, G. S. Linn, M. P. Milham, and C. E. Schroeder, "Limitations of ex vivo measurements for in vivo neuroscience," *Proceedings of the National Academy of Sciences*, vol. 114, no. 20, pp. 5243–5246, 2017.

[83] R. Dahnke, R. A. Yotter, and C. Gaser, "Cortical thickness and central surface estimation," *Neuroimage*, vol. 65, pp. 336–348, 2013.

[84] W. A. Fuller, *Measurement error models*, vol. 305. John Wiley & Sons, 2009.

[85] *Linear Regression with Errors in Both Variables: A Proper Bayesian Approach*, October 1999.

[86] M. D. Hoffman and A. Gelman, "The no-u-turn sampler: adaptively setting path lengths in hamiltonian monte carlo.," *Journal of Machine Learning Research*, vol. 15, no. 1, pp. 1593–1623, 2014.

[87] B. Carpenter, A. Gelman, M. D. Hoffman, D. Lee, B. Goodrich, M. Betancourt, M. Brubaker, J. Guo, P. Li, and A. Riddell, "Stan: A probabilistic programming language," *Journal of statistical software*, vol. 76, no. 1, 2017.

[88] C. Göksu, L. G. Hanson, H. R. Siebner, P. Ehses, K. Scheffler, and A. Thielscher, "Human in-vivo brain magnetic resonance current density imaging (mrcdi)," *NeuroImage*, vol. 171, pp. 26–39, 2018.

[89] P. C. Miranda, A. Mekonnen, R. Salvador, and G. Ruffini, "The electric field in the cortex during transcranial current stimulation," *Neuroimage*, vol. 70, pp. 48–58, 2013.

[90] G. B. Saturnino, A. Antunes, and A. Thielscher, "On the importance of electrode parameters for shaping electric field patterns generated by tdcs," *Neuroimage*, vol. 120, pp. 25–35, 2015.

[91] G. B. Saturnino, K. H. Madsen, and A. Thielscher, "Optimizing the electric field strength in multiple targets for multichannel transcranial electric stimulation," *bioRxiv*, 2020.

[92] S. Boyd, S. P. Boyd, and L. Vandenberghe, *Convex optimization*. Cambridge university press, 2004.

[93] J.-H. Park, S. B. Hong, D.-W. Kim, M. Suh, and C.-H. Im, "A novel array-type transcranial direct current stimulation (tdcs) system for accurate focusing on targeted brain areas," *IEEE Transactions on Magnetics*, vol. 47, no. 5, pp. 882–885, 2011.

[94] G. Ruffini, M. D. Fox, O. Ripolles, P. C. Miranda, and A. Pascual-Leone, "Optimization of multifocal transcranial current stimulation for weighted cortical pattern targeting from realistic modeling of electric fields," *Neuroimage*, vol. 89, pp. 216–225, 2014.

[95] S. Wagner, M. Burger, and C. H. Wolters, "An optimization approach for well-targeted transcranial direct current stimulation," *SIAM Journal on Applied Mathematics*, vol. 76, no. 6, pp. 2154–2174, 2016.

[96] S. Guler, M. Dannhauer, B. Erem, R. Macleod, D. Tucker, S. Turovets, P. Luu, D. Erdogmus, and D. H. Brooks, "Optimization of focality and direction in dense electrode array transcranial direct current stimulation (tdcs)," *Journal of neural engineering*, vol. 13, no. 3, p. 036020, 2016.

[97] S. Guler, M. Dannhauer, B. Erem, R. Macleod, D. Tucker, S. Turovets, P. Luu, W. Meleis, and D. H. Brooks, "Optimizing stimulus patterns for dense array tdcs with fewer sources than electrodes using a branch and bound algorithm," in *2016 IEEE 13th International Symposium on Biomedical Imaging (ISBI)*, pp. 229–232, IEEE, 2016.

[98] M. Fernandez-Corazza, S. Turovets, and C. H. Muravchik, "Unification of optimal targeting methods in transcranial electrical stimulation," *NeuroImage*, vol. 209, p. 116403, 2020.

[99] P. E. Gill and W. Murray, "Numerically stable methods for quadratic programming," *Mathematical programming*, vol. 14, no. 1, pp. 349–372, 1978.

[100] S. Boyd and J. Mattingley, "Branch and bound methods," *Notes for EE364b, Stanford University*, pp. 2006–07, 2007.

[101] A. Thielscher, A. Antunes, and G. B. Saturnino, "Field modeling for transcranial magnetic stimulation: a useful tool to understand the physiological effects of tms?," in *2015 37th annual international conference of the IEEE engineering in medicine and biology society (EMBC)*, pp. 222–225, IEEE, 2015.

[102] M. Attene, "A lightweight approach to repairing digitized polygon meshes," *The visual computer*, vol. 26, no. 11, pp. 1393–1406, 2010.

[103] T. Lipp and S. Boyd, "Variations and extension of the convex–concave procedure," *Optimization and Engineering*, vol. 17, no. 2, pp. 263–287, 2016.

[104] C. Schmidt, S. Wagner, M. Burger, U. van Rienen, and C. H. Wolters, "Impact of uncertain head tissue conductivity in the optimization of transcranial direct current stimulation for an auditory target," *Journal of neural engineering*, vol. 12, no. 4, p. 046028, 2015.

[105] N. Grossman, D. Bono, N. Dedic, S. B. Kodandaramaiah, A. Rudenko, H.-J. Suk, A. M. Cassara, E. Neufeld, N. Kuster, L.-H. Tsai, *et al.*, "Noninvasive deep brain stimulation via temporally interfering electric fields," *Cell*, vol. 169, no. 6, pp. 1029–1041, 2017.

[106] S. Rampersad, B. Roig-Solvas, M. Yarossi, P. P. Kulkarni, E. Santarnecchi, A. D. Dorval, and D. H. Brooks, "Prospects for transcranial temporal interference stimulation in humans: a computational study," *NeuroImage*, vol. 202, p. 116124, 2019.

[107] NIH, "Early stage testing of pharmacologic or device-based interventions for the treatment of mental disorders (r61/r33- clinical trial required)." `https://grants.nih.gov/grants/guide/rfa-files/RFA-MH-18-702.html`, 2018.

[108] M. Dannhauer, D. Brooks, D. Tucker, and R. MacLeod, "A pipeline for the simulation of transcranial direct current stimulation for realistic human head models using scirun/biomesh3d," in *2012 Annual International Conference of the IEEE Engineering in Medicine and Biology Society*, pp. 5486–5489, IEEE, 2012.

[109] SimBio Development Group, "SimBio: A generic environment for bio-numerical simulations." online, https://www.mrt.uni-jena.de/simbio, accessed Jun 4, 2020.

[110] S. Wagner, S. Rampersad, Ü. Aydin, J. Vorwerk, T. Oostendorp, T. Neuling, C. Herrmann, D. Stegeman, and C. Wolters, "Investigation of tdcs volume conduction effects in a highly realistic head model," *Journal of neural engineering*, vol. 11, no. 1, p. 016002, 2013.

[111] S. N. Makarov, W. A. Wartman, M. Daneshzand, K. Fujimoto, T. Raij, and A. Nummenmaa, "A software toolkit for tms electric-field modeling with boundary element fast multipole method: An efficient matlab implementation," *Journal of Neural Engineering*, 2020.

[112] Y. Renard and J. Pommier, "Getfem++, a generic finite element library in c++," *Laboratoire MIP, UMR*, vol. 5640, 2007.

[113] G. B. Saturnino, O. Puonti, J. D. Nielsen, D. Antonenko, K. H. Madsen, and A. Thielscher, "Simnibs 2.1: a comprehensive pipeline for individualized electric field modelling for transcranial brain stimulation," in *Brain and Human Body Modeling*, pp. 3–25, Springer, 2019.

[114] L. J. Gomez, M. Dannhauer, and A. V. Peterchev, "Fast computational optimization of tms coil placement for individualized electric field targeting," *bioRxiv*, 2020.

[115] H. Yazdanian, G. B. Saturnino, A. Thielscher, and K. Knudsen, "Fast evaluation of the biot-savart integral using fft for electrical conductivity imaging," *Journal of Computational Physics*, p. 109408, 2020.

[116] H. S. Suh, W. H. Lee, and T.-S. Kim, "Influence of anisotropic conductivity in the skull and white matter on transcranial direct current stimulation via an anatomically realistic finite element head model," *Physics in Medicine & Biology*, vol. 57, no. 21, p. 6961, 2012.

[117] O. Puonti, K. Van Leemput, G. B. Saturnino, H. R. Siebner, K. H. Madsen, and A. Thielscher, "Accurate and robust whole-head segmentation from magnetic resonance images for individualized head modeling," *NeuroImage*, p. 117044, 2020.

[118] M. Vermaas, M. Piastra, T. Oostendorp, N. Ramsey, and P. Tiesinga, "Femfuns: A volume conduction modeling pipeline that includes resistive, capacitive or dispersive tissue and electrodes.," *Neuroinformatics*, 2020.

[119] A. S. Aberra, B. Wang, W. M. Grill, and A. V. Peterchev, "Simulation of transcranial

magnetic stimulation in head model with morphologically-realistic cortical neurons," *Brain stimulation*, vol. 13, no. 1, pp. 175–189, 2020.

[120] M. Ridding and U. Ziemann, "Determinants of the induction of cortical plasticity by non-invasive brain stimulation in healthy subjects," *The Journal of physiology*, vol. 588, no. 13, pp. 2291–2304, 2010.

Appendix A

Value and limitations of intracranial recordings for validating electric field modeling for transcranial brain stimulation
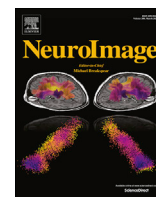
Value and limitations of intracranial recordings for validating electric field modeling for transcranial brain stimulation

Oula Puonti [a,b,1], Guilherme B. Saturnino [a,b,1], Kristoffer H. Madsen [a,c], Axel Thielscher [a,b,*]

[a] Danish Research Centre for Magnetic Resonance, Centre for Functional and Diagnostic Imaging and Research, Copenhagen University Hospital Hvidovre, Hvidovre, Denmark
[b] Department of Health Technology, Technical University of Denmark, Kgs. Lyngby, Denmark
[c] Department of Applied Mathematics and Computer Science, Technical University of Denmark, Kgs. Lyngby, Denmark

ARTICLE INFO

ABSTRACT

Comparing electric field simulations from individualized head models against in-vivo intra-cranial recordings is considered the gold standard for direct validation of computational field modeling for transcranial brain stimulation and brain mapping techniques such as electro- and magnetoencephalography. The measurements also help to improve simulation accuracy by pinning down the factors having the largest influence on the simulations. Here we compare field simulations from four different automated pipelines against intracranial voltage recordings in an existing dataset of 14 epilepsy patients. We show that modeling differences in the pipelines lead to notable differences in the simulated electric field distributions that are often large enough to change the conclusions regarding the dose distribution and strength in the brain. Specifically, differences in the automatic segmentations of the head anatomy from structural magnetic resonance images are a major factor contributing to the observed field differences. However, the differences in the simulated fields are not reflected in the comparison between the simulations and intra-cranial measurements. This apparent mismatch is partly explained by the noisiness of the intra-cranial measurements, which renders comparisons between the methods inconclusive. We further demonstrate that a standard regression analysis, which ignores uncertainties in the simulations, leads to a strong bias in the estimated linear relationship between simulated and measured fields. Ignoring this bias leads to the incorrect conclusion that the models systematically misestimate the field strength in the brain. We propose a new Bayesian regression analysis of the data that yields unbiased parameter estimates, along with their uncertainties, and gives further insights to the fit between simulations and measurements. Specifically, the unbiased results give only weak support for systematic misestimations of the fields by the models.

1. Introduction

Modeling the current flow distribution in the brain is in the core of many neuroimaging and functional brain mapping techniques. The currents-of-interest can be either externally induced by transcranial brain stimulation (TBS) methods, such as transcranial electrical stimulation (TES) or transcranial magnetic stimulation (TMS) or can result from neuronal activity in which case they can be measured using potential differences on the scalp (EEG) or by recording the produced magnetic fields (MEG). In TBS, the individual anatomy has a large, and often counter-intuitive, impact in shaping the current flow inside the cranium (Bungert et al., 2017; Datta et al., 2009; Laakso et al., 2015; Miranda

et al., 2013; Opitz et al., 2015). Similarly, the signal measured in EEG and MEG is dependent on the complex geometry of the head (Cho et al., 2015; Dannhauer et al., 2011; Stenroos et al., 2014). These findings have prompted a shift away from simplified anatomical models (Ravazzani et al., 1996) towards individualized head models based on structural magnetic resonance (MR) scans. Individualized modeling holds great promise particularly for TES, where several studies revealed a large inter-subject variability of the physiological stimulation effects (e.g., López-Alonso et al., 2014; Wiethoff et al., 2014). Part of this variability is likely explained by dosing differences due to anatomical variation. Individualized modeling enables dose control and can be used to systematically improve spatial targeting by automated tailoring of the

---

electrode positions and injected currents, ensuring that the highest field strengths are contained to the region-of-interest (Dmochowski et al., 2011; Saturnino et al., 2019a). This opens the door for personalized treatment approaches in a variety of brain disorders ranging from major depressive disorder (Csifcsák et al., 2018) to motor rehabilitation after stroke (Datta et al., 2011; Minjoli et al., 2017).

Although practically relevant results have been obtained from simulation studies, which support the usefulness of individualized head models, one of the key challenges is the direct in-vivo validation of the electric field simulations in the human brain. The modeling process includes uncertainties, mainly related to the segmentation of the anatomy (Nielsen et al., 2018) and spatial tissue conductivities (Saturnino et al., 2019b), which propagate onto the estimated fields. Optimally, one would use in-vivo field measurements in the brain to gauge the accuracy of the simulations. In practice this is, however, difficult: In-vivo measurements of the electric fields are experimentally very demanding and susceptible to measurement errors, creating unwanted uncertainty in the data that is supposed to be used as ground truth for validating the simulations. To-date, we are aware of three studies where head model validation using direct in-vivo intra-cranial measurements of the electric fields in humans is attempted. The first one by (Opitz et al., 2016) is focused on validating the assumption that the head acts as an ohmic conductor. The second one by (Huang et al., 2017) reports TES-induced voltage measurements on ten epilepsy patients with intra-cranial electrodes. The authors use the voltage measurements for assessing the correlations between the simulated and measured voltage differences and for calibrating the tissue conductivities of the individual head models. In similar vein (Opitz et al., 2018), compare simulated and measured fields in two epilepsy patients reporting slightly lower correlations compared to those in (Huang et al., 2017). The difference is probably explained by differences in the experimental procedures, as the recording and TES electrodes were quite close to each other and to nearby skull defects in the study of (Opitz et al., 2018), suggesting that discrepancies between real and modeled positions and anatomy might have had stronger effects on the field comparisons than in (Huang et al., 2017). (Huang et al., 2017) found that models based on "standard" literature values for the ohmic conductivities systematically overestimated the recorded voltage differences. On the other hand (Opitz et al., 2018), found underestimated fields in one of the studied patients, while the calculated e-fields were too high in the second patient. Recently (Göksu et al., 2018), demonstrated a novel non-invasive approach to reconstruct TES induced current densities in the brain from MR images of the current-generated magnetic fields (magnetic resonance current density imaging, MRCDI). They presented initial results on five subjects showing good agreement between simulated and measured current densities, with a moderate but systematic underestimation of the current densities by the models based on "standard" ohmic conductivities. Non-invasive measurements would be the preferred approach, not only due to ethical aspects relating to invasive studies, but also because invasive measurements change the volume conduction properties of the head, thus introducing additional modeling complexities. MRCDI is a promising step to the correct direction but needs further development before it can be applied for head model validation.

In this article, we compare four different automated methods for end-to-end electric field simulations starting from a structural MR scan, followed by segmentation of the anatomy and generation of a finite element (FEM) mesh, and finally calculating the electric field distribution in the brain for a given stimulation protocol. We reproduce and extend the analysis presented in (Huang et al., 2017) and (Huang et al., 2019) using a freely available data set from (Huang et al., 2017). Specifically, we set out to demonstrate four points: first, differences in the modeling pipelines, such as the choice of segmentation and FEM approaches, often result in clear differences in the electric field simulations that are in the range of what is considered physiologically relevant. Second, the field differences depend on the size of the differences between the automatic head segmentations. Third, the field differences are not reflected in the comparison between the simulated and measured fields, which can be

partly explained by the limitations of the validation data. Fourth, applying a standard linear regression analysis to compare the simulations and measurements leads to a biased estimate of the linear relationship between the two. In contrast, a more elaborate Bayesian regression analysis overcomes this problem, and allows for quantifying the uncertainty in the parameter estimates, which helps the interpretation of the fits between the simulations and measurements.

The results highlight the difficulty of validating the simulations, even when direct measurements are available, and point to a need for a more careful analysis of the available data and for adopting a strategic approach to future measurement studies in order to reach conclusive validations.

2. Material and methods

The data set consists of 14 epilepsy patients with intracranial EEG electrodes planted for surgical evaluation (Huang et al., 2017). For each subject there exists a T1-weighted MR scan, a manually corrected segmentation of the main tissue classes (white matter - WM, gray matter - GM, cerebro-spinal fluid - CSF, skull and scalp) along with annotations of the extra-cranial stimulation electrodes, subgaleal electrodes, intracranial electrode strip, and the surgical drain. The locations, in MNI and voxel coordinates, and measured voltages from the intracranial electrodes are provided as a text file. In general, the stimulation electrodes are placed medially over the frontal and occipital poles, with some exceptions, and transcranial alternating current stimulation (TACS) is performed with 1 mA baseline peak at 1Hz (Huang et al., 2017). Based on the manually corrected segmentations, we modeled the electrodes as 2×2 cm squares with 3 mm gel and rubber layers and determined their locations manually in each subject.

We compare two different software tools for generating individualized head models and simulating the electric fields induced by TES: *SimNIBS 2.1* (Saturnino et al., 2019) and *ROAST v2.7* (Huang et al., 2019). *SimNIBS 2.1* offers three alternative approaches for generating the anatomical head models, which we consider individually, giving in total four methods to compare. For completeness, we will next briefly describe each of the approaches.

2.1. Head model generation

- The default pipeline for head model generation in *SimNIBS 2.1*, called *headreco* (Nielsen et al., 2018), uses the segmentation routine from *SPM12* (https://www.fil.ion.ucl.ac.uk/spm/software/spm12/) (Ashburner and Friston, 2005), combined with an extended anatomical atlas (Huang et al., 2013), to generate a tissue segmentation from a set of possibly multi-contrast MR scans. After the initial segmentation, the tissue masks are cleaned using simple morphological operations to reduce noise and ensure that the tissues are contained within each other. Next, surfaces, represented as triangular elements, are extracted from the voxel segmentations. As a last step, the FEM mesh is generated by filling in the space between the surfaces with tetrahedra. Note, that due to the chosen meshing approach, which first generates surfaces, the tissue classes need to be nested which is ensured by the clean-up step after the initial segmentation. For further details we refer the reader to (Nielsen et al., 2018).
- The *headreco* pipeline supports detailed cortical surface reconstructions, which are generated using the computational anatomy toolbox (*CAT12*, http://www.neuro.uni-jena.de/cat/) implemented in *SPM12*. The cortical surfaces from *CAT12* replace the ones generated from the voxel segmentations in the standard *headreco* pipeline, while other parts of the pipeline remain the same. We denote this approach *headreco + CAT*.
- The predecessor of *headreco* in *SimNIBS*, called *mri2mesh* (Windhoff et al., 2013), combines the cortical surfaces and subcortical segmentation generated by *FreeSurfer* (https://surfer.nmr.mgh.harvard.edu/) (Fischl et al., 2002), with extra-cerebral tissue

segmentations from FSL's brain extraction tool (https://fsl.fmrib.o x.ac.uk/fsl/fslwiki) (Pechaud et al., 2006). Similar to *headreco* with *CAT12*, the cortical surfaces from *FreeSurfer* are combined with surfaces created from voxel segmentations in the other tissues, and the final FEM mesh is obtained by filling in tetrahedra.

- Similar to the standard version of *headreco*, the *ROAST v2.7* toolbox (https://www.parralab.org/roast/) (Huang et al., 2019) generates the tissue segmentations using *SPM12*, with the same extended anatomical atlas, and applies morphological operations to clean the segmentations. The main difference between the methods is in the post-processing and FEM meshing approach: whereas *headreco* first creates surfaces, roast generates a tetrahedral volume mesh directly from the voxel segmentation using CGAL (Fabri and Teillaud, 2011) called through the *iso2mesh* (http://iso2mesh.sourceforge.net/ cgi-bin/index.cgi) (Fang and Boas, 2009) toolbox. The restriction of nested tissue classes is thus relaxed, and anatomical details can potentially be better captured if the initial volume segmentation is accurate. However, the reconstructions of the tissue boundaries can be less accurate as the volume segmentation is meshed directly.

Data and code availability statement: The data set is freely available for download after registration at https://doi.org/10.6080/K0XW4GQ1. The software tools used for the analysis are distributed freely as opensource packages. The code for running the data analysis, described in the Analyses-section below, is included in the supplementary material.

2.2. Simulating the electric fields

The electric field calculations are performed in *SimNIBS 2.1* for the head models generated with its pipelines (*headreco, headreco + CAT* and *mri2mesh*) and in *ROAST v2.7* for the head models generated with *ROAST*. The current flowing through the electrodes is set to 1 mA, and the polarity adjusted to fit the recordings from (Huang et al., 2017) so that the direction of current flow is consistent with the measured data. Tissue and electrode conductivities were set to the literature values reported in (Huang et al., 2017).

Both *SimNIBS 2.1* and *ROAST v2.7* use the *GetDP* (Geuzaine, 2007) software to calculate electric potentials using the FEM method with first order tetrahedral elements. However, the post-processing of the simulations differs: *ROAST* uses *GetDP* to calculate the electric fields in each mesh node, while *SimNIBS* has native post-processing functions calculating the electric field for each mesh tetrahedra. The post-processing in *SimNIBS* is more consistent with the mathematical formulation of the Finite Element Method, where gradients are defined element-wise instead of node-wise (Zienkiewicz et al., 2013), and yields more physically plausible results, as the electric field values are discontinuous across tissue interfaces (Geselowitz, 1967). When interpolating or gridding results, *SimNIBS* uses the original mesh grid, keeping geometric consistency, while *ROAST* uses the *TriScatteredInterp* function in MATLAB (MathWorks, 2019), which does not preserve the original mesh, and instead creates a new Delaunay triangulation where the gridding is performed. Thus, the electric field values interpolated in *ROAST* do not observe tissue boundaries, as they do in *SimNIBS*.

3. Analyses

We performed two sets of analyses: the first one to quantify the differences in anatomical segmentation accuracy along with the differences in the simulated electric field distributions between the methods, and the second one to relate the electric field simulations to the measured potential differences in the intra-cranial electrodes. All the pipelines were run with default settings with the following exceptions:

- Both *headreco* and *headreco + CAT* were run with the *–d no-conform* option to avoid resampling of the input scans.

- For P04 in *headreco + CAT*, we set the vertex density (-v option) to 1.5 Nodes/mm^2
- For P014 in *mri2mesh*, we set the number of vertices (–numvertices option) to 120000.
- For P010 the MR scan was resampled to 1 mm^3 isotropic as *ROAST v2.7* does not account for anisotropic scans resulting in erroneous electric field estimates by effectively changing the electric conductivities along the axis where the anisotropy occurs. In the meantime, this bug has been fixed in a newer version of *ROAST* (2.7.1).
- For P06, we inverted the "x" component of the electric field calculated with *ROAST* to account for the fact that *ROAST* does not correct for the "x" axis flipping indicated by the header in the NifTi image.

The changes to the vertex densities in P04 and P014 were made as, after running the head model pipeline, we found that the head meshes were missing volumes (WM in P04 and CSF in P014). In both cases, increasing mesh density made surface decoupling more accurate and thus solved the problems in meshing the surfaces. The average edge size, number of nodes and tetrahedra in the final meshed obtained with each method is shown in Table 1.

3.1. Variability in segmentations and electric fields

Assessing the anatomical segmentation accuracy of the four methods requires a ground truth segmentation to compare against. The manually corrected segmentations were created by first running the *ROAST* segmentation tool on the T1-weighted scans, then automatically correcting the output using a custom script, and finally correcting the remaining errors by hand (Huang et al., 2017). However, the data set is very challenging to segment due to the relatively low (clinical) MR scan quality and surgical interventions, and some of the manually corrected segmentations still have inaccuracies (see Fig. 3). As the segmentation procedure is based on *ROAST*, the manually corrected segmentations could also be biased towards the automated *ROAST*, *headreco*, and *headreco + CAT* segmentations, which all use *SPM12* to segment the head tissues. To partially correct this issue, we generated a "consensus" head segmentation based on a multi-atlas approach using majority voting (Iglesias and Sabuncu, 2015). There, each of the segmentations obtained from the four automated pipelines, as well as the manually corrected segmentation, cast a single vote on the classification of each voxel, and the tissue with the most votes is selected. We can then compare the individual segmentations to the consensus using the Dice overlap score. The Dice score is defined as:

$$Dice(C, A) = \frac{2|C \cap A|}{|C| + |A|} \ ,$$

where *C* and *A* denote the consensus and the automated, or manually corrected, segmentation masks of a given tissue. It serves as an indication of the general segmentation differences between the four methods, such that we can see if a segmentation method consistently deviates from the consensus.

The differences between the simulated electric fields given by the methods were measured calculating the relative difference in the fields in

Table 1
Average edge length, number of nodes and number of tetrahedra across all meshes.

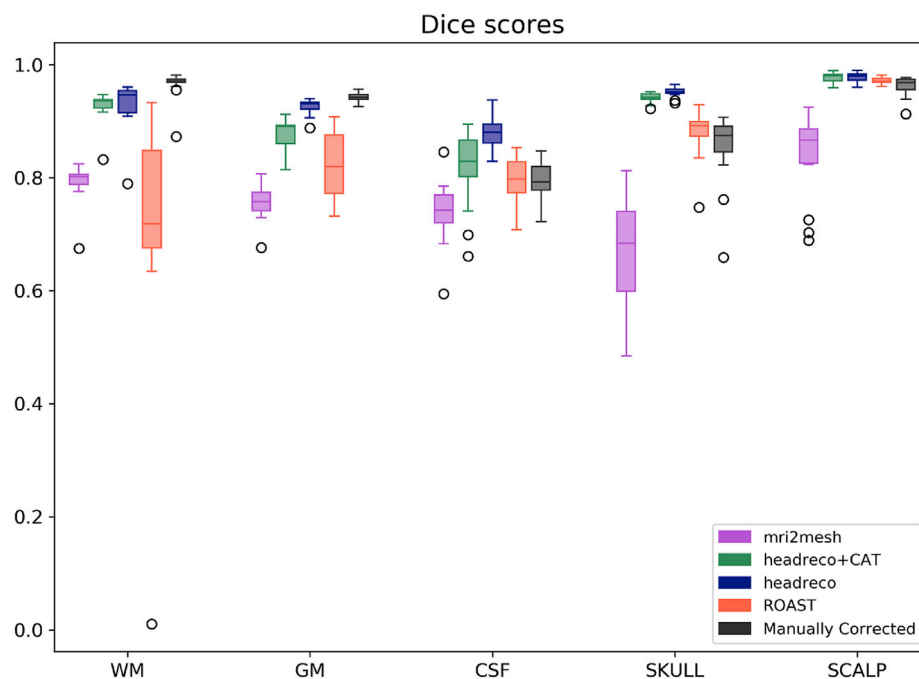|	mri2mesh	headreco + CAT	headreco	ROAST
Average edge length (mm)	1.95	2.12	2.21	2.78
Number of nodes	0.72×10^6	1.00×10^6	0.74×10^6	0.32×10^6
Number of tetrahedra	4.03×10^6	5.50×10^6	4.02×10^6	1.88×10^6

Fig. 1. Dice scores computed for each of the pipelines, and the manually corrected segmentations, in WM, GM, CSF, skull and scalp. On each box, the line marks the median, the box extends to lower and upper quartiles, whiskers extend up to 1.5 times the interquartile range, and data points beyond that are marked as outliers. The higher the score, the more similar the segmentations are to the consensus.

Fig. 2. Example segmentations from a subject where all segmentations agree. From left to right, top to bottom: the input T1-weighted MRI scan, consensus segmentation, manually corrected segmentation, *ROAST*, *headreco + CAT*, *headreco* and *mri2mesh*. Note that *mri2mesh* does not segment the subcortical gray matter. The black lines close to the cortex in the manually corrected segmentations correspond to the intra-cranial electrode strips. Lowest row shows the differences in the norm of the electric field on the cortex.
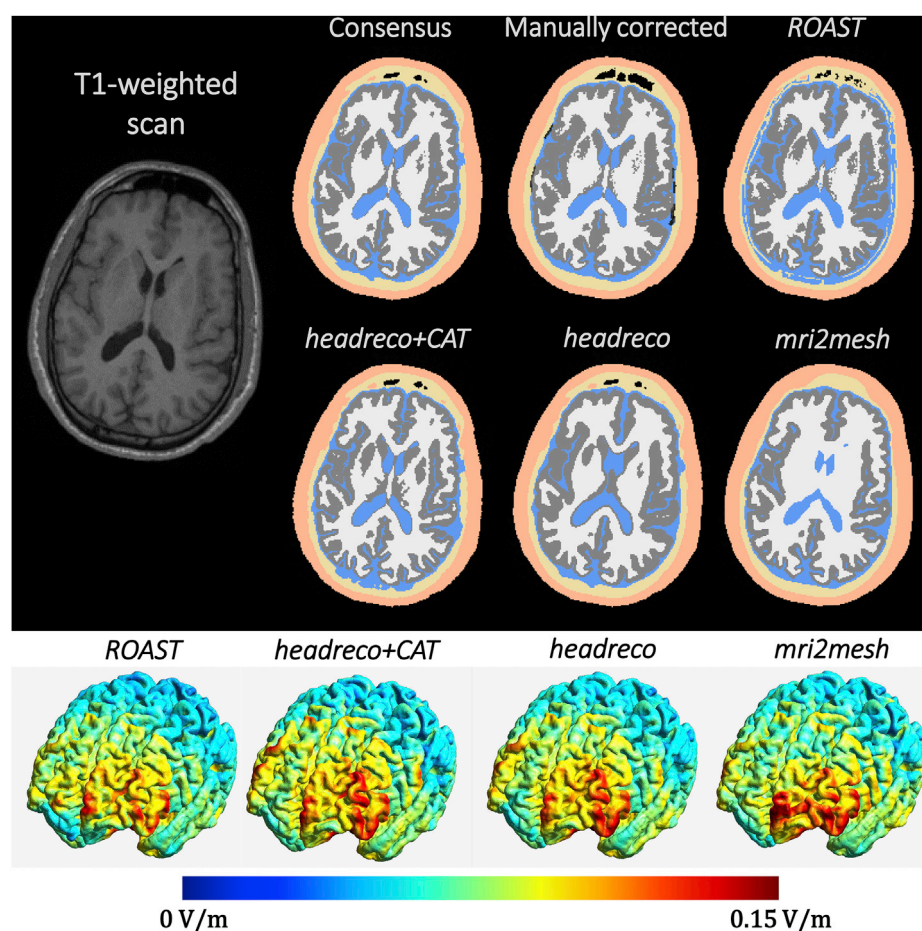
Fig. 3. Example segmentations from a subject where all segmentations disagree. From left to right, top to bottom: the input T1-weighted MRI scan, consensus segmentation, manually corrected segmentation, *ROAST, headreco + CAT, headreco* and *mri2mesh*. Note that *mri2mesh* does not segment the subcortical gray matter. The black lines close to the cortex in the manually corrected segmentations correspond to the intra-cranial electrode strips. Lowest row shows the differences in the norm of the electric field on the cortex.
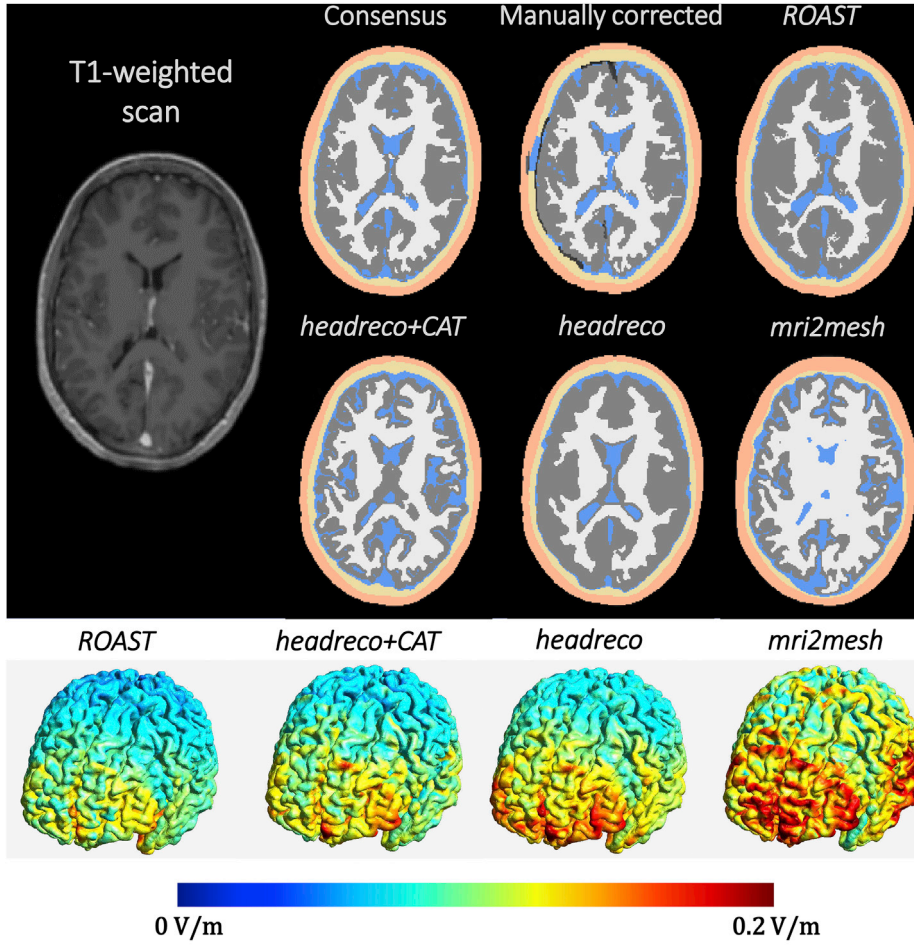
GM for each pair of methods. The relative field difference, akin to the Dice score, is defined as:

$$eDiff(\boldsymbol{E}_1, \boldsymbol{E}_2) = \frac{2\|\boldsymbol{E}_1 - \boldsymbol{E}_2\|}{\|\boldsymbol{E}_1 + \boldsymbol{E}_2\|} \quad . \tag{2}$$

The differences were evaluated in the middle cortical surface obtained from the CAT12 segmentation. Electric field values were interpolated from the gray matter region of the FEM meshes to the cortical surface. If necessary, electric field values were extrapolated by taking the nearest gray matter neighbor.

3.2. Fitting intracranial measurements

In this analysis, we wanted to relate the intracranial voltage recordings to the field simulations. As the electric field was not measured, but rather the voltage relative to a reference contact, we calculated pairwise voltage differences between consecutive electrode contacts and divided them by the distance between contacts. This corresponds to a coarse estimate of the electric field component along the electrode axis. To provide an unbiased comparison, the same procedure was done with the simulations, where the simulated voltages were sampled in the contact locations in *SimNIBS*, by performing barycentric interpolation based on the electric potentials calculated in the mesh nodes, and in *ROAST* by interpolating the gridded voltage values.

Next, we fitted a standard linear model for each subject and method:

$$\boldsymbol{y}_s = \beta_{s,m} \boldsymbol{x}_{s,m} + \boldsymbol{\varepsilon}_{s,m}$$
$$\boldsymbol{\varepsilon}_{s,m} \sim N(0, \sigma_{y,s})$$

or, equivalently

$$\boldsymbol{y}_s \sim N\left(\beta_{s,m} x_{s,m}, \sigma_{y,s}\right) . \tag{3}$$

Where $N(\mu, \sigma)$ denotes a normal distribution of mean μ and standard deviation σ, $\boldsymbol{x}_{s,m}$ is a vector of the simulated potential differences for subject s and method m, $\boldsymbol{y}_s$ is a vector of the recorded potential differences in subject s, and the noise $\varepsilon_{s,m}$ for each subject and method is assumed to be drawn from a normal distribution with mean zero and standard deviation $\sigma_{y,s}$. For each subject and segmentation, we report the slope $\beta_{s,m}$, the coefficient of determination (r^2) and correlation (ρ). This serves as a re-analysis of the results by (Huang et al., 2019, 2017) in comparing simulations to intracranial electrode recordings.

We found that the standard slope estimates were correlated with the measured field strengths, indicating that subjects with low signal had a systematic bias towards underestimated regression fits (see Results section for details). To account for the bias, we performed a hierarchical Bayesian regression analysis, where the slope of each subject and method $\beta_{s,m}$ is drawn from an underlying distribution for the group-level slope of each method β_m. In addition, we adopted a Bayesian errors-in-variables model (Gull, 2013; Minka, 1999), which allows accounting for noise in the measurements as well as uncertainties in the simulations that arise from noise in the MR scans, uncertain electrical conductivity values and segmentation errors. In short, the regression model now becomes:

$$\boldsymbol{y}_s \sim N\left(\beta_{s,m} \boldsymbol{x}_{s,m}^*, \sigma_{y,s}\right) \tag{4}$$

$$x_{s,m} \sim N\left(x_{s,m}^*, \sigma_{s,m}\right) \tag{5}$$

where $x_{s,m}^*$ is a vector of the unobserved "true" simulated values, and $x_{s,m}$ is a vector of the observed simulated potential differences. Note that in this model, not only measurement noise is considered, but also uncertainties in the simulations. We further assume that the slopes are generated as:

$$\beta_{s,m} \sim N(\beta_m, \sigma_{\beta,m}) \tag{6}$$

where β_m is the unobserved hyperparameter for the group average slope of method m, and the standard deviation $\sigma_{\beta,m}$ captures the subject-level variation of the slopes. If the estimated subject-specific slopes are close to each other this variation will be small, whereas if they are far apart the variation will be large. We further need to define prior distributions on the noise parameters, the average slope β_m, and the unobserved "true" simulations $x_{s,m}^*$. These, along with the full modeling details, can be found in the supplementary material. The Bayesian analysis was performed using Stan (Carpenter et al., 2017), specifically PyStan (https://pystan.readthedocs.io/en/latest/) for Python interfacing. The Stan code for running the analysis is provided in Supplementary Material 1.

The benefit of adopting this type of Bayesian modeling is three-fold: first, as mentioned before, the noise and uncertainties in the measurements and simulations can both be estimated in a principled way. Second, we can study the posterior distributions of the slope for each subject and method to see which values are supported by the data given the model. Third, we can evaluate the group differences between the methods using the posterior predictive distribution of the slope for an unseen subject.

4. Results

4.1. Variability in segmentations and electric fields

Here we aim to show that the different modeling pipelines yield different segmentations and electric field distributions, and that the differences between the simulations are large. Fig. 1 shows the Dice scores comparing the automated and manually corrected segmentations to the consensus segmentation in the five main head tissue classes: WM, GM, CSF, skull and scalp. The average Dice scores over all subjects and tissues, along with the standard deviations, for each method are: 0.757 ± 0.087 (mri2mesh), 0.908 ± 0.067 (headreco + CAT), 0.933 ± 0.040 (headreco), 0.836 ± 0.137 (ROAST), and 0.903 ± 0.078 (Manually Corrected). On average, the two headreco pipelines and the Manually Corrected segmentations are closest to the consensus obtaining a Dice score above 0.9, followed by ROAST and finally mri2mesh. As the consensus segmentation is based on votes from the different methods, there is a chance that it might be unfairly biased towards a subset of the segmentation approaches. In this study three of the five approaches originate from SimNIBS, which could lead to ROAST having lower Dice scores due the consensus segmentation agreeing more with SimNIBS-based methods. However, as four of the five approaches, namely headreco, headreco + CAT, ROAST and Manually Corrected, are based on SPM12 this is unlikely to be the case. To verify this, we additionally computed the Dice scores compared to a consensus segmentation where one of the SimNIBS methods (headreco) is excluded, see Supplementary Material 3. The Dice scores of ROAST and the Manually Corrected segmentations even decrease slightly, implying that the Dice scores in Fig. 1 are not favoring the segmentation approaches implemented in SimNIBS.

To get a better understanding where the segmentation differences arise from, we picked the subject where the methods agreed most (Fig. 2), i.e., highest average Dice score over tissues, subjects, and methods, and the subject where the methods disagreed the most (Fig. 3), i.e., lowest average Dice score over tissues, subjects, and methods. Two additional subjects with second-best and second-worst agreements are shown in the Supplementary Material 3, Figs. S22 and S23.

The differences in the norm of the electric field in the cortex exceed in part 50%, and also the positions of the most strongly simulated brain areas (the "hot spots") vary across methods. This would clearly change our interpretation of which brain areas get most strongly stimulated and how strong the stimulation effects might be. For example, in the case of the subject in Fig. 3, the e-field simulations based on mri2mesh reach 0.2V/m in the prefrontal cortex, but they hardly exceed 0.1 V/m in the simulations based on ROAST. While there is no consensus about the minimal field intensities that are required to cause reliable physiological stimulation effects, the data available so far from in-vitro and invasive recordings in animals suggest that fields stronger than 0.2 V/m are able to affect the neural activity under favorable conditions while fields below that might lack neural effects (Liu et al., 2018). Applying this threshold to the subject in Fig. 3, one would conclude that several brain areas got stimulated when considering the simulations based on mri2mesh, but that stimulation was fully ineffective when considering the ROAST results. In addition, only the simulations based on mri2mesh would indicate a stimulation of the temporal lobe, while this would not be the case when considering the other three simulation results.

It is also clear that the MR scans of the two subjects where the methods agree (Fig. 2 and S22), are of better quality in terms of contrast between tissues compared to the MR scans of the two subjects where the methods disagree (Fig. 3 and S23). Specifically, the gray-white matter contrast is higher in the T1w scans where the methods agree, whereas the T1w scans where the methods disagree seem to be contrast-enhanced, see e.g., the superior sagittal sinus posterior to the ventricles in Fig. 3 and S23. This shows that the uncertainties in the segmentations are directly related to input MR data quality, resulting in more disagreement between the methods when the contrast between tissues is poor. The poor agreement between mri2mesh and the consensus is explained by the fact that mri2mesh segments the subcortical GM and the whole cerebellum as WM, resulting in lower Dice scores for WM and GM. Furthermore, the extra-cerebral segmentations rely on a fairly simple method, which has been shown to be outperformed by the SPM12-based approaches (Nielsen et al., 2018). mri2mesh also does not model the air pockets in the head, which might affect the fields estimates for some electrode montages located close to the sinuses. The largest difference between the two headreco pipelines and ROAST seems to be that the ROAST segmentation is generally less smooth in the sense that the tissue segmentations are not spatially continuous. This is apparent even in the two cases where the MR contrast is good (Fig. 2 and S22). The consensus segmentation allows for visualizing the systematic segmentation errors across all methods by studying the two consensus segmentations where the methods agree the most (Fig. 2 and S22). We observe that the sulcal CSF seems to be often segmented as GM, and that the skull is under-segmented when spongy bone is present. Example segmentations of all the subjects from the automated methods are provided in Supplementary Material 2.

Next, we study the differences in the simulated electric fields between the automated methods. Table 2 shows the average relative difference between the electric field simulations (eDiff, Eq. (2)) for each pair of methods. The results from headreco and headreco + CAT agree most, which is expected as the only difference between the two is in the GM surface reconstruction. mri2mesh is the most different from all other methods, with differences in the range of upper 40%, which is likely due to two factors: first, the segmentation approach is different from the other methods, i.e., not based on SPM12, and second, mri2mesh does not

Table 2
Mean electric field differences (eDiff) between the methods measured in the middle gray matter surface.

Mean electric field difference (eDiff)			
	ROAST	headreco	headreco + CAT
mri2mesh	$49.0\% \pm 11.1\%$	$34.1\% \pm 6.7\%$	$34.1\% \pm 8.0\%$
headreco + CAT	$36.6\% \pm 12.3\%$	$21.4\% \pm 2.7\%$	
headreco	$34.3\% \pm 13.2\%$		

model the neck resulting in differences in electrode placement in those subjects with an electrode in the neck. *ROAST* has differences around 25% from the *headreco* methods, all of which share large parts of the segmentation algorithm, as they are based on *SPM12*. However, post-processing of the segmentations and the electric fields differs and is likely to cause most of the observed differences in the electric fields.

To link the segmentation differences to e-field differences, we calculated the average Dice scores over the tissues between the segmentations from each pair of methods and split the subjects to low and high Dice score groups based on the median. We then plotted the relative e-field differences (*eDiff,* Eq. (2)) in both groups for each pair of methods, which are shown in Fig. 4. In all comparisons the higher Dice score group, i.e., above median, has a lower relative e-field difference than the lower Dice score group, indicating that when the segmentations agree so do the field simulations. This effect can be seen also in the small difference between the high and low Dice score groups between *headreco* and *headreco + CAT* as the segmentations from both approaches are very similar to each other.

We visually explored the simulation results to get a qualitative overview of the typical segmentation differences that cause the e-field differences. Some informative examples are shown in Fig. 5. In general, we see that the amount of CSF has a large effect on the simulated electric fields likely due to shunting effects. The first row in Fig. 5 shows that if the amount of CSF is less, the simulated fields in the cortex can be much higher as the current does not redistribute through the highly conducting CSF. Thus, accurate segmentation of the GM sulci also becomes important for locally accurate field modeling. The second row shows a similar effect, where the skull is mislabeled either as CSF (left) or scalp (right). The final row in Fig. 5 shows spurious islands of GM voxels in the *ROAST* segmentation, which can lead to extremely high field estimates in GM as

these voxels are close to skull and surrounded by CSF. We note that segmenting out the CSF on this data set is challenging as no T2-weighted (T2w) scan is provided. As the skull-CSF border is highly visible in T2w scans, they typically contribute to an accurate placement of the skull-CSF border (Nielsen et al., 2018).

In Fig. 6, we show the norm of the electric field in WM, GM and CSF for both *ROAST* and *headreco + CAT* in subject P03. The effect of the different electric field post-processing schemes between *SimNIBS* and *ROAST* is quite striking: the interpolated field in *ROAST* is blurred, making the WM-GM border invisible and causing the large electric field estimates in the skull to bleed into CSF and to a lesser extent into GM. This effect makes the electric field estimates for CSF in *ROAST* clearly overestimated, as the fields in CSF are lower due to its high electric conductivity.

4.2. Fitting intracranial measurements

4.2.1. Standard regression analysis

We first present the results from a standard regression analysis to reproduce the comparison of the methods from (Huang et al., 2019). Fig. 7 shows the coefficient of determination (r^2) and the slope ($\beta_{s,m}$) of the standard linear regression (Eq. (3)) for each subject and method, and Table 3 shows the mean and standard deviation of both quantities, along with the correlation (ρ), across all subjects. Assessing Fig. 7 qualitatively, it seems that all methods perform approximately equal in predicting the recordings in terms of both the r^2 and the slope. Testing for differences using a one-way repeated measures ANOVA revealed no statistically significant differences in the r^2 values between the methods (p = 0.065) but did so for the slope values (p = 0.021). However, pairwise post hoc comparisons between the slope estimates of methods did not reveal any
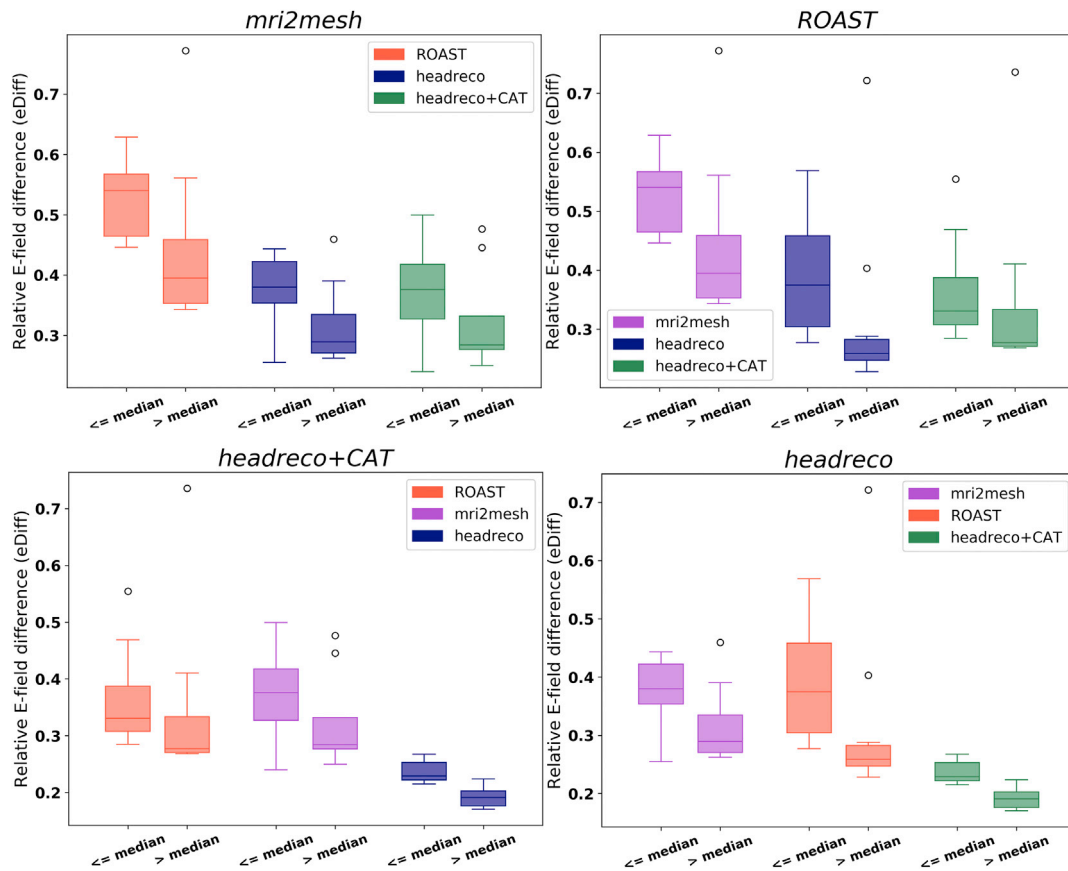

Fig. 4. The relative e-field differences (eDiff) for each pair of methods grouped by the average Dice score over tissues to either below or above median. Clockwise from upper left corner: *mri2mesh*, *ROAST*, *headreco + CAT* and *headreco*. Note that for all comparisons the above median group has a lower relative field difference, implying that when the segmentations agree better the simulations deviate less from each other.
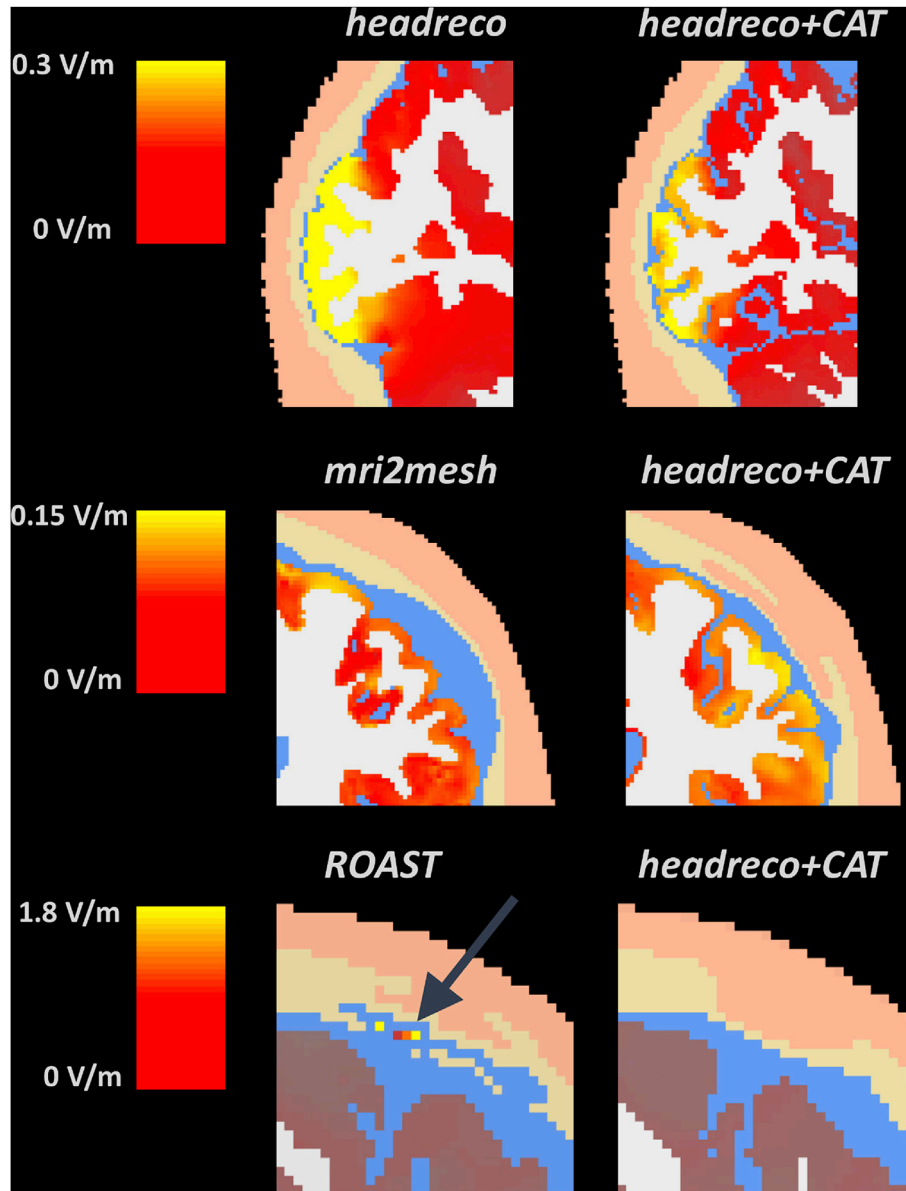
Fig. 5. Examples of segmentation and electric field norm differences. First row: the amount of estimated CSF and differentiation of GM sulci result in different fields. Second row: erroneous segmentation of skull as CSF results in lower fields as the thicker CSF layer allows for more shunting. Third row: spurious islands of GM voxels in *ROAST* can have very large field estimates. Note that the electric field scale is different between the figure rows.

differences using Tukey's Honest Significant Difference test. When not considering multiple comparisons in the post hoc tests, we find trends of differences between the slope estimates of *headreco* and *headreco + CAT* (p = 0.009), *headreco* and *ROAST* (p = 0.017), and *headreco + CAT* and *mri2mesh* (p = 0.027). The range of explained variance (r^2) seems to be large over the subjects, where in some subjects (P04 and P07) the modeled fields explain the measurements well, while in others (P06 and P09) the prediction is poor. These results are in line with the ones reported in (Huang et al., 2019, 2017; Opitz et al., 2018). In addition, we also observe that all methods tend to overestimate the measured potential differences as reported by (Huang et al., 2019), but that the correlations are similar for all methods and close to the ones reported for the head models generated from the manually corrected segmentations (Huang et al., 2017). Similar to the results in (Huang et al., 2019), we find no statistically significant differences in the accuracy of the field predictions between the methods. This result suggests that even though there are clear differences in the electric field simulations between the methods, as shown in Table 2, these differences are not reflected in the

comparison with the measurements. The large inter-subject variability in the regression fits likely explains the inconclusive result, but, as we show in the following, this variability is not a result of poor electric field simulations alone but is partly explained by the limitations of the intra-cranial measurements.

To link the intra-cranial measurements to the slope estimates from the standard regression, we plot the correlation between the strength of the recorded potential differences and the slope estimates in Fig. 8. We find a statistically significant correlation for all methods except *headreco*. That is, the linear relation is weak, i.e., the slope is close to zero, for the subjects where the measured signal is also weak. In contrast, the slope is steeper and closer to one for subjects where the measured signal is strongest. This implies that the slope estimates are underestimated in the standard regression analysis when there are large uncertainties present in the simulations. In fact, it is well-known that if noise in the so-called independent, or predictor, variables is unaccounted for, the regression coefficient will be underestimated (Frost and Thompson, 2000; Fuller, 1987). The problem persists even if the predicted and independent
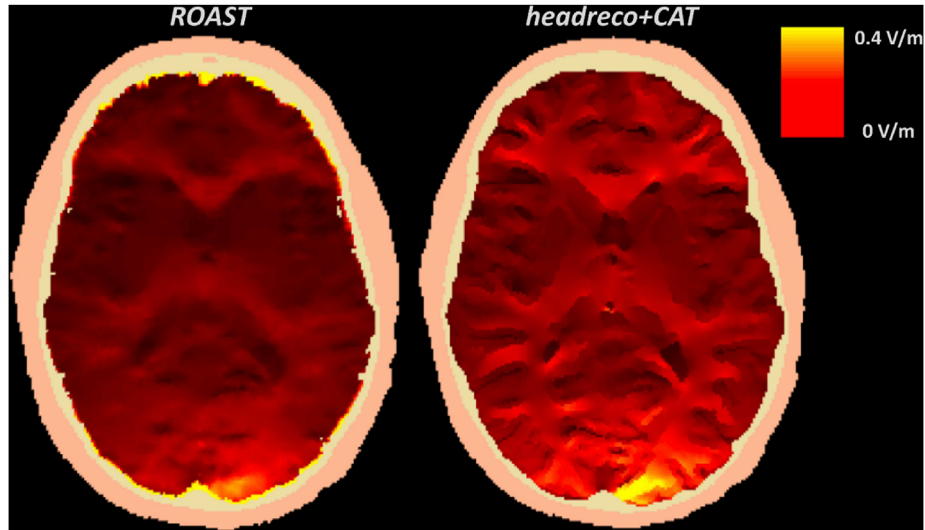
Fig. 6. The distribution of the norm of the electric field over the full brain volume for example subject P03 from *ROAST* and *headreco + CAT*. Note the differences in smoothness of the simulated fields.
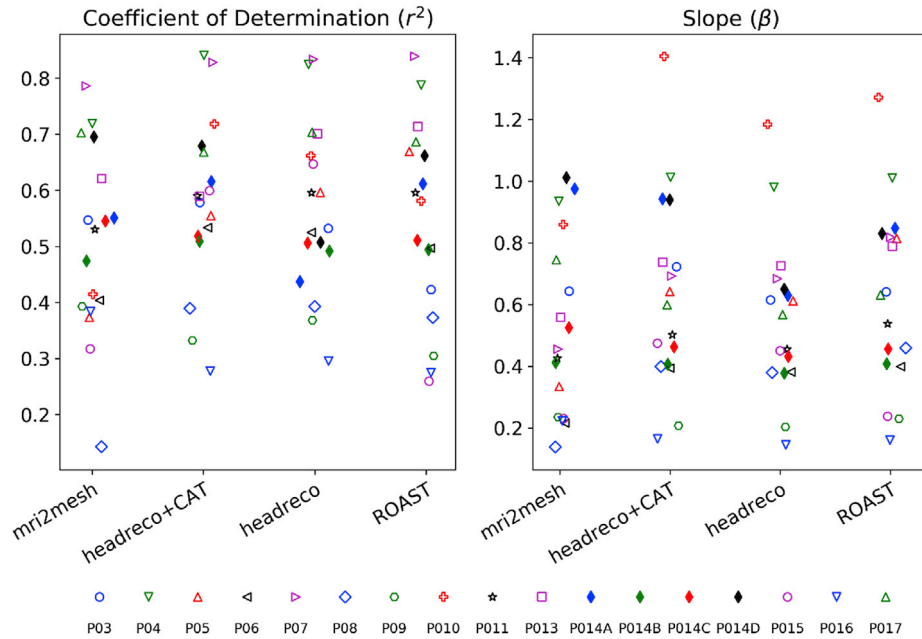

Fig. 7. Coefficient of determination (r^2) and slope ($\beta_{s,m}$) of the linear fit, for all subjects and methods.

Table 3

Mean ±Standard deviation of the coefficient of determination (r^2), slope (β) and correlation (ρ) for each head modeling pipeline, across all subjects.

	mri2mesh	headreco + CAT	headreco	ROAST
Coefficient of Determination (r^2)	0.506 ±0.163	0.580 ±0.150	0.567 ±0.148	0.554 ±0.175
Slope (β)	0.526 ±0.284	0.632 ±0.313	0.556 ±0.247	0.644 ±0.353
Correlation (ρ)	0.700 ±0.127	0.755 ±0.106	0.746 ±0.103	0.734 ±0.128

variables are exchanged as then the noise in the measurements is ignored, or if an intercept term is added.

To exemplarily demonstrate how the regression analysis is affected by the measurement data, we look at subject P014. Subject P014 received stimulation with four different electrode positions, which allows us to untangle the effect of the measured signal at the electrodes from the impact of the head model, as the FEM mesh is fixed for all four positions. Two of the electrode configurations (P014A and P014D, blue and black filled diamonds in Figs. 7 and 8) seem to have a good fit between simulations and measurements, based on the slope fits, for the majority of the pipelines, whereas the other two configurations (P014B and P014C, green and red filled diamonds) have poorer fits. This prompted us to conduct a full Bayesian regression analysis (Eqs. (4)–(6)), as outlined next.

4.2.2. Bayesian errors-in-variables regression

Fig. 9 shows the results of the Bayesian analysis for configurations P014C and P014D (red and black filled diamonds in Figs. 7 and 8, depicting the results of the classical regression analysis). Please see the Analyses section for a summary of the conducted analysis and
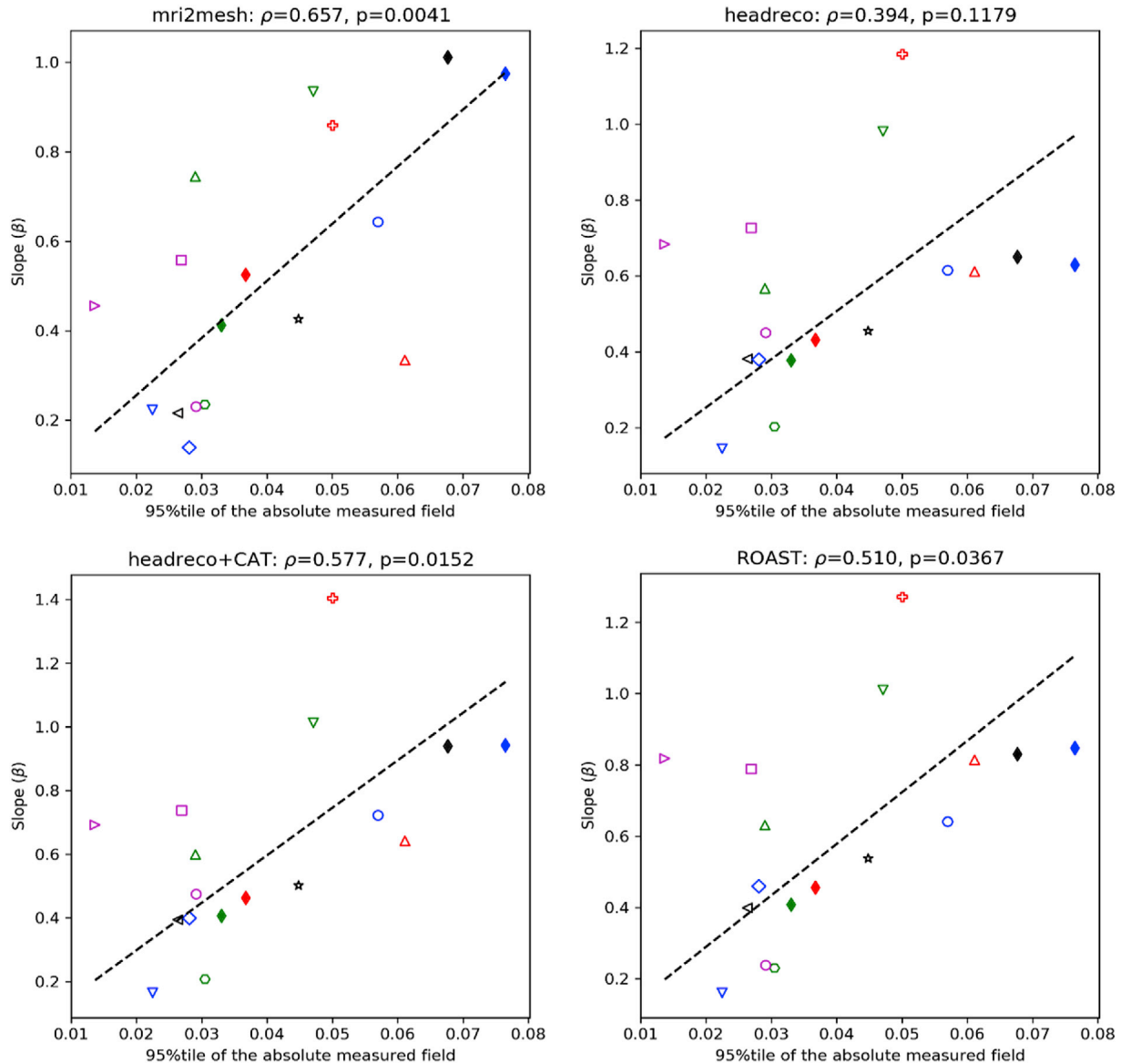
Fig. 8. Correlation between the 95th percentile of the absolute measured field and the slope estimates. Linear regression line without intercept shown in black. The correlation is significant for all methods except *headreco* and indicates that the standard slope estimates are likely biased.

Supplementary Material 1 for further details. The measured potential differences for P014C are closer to zero and look relatively noisier than for P014D. This results in a lower slope estimate and a wider 95% compatibility interval for P014C compared to P014D. This implies that some of the poor fits observed in Fig. 7 are not only due simulation errors, but rather the fact that in the absence of clear measurement signal, the uncertainties in the simulations dominate the linear fit and cause slope estimates close to zero. This gives more insight into the inter-subject variability observed in Fig. 7 and is not revealed by the standard regression analysis. Detailed analysis, similar to Fig. 9, on all subjects can be found in Supplementary Material 2.

To quantify the differences between the slope estimates from the standard and Bayesian analysis we sampled 4000 slope estimates from the normal distribution governing the slope of the standard regression in each subject, compared those in a pairwise manner to the slope samples from the posterior distribution in each subject, and computed the probability that the standard regression slope is smaller than the corresponding Bayesian one. The probabilities computed this way are: 0.867 for *mri2mesh*, 0.866 for *headreco + CAT*, 0.869 for *headreco*, and 0.861 for *ROAST,* revealing a large probability that the slopes obtained with the

standard analysis will be smaller than the ones obtained with the Bayesian analysis. The distribution of these pooled differences for each method over all subjects is shown in Supplementary Material 2 (Figure S18). All distributions have medians larger than zero indicating that the slope estimates from the Bayesian analysis are generally larger than the ones obtained from the standard regression analysis. To link this to a more classical statistical analysis, we performed paired Wilcoxon signed-rank tests between the standard slope estimates (Fig. 7) and the posterior means, which resulted in p-values < 0.001 for all segmentation methods. Thus, both the Bayesian analysis and a standard pairwise test between the slope estimates indicate that the regression results in Fig. 7 and Table 3, along with the results in (Huang et al., 2019) and (Huang et al., 2017) are underestimating the true slopes as they do not account for the uncertainties involved in the simulated fields. The analysis, results, and conclusions presented in (Huang et al., 2019) and (Huang et al., 2017) would benefit from being revisited with this underestimation in mind. We note that similar analyses of the correlation coefficients (Fig. 7, left and Table 3, second row) did not show differences between the standard and Bayesian regression, indicating that the correlation estimates from the two analyses agree to a large extent on this data set. The
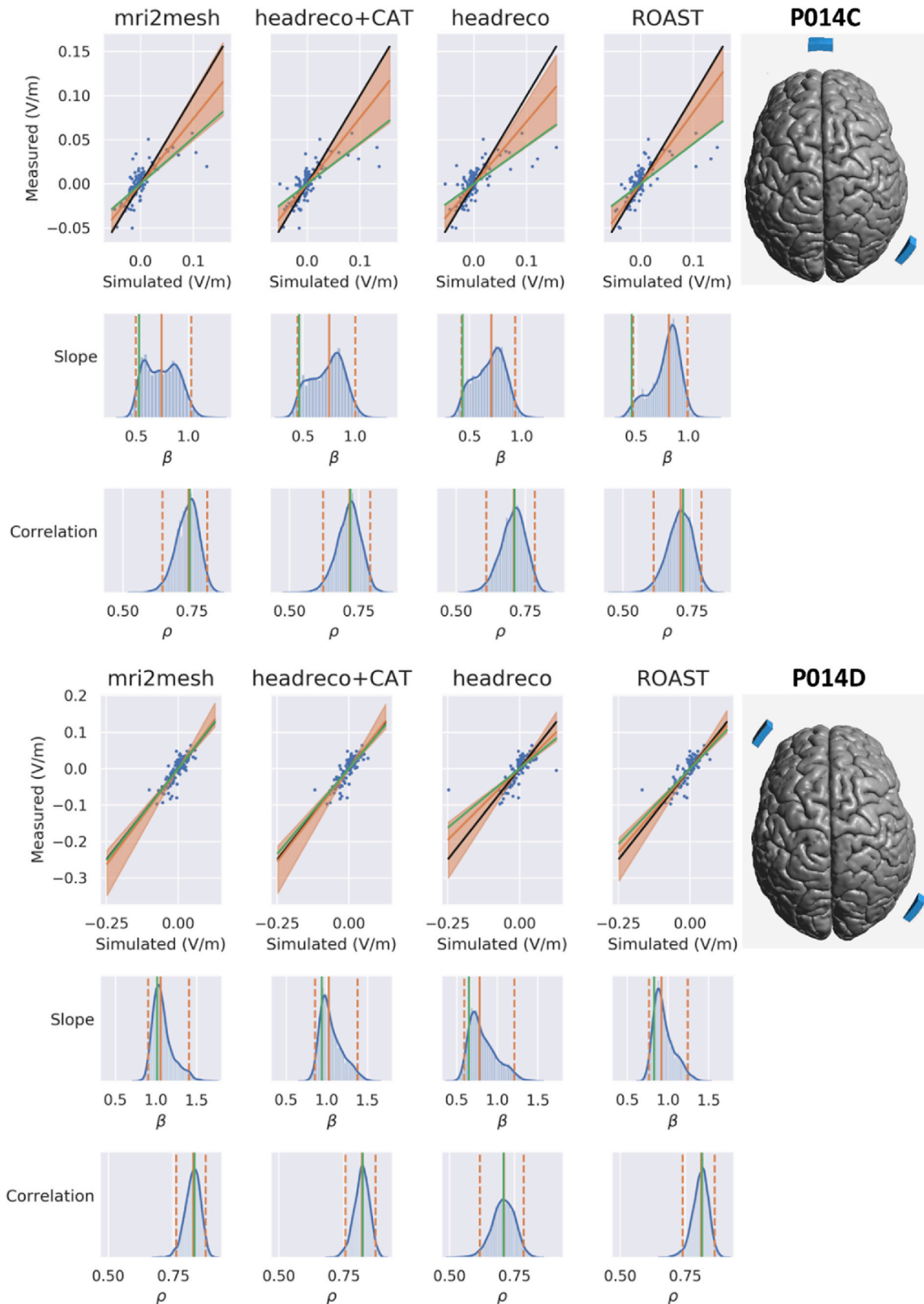
Fig. 9. Bayesian regression analysis for subject P014. The first panel shows results for P014C, and the second panel for P014D. In each scatter plot the black line denotes a slope of one, the orange line is the median of the posterior distribution for the slope with the shading denoting 95% compatibility interval, and the green line is the standard slope fit (as in Fig. 7). The histograms show the posterior distributions of the slope and correlation with the median denoted as an orange solid line, the 95% interval as a dashed line, and the green solid line denoting the standard fit (as in Fig. 7). Similar plots for all subjects are included in the supplementary material.
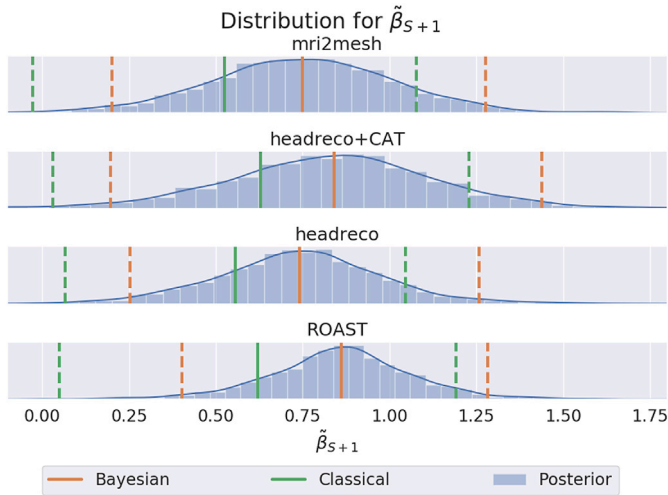
Distribution for $\tilde{\beta}_{S+1}$

Fig. 10. Posterior predictive distribution of the slope if a new subject were to be measured. Solid orange line denotes the median and dashed lines the 95% compatibility interval. The corresponding green lines denote the estimates for the median and 95% confidence interval for the standard analysis as in Fig. 7.

full analysis of the correlation coefficients can be found in Supplementary Material 2.

Next, we investigate if the Bayesian regression analysis reveals differences between the simulation pipelines not picked up by the standard regression analysis. To compare differences between the methods, we first pooled the differences between the slope samples from the posterior distributions for each pair of methods over all subjects. The distribution, along with the individual slope posteriors for all subjects and methods, is shown in Supplementary Material 2 (Figure S19). In general, we find that the differences between methods are small as the peaks of the difference distributions are close to zero, although more extreme differences are also supported by the model given the data. We also plotted the posterior predictive distributions of the slope $\tilde{\beta}_{S+1}$ for an unseen subject given the data, overlaid with the median and 95% confidence interval of the slopes estimated using the standard regression analysis in Fig. 10. This distribution can be estimated by sampling from Equation (6) using the posterior estimates for the hyperparameters β_s and $\sigma_{s,m}$. The posterior predictive distribution tells us, which slope values we should expect, given the data we have seen, if a new subject were to be measured. Here, we see some differences between the methods, namely that *headreco + CAT* and *ROAST* seem to predict higher median slope values for an unseen subject although the variability remains high. Importantly, however, a slope of one, indicating perfect linear fit between simulations and measurements, is well within the 95% compatibility interval (dashed orange lines) for all methods. This observation can be confirmed when inspecting the Bayesian regression results on the individual level (Suppl. Material 2), where a slope of one is contained in the 95% compatibility interval in most of the subjects. Finally, Table 4 lists the summary statistics for the posterior predictive distribution of the slope for each method.

To conclude, in contrast to the standard analysis, the Bayesian alternative reveals that the slope estimates supported by the data can vary hugely depending on the measured signal. This implies that linking modeling differences, resulting from segmentation and FEM, to intra-

cranial measurements is extremely difficult on this data set due to the noisy recordings. Furthermore, interpreting the results from the standard analysis can lead to overly confident conclusions, such that the simulated fields systematically overestimate the measured fields, if the variability in the parameter estimates is not accounted for.

5. Discussion

In the current work, we analyzed an openly available dataset (Huang et al., 2017) with intracranial electric potential recordings, MR scans and manually corrected segmentations to relate electric field simulations from four simulation pipelines to measured data. First, we showed that the differences in the segmentation and FEM modeling approaches in the software pipelines result in clear differences in the simulated electric field distributions. Next, we linked the simulations to the intra-cranial measurements using standard statistical analysis showing that all methods predict the measurements equally well even though the simulated fields differ up to 49%. This result was also found previously by (Huang et al., 2019). We extended this analysis using a Bayesian errors-in-variables regression showing that the slope estimates from the standard analysis are underestimated, and further demonstrating how the noisiness of the recorded data results in larger uncertainties in the regression parameter estimates.

The results highlight two important points: first, although intra-cranial recordings are considered the gold standard for validating computational electric field models, careful analysis of the fit between simulations and measurements is needed to avoid overly confident conclusions on how well, or poorly, the simulations match the measured data. Specifically, the noise in the measurements can affect a standard linear regression analysis leading to the incorrect conclusion that the simulations systematically overestimate the measured fields as shown in Fig. 7. Second, modeling the noise in the measurements and the uncertainty in the simulated e-field values, along with a fully Bayesian treatment of the regression analysis, is important for obtaining unbiased slope estimates and for evaluating if the variability in the slope estimates is too high for conclusive validation of the simulations. Decreasing this variability by increasing the quality of the measurements should be the main goal for future validation attempts. As exemplified by subject P014 in Fig. 9, the location of the stimulation electrodes has a large effect on how much signal is measured at the intra-cranial electrodes. The location of the stimulation electrodes should be carefully planned, as the intracranial electrodes can measure potential differences only in the plane defined by the electrode strip (Huang et al., 2017), to make conclusive validation possible. Additionally, measurements of the electric field in all three directions would likely distinguish differences between field simulations better but are difficult in practice with intra-cranial electrodes. Complementing intra-cranial recordings with new, non-invasive techniques, such as MRCDI, for volume measurements of the electric fields seems thus important for future validations of individualized field modeling.

Another important factor for validation is the quality of the MR scans. As shown in Figs. 2 and 3, the contrast between the tissues directly relates to the variability of the segmentations. This introduces an additional source of uncertainty on top of the measurement noise, and the two are difficult to untangle in the regression analysis. The data set analyzed here consists of a clinical population, with only T1-weighted MR scans available, where the data quality is understandably variable. Future studies would benefit from including a T2-weighted scan, which has been shown to help with skull segmentation accuracy of automated methods

Table 4

Posterior median, 97.5th percentile (+) and 2.5th percentile (−) of the slope predictive distribution for the slope ($\tilde{\beta}_{S+1}$) for each head modeling pipeline, given data for all subjects. The values correspond to the orange lines in Figure 13.

	mri2mesh	*headreco + CAT*	*headreco*	*ROAST*
Slope ($\tilde{\beta}_{S+1}$)	$0.749 \pm {}^{1.276}_{0.202}$	$0.841 \pm {}^{1.438}_{0.196}$	$0.741 \pm {}^{1.257}_{0.254}$	$0.862 \pm {}^{1.282}_{0.402}$

(Nielsen et al., 2018) and would also help in labeling the cortical CSF. Furthermore, modeling software should integrate steps for checking the segmentations and for manual corrections, if necessary, as standard procedures.

In prior articles based on this dataset (Huang et al., 2019, 2017), the comparisons between simulations and recordings have relied on a standard linear regression analysis. In this work, we reproduced the results from (Huang et al., 2019), in Fig. 7 and Table 3, where no difference between the methods was found. In (Huang et al., 2017) the authors compare simulations based on the manually corrected head models to intra-cranial recordings and, based on these, optimize the tissue conductivities on a subject-to-subject basis. In both articles, the simulations are found to overestimate the recorded potential differences based on the slope estimates from the standard linear regression. This overestimation is likely overstated due to the bias in the slope estimates and are hard to put into perspective as the uncertainties in the estimates are not assessed. This problem also links to the optimization of the tissue conductivities in (Huang et al., 2017), which relies on minimizing the squared error between the simulations and recordings, where both are assumed to be noiseless. It seems likely that this procedure provides biased conductivity estimates. Regardless of its limitations, this open-source data set is at the moment still unique and we acknowledge its importance for validating volume conductor models of the head. We would like to encourage its further curation to ameliorate some of the mentioned limitations, e.g. by updating the manually corrected segmentations to represent the underlying anatomy as accurately as possible. We also hope that the issues raised here give helpful guidance for planning future validation attempts.

Author contributions

Oula Puonti: Conceptualization, Methodology, Software, Formal analysis, Visualization, Writing - Original Draft. **Guilherme B. Saturnino**: Conceptualization, Methodology, Software, Formal analysis. **Kristoffer H. Madsen**: Conceptualization, Writing - Review & Editing. **Axel Thielscher**: Conceptualization, Writing - Review & Editing, Supervision, Funding acquisition.

Declaration of competing interestCOI

Nothing to declare.

Acknowledgements

Appendix A. Supplementary data

Supplementary data to this article can be found online at https://doi.org/10.1016/j.neuroimage.2019.116431.

References

Ashburner, J., Friston, K.J., 2005. Unified segmentation. Neuroimage. https://doi.org/10.1016/j.neuroimage.2005.02.018.

Bungert, A., Antunes, A., Espenhahn, S., Thielscher, A., 2017. Where does TMS stimulate the motor cortex? Combining electrophysiological measurements and realistic field estimates to reveal the affected cortex position. Cerebr. Cortex. https://doi.org/10.1093/cercor/bhw292.

Carpenter, B., Guo, J., Hoffman, M.D., Brubaker, M., Gelman, A., Lee, D., Goodrich, B., Li, P., Riddell, A., Betancourt, M., 2017. Stan : a probabilistic programming language. J. Stat. Softw. https://doi.org/10.18637/jss.v076.i01.

Cho, J.H., Vorwerk, J., Wolters, C.H., Knösche, T.R., 2015. Influence of the head model on EEG and MEG source connectivity analyses. Neuroimage. https://doi.org/10.1016/j.neuroimage.2015.01.043.

Csifcsák, G., Boayue, N.M., Puonti, O., Thielscher, A., Mittner, M., 2018. Effects of transcranial direct current stimulation for treating depression: a modeling study. J. Affect. Disord. https://doi.org/10.1016/j.jad.2018.02.077.

Dannhauer, M., Lanfer, B., Wolters, C.H., Knösche, T.R., 2011. Modeling of the human skull in EEG source analysis. Hum. Brain Mapp. https://doi.org/10.1002/hbm.21114.

Datta, A., Baker, J.M., Bikson, M., Fridriksson, J., 2011. Individualized model predicts brain current flow during transcranial direct-current stimulation treatment in responsive stroke patient. Brain Stimul. https://doi.org/10.1016/j.brs.2010.11.001.

Datta, A., Bansal, V., Diaz, J., Patel, J., Reato, D., Bikson, M., 2009. Gyri-precise head model of transcranial direct current stimulation: improved spatial focality using a ring electrode versus conventional rectangular pad. Brain Stimul. https://doi.org/10.1016/j.brs.2009.03.005.

Dmochowski, J.P., Datta, A., Bikson, M., Su, Y., Parra, L.C., 2011. Optimized multi-electrode stimulation increases focality and intensity at target. J. Neural Eng. https://doi.org/10.1088/1741-2560/8/4/046011.

Fabri, A., Teillaud, M., 2011. CGAL, Computational geometry algorithms library. In: 10e Colloque National En Calcul Des Structures.

Fang, Q., Boas, D.A., 2009. Tetrahedral mesh generation from volumetric binary and grayscale images. In: Proceedings - 2009 IEEE International Symposium on Biomedical Imaging: from Nano to Macro. ISBI. https://doi.org/10.1109/ISBI.2009.5193259, 2009.

Fischl, B., Salat, D.H., Busa, E., Albert, M., Dieterich, M., Haselgrove, C., Van Der Kouwe, A., Killiany, R., Kennedy, D., Klaveness, S., Montillo, A., Makris, N., Rosen, B., Dale, A.M., 2002. Whole brain segmentation: automated labeling of neuroanatomical structures in the human brain. Neuron. https://doi.org/10.1016/S0896-6273(02)00569-X.

Frost, C., Thompson, S.G., 2000. Correcting for regression dilution bias: comparison of methods for a single predictor variable. J. R. Stat. Soc. Ser. A Stat. Soc. https://doi.org/10.1111/1467-985X.00164.

Fuller, W.A., 1987. Measurement Error Models. John Wiley & Sons. https://doi.org/10.1002/9780470316665.

Geselowitz, D.B., 1967. On bioelectric potentials in an inhomogeneous volume conductor. Biophys. J. 7, 1–11. https://doi.org/10.1016/S0006-3495(67)86571-8.

Geuzaine, C., 2007. GetDP: a general finite-element solver for the de Rham complex. Proc. Appl. Math. Mech. 7, 1010603–1010604. https://doi.org/10.1002/pamm.200700750.

Göksu, C., Hanson, L.G., Siebner, H.R., Ehses, P., Scheffler, K., Thielscher, A., 2018. Human in-vivo brain magnetic resonance current density imaging (MRCDI). Neuroimage. https://doi.org/10.1016/j.neuroimage.2017.12.075.

Gull, S.F., 2013. Bayesian data analysis: straight-line fitting. In: Maximum Entropy and Bayesian Methods. https://doi.org/10.1007/978-94-015-7860-8_55.

Huang, Y., Datta, A., Bikson, M., Parra, L.C., 2019. Realistic vOlumetric-Approach to Simulate Transcranial Electric Stimulation – ROAST – a fully automated open-source pipeline. J. Neural Eng. https://doi.org/10.1088/1741-2552/ab208d.

Huang, Y., Dmochowski, J.P., Su, Y., Datta, A., Rorden, C., Parra, L.C., 2013. Automated MRI segmentation for individualized modeling of current flow in the human head. J. Neural Eng. 10.

Huang, Y., Liu, A.A., Lafon, B., Friedman, D., Dayan, M., Wang, X., Bikson, M., Doyle, W.K., Devinsky, O., Parra, L.C., 2017. Measurements and models of electric fields in the in vivo human brain during transcranial electric stimulation. Elife 6. https://doi.org/10.7554/eLife.18834.

Iglesias, J.E., Sabuncu, M.R., 2015. Multi-atlas segmentation of biomedical images: a survey. Med. Image Anal. https://doi.org/10.1016/j.media.2015.06.012.

Laakso, I., Tanaka, S., Koyama, S., De Santis, V., Hirata, A., 2015. Inter-subject variability in electric fields of motor cortical tDCS. Brain Stimul. https://doi.org/10.1016/j.brs.2015.05.002.

Liu, A., Vöröslakos, M., Kronberg, G., Henin, S., Krause, M.R., Huang, Y., Opitz, A., Mehta, A., Pack, C.C., Krekelberg, B., Berényi, A., Parra, L.C., Melloni, L., Devinsky, O., Buzsáki, G., 2018. Immediate neurophysiological effects of transcranial electrical stimulation. Nat. Commun. https://doi.org/10.1038/s41467-018-07233-7.

López-Alonso, V., Cheeran, B., Río-Rodríguez, D., Fernández-Del-Olmo, M., 2014. Inter-individual variability in response to non-invasive brain stimulation paradigms. Brain Stimul. https://doi.org/10.1016/j.brs.2014.02.004.

MathWorks, 2019. TriScatteredInterp Documentation. WWW Document]. Doc. MATLAB R2018b.

Minjoli, S., Saturnino, G.B., Blicher, J.U., Stagg, C.J., Siebner, H.R., Antunes, A., Thielscher, A., 2017. The impact of large structural brain changes in chronic stroke patients on the electric field caused by transcranial brain stimulation. NeuroImage Clin. https://doi.org/10.1016/j.nicl.2017.04.014.

Minka, T.P., 1999. Linear Regression with Errors in Both Variables: A Proper Bayesian Approach.

Miranda, P.C., Mekonnen, A., Salvador, R., Ruffini, G., 2013. The electric field in the cortex during transcranial current stimulation. Neuroimage. https://doi.org/10.1016/j.neuroimage.2012.12.034.

Nielsen, J.D., Madsen, K.H., Puonti, O., Siebner, H.R., Bauer, C., Madsen, C.G., Saturnino, G.B., Thielscher, A., 2018. Automatic skull segmentation from MR images for realistic volume conductor models of the head: assessment of the state-of-the-art. Neuroimage 1–12. https://doi.org/10.1016/j.neuroimage.2018.03.001.

Opitz, A., Falchier, A., Yan, C.G., Yeagle, E.M., Linn, G.S., Megevand, P., Thielscher, A., Deborah, R.A., Milham, M.P., Mehta, A.D., Schroeder, C.E., 2016. Spatiotemporal structure of intracranial electric fields induced by transcranial electric stimulation in humans and nonhuman primates. Sci. Rep. 6, 1–11. https://doi.org/10.1038/srep31236.

Opitz, A., Paulus, W., Will, A., Thielscher, A., 2015. Anatomical determinants of the electric field during transcranial direct current stimulation. Neuroimage 109, 2. https://doi.org/10.1016/j.neuroimage.2015.01.033.

Opitz, A., Yeagle, E., Thielscher, A., Schroeder, C., Mehta, A.D., Milham, M.P., 2018. On the importance of precise electrode placement for targeted transcranial electric stimulation. Neuroimage. https://doi.org/10.1016/j.neuroimage.2018.07.027.

Pechaud, M., Jenkinson, M., Smith, S., FMRIB), O.U.C. for F.M. of the B., 2006. Bet2 - MRI-Based Esimation of Brain, Skull and Scalp Surfaces FMRIB Technical Report TR06MP1, pp. 81–87. https://doi.org/10.1007/s13398-014-0173-7.2. Report XXXIII.

Ravazzani, P., Ruohonen, J., Grandori, F., Tognola, G., 1996. Magnetic stimulation of the nervous system: induced electric field in unbounded, semi-infinite, spherical, and cylindrical media. Ann. Biomed. Eng. https://doi.org/10.1007/BF02684229.

Saturnino, G.B., Puonti, O., Nielsen, J.D., Antonenko, D., Madsen, K.H.H., Thielscher, A., 2019. SimNIBS 2.1: A comprehensive pipeline for individualized electric field modelling for transcranial brain stimulation. In: Makarov, S., Horner, M., Noetscher, G. (Eds.), Brain and Human Body Modeling: Computational Human Modeling at EMBC 2018 [Internet], Chapter 1. Cham (CH): Springer, pp. 3–25, 2019, ISBN-13: 978-3-030-21293-3.

Saturnino, G.B., Siebner, H.R., Thielscher, A., Madsen, K.H., 2019a. Accessibility of cortical regions to focal TES: dependence on spatial position, safety, and practical constraints. Neuroimage. https://doi.org/10.1016/j.neuroimage.2019.116183.

Saturnino, G.B., Thielscher, A., Madsen, K.H., Knösche, T.R., Weise, K., 2019b. A principled approach to conductivity uncertainty analysis in electric field calculations. Neuroimage. https://doi.org/10.1016/j.neuroimage.2018.12.053.

Stenroos, M., Hunold, A., Haueisen, J., 2014. Comparison of three-shell and simplified volume conductor models in magnetoencephalography. Neuroimage. https://doi.org/10.1016/j.neuroimage.2014.01.006.

Wiethoff, S., Hamada, M., Rothwell, J.C., 2014. Variability in response to transcranial direct current stimulation of the motor cortex. Brain Stimul. https://doi.org/10.1016/j.brs.2014.02.003.

Windhoff, M., Opitz, A., Thielscher, A., 2013. Electric field calculations in brain stimulation based on finite elements: an optimized processing pipeline for the generation and usage of accurate individual head models. Hum. Brain Mapp. 34, 923–935. https://doi.org/10.1002/hbm.21479.

Zienkiewicz, O.C., Taylor, R.L., Zhu, J., 2013. The Finite Element Method: its Basis and Fundamentals. Elsevier. https://doi.org/10.1016/C2009-0-24909-9.

Appendix B

Accessibility of cortical regions to focal TES: Dependence on spatial position, safety, and practical constraints

Accessibility of cortical regions to focal TES: Dependence on spatial position, safety, and practical constraints

Guilherme Bicalho Saturnino [a,b], Hartwig Roman Siebner [a,c,d], Axel Thielscher [a,b,*,1],
Kristoffer Hougaard Madsen [a,e,1]

[a] Danish Research Centre for Magnetic Resonance, Centre for Functional and Diagnostic Imaging and Research, Copenhagen University Hospital Hvidovre, Denmark
[b] Department of Health Technology, Technical University of Denmark, Kgs Lyngby, Denmark
[c] Department of Neurology, Copenhagen University Hospital Bispebjerg, Copenhagen, Denmark
[d] Institute for Clinical Medicine, Faculty of Medical and Health Sciences, University of Copenhagen, Copenhagen, Denmark
[e] Department of Applied Mathematics and Computer Science, Technical University of Denmark, Kgs. Lyngby, Denmark

ARTICLE INFO

ABSTRACT

Transcranial electric stimulation (TES) can modulate intrinsic neural activity in the brain by injecting weak currents through electrodes attached to the scalp. TES has been widely used as a neuroscience tool to investigate how behavioural and physiological variables of brain function are modulated by electric stimulation of specific brain regions. For an unambiguous interpretation of TES experiments, it is important that the electric fields can be steered towards one or several brain regions-of-interest. However, the conductive proprieties of the human head impose inherent physical limitations on how focal the electric fields in the brain produced by multi-electrode TES can be. As a rule of thumb, it is not feasible to selectively target deep brain areas with TES, although focusing the field in some specific deeper locations might be possible due to favourable conductive properties in the sur-rounding tissue. In the present study, we first propose a computationally efficient method for the automatic determination of electrode placements and stimulation intensities to optimally affect a given target position. We provide a robust implementation of the optimization procedure that is able to adhere to safety constraints, while explicitly controlling both the number of active electrodes and the angular deviation of the field in the target area relative to the desired field direction. Leveraging the high computational efficiency of our method, we system-atically assess the achievable focality of multi-electrode TES for all cortex positions, thereby investigating the dependence on the chosen constraints. Our results provide comprehensive insight into the limitations regarding the achievable TES dose and focality that are imposed by the biophysical constraints and the safety considerations of TES.

1. Introduction

Transcranial Electric Stimulation (TES) is a non-invasive brain stim-ulation method which aims to facilitate or inhibit neural activity by means of weak currents (usually ≤ 2 mA) applied though scalp elec-trodes. The applied current waveform ranges from direct current (TDCS), alternating currents (TACS) to random noise (TRNS). In the last few years, TES has become a widely used tool for neuromodulation in neuroscience research (Parkin et al., 2015) and clinical applications (Nitsche et al., 2009). However, TES still suffers from a large inter-subject variability (Horvath et al., 2015, 2014; Parkin et al., 2015). One

important source of variability is related to the conductive proprieties of the human head. These properties cause the electric fields generated in the brain to exhibit complex, often non-obvious patterns, that depend on the individual anatomy. Therefore, intuitive rule-of-thumb approaches may produce unexpected stimulation patterns and might even miss the intended stimulation target (Miranda et al., 2013; Saturnino et al., 2015). Additionally, these montages stimulate large areas, which makes it difficult to attribute an experimental outcome to the stimulation of a particular brain region. In this context, pseudo-monopolar montages (i.e., ring montages or 4x1 montages) have been recently introduced in order to produce more focal stimulation effects than the classical bi-polar

two-electrode montages using a single anode and cathode (Heise et al., 2016; Kuo et al., 2013). In addition, modelling the electric fields might help to reduce the uncertainty of the affected brain areas, allowing more careful planning of individualized electrode montages for targeting a given area of interest. However, manually optimizing montages based on electric field models may imply a lengthy iterative procedure of trial-and-error, especially if one is to fully leverage the potential of multi-channel TES setups. Therefore, methods have been proposed to automatically calculate optimal electrode positions for TES with the aim of targeting given brain regions in an individualized fashion (Dmochowski et al., 2011; Guler et al., 2016a; Park et al., 2011; Ruffini et al., 2014; Sadleir et al., 2012; Wagner et al., 2015).

Determining optimal electrode positions and the corresponding current intensities is a non-linear and non-convex optimization problem. By using a discrete grid of putative electrode positions (e.g., based on the EEG 10–20 system) rather than representing the electrode positions as continuous variables, the problem can be relaxed such that it is convex in certain cases. To the best of our knowledge, the first studies that propose automated methods to optimize multi-channel electrode montages in TES were presented by Dmochowski et al. (2011) and Park et al. (2011). Since then, several additional methods have been published (Sadleir et al., 2012; Ruffini et al., 2014; Wagner et al., 2015; Guler et al., 2016a). These methods share the same basic approach to employ grids of fixed electrode positions, but they differ, among others, in the way the optimization problems are set-up and how they account for the constraints set by the safety limits for TES and for other practical aspects such as a limited number of available stimulation channels. For example, in the framework proposed by Dmochowski et al. (2011), optimization of the electrode montage is performed either by solving a least squares problem or a linearly constrained quadratic problem, similar to what we propose in the current work. Both settings can be constrained to account for the safety limits. This approach is relatively simple and has several practical advantages over more complex approaches in terms of reliability and speed, but the limitation to a maximal number of channels is not tackled. Guler et al. (2016b) and Ruffini et al. (2014) proposed extended methods based on the branch-and-bound algorithm (Boyd and Mattingley, 2007) and a genetic algorithm, respectively, to overcome this problem, but in both cases at the cost of strongly increased computation times.

In the present study, we propose a novel optimization approach for multi-electrode TES, which can account for the TES safety limits and limited numbers of stimulation channels in an exact and optimal way while offering high computational efficiency. The optimization approach takes practically meaningful parameters as input, such as the target location, the desired electric field at the target, the safety limits governing the maximally injected current strengths and the maximum number of available channels to fully define the problem. We also introduce a new algorithm for constraining the number of active electrodes, where we reduce the time complexity from a few hours, as previously reported (Guler et al., 2016b; Ruffini et al., 2014), to a less than 1 min while ensuring optimality.

In addition to characterizing features and performance of the new optimization approach, we use it to systematically map the achievable targeting accuracy and focality across the complete cortex in line with the procedure proposed in (Dmochowski et al., 2017; Huang and Parra, 2019). Specifically, we perform a step-by-step investigation of how the safety limits imposed on the electrode currents, the limited numbers of channels available in TES systems, the selected electric field strength in the target and the amount of alignment of the electric field with the desired field direction affect the quality of the optimized electric fields.

2. Materials and methods

2.1. Theoretical framework

TES applies currents at relatively low frequencies (<10 kHz) at which the head tissues are predominantly resistive and wave effects do not occur (Plonsey and Heppner, 1967), so that the electric fields can be well described in a quasi-static regime. In this case, the field in the human head is governed by the Laplace equation, meaning that the total electric field $\vec{E}(\vec{p})$ created by current injections through multiple (say n) electrodes can be described as the sum of the fields $\vec{E}_i(\vec{p})$ caused by the current flows between single n-1 electrodes, and an arbitrarily selected common reference electrode (Dmochowski et al., 2011):

$$\vec{E}(\vec{p}) = \sum_{i=1}^{n-1} \vec{E}_i(\vec{p}). \tag{1}$$

Here, $\vec{p}$ denotes a position in the head, and $\vec{E}_i$ are the fields created by the current flow between the i-th electrode and the reference electrode. Also, the electric fields scale linearly with the strength of the injected currents, so that the total field can be expressed as a linear superposition of the fields created by unit currents through the electrodes

$$\vec{E}(\vec{p}) = \sum_{i=1}^{n-1} \vec{E}_i(\vec{p}) = \sum_{i=1}^{n-1} \vec{E}_i(\vec{p}, I_i = 1) x_i \tag{2}$$

with x_i being the current injected into the i-th electrode, and vector $\vec{E}_i(\vec{p}, I_i = 1)$ the electric field caused by a unit current flowing between the i-th electrode and the reference electrode. When assessing $\vec{E}_i(\vec{p}, I_i = 1)$ at a set of m positions in the head, the result can be compactly represented as a vector of length $3m$:

$$\mathbf{e}_i = \begin{bmatrix} e_{i,1}^x \\ e_{i,2}^x \\ \vdots \\ e_{i,m}^x \\ e_{i,1}^y \\ \vdots \\ e_{i,m}^z \end{bmatrix}. \tag{3}$$

If we also represent the currents injected in the n-1 electrodes as vector $\mathbf{x}_a = [x_1\ x_2\ \ldots\ x_{n-1}]^T$, the resulting electric field $\mathbf{e}$ can be determined by a simple matrix multiplication:

$$\mathbf{e} = \mathbf{A}_a \mathbf{x}_a, \tag{4}$$

where

$$\mathbf{A}_a = [\mathbf{e}_1 \mathbf{e}_2 \ldots \mathbf{e}_{n-1}]. \tag{5}$$

The matrix $\mathbf{A}_a$ has the size of $3m \times (n\text{-}1)$ and is referred to as the lead-field matrix (Dmochowski et al., 2011). This matrix is also widely used in EEG source reconstruction, and can be interpreted as an electrical model of the head (Dmochowski et al., 2017). Here, we apply an extended lead-field matrix that includes the reference electrode, as this resulted in a better stability and simpler implementation of the optimization procedure (for further details see below). This is done by introducing a $n \times n - 1$ matrix $\mathbf{P}$

$$\mathbf{P} = \begin{bmatrix} \mathbf{I}_{n-1 \times n-1} \\ -\mathbf{1}_{n-1}^T \end{bmatrix}, \tag{6}$$

where vector $\mathbf{1}_{n-1}^T = \begin{bmatrix} 1 & 1 & \cdots & 1 \end{bmatrix}_{1 \times n-1}$ and the matrix $\mathbf{I}_{n-1 \times n-1}$ is the $(n-1) \times (n-1)$ identity matrix. Applying $\mathbf{P}$ and its pseudo inverse $\mathbf{P}^\dagger$ to Eq. (5), we obtain

$$\mathbf{e} = (\mathbf{A}_a \mathbf{P}^\dagger)(\mathbf{P}\mathbf{x}_a), \tag{7}$$

$$e = Ax, \quad (8)$$

where A is the extended lead-field matrix of size $3m \times n$, and the vector $x = [x_1 \ x_2 \ . . . . . .x_n]^{\mathrm{T}}$ includes the currents injected in all n electrodes, including the reference electrode. Column i of A corresponds to the electric field which is created by injecting a unit current in the i-th electrode, while extracting currents of strength $1/(n\text{-}1)$ at the remaining n-1 electrodes. After applying the transformation, the system in Eq. (8) becomes ill-posed. That is, it admits many values of x that result in the same electric field e. However, the only physically plausible solution can be retrieved by imposing Kirchhoff's current law, i.e. that the sum of all incoming and outgoing currents through the electrodes must be zero:

$$\sum_{i=1}^{n} x_i = \mathbf{1}_n^{\mathrm{T}} x = 0. \quad (9)$$

The matrix-vector product formulation for the electric field (Eq. (8)) allows the evaluation of some quantities of interest that are relevant for the optimization procedure described further down:

2.1.1. Mean electric field component in a target region along a specific direction

In continuous form, the mean field component $\langle \overrightarrow{E} \cdot \widehat{n} \rangle_{\Omega_\tau}$ in a target volume or area Ω_τ and along a target direction $\widehat{n}$ is given by

$$\langle \overrightarrow{E} \cdot \widehat{n} \rangle_{\Omega_\tau} = \frac{1}{G_\tau} \int_{\Omega_\tau} \overrightarrow{E} \cdot \widehat{n} \, dG, \quad (10)$$

where G_τ is the total volume or area (depending on the geometry under consideration) of the region Ω_τ. For a discretized head model, we sample the electric fields at a set of positions, each position representing the electric field in a small volume or area g_i. We can therefore write the mean field component at the target area in discrete form as

$$\langle \overrightarrow{E} \cdot \widehat{n} \rangle_{\Omega_\tau} = \frac{N_\tau A x}{\mathbf{1}^{\mathrm{T}} g_\tau}, \quad (11)$$

where g_τ is a vector of volumes or areas of the positions in the mesh if it is in the target region Ω_τ, and zero otherwise. The matrix N_τ is defined as

$$N_\tau = \begin{bmatrix} n^x g_\tau^{\mathrm{T}} & n^y g_\tau^{\mathrm{T}} & n^y g_\tau^{\mathrm{T}} \end{bmatrix}, \quad (12)$$

where n^x, n^y and n^z are the x, y and z components of the target direction $\widehat{n}$. We can simplify Eq. (11) so that the mean electric field component is represented as a vector-vector multiplication

$$\langle \overrightarrow{E} \cdot \widehat{n} \rangle_{\Omega_\tau} = l^{\mathrm{T}} x, \quad (13)$$

where

$$l^{\mathrm{T}} = \frac{N_\tau A}{\mathbf{1}^{\top} g_\tau}. \quad (14)$$

2.1.2. Total energy delivered

The total energy stored in an electric field in a volume Ω_0 is given by (Griffiths, 1999)

$$U = \frac{\varepsilon_o}{2} \int_{\Omega_0} |\overrightarrow{E}(\overrightarrow{p})|^2 \, dV. \quad (15)$$

Here, we define a quantity proportional to the energy. In the discretized space, the integral in Eq. (15) can be calculated in the discretized head model as

$$\int_{\Omega_0} |\overrightarrow{E}(x)|^2 dV = e^{\mathrm{T}} \begin{bmatrix} G_0 & 0 & 0 \\ 0 & G_0 & 0 \\ 0 & 0 & G_0 \end{bmatrix} e, \quad (16)$$

where G_0 is a diagonal matrix with element area or volumes, if the element is in Ω_0, and zero elsewhere. Using the relation in Eq. (8), we can write

$$\int_{\Omega_0} |\overrightarrow{E}(\overrightarrow{p})|^2 = x^{\mathrm{T}} Q x, \quad (17)$$

where

$$Q = A^{\mathrm{T}} \begin{bmatrix} G_0 & 0 & 0 \\ 0 & G_0 & 0 \\ 0 & 0 & G_0 \end{bmatrix} A. \quad (18)$$

2.2. Angle between mean electric field and target direction

This quantity can be defined in continuous form, over a target area Ω_τ as

$$\theta = \arctan \left(\frac{\sqrt{\frac{1}{G_\tau} \int_{\Omega_\tau} \left(\overrightarrow{E} \cdot \widehat{n}_{t_1} \right)^2 + \left(\overrightarrow{E} \cdot \widehat{n}_{t_2} \right)^2 dG}}{\langle \overrightarrow{E} \cdot \widehat{n} \rangle_{\Omega_\tau}} \right), \quad (19)$$

where $\widehat{n}_{t_1}$ and $\widehat{n}_{t_2}$ are two mutually orthogonal directions, which are also orthogonal to the target direction $\widehat{n}$. The discrete form can be written as

$$\theta = \arctan \left(\frac{\sqrt{x^{\mathrm{T}} Q_{\mathbf{tan}} x}}{l^{\mathrm{T}} x} \right), \quad (20)$$

where $Q_{\mathbf{tan}}$ is given by

$$Q_{\mathbf{tan}} = \frac{1}{G_\tau} A^{\mathrm{T}} \left(\begin{bmatrix} \left(n_{t_1}^x\right)^2 g_\tau & 0 & 0 \\ 0 & \left(n_{t_1}^y\right)^2 g_\tau & 0 \\ 0 & 0 & \left(n_{t_1}^z\right)^2 g_\tau \end{bmatrix} + \begin{bmatrix} \left(n_{t_2}^x\right)^2 g_\tau & 0 & 0 \\ 0 & \left(n_{t_2}^y\right)^2 g_\tau & 0 \\ 0 & 0 & \left(n_{t_2}^z\right)^2 g_\tau \end{bmatrix} \right) A. \quad (21)$$

2.3. Forward simulations of the TES electric fields

We used the SimNIBS 2.1 software package (Thielscher et al., 2015) to calculate the electric fields that form the columns of the lead-field matrix A_a, which we then transformed into the extended lead-field matrix A as stated above. SimNIBS utilizes the Finite Element Method (FEM) with first order tetrahedral elements to calculate electric potentials ϕ by solving the homogeneous Laplace equation

$$\nabla \cdot (\sigma \nabla \phi) = 0, \quad (22)$$

where σ is the ohmic conductivity of the medium. Simulations were performed by applying Dirichlet boundary conditions at the outer boundaries of the ith electrode as well as the return electrode. The electric field

$$\overrightarrow{E} = -\nabla \phi, \quad (23)$$

and the current density

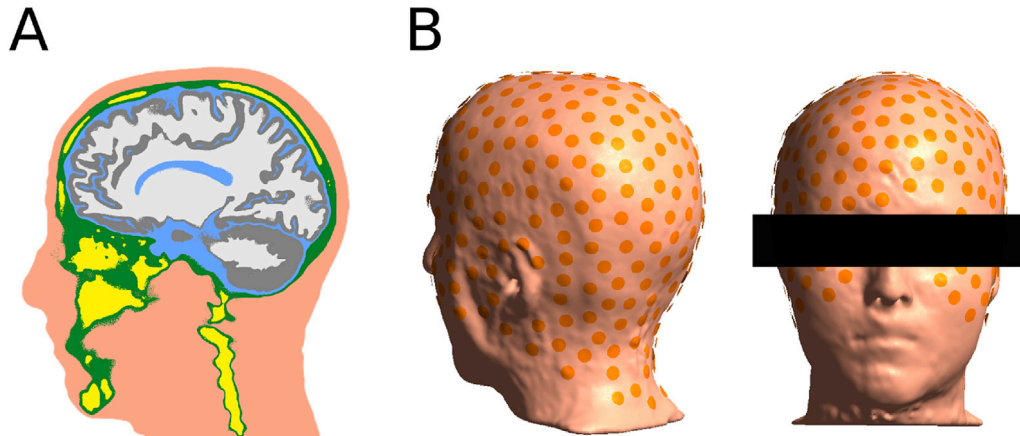$$\overrightarrow{J} = \sigma \overrightarrow{E}, \quad (24)$$

Fig. 1. A) Sagittal view of the head model. The modelled tissue types were brain grey matter (grey), white matter (white), corticospinal fluid (blue), compact bone (green), spongy bone (yellow), scalp (pink) and the vitreous bodies of the eyes (not visible). B) Electrode montage with 288 electrode positions.

were then calculated and the fields were re-scaled to ensure a unit current flow between the electrodes.

The simulations were performed using a head model of a healthy volunteer (Nielsen et al., 2018), created based on existing T1-and T2-weighted magnetic resonance images. Details on image acquisition can be found in (Windhoff et al., 2013). The head model has about 4×10^6 tetrahedra and 7×10^5 nodes and was automatically created using the *headreco* routine of SimNIBS 2.1. Conductivities of all tissues were assumed to be isotropic, and the values were assigned to 0.126 S/m (WM), 0.275 S/m (GM), 1.654 S/m (CSF), 0.025 S/m (spongy bone), 0.008 S/m (compact bone), 0.50 S/m (vitreous bodies), 0.465 S/m (scalp), 1 S/m (electrodes) (Saturnino et al., 2015). Electrodes were modelled as small cylinders (1 cm diameter, 2 mm thickness) with homogeneous conductivity, corresponding approximately to electrode gel. Fig. 1A shows a sagittal view of the head model with its different tissues.

For optimizing the TES electric fields, we used a fixed electrode grid, shown in Fig. 1B. This grid has 288 electrodes, which were positioned semi-automatically to cover the head, neck and face. Additionally, we also created grids with 102, 190, and 381 electrode positions to assess how the field in the cortex depends on density of the electrode grid (Suppl. Fig. S1).

2.4. Optimization of electrode currents

When optimizing a TES montage, one might be interested in maximizing the strength of the field at the target. Alternatively, one might want to obtain a focal field while at the same time ensuring that a certain strength of the field is maintained at the target or even at multiple targets simultaneously. In addition to controlling its strength, one might also aim to control the angle of the electric field relative to the orientation of the cortical sheet at the target precisely. In practice, one is often faced with the need to obtain the best possible solution for a limited number of available stimulation channels. To tackle this large variety of optimizations and constraints, we formulated ten different optimization problems, shown in Table 1. The problems are described in detail in the sections below.

2.4.1. Without safety constraints

In the simplest setting, we aim to create a given electric field in a target area and direction, while avoiding the other brain areas as well as possible, disregarding the safety constraints that limit how much current one can inject. We formulated this optimization as Problem 1:

Problem 1. Maximization of focality given a target electric field, with no safety constraints. The electrode currents, x, is the optimization variable.

Table 1
Optimization problems explored in this paper. The objective refers to what the optimization problem aims to achieve, and the constraints define which requirements the solution must obey. The problem class is a mathematical classification of the problem, and determines the methods, which can be used to effectively solve the problem.

Problem	Objective	Constraints	Problem Class
1	Maximize the focality (minimize total energy)	• Maintain the desired electric field in the target	QP
2	Maximize the field in the target	• Obey safety constraints (total and per-electrode current injected)	LP
3	Maximize the focality	• Maintain the desired electric field in the target • Obey safety constraints	QP
4	Maximize the focality	• Maintain the desired electric field in the target • Obey safety constraints • Control the number of active electrodes	Combinatorial
5	Maximize the field in the target	• Obey safety constraints • Control the field angle in the target	QCLP
6	Maximize the focality	• Maintain the desired electric field in the target • Obey to the safety constraints • Control the field angle in the target.	QCQP
7	Maximize the focality	• Maintain the desired electric field in the target • Obey safety constraints • Control the field angle in the target • Control the number of active electrodes.	Combinatorial
8	Maximize the focality	• Maintain the desired electric fields in *multiple* targets • Obey safety constraints	QP
9	Maximize the field in *multiple* targets	• Do not exceed a maximum electric field in each target • Obey safety constraints	LP
10	Maximize the focality	• Maintain the desired electric fields in multiple targets • Obey safety constraints • Control the number of active electrodes.	Combinatorial

$$\text{minimize} \quad \boldsymbol{x}^{\mathrm{T}}\boldsymbol{Q}\boldsymbol{x} \quad \text{(P1.1)}$$
$$\text{subject to} \quad \boldsymbol{l}^{\mathrm{T}}\boldsymbol{x} = t \quad \text{(P1.2)}$$
$$\mathbf{1}^{\mathrm{T}}\boldsymbol{x} = 0 \quad \text{(P1.3)}$$

The objective in this optimization problem (Eq. (P1.1)) is to minimize the energy (Eq. (17)). However, we also want to ensure to reach a certain value t for the electric field at our target region and direction (Eq. (P1.2)), Eq. (13)). This is similar to the Linearly constrained minimum variance (LCMV) algorithm proposed in (Dmochowski et al., 2011), with the key difference that the constraint (Eq. (P1.2)) is to reach the a given average field component in the target region, instead of exactly matching all electric field component in each target location. This means that we have effectively less equality constraints, leaving more degrees of freedom to the solutions. However, this also means that we do not have the same precise control of the field alignment in the target region as (Dmochowski et al., 2011). To reach the objective, we can manipulate the vector of injected currents x, but we must obey Kirchhoff's current law (Eq. (P1.2), Eq. (9)). The choices for the regions Ω_0, Ω_t and of the direction $\hat{n}$ are implicit in the matrices $\boldsymbol{Q}$ and $\boldsymbol{l}$. Problem 1 is an equality-constrained quadratic programming (QP) problem, and due to convexity and its simplicity, the solution that can be computed directly and efficiently (Boyd and Vandenberghe, 2004).

It is interesting to note that the matrix $\boldsymbol{Q}$ is $n \times n$ and $\boldsymbol{l}^{\mathrm{T}}$ is $1 \times n$, while the leadfield matrix A is $3m \times n$. In TES optimization, n is the number of electrodes (in the range of 32–500) while m is the number of positions in the region of interest (the brain or the whole head), typically between 10^5 and 10^6. Therefore, this formulation reduces the size of the problem, which is closely linked to computation time, by 3–4 orders of magnitude when comparing with formulations that use the leadfield matrix directly such as the genetic algorithm proposed in (Ruffini et al., 2014), or the formulation proposed by (Wagner et al., 2015).

2.4.2. With safety constraints

The most common safety constraint in TES is to limit the total injected current to a given value I_{tot}. As the total inflowing current is equal to the total outflowing current (as per Kirchhoff's current law), we can write this constraint as

$$\sum_{i=1}^{n} |x_i| \leq 2I_{tot}. \tag{25}$$

Which corresponds to

$$\|\boldsymbol{x}\|_1 \leq 2I_{tot}, \tag{26}$$

where $\|\cdot\|_1$ denotes the L1-norm. When using small electrodes, it can also be of interest to limit the current flowing through each electrode to a given value I_{ind} (inflowing or outflowing) to avoid skin irritation, discomfort and heating at individual electrode interfaces. This corresponds to a bound constraint on the current through each electrode

$$-I_{ind} \leq x_i \leq I_{ind}, \; i = 1, \, 2, \, \ldots, \, n. \tag{27}$$

The simplest optimization which considers the safety constraints (Eq. (26) and Eq. (27)) is Problem 2:

Problem 2. Maximization of the electric field at a target, including safety constraints.

$$\text{maximize} \quad \boldsymbol{l}^{\mathrm{T}}\boldsymbol{x} \quad \text{(P2.1)}$$
$$\text{subject to} \quad \mathbf{1}^{\mathrm{T}}\boldsymbol{x} = 0 \quad \text{(P2.2)}$$
$$\|\boldsymbol{x}\|_1 \leq 2I_{tot} \quad \text{(P2.3)}$$
$$-I_{ind} \leq x_i \leq I_{ind}, \quad i = 1, \, 2, \, \ldots, \, n \quad \text{(P2.4)}$$

Here, the objective (Eq. (P3.1)) is to maximize the field at the target region and direction (Eq. (13)) while obeying Kirchhoff's current law (Eq. (P2.2), Eq. (9)) and the safety constraints. In this problem, we do not consider the focality of the field. This is an instance of a linear programming (LP) problem, similar to the *intensity optimization* problem in

(Dmochowski et al., 2011), with the difference being the definition of the matrix $\boldsymbol{l}$ (see the description of Problem 1 for more information). In our implementation, we solved it using the SciPy implementation of the simplex algorithm (Dantzig, 1963). However, there exists a very simple solution to this problem, as one can show that Problem 2 can be solved by simply choosing the largest and the smallest entries in $\boldsymbol{l}$, setting the electrode currents in those electrodes to I_{ind} and $-I_{ind}$, and repeating the process until the safety constraint in Eq. (P2.3) is reached. This results in ceil$(2I_{tot}/I_{ind})$ active electrodes. A similar procedure has been previously described in (Fernandez-corazza et al., 2019).

To obtain a focal field, we introduce Problem 3:

Problem 3. Obtain a focal field given a target electric field, including safety constraints.

$$\text{minimize} \quad \boldsymbol{x}^{\mathrm{T}}\boldsymbol{Q}\boldsymbol{x} \quad \text{(P3.1)}$$
$$\text{subject to} \quad \boldsymbol{l}^{\mathrm{T}}\boldsymbol{x} = t \quad \text{(P3.2)}$$
$$\mathbf{1}^{\mathrm{T}}\boldsymbol{x} = 0 \quad \text{(P3.3)}$$
$$\|\boldsymbol{x}\|_1 \leq 2I_{tot} \quad \text{(P3.4)}$$
$$-I_{ind} \leq x_i \leq I_{ind}, \quad i = 1, \, 2, \, \ldots, \, n \quad \text{(P3.5)}$$

Problem 3 similar to the linearly constrained minimum variance (LCMV) approach described in (Dmochowski et al., 2011), but with both the L1 and individual electrode constraints. Again, one key difference is the definition of the equality constraint (Eq. (P3.2)), which is explained above. This formulation fully specifies the optimization problem with a few and intuitively interpretable parameters to be defined by the user: a target direction, a target region, the desired average field in the target region t, the maximal current through each electrode I_{ind}, and the maximum total current injected I_{tot}. Problem 3 can be transformed into a quadratic problem (QP) in standard form (Boyd and Vandenberghe, 2004) and solved with standard QP algorithms. For this study, we implemented the active-set method described in (Gill and Murray, 1978) in Python, using the NumPy and SciPy packages (van der Walt et al., 2011), as in our experience, employing the generic convex optimizer CVXPY (Diamond and Boyd, 2016) is computationally inefficient and often fails to converge. Our implementation has robustly converged in thousands of different settings with minimal computational effort, as shown in the Results section. In our implementation, if the value for t is chosen too high in relation to the values I_{tot} and I_{ind}, Problem 3 becomes infeasible and we fall back to solving Problem 2. We chose this approach as it is guaranteed to give the same solution, as one would obtain by successively lowering the target t in Problem 3 until it becomes just feasible.

2.4.3. Constraining the number of active electrodes

In practice, a limited number of stimulation channels is available, so that it is important to constrain the number of active electrodes to a number N. This corresponds to an additional constraint in the form

$$\|\boldsymbol{x}\|_0 \leq N, \tag{28}$$

where $\|\cdot\|_0$ is the L0-norm (or cardinality), that is, the number of non-zero elements in the vector. As discussed above in the description of Problem 2, the L0-norm of the result obtained when maximizing the intensity at the target (Problem 2) is naturally constrained by the safety constraints. However, applying this constraint to Problem 3, we obtain Problem 4:

Problem 4. Obtain a focal field, given a target electric field, including safety constraints and limiting the number of active electrodes.

$$\text{minimize} \quad \boldsymbol{x}^{\mathrm{T}}\boldsymbol{Q}\boldsymbol{x} \quad \text{(P4.1)}$$
$$\text{subject to} \quad \boldsymbol{l}^{\mathrm{T}}\boldsymbol{x} = t \quad \text{(P4.2)}$$
$$\mathbf{1}^{\mathrm{T}}\boldsymbol{x} = 0 \quad \text{(P4.3)}$$
$$\|\boldsymbol{x}\|_1 \leq 2I_{tot} \quad \text{(P4.4)}$$
$$-I_{ind} \leq x_i \leq I_{ind}, \quad i = 1, \, 2, \, \ldots, \, n \quad \text{(P4.5)}$$
$$\|\boldsymbol{x}\|_0 \leq N \quad \text{(P4.6)}$$

Due to the new constraint (Eq. (P4.6)), Problem 4 is non-convex. In fact, this type of problem is of combinatorial complexity (Boyd and Vandenberghe, 2004). Therefore, obtaining the globally optimal solution to the problem in a computationally efficient way can be challenging. Here, we use a Branch-and-Bound method (Boyd and Mattingley, 2007) that stems from the same class of methods as used in (Guler et al., 2016b). Details of the algorithm are described in the supplementary material. Shortly, the Branch-and-Bound algorithm consists of successively partitioning (branching) a given region of the parameter space $\mathscr{C}$, which defines active and inactive electrodes. We define a lower bound $\Phi_{lb}(\mathscr{C})$ and an upper bound $\Phi_{ub}(\mathscr{C})$ function that can calculate bounds the optimum value of the objective function (Eq. (P4.1)) within the parameter space $\mathscr{C}$ (see the supplementary material for mathematical details on the bound functions). Repeated branching of the parameter space and evaluation of the bounds results in narrowing down the parameter space, eventually giving us a solution, which is certified to be close to the global optimum.

For quickly searching the parameter space, we make use of the fact that the constraint on the total injected current I_{tot} (Eq. (26)) involves the sum of the absolute values (the L1-norm) of the vector of current values x. This term is well-investigated (Tibshirani, 1996) and is known to induce sparsity of the solutions (i.e., many non-active electrodes). Therefore, the solutions of Problem 3 tend to be sparse. We can also add more L1 constraints as a relaxation of the L0 constraint to obtain tight lower bounds $\Phi_{lb}(\mathscr{C})$ for the branch-and-Bound algorithm.

In the current paper, we stopped the Branch-and-Bound iterations once we obtained solutions which are certified to be within 10% of the global optima. For a problem with 288 possible electrode positions, but only six active electrodes, we only needed more than 20 steps of the Branch-and-Bound algorithm in about 1% of the positions studied. The optimal value is typically found within the first few iterations, and the remaining iterations are required to certify that the solution found is indeed close to the global solution. This behaviour is expected, as the employed L1-heuristcs gives often good approximations of the L0 norm (Boyd and Mattingley, 2007). For problems where more active electrodes are allowed, the algorithm tends to converge even faster, as the L0 constraint plays a smaller role in limiting the solution.

2.4.4. Constraining the angular deviation of the electric field in the target

The TES effects on neural activity depend on the direction of the electric field relative to the neural target structures. Specifically, it is often assumed that TES acts predominantly via the polarization of cortical pyramidal cells, so that it is most effective when the fields are oriented normally to the local cortical surface (Stagg and Nitsche, 2011). It is unclear how sensitive the physiological TES effects are to deviations of the field from a perfect normal orientation. In addition, for many target positions, we may have to trade-off field intensity and the accuracy if we want to reach the optimal direction during optimization. For those reasons, it is helpful to have a flexible control of the acceptable amount of deviation from the ideal orientation during the optimization process. Our optimization scheme gives the possibility to constrain the angle between the mean electric field vector in the target and the selected target direction to a given maximal value θ_{max}. From Eq. (20), we have that:

$$\arctan\left(\frac{\sqrt{x^T Q_{tan} x}}{l^T x}\right) \leq \theta_{max} \tag{29}$$

$$\left(\frac{\sqrt{x^T Q_{tan} x}}{l^T x}\right) \leq \tan(\theta_{max}) \tag{30}$$

$$\frac{x^T Q_{tan} x}{\left(l^T x\right)^2} \leq \tan^2(\theta_{max}), \; l^T x \geq 0 \tag{31}$$

Considered in isolation, this constraint is non-convex. However, in combination with the constraint to reach a mean electric field in the target $l^T x = t$, it can be reformulated as a quadratic constraint in the form

$$x^T Q_{tan} x \leq \tan^2(\theta_{max}) t^2 \tag{32}$$

Adding this constraint to Problem 2, we obtain Problem 5, which is a quadratically constrained linear programming (QCLP) problem:

Problem 5. Maximization of the electric field at a target, including safety constraints and angle constraint.

maximize	$l^T x$	(P5.1)
subject to	$1^T x = 0$	(P5.2)
	$\|x\|_1 \leq 2I_{tot}$	(P5.3)
	$-I_{ind} \leq x_i \leq I_{ind}, \quad i = 1, 2, \ldots, n$	(P5.4)
	$x^T Q_{tan} x \leq \tan^2(\theta_{max}) t^2$	(P5.5)

Similarly, when also considering the focality as formulated in Problem 3, we obtain Problem 6 which is a quadratically constrained quadratic programming (QCQP) problem.

Problem 6. Obtain a focal field, given a target electric field, including safety constraints and angle constraints.

minimize	$x^T Q x$	(P6.1)
subject to	$l^T x = t$	(P6.2)
	$1^T x = 0$	(P6.3)
	$\|x\|_1 \leq 2I_{tot}$	(P6.4)
	$-I_{ind} \leq x_i \leq I_{ind}, \quad i = 1, 2, \ldots, n$	(P6.5)
	$x^T Q_{tan} x \leq \tan^2(\theta_{max}) t^2$	(P6.6)

In our implementation, we solve Problems 5 and 6 by adding the angle constraint (Eq. (P5.6) and Eq. (P6.6)) to the objective weighted by a variable λ ($\lambda \geq 0$), and iterating over values of λ to find the smallest value of λ where the angle constraint is fulfilled. The angle constraint can also be combined with the constrained on the number of active electrodes, resulting in Problem 7.

Problem 7. Obtain a focal field given a target electric field, including safety constraints, angle constraints and a constraint on the maximum number of active electrodes.

minimize	$x^T Q x$	(P7.1)
subject to	$l^T x = t$	(P7.2)
	$1^T x = 0$	(P7.3)
	$\|x\|_1 \leq 2I_{tot}$	(P7.4)
	$-I_{ind} \leq x_i \leq I_{ind}, \quad i = 1, 2, \ldots, n$	(P7.5)
	$x^T Q_{tan} x \leq \tan^2(\theta_{max}) t^2$	(P7.6)
	$\|x\|_0 \leq N$	(P7.7)

To solve this problem, we run a branch-and-bound function at each value of the parameter λ. Problems 5–7 can also be solved with a conic solver (Boyd and Vandenberghe, 2004).

2.4.5. Optimization for multiple targets

We can also use the algorithm to optimize the electric fields in several distant targets at once. The simplest way to do it is to extent the definition of the target area Ω_τ. However, as the operator l^T calculates the average across the entire target region, it might cause a bias towards one "easier to reach" target over others. We overcome this by defining multiple independent target regions $\Omega_{\tau_1}, \Omega_{\tau_2}, \ldots, \Omega_{\tau_q}$ and enforcing the equality constraint (Eq. (13)) for each region individually. With this setting, we can also define different target values $t_1, t_2, \ldots, t_q$ for each target region. By adding multiple targets to Problem 3, we obtain Problem 8.

Problem 8. Obtain a focal electric field with multiple targets

minimize $\quad x^{\mathrm{T}}Qx$ $\hspace{4cm}$ (P8.1)

subject to $\quad \begin{bmatrix} l_1^{\mathrm{T}} \\ l_2^{\mathrm{T}} \\ \vdots \\ l_q^{\mathrm{T}} \end{bmatrix} x = \begin{bmatrix} t_1 \\ t_2 \\ \vdots \\ t_q \end{bmatrix}$ $\hspace{2.5cm}$ (P8.2)

$\mathbf{1}^{\mathrm{T}}x = 0$ $\hspace{4cm}$ (P8.3)

$\|x\|_1 \leq 2I_{\mathrm{tot}}$ $\hspace{3.5cm}$ (P8.4)

$-I_{\mathrm{ind}} \leq x_i \leq I_{\mathrm{ind}}, \quad i = 1, 2, \ldots, n$ $\hspace{0.5cm}$ (P8.5)

Problem 8 is still a QP, so it can be solved using the same algorithms as used for Problem 3. In cases where Problem 8 is infeasible because the target field values cannot be reached in at least one of the targets, we instead solve Problem 9.

Problem 9. Maximize the electric field at multiple targets

maximize $\quad \mathbf{1}^{\mathrm{T}} \begin{bmatrix} l_1^{\mathrm{T}} \\ l_2^{\mathrm{T}} \\ \vdots \\ l_q^{\mathrm{T}} \end{bmatrix} x$ $\hspace{2.5cm}$ (P9.1)

subject to $\quad \begin{bmatrix} l_1^{\mathrm{T}} \\ l_2^{\mathrm{T}} \\ \vdots \\ l_q^{\mathrm{T}} \end{bmatrix} x \leq \begin{bmatrix} t_1 \\ t_2 \\ \vdots \\ t_q \end{bmatrix}$ $\hspace{2.5cm}$ (P9.2)

$\mathbf{1}^{\mathrm{T}}x = 0$ $\hspace{4cm}$ (P9.3)

$\|x\|_1 \leq 2I_{\mathrm{tot}}$ $\hspace{3.5cm}$ (P9.4)

$-I_{\mathrm{ind}} \leq x_i \leq I_{\mathrm{ind}}, \quad i = 1, 2, \ldots, n$ $\hspace{0.5cm}$ (P9.5)

That is, we maximize the electric field across all targets, but ensure that the mean electric field at each target does not exceed the given target value (Eq. (P9.2)). This prevents one easy-to-hit target to take over the objective function (Eq. (P9.1)), and thus we obtain a field best approaches the target intensities values t_i but without surpassing it. Finally, we add the constraint to the number of active electrodes, obtaining Problem 10:

Problem 10. Obtain a focal electric field with multiple targets, with a constrained number of electrodes.

minimize $\quad x^{\mathrm{T}}Qx$ $\hspace{4cm}$ (P10.1)

subject to $\quad \begin{bmatrix} l_1^{\mathrm{T}} \\ l_2^{\mathrm{T}} \\ \vdots \\ l_q^{\mathrm{T}} \end{bmatrix} x = \begin{bmatrix} t_1 \\ t_2 \\ \vdots \\ t_q \end{bmatrix}$ $\hspace{2.5cm}$ (P10.2)

$\mathbf{1}^{\mathrm{T}}x = 0$ $\hspace{4cm}$ (P10.3)

$\|x\|_1 \leq 2I_{\mathrm{tot}}$ $\hspace{3.5cm}$ (P10.4)

$-I_{\mathrm{ind}} \leq x_i \leq I_{\mathrm{ind}}, \quad i = 1, 2, \ldots, n$ $\hspace{0.5cm}$ (P10.5)

$\|x\|_0 \leq N$ $\hspace{4cm}$ (P10.6)

Problems 8–9 can all be solved with the same QP, LP and Branch-and-Bound solvers presented earlier. We can also constrain the angle at each target individually, by adding one angle constraint (Eq. (31)) for each target region. This problem will not be addressed in the current work.

2.5. Performance and error metrics

We define several metrics to characterize the quality of the electric field distributions achieved by the optimization approaches:

2.5.1. Targeting error

Often the maximal electric field will not be in the target node. Therefore, we measure the Euclidian distance between the node where the maximum electric field strength $|\vec{E}|$ occurs and the target position (Dmochowski et al., 2017).

2.5.2. Effective area

In order to quantify the achieved focality of the optimized electric field, this metric weights the area of the region Ω_0 by the electric field strength. This metric is closely related to the energy (Eq. (6)). To enable direct comparison across conditions, we normalize it by the electric field at the target position:

$$|\vec{E}|_{\mathrm{area}} = \frac{\sum_{i=1}^{m} |\vec{E}_i| g_i}{l^{\mathrm{T}}x}. \tag{33}$$

Here, $\vec{E}_i$ is the electric field in the i-th element and g_i its area.

2.5.3. Area with $|\vec{E}|$ exceeding 50% of the target electric field

As an alternative index of focality, we use the total area with an electric field strength larger or equal 50% of the target electric field t:

$$A_{\mathrm{stim}} = \sum_{i=1}^{m} \begin{cases} g_i, & |\vec{E}_i| \geq 0.5t \\ 0, & \text{otherwise} \end{cases}. \tag{34}$$

The targeting error, the effective area and the stimulated area serve to quantify different aspects of the quality of the solution. The targeting error assesses how close the strongest stimulated point was to the target, and the focality measures give insight into how much the field could be focused there. Specifically, the effective area closely resembles the energy (Eq. (15)) and hence is directly related to the optimization procedure. We therefore expect this metric to increase monotonically as we impose tighter constraints on the optimization. In contrast, the targeting error is not directly assessed in the optimization procedure, therefore the dependence on the constraints is less predictable. In order to enable easier comparisons across the tested conditions, we report differences of the above metrics when appropriate. For the targeting error, we report absolute differences in [mm]. For the Effective Area, we calculate the difference in [%] relative to a reference condition:

$$\Delta(\text{Effective Area}) = 100 \times \frac{\text{Effective Area} - \text{Effective Area}_{\mathrm{ref}}}{\text{Effective Area}_{\mathrm{ref}}}\%. \tag{35}$$

2.6. Evaluation of optimization performance across the brain

We systematically evaluated the performance of the optimization approach for target positions distributed across the complete cortex. This evaluation was initially performed for the optimization without safety constraints (Problem 1), and then repeated after successively adding constraints for safety (Problems 2 and 3), the number of electrodes (Problem 4) and field angle in the target (Problems 6 and 7). We extracted the electric field values created by the optimized montages in the middle of the grey matter layer, which is where TES is expected to be effective in modulating the membrane potential of pyramidal cells (Stagg and Nitsche, 2011). For that, we first determined the location of the middle grey matter sheet by taking the average of the pial and white matter surfaces of the FreeSurfer segmentation. This surface was then corrected for self-intersections and degenerate triangles, and down-sampled to 20,000 nodes using MeshFix (Attene, 2010). We then interpolated the columns of the lead-field matrix (which correspond to electric fields) into the nodes of this surface mesh using the super-convergent patch recovery (SPR) approach described in (Saturnino et al., 2018). To map the optimal fields across the cortex, we optimized the electric field to target at each mesh node, one at a time, and

calculated the field metrics. The procedure is described in Algorithm 1.

Algorithm 1.   Mapping Procedure

Input: Leadfield A, Areas or Volumes g, Target Orientations N, Optimization problem $\mathcal{P}$

1. **Initialize** empty vectors $\mathbf{v}_T, \mathbf{v}_E$ and $\mathbf{v}_A$ to store the measures described in the *Performance and Error Metrics* section
2. **Calculate** Energy Matrix Q (Eq. 18)
3. **For** each column i in A
4.   **Calculate** l^T and $Q_{\mathbf{tan}}$ for the row i and direction N_i
5.   **Solve** the optimization problem $\mathcal{P}$, obtaining the electrode currents x
6.   **Calculate** the electric field $e = Ax$
7.   **Calculate** the performance and error metrics and store them in $\mathbf{v}_T, \mathbf{v}_E$ and $\mathbf{v}_A$
8. **Return** $\mathbf{v}_T, \mathbf{v}_E$ and $\mathbf{v}_A$

Algorithm 1: Mapping Procedure

This approach is similar to previously published studies (Dmochowski et al., 2017; Huang and Parra, 2019). For the figures shown in the paper, the target direction of the electric field $\hat{n}$ was chosen normal to the local surface orientation. In the supplementary material, complementary results are depicted which show metrics averaged over two optimizations, with orthogonal directions defined in the tangent plane.

3. Results

3.1. Comparison to ad-hoc montages

To provide intuitive insight into the prospects and limitations of optimized multichannel TES montages, we compared the electric fields obtained by ad-hoc montages versus the fields created by optimized approaches. We started by simulating a "classical" montage to target the left motor cortex using two pad electrodes (upper row of Fig. 2A), which results in a non-focal field distribution. We then derived an optimized montage which generates the same electric field in the sulcal wall of the hand knob (Yousry et al., 1997). For that, we extracted the field caused by the "classical" montage at the centre position of the hand knob (shown in the third column of Fig. 2A) and used it as input (i.e., as target value t) for an optimization with the safety constraints (Problem 3, $I_{\mathrm{ind}} = 1$ mA, $I_{\mathrm{tot}} = 2$ mA) and using 288 electrode positions (Fig. 1B). It is evident that optimization significantly improved the field focality over the Ad-hoc montage (lower row of Fig. 2A). Next, we compared a centre-surround ring montage, aimed at creating an electric field in the crown of left precentral gyrus forming the hand knob, to the optimized montage that creates the same field in the target position (Fig. 2B; same safety constraints and number of electrode positions as in the example before). While the ring montage already induces a quite focal field, this is still improved by the optimized montage. Finally, we compared ad-hoc vs. optimized montages for the stimulation of a slightly deeper area in the left cingulate sulcus (Fig. 2C). In order to maximize the field in that region, we intuitively chose the positions of the two pad electrodes for the ad-hoc montage to be on the left and right sides of the head at approx. the same height as the target. The optimized montage achieves substantially better focality, but still causes the strongest fields in extended areas of the brain surface. This example highlights the fact that the TES optimization is fundamentally limited by the underlying physics of the head which acts as ohmic volume conductor. The focality metrics for these montages are shown in Table 2. Again, a clear improvement of all metrics is obtained when comparing with the ad-hoc approaches. It is interesting to note that the optimized montages shown in Fig. 2 have only few active electrodes. This behaviour of the optimization approach is further investigated below.

3.2. Maximally achievable focality without safety constraints

To establish a best-case scenario, we optimized the electric field focality at each of the 20,000 positions in the middle of the modelled grey matter sheet, without considering safety constraints (Problem 1). The target orientations $\hat{n}$ were chosen normal to the surface, and the target electric field was set to $t = 0.3$V/m. Please notice that the later value is arbitrary, as safety constraints were not considered and the focality metrics are normalized. The latter will thus not change when settings a different target electric field. The metrics for the optimized fields are shown in Fig. 3. It is interesting to notice that, even for this best-case scenario without safety constraints, the metrics differ strongly depending on the position of the cortical target. Areas in inferior regions, in the sulci and in medial portions of the brain exhibit increased targeting errors and a worse focality than targets in superficial gyri. Again, this is to be expected, because the currents necessarily need to flow through other brain areas to hit deeper targets. Furthermore, we note that the two area-based metrics (Effective Area and Area with $|\vec{E}| > 0.5t$) have very similar qualitative behaviours, therefore we only report the Effective Area in rest of the study. We opted for this area metric, as it does not require choosing an arbitrary cut-off value.

The grid of electrode positions is required to have a sufficiently high density in order to minimize the targeting error and to obtain fields that are as focal as possible. We determined an adequate grid density by optimizing the electric field focality (Problem 1) for grids with with $n = 102, 190, 288$, and 381 scalp electrodes (Suppl. Fig. S2). Both the targeting accuracy and the focality improve with increasing number of electrodes for up to 288 positions, but improve only marginally further for 381 positions. This is expected, as the conductive proprieties of the head, in particular the low conductivity of the skull coupled with the comparatively high conductivity of CSF, cause the electric fields to spatially disperse and intrinsically limit the achievable spatial resolution (Dmochowski et al., 2012). These findings motivated our choice of using 288 positions in the main part of the study. In Suppl. Figs. S3 and S4 we additionally show focality results for subcortical targets and targets oriented tangentially to the cortical sheet, respectively, where the same patterns can be observed.

3.3. Maximally achievable intensity in the presence of safety constraints

In practice, the above best-case scenario cannot be reached due to the requirement that safety constraints are obeyed. Naturally, limiting the current that is injected in the electrodes will also limit the strength of the field that can be achieved in the brain. In a first step, we were thus interested in the maximal strength of the field that can be reached at each cortex position when the current injected in each individual electrode has
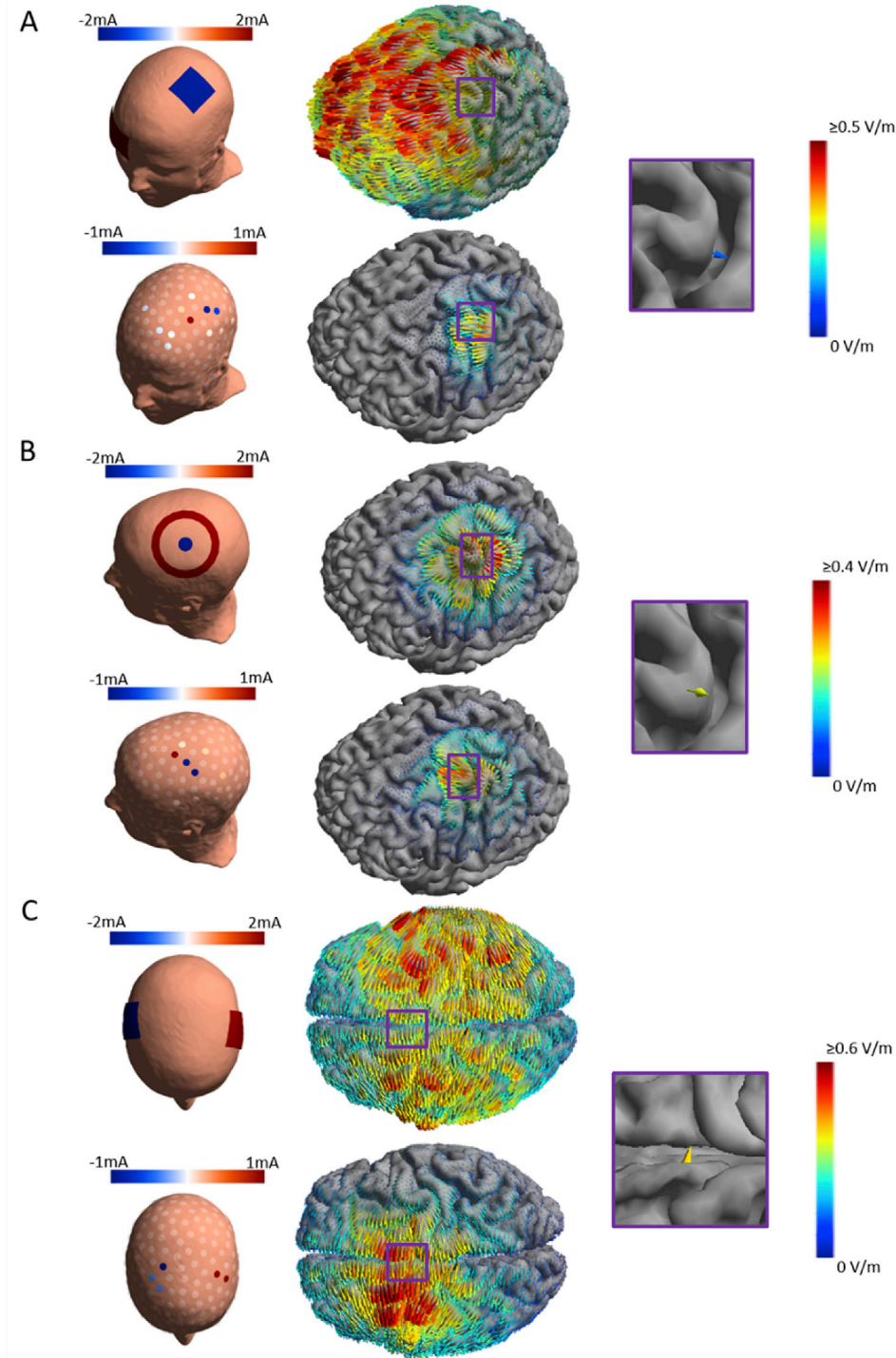
Fig. 2. Comparison between ad-hoc and optimized multi-electrode montages. A) Upper row: "Classical" montage to stimulate the left motor cortex, here with a 5×5 cm^2 square electrode over the left hand knob and a 7×5 cm^2 rectangular "return" electrode over the contralateral supraorbital area. Lower row: Optimized montage that achieves the same field in the sulcal wall in the central part of the hand knob. Current strength in the electrodes is coded as varying levels of red and blue, with inactive electrodes being shown as white and semi-transparent. Third column: Target field at the centre position of the hand knob used as input for the optimization. The target field matches the electric field caused by the "classical" montage at the same position. B) Fields caused by a centre-surround ring montage centred above the left hand knob, and the corresponding optimized multi-electrode montage. The ring montage consists of a circular electrode with 2 cm diameter and ring electrode with 7.5 cm inner and 10 cm outer diameter. C) Stimulation of a position in the left cingulate sulcus. The ad-hoc montage consists of two 5×5 cm^2 square electrodes positioned laterally at the same height as the target position.

to stay within $I_{ind} = 1$ mAand the current injected in total has to be within $I_{tot} = 2$ mA. For that, we determined the maximal electric field in the 20,000 cortical positions without aiming to reach a focal stimulation (Problem 2), again using a target orientation normal to the cortical sheet and a grid of 288 electrode positions in the calculations. Expectedly, the maximally achievable field was highest at gyral targets for which it reached 0.6 V/m at some positions (Fig. 4). Substantially weaker fields could be achieved in sulcal and deep targets, which, however, still exceeded 0.3 V/m at most positions. As focality was not enforced, both the targeting error and the focality (Effective Area) were far worse than in for the best-case scenario (Fig. 3).

In Suppl. Fig. S5, we repeated the analysis above for lead-fields with $n = 102, 190, 288$ and 381 electrodes. The achievable field intensity at the target increased up to 288 electrodes, but was almost unchanged when further increasing the number of electrodes to 381. Suppl. Figs. S6 and S7 show the same analysis for subcortical targets and for targets with tangent orientations to the cortical sheet, respectively, confirming the above results.

3.4. Effect of safety constraints on the optimization of focality

Compared to the mere maximization of the intensity in the target, a

Table 2
Performance metrics for the ad-hoc and optimized montages for the 3 targets shown in Fig. 2. The optimized montages consistently have lower targeting errors (distance between the electric field maximum and the desired target position) and better focality. Unsurprisingly, the difference is strongest for the "standard" motor cortex montage (Fig. 2A). Focality was assessed by measuring the total area affected by an electric field of at least 50% of the target electric field, and by calculating the "Effective stimulation area" (i.e., the area weighted by the norm of the electric field, normalized by the electric field at the target; short: "Effective area"). The total area of the middle cortical sheet is.1744 cm^2.

		Targeting Error (mm)	Area with (cm^2)	Effective Area (cm^2)
Hand Knob	Ad hoc	84	1744	3853
(Sulcal Wall)	Optimal	12	238	470
	Difference	−72 mm	−86%	−86%
Hand Knob	Ad hoc	13	102	214
(Gyral Crown)	Optimal	4	57	200
	Difference	−9 mm	−44%	−7%
Premotor	Ad hoc	37	1132	1048
	Optimal	17	347	638
	Difference	−20 mm	−69%	−39%

more refined strategy is to make the field as focal as possible while ensuring that a desired, sufficiently high intensity is achieved at the target location. Fig. 5 shows the performance of this strategy when obeying safety constraints of $I_{ind} = 1$ mA and $I_{tot} = 2$ mA and ensuring a target field strength of $t = 0.2$ V/m. The results depend strongly on the target position, and a high targeting error and low focality dominate for deep targets. Comparison of the results to those obtained for optimization without safety constraints (Fig. 3A&C) shows that the targeting error and the effectively stimulated area increase most in inferior and medial brain regions, i.e. in areas that are difficult to target in general. Suppl. Figs. S9

and S10 show the same analysis for subcortical targets and for targets with tangential orientations to the cortical sheet, respectively, confirming the above results.

Without safety constraints in place, the optimization algorithm minimizes the overall electric field in the cortex by mainly two strategies: (1) Selecting nearby electrodes in order to increase the focality of the field in the cortex. However, this causes extensive shunting, and therefore high current is needed. (2) Cancelling out electric fields outside the target region by injecting small currents through many electrodes, so that their fields mutually cancel out in non-target regions. However, limiting the total amount of injected currents limits the usage of close-by electrodes, which are ineffective due to the high degree of shunting, and strongly reduces the extent to which compensatory currents can be applied.

Expectedly, this effect is more pronounced for higher target fields, where most or all of the allowed current is fed into the head through a few electrodes in order to achieve the required field in the target. In turn, little current is left that can be used to create cancelation fields (please see Suppl. Fig. S8 for a demonstration of this effect for target electric fields varied between 0.1 V/m, 0.2 V/m and 0.3 V/m). This results in a trade-off between intensity at the target and focality, as it was also reported by (Dmochowski et al., 2017a; Dmochowski et al., 2011).

In addition to the inferior and medial parts of the brain, regions around the longitudinal fissure are affected most by the safety constraints. Due to the high conductivity of CSF, the currents in brain areas close to the longitudinal fissure tend to point preferentially towards or away from the fissure. For optimization without safety constraints and with a low target intensity, this effect is counteracted by invoking many electrodes, thereby cancelling undesired field directions. However, limiting the totally induced current reduces the effectiveness of this cancellation approach.

Optimizing with safety constraints resulted in spurious small improvements in the Targeting Error at some cortical positions compared to
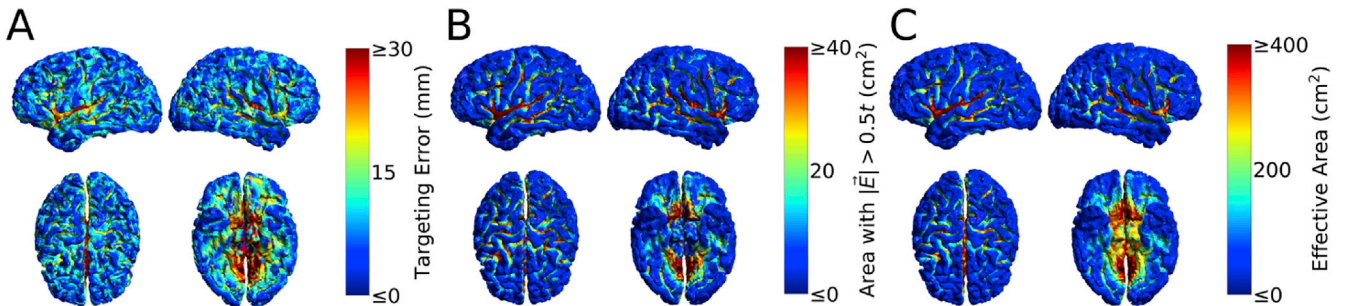

Fig. 3. Performance metrics for optimization of the field focality using a lead-field with $n = 288$ electrode positions. The target field direction was selected as normal to the local cortical surface and safety constraints were not taken into account (Problem 1). The middle of the cortical sheet was represented by 20,000 nodes, and separate optimizations were performed for each of the nodes. The resulting values for the targeting error and achieved focality were color-coded and shown on the middle-cortical surface defined by the 20,000 nodes. A) Targeting error. B) Total area affected by an electric field of at least 90% of the target electric field. C) Effective Area (Area weighted by electric field, normalized by the target electric field).
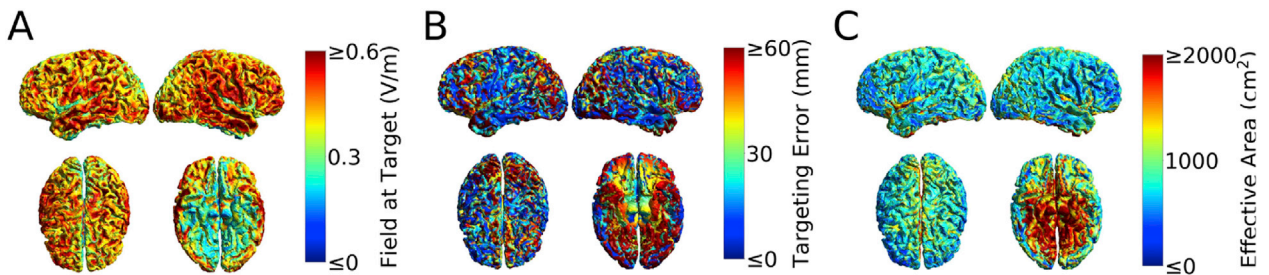

Fig. 4. Maximum intensity and performance metrics achieved when using $n = 288$ electrode positions and safety constraints $I_{ind} = 1$ mA and $I_{tot} = 2$ mA. We maximized the electric field intensity (Problem 2) normal to the cortical sheet. A) Maximally achievable field in the target position. B) Targeting Error. C) Effective Area.
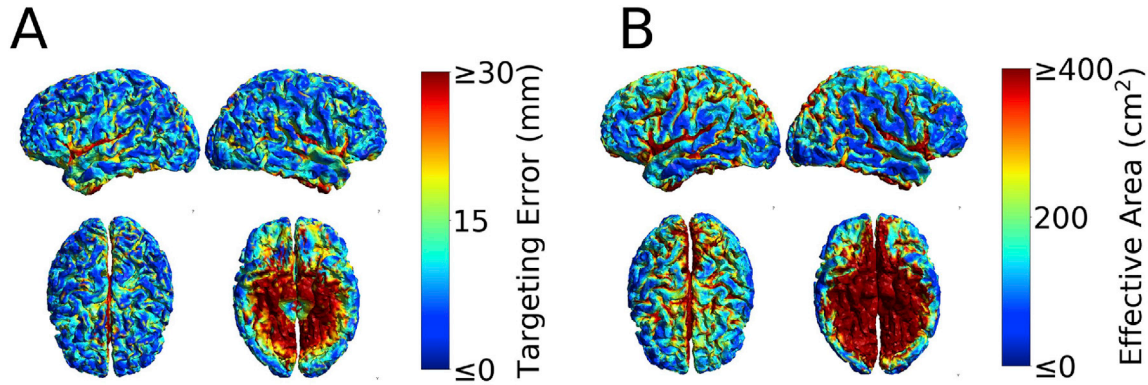
Fig. 5. Performance metrics for optimization of the field focality with safety constraints ($I_{ind} = 1$ mA, $I_{tot} = 2$ mA) and a target intensity of $t = 0.2$ V/ m (Problem 3). The direction of the target field was selected as normal to the local cortical surface. The montage with 288 electrodes was used. A) Targeting error. B) Effective Area.

the case without constraints (blue dots in Fig. 5B). This results from the fact that the targeting error is not directly assessed during the optimization procedure. In contrast, the effectively stimulated area is closely related to the delivered energy. As the latter is minimized by the optimization approach, adding safety constraints results in a consistent increase in the Effective Area for all positions.

3.5. Effect of constraining the number of active electrodes

To evaluate the effect of constraining the number of active electrodes (Problem 4) on the electric field focality, we started by evaluating different approaches to reduce the number of active electrodes. We selected the safety constraints $I_{ind} = 1$ mA, $I_{tot} = 2$ mA and target field strength of $t = 0.2$ V/m, because the results in Figs. 4 and 5 showed that this value could still be achieved with relative ease at most cortical positions for the selected safety constraints, but was high enough to make the electrode selections challenging. We tested the performance of three approaches, termed "Full B–B", "Selected B–B″ and "Projection" in constraining the active electrodes to $N = 4$. The "Full B–B" approach applies the Branch-and-Bound algorithm (for details, see description in the Methods and in supplementary chapter S.1) on all 288 electrodes. The "Selected B–B″ preselects a subset of potentially relevant electrodes using an initial optimization with $I_{tot\_pre} = 3I_{tot} = 6$ mA, and applies the Branch-and-Bound algorithm to this subset only. By that, the computationally more expensive Branch-and-Bound algorithm is applied to fewer electrodes, making the convergence faster. The "Projection" approach runs an optimization with safety constraints, selects the N electrodes with highest current, and runs another optimization involving only those electrodes.

Generally, restricting the number of active electrodes tends to increase the targeting errors (Fig. 6A & B shows difference plots relative to the optimizations with safety constraints depicted in Fig. 5A & B) and decreases the focality particularly at gyral crowns. While the three approaches perform similar with respect to minimizing the targeting error, the "Projection" approach is clearly inferior to the two Branch-and-Bound algorithms in maintaining a focal stimulation when compared to the optimizations without restricted number of active electrodes (Fig. 6B). The two Branch-and-Bound algorithms perform very similar, so that we used the faster "Selected B–B" algorithm for the subsequent optimizations with restricted number of electrodes. These results imply that our method for electrode selection outperforms the simpler "Projection" method, and that the "Selected B–B" heuristic performs very similar to the "Full-BB" approach, albeit being faster.

We evaluated the effect of limiting the number of electrodes on the achieved field focality (Problem 4). Fig. 7 shows the effect of limiting the number of active electrodes N to 4, 6 and 8. The other parameters were set to $t = 0.2$ V/m, $I_{ind} = 1$ mA, $I_{tot} = 2$ mA and "Selected B–B". The figure depicts a comparison with the field metrics obtained with and

without constraining the number of electrodes (Fig. 5A & B) for normal field orientations. Allowing for only four active electrodes seems to produce less focal electric fields in most of the brain. However, the electric field focality seem to improve strongly when allowing for six electrodes to be active. Further improvements, mainly in the gyral crowns, can be achieved using eight active electrodes. Increasing the number of electrodes beyond eight improves the results only marginally further. Suppl. Figs. S11 and S12 show the corresponding results for subcortical targets and tangential target orientations, respectively, confirming the above results. Taken together, even though a dense electrode grid is needed to ensure that the best electrode positions can be chosen by the optimization procedure, our results indicate that users of multichannel stimulators benefit little from using more than 8 active electrodes for most cortical targets.

It is interesting to notice that the electric field in inferior positions is not affected by limiting the number of electrodes to four. This is because 0.2 V/m is close to the maximum electric field in these positions (see Fig. 4). As pointed out in the *Methods*, the maximum electric field is achieved with $\text{ceil}(2I_{tot}/I_{ind}) = 4$ electrodes, meaning that the maximum number of active electrodes in these positions is naturally limited to four.

3.6. Effect of constraining the angular deviation of the electric field in the target

We evaluate the effect of explicitly constraining the angle of the electric field in the target region, in addition to obeying safety constraints (Problem 6). Fig. 8 shows the results for constraining the maximum angle to $\theta_{max} = 15$, 22.5 and 30 in relation to the desired target field direction that was chosen to be normal to the cortical sheet. The other optimization parameters were set to $t = 0.2$ V/m, $I_{ind} = 1$ mA and $I_{tot} = 2$ mA. The results are shown as difference plots relative to the results depicted in Fig. 5A & B.

Interestingly, the angle constraint causes only a slight reduction in the achievable targeting accuracy and field focality in most brain areas, except for regions that are above the low conductive skull base and are surrounded by large amounts of CSF (Fig. 1A). At the latter positions, the electric fields exhibit a profound tendency to point in the lateral direction towards CSF, so that targeting accuracy and field focality are compromised by enforcing a field direction normal to the cortical sheet. Suppl. Figs. S13 and S14 show the same analysis for subcortical targets and for targets with tangent orientations to the cortical sheet, respectively, confirming the above results.

Constraining also the number of active electrodes, in addition to constraining the angle of the electric field in the target region and obeying to the safety constraints, can be done with low additional cost with regards to the achievable targeting accuracy and field focality (Problem 7). As an example, Fig. 9 shows the results for constraining number of electrodes to N = 4, 6 and 8 and the field direction in the
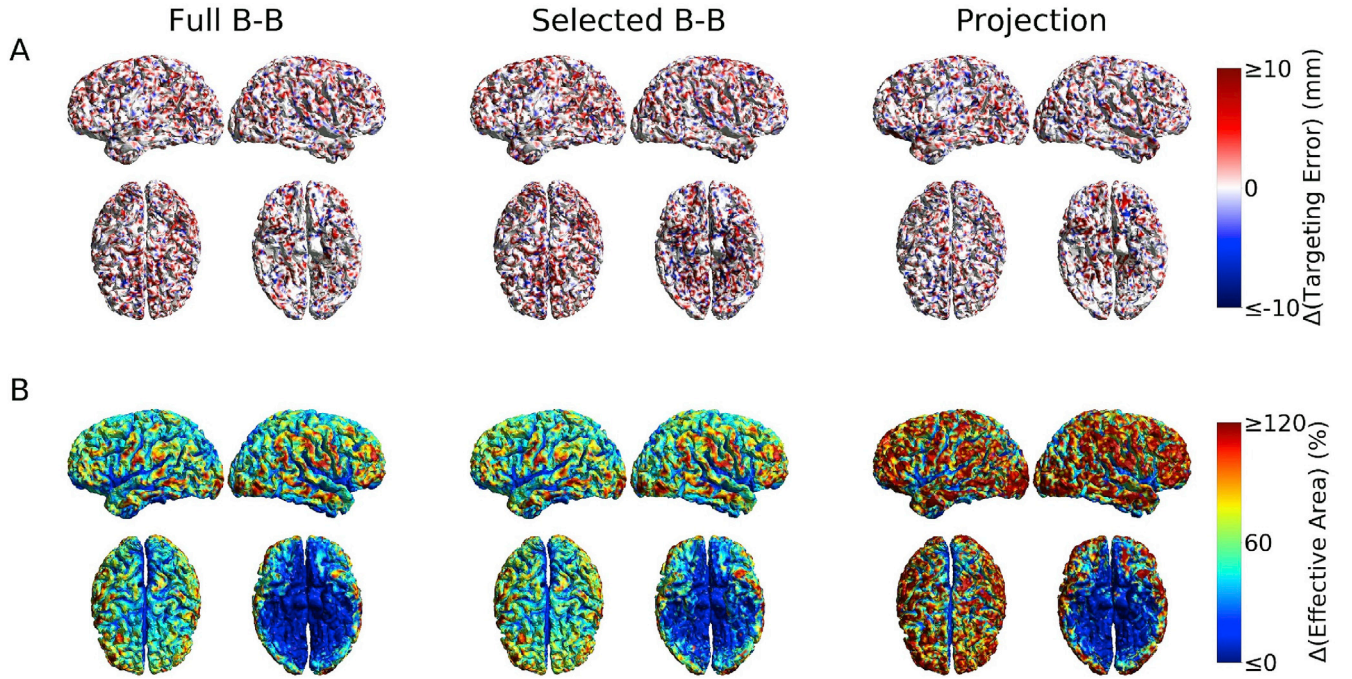
Fig. 6. Comparison of three methods to restrict the number of active electrodes during optimization of the field focality in the brain (Problem 4). The optimization parameters were $I_{ind} = 1$ mA, $I_{tot} = 2$ mA, $t = 0.2$ V/m and the number of active electrodes was exemplarily restricted to $N = 4$. A) Difference in the achieved Targeting Error, assessed relative to the optimizations without restrictions of the number of active electrodes, but otherwise identical settings (Fig. 5A). B) Difference in the Effective Area, relative to the corresponding optimizations without restrictions of the number of active electrodes (Fig. 5B). Left columns in A and B: Branch-and-Bound algorithm performed on all electrodes (Full B–B). Middle columns: Branch-and-Bound algorithm performed on a pre-selected set of electrodes (Selected B–B). The pre-selection was performed by solving an optimization problem with relaxed safety constraints ($I_{tot} \leftarrow 3I_{tot}$), thereby locating electrodes that might potentially contribute to the final optimized montage. Right columns: The "Projection" approach runs an optimization with safety constraints, selects the N electrodes with highest current, and runs another optimization involving only those electrodes.
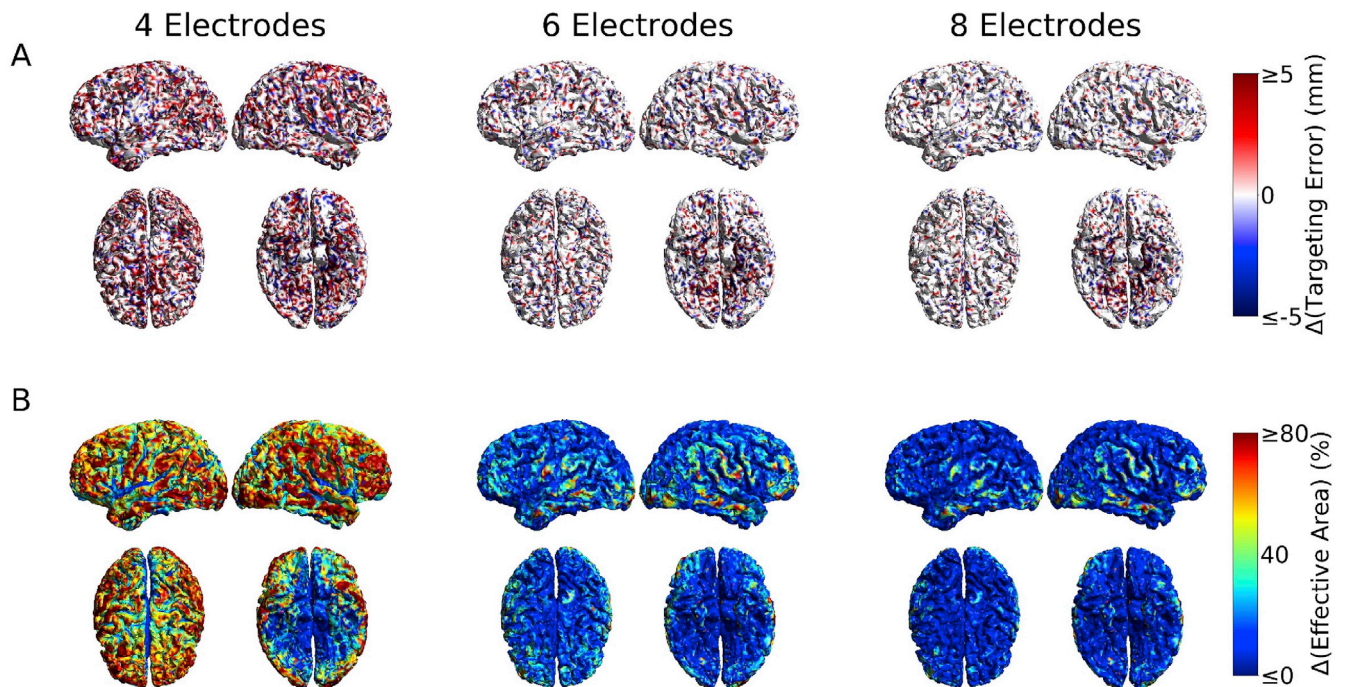

Fig. 7. Effect of varying the number of active electrodes during optimization of the field focality in the brain (Problem 4). The maximum number of active electrodes was restricted to $N = 4$, 6 and 8. The other optimization parameters were set to $t = 0.2$ V/m, $I_{ind} = 1$ mA, $I_{tot} = 2$ mA and the method to "Selected B–B" A) Difference in Targeting Error relative to the optimizations accounting only for the safety constraints (Fig. 5A). B) Difference in the Effective Area relative to the optimizations accounting only for the safety constraints (Fig. 5B).
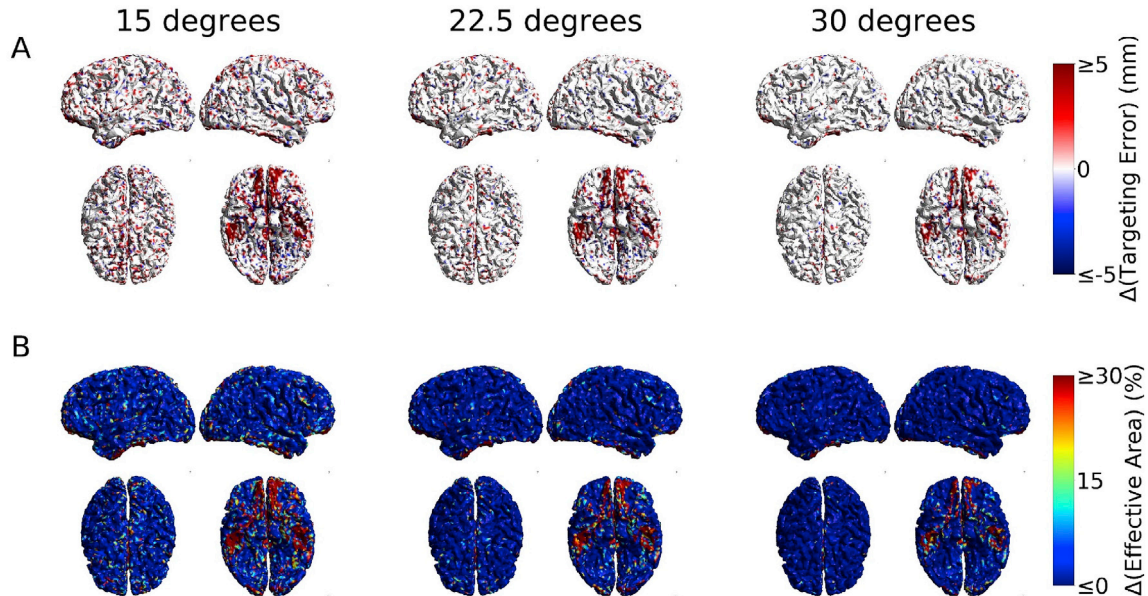
Fig. 8. Effect of constraining the field direction in the target during optimization of the field focality in the brain (Problem 6). The field direction was constrained to deviate by maximally $\theta_{max} = 15°$, $22.5°$, and $30°$ from the specified target direction (other parameters: $t = 0.2$ V/m, $I_{ind} = 1$mA, $I_{tot} = 2$mA). The number of active electrodes was not constrained. A) Difference in Targeting Error relative to the optimizations accounting only for the safety constraints (Fig. 5A). B) Difference in the Effective Area relative to the optimization accounting only for the safety constraints (Fig. 5B).

target to $\theta_{max} = 22.5$. The other optimization parameters were set to $t = 0.2$V/m, $I_{ind} = 1$ mA, $I_{tot} = 2$ mA and "Selected B–B". The results are shown as difference plots relative to the results depicted in Fig. 5A & B.

The similarity between the results in Figs. 9 and 7 demonstrates that ensuring that the field only deviates slightly from the desired field direction can be done at a small additional cost and confirms that a relatively small number of active electrodes (~8) is still sufficient in that case. Suppl. Figs. S15 and S16 show the same analysis for subcortical targets and for targets with tangent orientations to the cortical sheet, respectively, confirming the above results.

3.7. Multi-target optimization

To demonstrate the performance of our approach for multi-target optimization (Problem 10), we tested a configuration where the gyral crowns of the left and right hand knob areas of the motor cortices where simultaneously targeted (N = 4 to 10 in steps of 2, $t = 0.2$V/m in both targets, $I_{ind} = 1$ mA, $I_{tot} = 2$ mA, "Selected B–B″). The field direction was chosen normal to the local cortical surface at both targets. Two sets of optimizations were performed, the first with the field directions pointing outwards at both targets (out/out) and an additional configuration where the local field directions were opposite (in/out).

The resulting electric fields are shown in Fig. 10, confirming that the
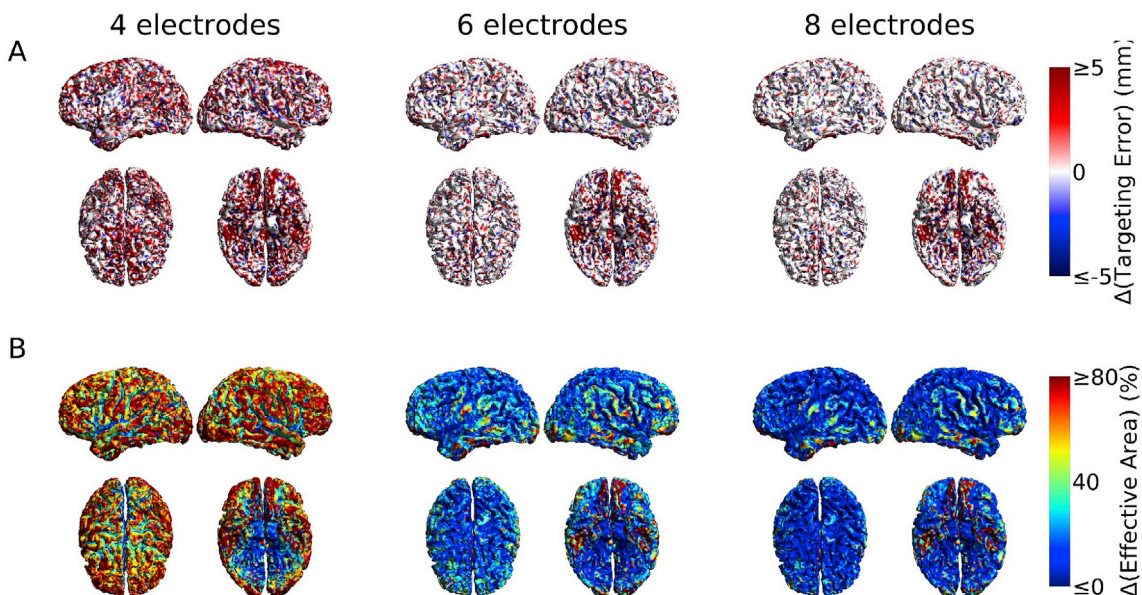

Fig. 9. Effect of constraining the maximal number of active electrodes to $N = 4$, 6 and 8with simultaneous constraints of the field direction during optimization of the field focality in the brain (Problem 7). The field direction was constrained to deviate by maximally $\theta_{max} = 22.5°$ from the target direction ($t = 0.2$ V/m, $I_{ind} = 1$ mA, $I_{tot} = 2$ mA). A) Difference in Targeting Error relative to the optimizations accounting only for the safety constraints (Fig. 5A). B) Difference in the Effective Area relative to the optimization accounting only for the safety constraints (Fig. 5B).
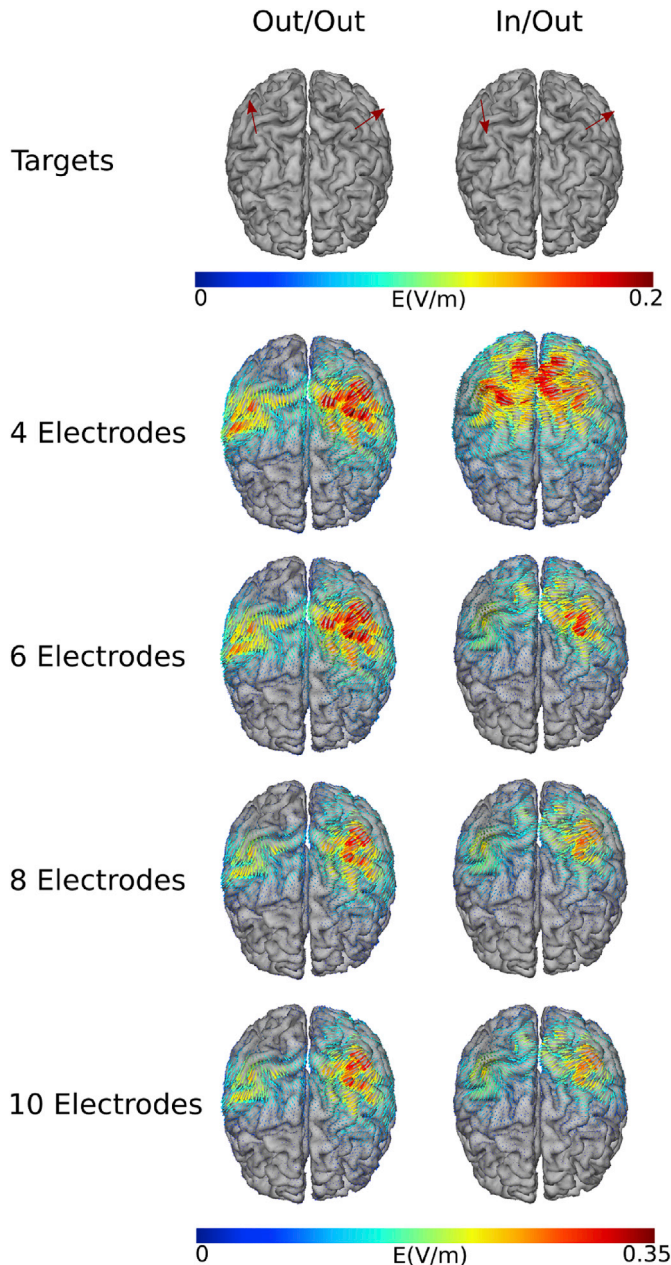
Fig. 10. Electric field distributions with optimized focality for simultaneous targeting of the left and right handknob areas of the motor cortices (Problem 10). The constraints were set to ($t = 0.2$V/m in each of the two targets, $I_{ind} = 1$ mA, $I_{tot} = 2$ mA), and the number of electrodes was constrained to $N = 4$, 6, 8 and 10. In the left column, we set the fields in both targets to point outwards, and in the right column, we set the field in the right motor cortex to point inward and the field in the left motor cortex to point outwards.

fields are indeed focused around the two targets. The two electric field hotspots become more confined and are gradually decoupled from each other as the number of active electrodes increases from 4 to 8. Further increasing to 10 active electrodes gives little additional improvement. This is confirmed by the metrics for the targeting accuracy and field focality (Suppl. Table 1) for the fields shown in Fig. 10. Taken together, our formulation of the optimization problem allows for a balanced simultaneous targeting of multiple brain regions. Even in the case of two targets, we do not see large benefits of using more than 8 active electrodes. However, only two target combinations were tested here, so that is unclear whether this observation holds in general.

Table 3
Time to run the optimization algorithm under various settings. To acquire the timing, we ran optimizations on 1000 randomly selected points on the sub-sampled grey matter surface, using the leadfield created with 288 electrodes.

Problem #	Min. time (s)	Median time (s)	Max. time (s)
2	0.48	0.49	0.72
3	0.49	0.68	1.15
4	0.68	1.39	9.14
6	0.47	0.94	3.60
7	0.77	3.82	138.6

3.8. Time to run optimizations

In order to evaluate the time required for the optimizations with our algorithms, we assessed the times for solving Problems 2, 3, 4, 6 and 7 with safety constraints $I_{ind} = 1$ mA and $I_{tot} = 2$ mA. For all except Problem 2 (that maximizes the intensity), a target intensity of $t = 0.2$ V/m was used. In addition, the number of active electrodes was constrained to $N = 6$ using the "Selected B–B″" algorithm and the angle deviation was constrained to $\theta_{max} = 22.5°$, if required by the tested problem. We used the lead-field defined on the simplified middle grey matter model (20,000 nodes) and with $n = 288$ electrodes. We recorded the time taken to calculate the Q, l and Q_t matrices and perform the optimizations a random sample of 1000 positions with targets defined in a direction normal to the cortical surface on a Lenovo ThinkPad laptop computer with an Intel i7-7500U processor (2 cores, 4 threads), 16 GB of memory, a SSD hard-drive and running Ubuntu Linux 18.04.

Table 3 shows the minimum, median and maximum time to run the optimizations. Problem 2 (intensity maximization) is the simplest problem to solve as it is a linear programming problem, which is reflected by the timing results. Problem 3 (optimization of field focality) is a more complex quadratic programming problem, but is still solved in less than a second in most cases by our implementation. Problem 4 (optimization of field focality with constraints on the number of active electrodes) is not a convex problem anymore. However, the timings show that the implemented Branch-and-Bound algorithm handles the L0 constraint efficiently, as the median times are only two times larger than the ones observed in the problem without constraint on the number of active electrodes. Problem 6 (optimization of field focality with constraints on the field angle in the target) is solved in a sub-optimal way, as a conic solver would be more appropriate, but still requires less than 1 s in most cases. Problem 7 (optimization of field focality with constraints on the field angle in the target and the number of active electrodes) is the most demanding case but is still solved in a few seconds on average and a few minutes in worst case.

4. Discussion and conclusion

4.1. Summary of the algorithm and implementation

Several and in part opposing objectives exist for the optimization of multi-electrode TES montages (e.g., intensity at the target vs. field focality) and the optimization results are further influenced by safety and technical constraints (e.g., limits on the maximally injected current and maximal number of active electrodes). These different combinations of objectives and constraints give rise to a variety of optimization problems, which have different solutions and often require different algorithms. In the current paper, we consider several practically relevant optimization problems for multi-electrode TES montages and use a common mathematical framework to sort these problems according to their characteristics and complexity.

Unless the aim is to maximize the field in the target (Problems 2, 5 and 9), most of the considered problems share the common objective to minimize the field energy in the brain in order to obtain focal fields. In our implementation, the user sets them up by defining the desired

strength and direction of the electric field in the target region, which are practically meaningful and intuitive parameters. All considered problems, except Problem 1, which is a theoretical best-case scenario, obey safety limits, which are defined by upper limits of the currents injected per electrode and in total. When desired, also the maximal number of active electrodes can be set to match the number of available stimulation channels, and fine control of the maximal angular deviation of the target field from the desired direction can be established in addition.

Our approach shares several features with previously published work. For example, Guler et al. (2016a) proposed an optimization problem that is based on similar quantities as used in the current work (field at target, energy and current injection limits). However, in his approach, the maximum energy is selected by the user while the field in the target region and direction is maximized. We believe that our approach has the advantage of using a more intuitive parameter as user input, as electric field values that can serve as reference are often reported in simulation studies, while energy values are rarely stated. Dmochowski et al. (2011) proposed two types of optimization problems, a least squares approach and a linearly constrained minimum variance approach (LCMV). The least squares approach is based on the selection of a target region and field direction, followed by a manual tuning of a weight parameter until an acceptable field intensity is achieved in the target. The LCMV approach closely resembles our optimization of the field focality as done in Problem 2. The main difference is that in the LCMV approach defined by Dmochowski et al. all electric field components in the complete target region need to be specified and fulfilled exactly, while we use a more relaxed constraint, in which only the average strength of the field in the target along the specified direction needs to be fulfilled. As our approach leaves more degrees of freedom for the solution, we expect to obtain more focal fields, albeit at the cost of less control of the field at the target. Other approaches use different quantities, such as Wagner et al. (2015) where the user selects a maximum field value outside the target region, or Ruffini et al. (2014) where a similarity measure to a target field is optimized.

We addressed the practically important issue of limiting the number of electrodes, given that TES stimulators usually have a small number of channels available. This was done in a principled and efficient way by using Branch-and-Bound algorithms. Noticeably, this algorithm does not only promote quick convergence, but also certifies that the obtained solution is close to the global optimum. Branch-and-bound algorithms were already considered for a similar problem (Guler et al., 2016b), but with substantially lower performance requiring a few hours to converge for a single simulation. The higher efficiency of our implementation (Table 3) is probably due to more suitable upper and lower bound functions and the state-space definition. In addition, we established and evaluated a useful heuristic for further accelerating the Branch-and-Bound algorithm by preselecting "candidate" electrodes (Figs. 6 and 7). Competing algorithms such as Genetic Algorithms (Ruffini et al., 2014) provide no guarantee of convergence towards or proximity to the global optima, and are also reported to need in the order of a few hours to converge.

To the best of our knowledge, this is the first optimization study that explicitly controls the electric field angle in the target, besides the LCMV approach by (Dmochowski et al., 2011), where the angle needs to be reached exactly. Our implementation was successful in solving the underlying problem (a QCQP), and reasonably efficient obtaining results in less than 1 s in most cases. The implementation is likely less efficient than a cone solver, but it has the advantage of keeping the code base simpler due to its similarity to the other considered problems. This new procedure will allow for more in-depth investigations of the effect of angle on TES outcome.

4.2. Summary of findings

The efficiency of the optimization algorithms, together with the practically meaningful and intuitive input parameters in our optimizations, allowed us to perform an extensive mapping of the optimizations and test the effect of various constraints and parameter choices across the entire cortex. Our results demonstrate that local anatomy plays a significant role, as a far better field focality, better targeting accuracy and higher intensities can be obtained for targets in superficial brain areas compared to sulcal or deep targets (Figs. 3 and 4). This is the case even for a theoretical best-case scenario without safety constraints. Compared to this scenario, adding safety constraints strongly reduces the obtainable field focality and targeting accuracy further, in particular for deeper targets (Fig. 5). These observations are also in line with the intensity-focality trade-off reported in (Dmochowski et al., 2011; see our Suppl. Figs. S8–S10). Finally, additionally constraining the angle of the field in the target to meet the desired direction has a low additional penalty for most target positions (Fig. 8). While the results in the main paper were obtained for cortical targets being oriented normally to the grey matter sheet, we confirmed that the findings generalize to tangential target directions and to targets in deep areas (Suppl. Figs. S1–S16).

It seems beneficial to perform the optimization of multi-electrode TES montages on a fine electrode grid (up to ~300 electrodes, Suppl. Figs. S2–S7), so that the optimization procedure can do fine adjustments of the positions of the active electrodes in order to obtain the most focal and intense electric fields. This is particularly relevant when aiming to focus the field on superficial parts of the brain. However, it is important to note that this fine grid is only required for the planning of the optimized montage using the virtual head model, while only a few active electrodes are finally required for the stimulation. However, this suggests that the positions of these electrodes are required to be accurately controlled in practice.

We observed that constraints on the total current delivered (sum of absolute electrode currents) severely limits the benefit of increasing the number of active electrodes beyond ~8, at least when targeting a single area. This happens because the limits on the total current also limit the ability to recruit secondary electrodes for cancelling the field in positions of undesired stimulation, and therefore has effect similar to limiting the total number of electrodes. A counterintuitive consequence of this is that a limitation of the total current actually causes more energy to be delivered to the brain, given that the target field intensity can be met. Therefore, in order to archive the full benefit of focal optimized multi-electrode stimulation, it would be useful to consider an extension of the implemented safety constraints and possibly rather ensure that the maximum current density in relevant tissues classes are kept below a safety limit. In particular, limiting the current density in the skin to avoid discomfort and heating of tissue due to stimulation not only immediately beneath, but also in between the electrodes might be a rationale choice for maximizing the benefit of focal optimized multi-electrode TES.

Our implementation of TES multi-electrode optimization also allows for the incorporation of multiple targets. We exemplarily demonstrated that the algorithm successfully created balanced focal fields around two distant target regions, while also keeping the number of active electrodes at a reasonably low number (Fig. 10). For targets placed closely together, we might not be able to fully decouple the electric fields around each target, in contrast to the situation tested in Fig. 10. This happens as the electrodes involved in the stimulation of one target cause a significant electric field also in the other target, as observed previously in (Saturnino et al., 2017), so that a stimulation of the region between the two targets cannot be fully avoided.

4.3. Limitations

Even though we explored a large range of parameters, some were kept constant during all tests, most importantly the head model and the safety constraints. Inter-individual variations in anatomy can impact on the exact values for the optimum field focality, especially in the case of disease (Dmochowski et al., 2013). However, we do not expect to reach fundamentally different conclusions on the influence of the optimization parameters or constraints when changing the head model. Even though

specific anatomical features might enhance or counteract the effect of, for example, adding safety constraints or limiting the number of electrodes, these effects stem from the underlying physics involved in TES generated electric fields. Changing the safety constraints may have an effect on the focality-intensity trade-off (Fig. 5) and on the number of electrodes needed for a focal stimulation (Figs. 7 and 9). If we increase the total current bound I_{tot}, we would expect the trade-off to persist, yet to be less pronounced, because we more of the total current budget can be used then to cancel out electric fields outside the target area. Decreasing the individual current bound I_{ind} while keeping the total current bound I_{tot} constant would result in more active electrodes and likely less focal fields, as electrodes in sub-optimal positions would be needed to reach the desired electric field at the target.

Importantly, there are many other factors besides variations in the strength and spatial distribution of the electric field that can cause variability in the outcome of an TES experiment, such as the brain state, age, genetics and neurochemistry (Karabanov et al., 2016; Ridding and Ziemann, 2010), which are not addressed within the optimization framework presented in the current work.

5. Conclusion

We introduce a new algorithm to optimize TES electric fields and assess the impact of optimization parameters and constraints. We show that the maximally achievable field focality is fundamentally limited by the anatomy of the head and its physical properties, and demonstrate a focality-intensity trade-off. Given commonly implemented safety constraints, we show that there is little benefit in using more than eight electrodes for TES electrode montages, even though the optimization benefits of using a fine electrode grid for planning the electrode montage. Furthermore, we found that the electric field can be controlled with little penalty on field focality and that multiple distant targets can be optimized while keeping effects of the stimulation balanced. The optimization code used for this study will be available in a future version of our open source software SimNIBS. This study was limited to traditional TES methods. More recent methods, such as Temporally Interfering (TI) Electric Fields (Grossman et al., 2017) might be able to generate more focal fields in deeper brain areas than traditional TES methods. Algorithms to optimize TI fields and study their limits and relationship to optimization parameters and constraints are an interesting topic for future research.

Declaration of interest

Acknowledgements

Appendix A. Supplementary data

Supplementary data to this article can be found online at https://doi.org/10.1016/j.neuroimage.2019.116183.

References

Attene, M., 2010. A lightweight approach to repairing digitized polygon meshes. Vis. Comput. 26, 1393–1406. https://doi.org/10.1007/s00371-010-0416-3.

Boyd, S., Mattingley, J., 2007. Branch and Bound Methods. Notes EE364b. Stanford Univ, pp. 1–19.

Boyd, S., Vandenberghe, L., 2004. Convex Optimization. Cambridge university press.

Dantzig, G.B., 1963. Linear Programming and Extensions. Rand Corporation Research Study Princeton Univ. Press, Princeton, NJ.

Diamond, S., Boyd, S., 2016. CVXPY: A Python-Embedded Modeling Language for Convex Optimization.

Dmochowski, J.P., Bikson, M., Parra, L.C., 2012. The point spread function of the human head and its implications for transcranial current stimulation. Phys. Med. Biol. 57, 6459–6477. https://doi.org/10.1088/0031-9155/57/20/6459.

Dmochowski, J.P., Datta, A., Bikson, M., Su, Y., Parra, L.C., 2011. Optimized multi-electrode stimulation increases focality and intensity at target. J. Neural Eng. 8, 046011. https://doi.org/10.1088/1741-2560/8/4/046011.

Dmochowski, J.P., Datta, A., Huang, Y., Richardson, J.D., Bikson, M., Fridriksson, J., Parra, L.C., 2013. Targeted transcranial direct current stimulation for rehabilitation after stroke. Neuroimage 75, 12–19. https://doi.org/10.1016/j.neuroimage.2013.02.049.

Dmochowski, J.P., Koessler, L., Norcia, A.M., Bikson, M., Parra, L.C., 2017. Optimal use of EEG recordings to target active brain areas with transcranial electrical stimulation. Neuroimage 157, 69–80. https://doi.org/10.1016/j.neuroimage.2017.05.059.

Fernandez-corazza, M., Turovets, S., Muravchik, C., 2019. Unification of Optimal Targeting Methods in Transcranial Electrical Stimulation bioRxiv 557090. https://doi.org/10.1101/557090.

Gill, P.E., Murray, W., 1978. Numerically stable methods for quadratic programming. Math. Program. 14, 349–372. https://doi.org/10.1007/BF01588976.

Griffiths, D.J., 1999. Introduction to Electrodynamics. Prentice Hall.

Grossman, N., Bono, D., Dedic, N., Kodandaramaiah, S.B., Rudenko, A., Suk, H.J., Cassara, A.M., Neufeld, E., Kuster, N., Tsai, L.H., Pascual-Leone, A., Boyden, E.S., 2017. Noninvasive deep brain stimulation via temporally interfering electric fields. Cell 169, 1029–1041 e16. https://doi.org/10.1016/j.cell.2017.05.024.

Guler, S., Dannhauer, M., Erem, B., Macleod, R., Tucker, D., Turovets, S., Luu, P., Erdogmus, D., Brooks, D.H., 2016a. Optimization of focality and direction in dense electrode array transcranial direct current stimulation (tDCS). J. Neural Eng. 13, 1–14. https://doi.org/10.1088/1741-2560/13/3/036020.

Guler, S., Dannhauer, M., Erem, B., Macleod, R., Tucker, D., Turovets, S., Luu, P., Meleis, W., Brooks, D.H., 2016b. Optimizing stimulus patterns for dense array TDCS with fewer sources than electrodes using a branch and bound algorithm. Proc. - Int. Symp. Biomed. Imaging 2016–June 229–232. https://doi.org/10.1109/ISBI.2016.7493251.

Heise, K.-F., Kortzorg, N., Saturnino, G.B., Fujiyama, H., Cuypers, K., Thielscher, A., Swinnen, S.P., 2016. Evaluation of a modified high-definition electrode montage for transcranial alternating current stimulation (tACS) of pre-central areas. Brain Stimul 9, 700–704. https://doi.org/10.1016/j.brs.2016.04.009.

Horvath, J.C., Carter, O., Forte, J.D., 2014. Transcranial direct current stimulation: five important issues we aren't discussing (but probably should be). Front. Syst. Neurosci. 8, 1–8. https://doi.org/10.3389/fnsys.2014.00002.

Horvath, J.C., Forte, J.D., Carter, O., 2015. Evidence that transcranial direct current stimulation (tDCS) generates little-to-no reliable neurophysiologic effect beyond MEP amplitude modulation in healthy human subjects: a systematic review. Neuropsychologia 66, 213–236. https://doi.org/10.1016/j.neuropsychologia.2014.11.021.

Huang, Y., Parra, L.C., 2019. Can transcranial electric stimulation with multiple electrodes reach deep targets? Brain Stimul 12, 30–40. https://doi.org/10.1016/j.brs.2018.09.010.

Karabanov, A., Thielscher, A., Siebner, H.R., 2016. Transcranial brain stimulation. Curr. Opin. Neurol. 29, 397–404. https://doi.org/10.1097/WCO.0000000000000342.

Kuo, H.I., Bikson, M., Datta, A., Minhas, P., Paulus, W., Kuo, M.F., Nitsche, M.A., 2013. Comparing cortical plasticity induced by conventional and high-definition 4 × 1 ring tDCS: a neurophysiological study. Brain Stimul 6, 644–648. https://doi.org/10.1016/j.brs.2012.09.010.

Miranda, P.C., Mekonnen, A., Salvador, R., Ruffini, G., 2013. The electric field in the cortex during transcranial current stimulation. Neuroimage 70, 48–58. https://doi.org/10.1016/j.neuroimage.2012.12.034.

Nielsen, J.D., Madsen, K.H., Puonti, O., Siebner, H.R., Bauer, C., Madsen, C.G., Saturnino, G.B., Thielscher, A., 2018. Automatic skull segmentation from MR images for realistic volume conductor models of the head: assessment of the state-of-the-art. Neuroimage 1–12. https://doi.org/10.1016/j.neuroimage.2018.03.001.

Nitsche, M.A., Boggio, P.S., Fregni, F., Pascual-Leone, A., 2009. Treatment of depression with transcranial direct current stimulation (tDCS): a Review. Exp. Neurol. 219, 14–19. https://doi.org/10.1016/j.expneurol.2009.03.038.

Park, J.H., Hong, S.B., Kim, D.W., Suh, M., Im, C.H., 2011. A novel array-type transcranial direct current stimulation (tDCS) system for accurate focusing on targeted brain areas. IEEE Trans. Magn. 47, 882–885. https://doi.org/10.1109/TMAG.2010.2072987.

Parkin, B.L., Ekhtiari, H., Walsh, V.F., 2015. Non-invasive human brain stimulation in cognitive neuroscience: a primer. Neuron 87, 932–945. https://doi.org/10.1016/j.neuron.2015.07.032.

Plonsey, R., Heppner, D.B., 1967. Considerations of quasi-stationarity in electrophysiological systems. Bull. Math. Biophys. 29, 657–664.

Ridding, M.C., Ziemann, U., 2010. Determinants of the induction of cortical plasticity by non-invasive brain stimulation in healthy subjects. J. Physiol. 588, 2291–2304. https://doi.org/10.1113/jphysiol.2010.190314.

Ruffini, G., Fox, M.D., Ripolles, O., Miranda, P.C., Pascual-Leone, A., 2014. Optimization of multifocal transcranial current stimulation for weighted cortical pattern targeting from realistic modeling of electric fields. Neuroimage 216–225. https://doi.org/10.1016/j.neuroimage.2013.12.002.

Sadleir, R.J., Vannorsdall, T.D., Schretlen, D.J., Gordon, B., 2012. Target optimization in transcranial direct current stimulation. Front. Psychiatry 3, 1–13. https://doi.org/10.3389/fpsyt.2012.00090.

Saturnino, G.B., Antunes, A., Thielscher, A., 2015. On the importance of electrode parameters for shaping electric field patterns generated by tDCS. Neuroimage 120, 25–35. https://doi.org/10.1016/j.neuroimage.2015.06.067.

Saturnino, G.B., Madsen, K.H., Siebner, H.R., Thielscher, A., 2017. How to target inter-regional phase synchronization with dual-site Transcranial Alternating Current Stimulation. Neuroimage 163, 68–80. https://doi.org/10.1016/j.neuroimage.2017.09.024.

Saturnino, G.B., Thielscher, A., Madsen, K.H., Knösche, T.R., Weise, K., 2018. A principled approach to conductivity uncertainty analysis in electric field calculations. Neuroimage 821–834. https://doi.org/10.1016/j.neuroimage.2018.12.053.

Stagg, C.J., Nitsche, M.A., 2011. Physiological basis of transcranial direct current stimulation. Neuroscience 17, 37–53. https://doi.org/10.1177/1073858410386614.

Thielscher, A., Antunes, A., Saturnino, G.B., 2015. Field modeling for transcranial magnetic stimulation: a useful tool to understand the physiological effects of TMS? Proc. Annu. Int. Conf. IEEE Eng. Med. Biol. Soc. EMBS 222–225. https://doi.org/10.1109/EMBC.2015.7318340.

Tibshirani, R., 1996. Regression shrinkage and selection via the lasso. J. R. Stat. Soc. Ser. B 58, 267–288. https://doi.org/10.1111/j.2517-6161.1996.tb02080.x.

van der Walt, S., Colbert, S.C., Varoquaux, G., 2011. The NumPy array: a structure for efficient numerical computation. Comput. Sci. Eng. 13, 22–30. https://doi.org/10.1109/MCSE.2011.37.

Wagner, S., Burger, M., Wolters, C.H., 2016. An optimization approach for well-targeted transcranial direct current stimulation. SIAM J. Appl. Math. 76 (6), 2154–2174. https://doi.org/10.1137/15M1026481.

Windhoff, M., Opitz, A., Thielscher, A., 2013. Electric field calculations in brain stimulation based on finite elements: an optimized processing pipeline for the generation and usage of accurate individual head models. Hum. Brain Mapp. 34, 923–935. https://doi.org/10.1002/hbm.21479.

Yousry, T.A., Schmid, U.D., Alkadhi, H., Schmidt, D., Peraud, A., Buettner, A., Winkler, P., 1997. Localization of the motor hand area to a knob on the precentral gyrus. A new landmark. Brain 120, 141–157. https://doi.org/10.1093/brain/120.1.141.

Appendix C

Optimizing the Electric Field Strength in Multiple Targets for Multichannel Transcranial Electric Stimulation

Optimizing the Electric Field Strength in Multiple Targets for Multichannel Transcranial Electric Stimulation

Guilherme B. Saturnino[1,2], Kristoffer H. Madsen[1,3], Axel Thielscher[1,2]

[1]Danish Research Centre for Magnetic Resonance, Centre for Functional and Diagnostic Imaging and Research, Copenhagen University Hospital Hvidovre, Hvidovre, Denmark
[2]Department of Health Technology, Technical University of Denmark, Kgs. Lyngby, Denmark
[3]Department of Applied Mathematics and Computer Science, Technical University of Denmark, Kgs. Lyngby, Denmark

Corresponding author: Axel Thielscher (axelt@drcmr.dk)

Abstract

Objective:
Most approaches to optimize the electric field pattern generated by multichannel Transcranial Electric Stimulation (TES) require the definition of a preferred direction of the electric field in the target region(s). However, this requires knowledge about how the neural effects depend on the field direction, which is not always available. Thus, it can be preferential to optimize the field strength in the target(s), irrespective of the field direction. However, this results in a more complex optimization problem.

Approach:
We introduce and validate a novel optimization algorithm that maximizes focality while controlling the electric field strength in the target to maintain a defined value. It obeys the safety constraints, allows limiting the number of active electrodes and allows also for multi-target optimization.

Main Results:
The optimization algorithm outperformed naïve search approaches in both quality of the solution and computational efficiency. Using the amygdala as test case, we show that it allows for reaching a reasonable trade-off between focality and field strength in the target. In contrast, simply maximizing the field strength in the target results in far more extended fields. In addition, by maintaining the pre-defined field strengths in the targets, the new algorithm allows for a balanced stimulation of two or more regions.

Significance:
The novel algorithm can be used to automatically obtain individualized, optimal montages for targeting regions without the need to define preferential directions. It will automatically select the field direction that achieves the desired field strength in the target(s) with the most focal stimulation pattern.

1. Introduction

Transcranial electric stimulation (TES) methods inject weak direct or alternating currents via scalp electrodes in order to create an electric field in the brain that modulates neural activity [1]. In order to improve the robustness of the stimulation outcome and to be able to causally relate the behavioral stimulation effects with the modulation of specific brain areas, it is important to limit the electric field region to one or more regions of interest. However, as the electric field is shaped by the individual head anatomy [2], targeting TES electric fields is not a trivial task. Therefore, multiple optimization approaches have been proposed in order to automatically plan multichannel TES interventions [3–9].

Most TES optimization methods aim to maximize, control or approximate projections of the electric field in a specific direction in the target region, rather than the absolute field strength (or norm) irrespective of direction. This can be a good choice for many cortical targets, as it is thought that the physiological TES effects are direction dependent, such that an electric field pointing into and out of the cortical surface correspond to anodal and cathodal stimulation [10,11]. However, a preferential direction might not always be clearly defined, such as in the case of subcortical targets. Instead, optimizing the electric field strength might be preferred in this case. This problem was tackled in two prior studies that proposed methods to maximize the field strength in a single target without control of the focality of the resulting field [4,5].

Here, we introduce a novel TES optimization algorithm which controls the field strength in one or more targets while minimizing it elsewhere and at the same time complying with safety constraints and limiting the number of active electrodes. Controlling the target field strength to reach a desired value instead of maximizing it allows for leveraging the trade-off between strength and focality, and for the balanced stimulation of two or more targets. We show that our approach outperforms naïve brute-force search and demonstrate that it succeeds in optimizing montages for the balanced stimulation of the bilateral amygdala.

2. Methods

2.1 Head Model

We used the example head model from SimNIBS 3.1 (www.simnibs.org) [12] *Ernie* with six tissues compartments, White Matter (WM), Gray Matter (GM), Cerebrospinal Fluid (CSF), Skull, Scalp, and Eyes (figure 1(a)). The standard tissue conductivities in SimNIBS were used [13]. Details of the MR image types and parameters and of the methods used to create the head model are given in [14].

2.2 Electric Field Simulations

The optimization algorithm builds upon a leadfield matrix A [9,15], which is constructed by selecting a fixed return electrode and then injecting a unity current sequentially through each remaining electrode. The leadfield allows for quick evaluations of the electric fields produced by any current combination by leveraging the linearity of the field with respect to the injected currents. Here, we used $n = 74$ electrodes placed according to the EEG 10-10 system and performed simulations in SimNIBS 3.1 using Neumann boundary conditions in the electrode surfaces and the MKL PARDISO solver [16].

2.3 Mathematical Formulation

The mean electric field strength in a target region Ω_t is given by

$$\frac{1}{V_{\Omega_t}} \int_{\Omega_t} \|E\| \, dV = \frac{1}{V_{\Omega_t}} \int_{\Omega_t} \sqrt{E_x^2 + E_y^2 + E_z^2} \, dV, \tag{1}$$

where E is the electric field and V_{Ω_t} the volume of the target region. We can approximate the mean of the norm by

$$\frac{1}{V_{\Omega_t}} \int_{\Omega_t} \|E\| \, dV \approx \sqrt{\frac{1}{V_{\Omega_t}} \int_{\Omega_t} E_x^2 + E_y^2 + E_z^2 \, dV}, \tag{2}$$

which is a good approximation for a small target region, or if the electric field is approximately constant inside Ω_t. Using this approximation and discretizing the system, we can write the equation above as

$$\frac{1}{V_{\Omega_t}} \int_{\Omega_t} \|E\| \, dV \approx \sqrt{x^\top Q_t x^\top}, \tag{3}$$

where x is an $n \times 1$ vector of electrode currents, and Q_t is a $n \times n$ symmetric positive semidefinite matrix given by

$$Q_t = \frac{1}{V_{\Omega_t}} A^\top G_t A. \tag{4}$$

G_t is a diagonal matrix with zeros in entries outside the target region and element volume values for entries inside the target region.

2.4 Optimization Problems

We set up an optimization problem to minimize the field outside the target region, while keeping the mean field strength in the target region at a desired value t, in line with [9]:

$$\text{minimize} \quad x^\top Q x \tag{P1.1}$$

$$\text{subject to} \quad x^\top Q_t x = t^2 \tag{P1.2}$$

$$\mathbf{1}^\top x = 0 \tag{P1.3}$$

$$\|x\|_1 \leq 2 I_{\text{tot}} \tag{P1.4}$$

$$-I_{\text{ind}} \leq x_i \leq I_{\text{ind}}, \quad i = 1, 2, \dots, n \tag{P1.5}$$

Problem 1: Minimize field energy while controlling the electric field strength in the target region.

Here, P1.1 calculates the total field energy, P1.2 controls the field strength in the target, P1.3 enforces Kirchhoff's law, P1.4 limits the total current injected, and P1.5 limits the current injected through each electrode. Please see [9] for more details. In the following, we only consider the field energy in GM for optimization (P1.1). However, in general, any region can be used.

We can extend Problem 1 to limit the number of active electrodes to N, and to control the electric field strength in n_t target regions:

$$\text{minimize} \quad \boldsymbol{x}^\top \boldsymbol{Q} \boldsymbol{x} \qquad\qquad\qquad \text{(P2.1)}$$

$$\text{subject to} \quad \boldsymbol{x}^\top \boldsymbol{Q}_{t_i} \boldsymbol{x} = t_i^2, \qquad i = 1, \dots, n_t \qquad \text{(P2.2)}$$

$$\mathbf{1}^\top \boldsymbol{x} = 0 \qquad\qquad\qquad \text{(P2.3)}$$

$$\|\boldsymbol{x}\|_1 \leq 2I_{\text{tot}} \qquad\qquad\qquad \text{(P2.4)}$$

$$-I_{\text{ind}} \leq x_i \leq I_{\text{ind}}, \qquad i = 1, 2, \dots, n \qquad \text{(P2.5)}$$

$$\|\boldsymbol{x}\|_0 \leq N \qquad\qquad\qquad \text{(P2.6)}$$

Problem 2: Minimize field energy while controlling the electric field strength in n_t regions and limiting the number of active electrodes to N

2.5 Implementation

In contrast to the control of a field component along a specific direction, constraint P1.2 makes problem 1 non-convex. However, this constraint can be dealt with effectively using convex-concave programming (CCP) [17]. This class of optimization algorithms works in problems where each term can be written as a difference of a convex and a concave function, called difference of convex (DC) programming problems. It then proceeds by linearizing the concave part of the functions, thereby obtaining convex optimization problems which can be readily solved.

In order to apply the CCP algorithm, we first substitute the equality constraint P1.2 with an inequality constraint

$$\boldsymbol{x}^\top \boldsymbol{Q}_t \boldsymbol{x} \geq t^2. \qquad\qquad\qquad (5)$$

Any solution to the modified problem is also a solution to the original one, as for any point $\boldsymbol{x}'$ in the feasible region of the modified problem there exists another point $x'' = x' \big/ \sqrt{x^\top Q_t x^\top}$, which fulfills both constraint P1.2 and Inequality 5 and has a smaller objective value. Linearizing inequality 5 around a point $\boldsymbol{x}_k$, we obtain the term

$$2\boldsymbol{x}_k^\top \boldsymbol{Q}_t \boldsymbol{x} - \boldsymbol{x}_k^\top \boldsymbol{Q}_t \boldsymbol{x}_k \geq t^2. \qquad\qquad\qquad (6)$$

Because of the convexity of the quadratic term, any point that obeys inequality 6 also obeys Inequality 5. We then solve at each step k an optimization problem:

$$\text{minimize} \quad x^\top Q x + \xi_k s \qquad\qquad\qquad \text{(P3.1)}$$

$$\text{subject to} \quad -2x_k^\top Q_t x \leq s - t^2 - x_k^\top Q_t x_k \qquad \text{(P3.2)}$$

$$\mathbf{1}^\top x = 0 \qquad\qquad\qquad\qquad \text{(P3.3)}$$

$$\|x\|_1 \leq 2I_{\text{tot}} \qquad\qquad\qquad \text{(P3.4)}$$

$$-I_{\text{ind}} \leq x_i \leq I_{\text{ind}}, \quad i = 1, 2, \dots, n \qquad \text{(P3.5)}$$

$$s \geq 0 \qquad\qquad\qquad\qquad\quad \text{(P3.6)}$$

Problem 2: Linearization of problem 1 around a point x_k

where ξ_k is a nondecreasing penalty term and s is a slack variable. The introduction of the slack variable allows for the algorithm to be initialized at a point x_0 which violates inequality 5, and for it to better explore the optimization domain and find regions of lower objective value [17]. In order to obtain a feasible solution, we increase the penalty term at each iteration by a factor $\mu > 1$, until a maximum value of ξ_{max} is reached

$$\xi_{k+1} = \min(\mu \xi_k, \xi_{\text{max}}). \qquad\qquad\qquad (7)$$

For the current work, we used

$$\xi_0 = \frac{x_0^\top Q x_0}{x_0^\top Q_t x_0} \times 10^{-2}, \qquad\qquad\qquad (8)$$

$$\xi_{\text{max}} = \xi_0 \times 10^4, \qquad\qquad\qquad\qquad (9)$$

$$\mu = 2. \qquad\qquad\qquad\qquad\quad (10)$$

The initial points x_0 are obtained by solving the constrained eigenvalue problem

$$\begin{cases} Q_t \, x = \lambda x \\ \mathbf{1}^\top x = 0 \end{cases}, \qquad\qquad\qquad (11)$$

and then scaling the eigenvalues so that they obey constraints (P1.4) and (P1.5). In order to obtain solutions closer to the global optimum, we performed a total of 20 starts for each optimization. We considered that the optimization converged when the objective stopped decreasing and the electric field strength in the target stopped increasing

$$\begin{cases} x_{k-1}^\top Q x_{k-1} - x_k^\top Q x_k < \delta_0 \\ x_k^\top Q_t x_k - x_{k-1}^\top Q_t x_{k-1} < \delta_t \end{cases}, \qquad (12)$$

where

$$\delta_0 = x_{k-1}^\top Q x_{k-1} \times 10^{-3}, \qquad\qquad (13)$$

$$\delta_t = x_{k-1}^\top Q_t x_{k-1} \times 10^{-3}. \qquad\qquad (14)$$

Notice that, if the target strength value t is too large, it might not be reachable, which makes problem 1 infeasible. In this case, the slack term $\xi_k s$ dominates and the optimization algorithm will naturally convert to a problem of maximizing field strength in the target region.

In order to deal with many target regions simultaneously (Constraint P2.2), we go through the same steps as with a single constraint, but modify the constrained eigenproblem used for initialization (Equation 11) to use the sum of the Q_{t_i} matrices.

Constraining the number of active electrodes (Constraint P2.6) leads to a combinatorial problem. However, this problem can be efficiently solved using the branch-and-bound algorithm described in [9].

2.6 Validation

In order validate our optimization algorithm, we used it to optimize 1000 randomly chosen GM target regions, each with a 10mm radius. To test whether the results obtained were indeed optimal, we compared the solutions to the best value obtained by optimizing the electric fields while controlling directional components (i.e. solving Problem 3 in [9]) in 25 directions equally spaced in a half-sphere.

Afterwards, we performed optimizations while controlling the field strength in two targets simultaneously. Two hundred pairs of target regions were randomly selected in GM. To validate the algorithm, we compared the results with the best values obtained from minimizing the total field energy while controlling the field component in each target independently (Problem 8 in [9]). We searched all combinations of 12 equally spaced directions in a half sphere for one of the targets and 25 directions in a full sphere for the other target, which gives a total of 300 directions. In all cases, we limited the total current injected to 2 mA and the current injected per electrode to 1mA. The target intensity was set to 0.2 V/m. Performance of the optimization was assessed using ratio of the energy (P1.1) of the solutions obtained with the optimization and the search method (ratios < 1 indicate better performance of the optimization method).

2.7 Subcortical Target

To illustrate the effect of the target field strength on the electric field, we optimized electrode montages while controlling the field strength either in the left amygdala (figure 1(b)-(c)) or the bilateral amygdala (figure 2), and also maximized the field strength in these regions. The current flow through each electrodes was limited to 1 mA, the total current injected to 4 mA and the number of active electrode was limited to 8 using the branch-and-bound algorithm described in [9]. The target intensity was set to 0.2 V/m, 0.4 V/m or maximized. In the two-target case, the later was done while keeping the electric field strength in both targets the same. Even though the images show the electric field in grey and white matter, only the electric field in gray matter was considered during optimization.

3. Results

3.1 Validation

When controlling the field strength of one target, our optimization approach outperformed the naïve search in all the cases (range of energy ratios between optimized vs searched solutions: 0.87 to 0.99; 95% confidence interval, CI), while running ~1.7 times faster (2.2 vs. 3.7 seconds). For the two-target control, the optimization was better in 99.5% of the cases (range of energy ratios between optimized vs naïve search: 0.82 to 0.97; 95% CI), while running ~3.5 times faster (4.0 vs. 14.5 seconds).

3.2 Subcortical Target

The peak electric fields are not located in the subcortical target, but in more superficial structures (figure 1(b)), which is expected from earlier findings [9]. Interestingly, however, as the field strength in the target increases, the fields in superficial regions get disproportionally stronger (i.e. the focality decreases strongly). This is expected due to physical limitations in the distribution of electric fields [3,9]: Increasing the field strength in the target is achieved by increasing the distance between anodes and cathode (Figure 1C), which lowers focality. This suggests that controlling the field strength rather than simply maximizing is preferred to maintain a better focality.

Figure 2 shows the same intensity-focality trade-off for the two target case. Interestingly, the trade-off between 0.2 V/m and 0.4 V/m seems small. The electrode montages changes from being symmetric along the sagittal plane to a frontal-posterior montage as the target intensity increases beyond 0.4 V/m (Figure 2B).

4. Discussion

Our new algorithm is capable of optimizing the focality of multichannel TES montages while controlling the field strength in multiple targets. The algorithm performs better than simple search both in terms of the optimality of the solution and time. When compared to the results obtained by maximizing the field strength in the target, the algorithm can strongly improve the focality of the stimulation at merely moderately weaker fields in the target.

Exemplary optimization of the field strength in the uni- and bilateral amygdala reveal that relatively high field strengths can be obtained also for bilateral targeting, but also shows an expected intensity-focality trade-off and stronger fields in cortical regions. Controlling the field strengths in the bilateral amygdala rather than merely maximizing it achieves a balanced montage in which both targets are similarly stimulated.

For superficial targets, it might often be more desirable to control a specific field component in order to ensure that the field is oriented perpendicularly to the cortical surface in the target area. For subcortical targets, however, a preferential direction might not be easily defined and the control of the field strength might be preferred. The new algorithm is computationally efficient and obeys safety and practical constraints, rendering it suited for use in empirical TES studies. It will be released as open source in a future version of the transcranial brain stimulation simulation and optimization software SimNIBS [12].

5. Acknowledgments

References

[1]   Liu A, Vöröslakos M, Kronberg G, Henin S, Krause M R, Huang Y, Opitz A, Mehta A, Pack C C, Krekelberg B, Berényi A, Parra L C, Melloni L, Devinsky O and Buzsáki G 2018 Immediate neurophysiological effects of transcranial electrical stimulation *Nat. Commun.* **9**

[2]   Opitz A, Paulus W, Will A and Thielscher A 2015 Anatomical determinants of the electric field during transcranial direct current stimulation *Neuroimage* **109** 2

[3]   Dmochowski J P, Datta A, Bikson M, Su Y and Parra L C 2011 Optimized multi-electrode stimulation increases focality and intensity at target *J. Neural Eng.* **8** 046011

[4]   Park J H, Hong S B, Kim D W, Suh M and Im C H 2011 A novel array-type transcranial direct current stimulation (tDCS) system for accurate focusing on targeted brain areas *IEEE Trans. Magn.* **47** 882–5

[5]   Dmochowski J P, Datta A, Huang Y, Richardson J D, Bikson M, Fridriksson J and Parra L C 2013 Targeted transcranial direct current stimulation for rehabilitation after stroke *Neuroimage* **75** 12–9

[6]   Ruffini G, Fox M D, Ripolles O, Miranda P C and Pascual-Leone A 2014 Optimization of multifocal transcranial current stimulation for weighted cortical pattern targeting from realistic modeling of electric fields *Neuroimage* **89** 216–25

[7]   Wagner S, Burger M and Wolters C H 2016 An Optimization Approach for Well-Targeted Transcranial Direct Current Stimulation *SIAM J. Appl. Math.* **76** 2154–74

[8]   Guler S, Dannhauer M, Erem B, Macleod R, Tucker D, Turovets S, Luu P, Erdogmus D and Brooks D H 2016 Optimization of focality and direction in dense electrode array transcranial direct current stimulation (tDCS) *J. Neural Eng.* **13** 1–14

[9]   Saturnino G B, Siebner H R, Thielscher A and Madsen K H 2019 Accessibility of cortical regions to focal TES: Dependence on spatial position, safety, and practical constraints *Neuroimage* **203** 116183

[10]   Bindman L J, Lippold O C J and Redfearn J W T 1964 The action of brief polarizing currents on the cerebral cortex of the rat (1) during current flow and (2) in the production of long-lasting after-effects *J. Physiol.* **172** 369–82

[11]   Stagg C J and Nitsche M A 2011 Physiological Basis of Transcranial Direct Current Stimulation *Neurosci.* **17** 37–53

[12]   Thielscher A, Antunes A and Saturnino G B 2015 Field modeling for transcranial magnetic stimulation: A useful tool to understand the physiological effects of TMS? *2015 37th Annual International Conference of the IEEE Engineering in Medicine and Biology Society (EMBC)* (IEEE) pp 222–5

[13]   Saturnino G B, Madsen K H and Thielscher A 2019 Electric field simulations for transcranial brain stimulation using FEM: An efficient implementation and error analysis *J. Neural Eng.* **16**

[14]   Nielsen J D, Madsen K H, Puonti O, Siebner H R, Bauer C, Madsen C G, Saturnino G B and Thielscher A 2018 Automatic skull segmentation from MR images for realistic volume conductor models of the head: Assessment of the state-of-the-art *Neuroimage* **174** 587–98

[15]   Dmochowski J P, Koessler L, Norcia A M, Bikson M and Parra L C 2017 Optimal use of EEG recordings to target active brain areas with transcranial electrical stimulation *Neuroimage* **157** 69–80

[16]   Intel 2019 Intel MKL PARDISO - Parallel Direct Sparse Solver Interface

[17]   Lipp T and Boyd S 2016 Variations and extension of the convex–concave procedure *Optim. Eng.* **17** 263–87

Figure Legends

Figure 1

(a)
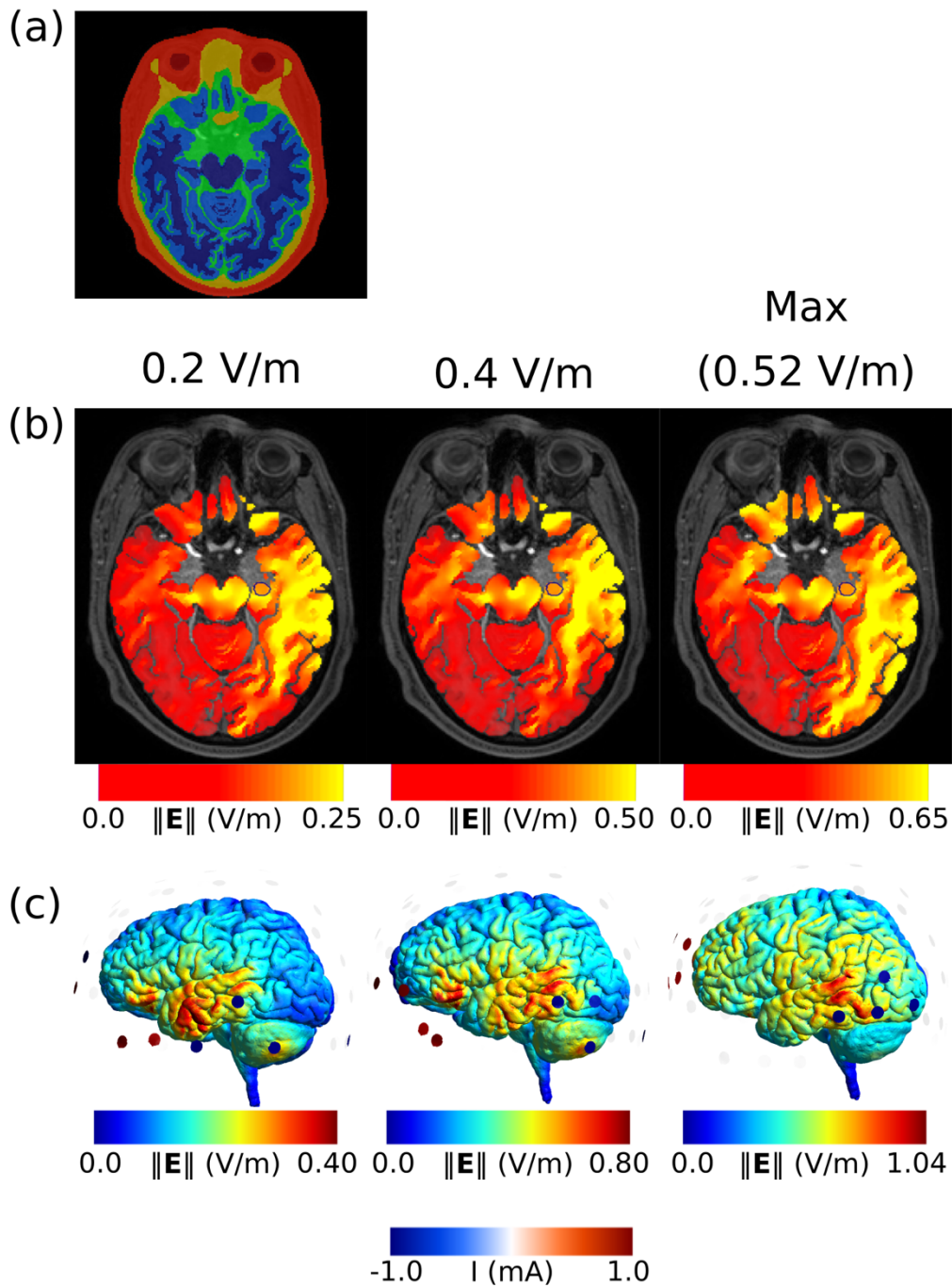
(a) Horizontal slice through the Ernie head model, automatically created by the SimNIBS *headreco* pipeline. The six tissues are white matter (dark blue), gray matter (light blue), CSF (green), skull (yellow) and scalp (red). (b) Optimized electric fields in gray and white matter while controlling the field strength in the left caudal amygdala to be 0.2 V/m, 0.4 V/m, or while maximizing it. The target is delineated in blue. Notice that the color scale changes proportionally with the electric field in the target. (c) Optimized electric fields in the central gray matter surface together with the active electrodes.

Figure 2
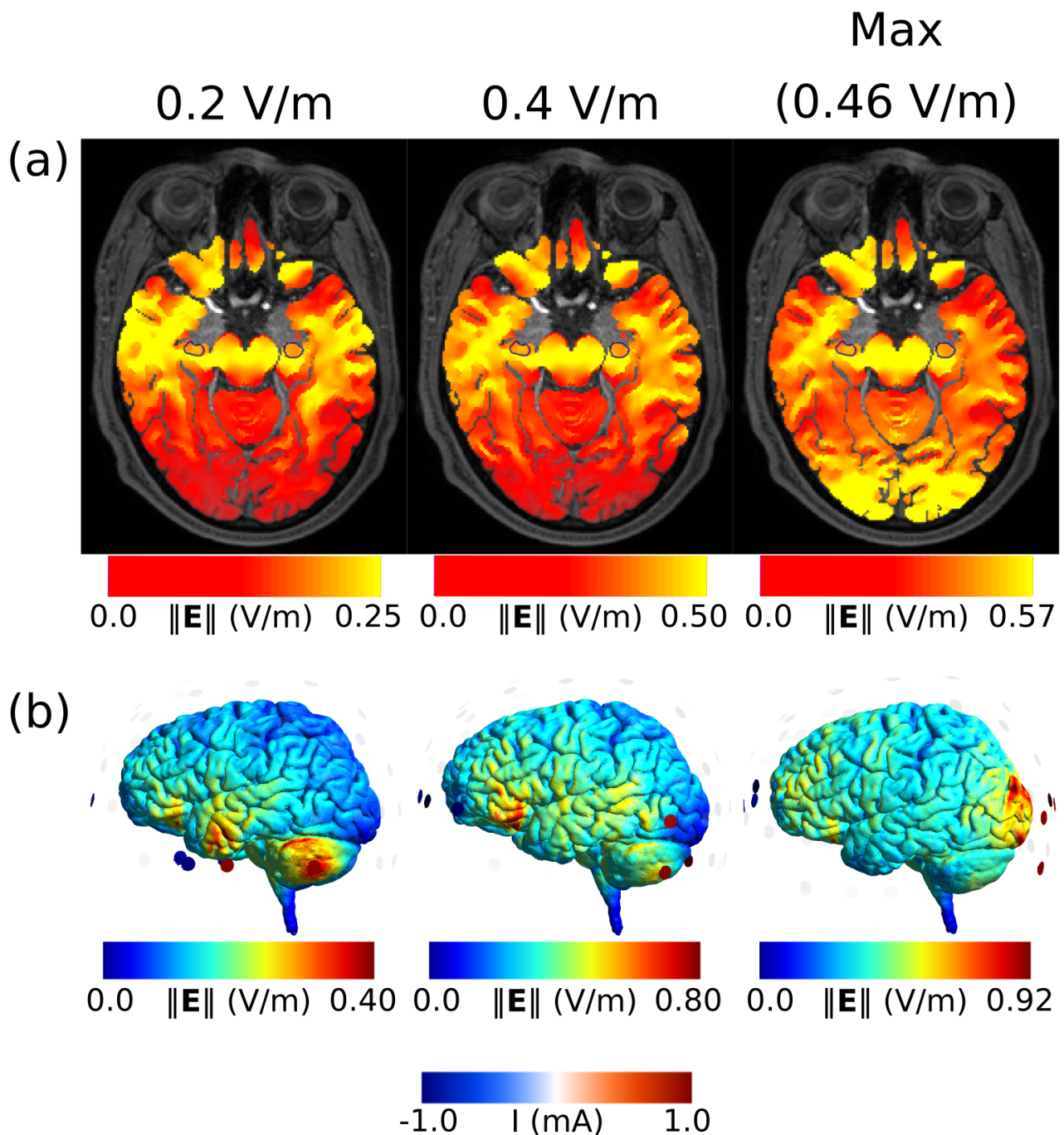
(a) Optimized electric fields in gray and white matter while controlling the field strength inside the two targets delineated in blue. The electric field strength in both targets was set to 0.2 V/m, 0.4 V/m, and increased further until the achieved field strength started differing between both targets. The color scale changes proportionally with the electric field strength in the target. (b) Optimized electric fields shown in the central gray matter surface with the electrode montages overlaid.

Appendix D

SimNIBS 2.1: A Comprehensive Pipeline for Individualized Electric Field Modelling for Transcranial Brain Stimulation

Chapter 1

SimNIBS 2.1: A Comprehensive Pipeline for Individualized Electric Field Modelling for Transcranial Brain Stimulation

Guilherme B. Saturnino, Oula Puonti, Jesper D. Nielsen, Daria Antonenko, Kristoffer H. Madsen, and Axel Thielscher

1.1 Introduction

Non-invasive brain stimulation (NIBS) aims at modulating brain activity by inducing electric fields in the brain [1]. The electric fields are generated either by a magnetic coil, in the case of transcranial magnetic stimulation (TMS), or by a current source and electrodes placed directly on the scalp, in the case of transcranial electric stimulation (TES). In both cases, the induced electric fields in the brain have a complex and often counter-intuitive spatial distribution, which is dependent on the individual anatomy of a target subject. In recent years, there has been a growing interest in moving away from a one-size-fits-all stimulation approach in NIBS to more individually informed protocols [2]. The driving force behind this shift is the

Guilherme B. Saturnino and Oula Puonti contributed equally to this chapter.

G. B. Saturnino · A. Thielscher (✉)
Danish Research Centre for Magnetic Resonance, Centre for Functional and Diagnostic Imaging and Research, Copenhagen University Hospital Hvidovre, Hvidovre, Denmark

Department of Health Technology, Technical University of Denmark,
Kongens, Lyngby, Denmark
e-mail: axelt@drcmr.dk

O. Puonti
Danish Research Centre for Magnetic Resonance, Centre for Functional and Diagnostic Imaging and Research, Copenhagen University Hospital Hvidovre, Hvidovre, Denmark

J. D. Nielsen · K. H. Madsen
Danish Research Centre for Magnetic Resonance, Centre for Functional and Diagnostic Imaging and Research, Copenhagen University Hospital Hvidovre, Hvidovre, Denmark

Department of Applied Mathematics and Computer Science, Technical University of Denmark, Kongens, Lyngby, Denmark

D. Antonenko
Department of Neurology, Universitätsmedizin Greifswald, Greifswald, Germany

widely reported variation of NIBS effects within and between individuals [3], which could be explained in part by the interplay of the individual anatomy and the electric field propagation [4]. Although software tools have become available that generate realistic anatomical models of the head based on magnetic resonance imaging (MRI) scans and use those models to numerically estimate the electric field induced in the brain, they are still not predominantly used in NIBS studies. This is likely due to the lack of robustness and usability of the previous generation of tools, in turn hampering the individualized application of NIBS in both mapping the human brain function and as a rehabilitation tool in various neuropathologies [5, 6].

The aim of SimNIBS is to facilitate the use of individualized stimulation modelling by providing easy-to-use software tools for creating head models, setting up electric field simulations, and visualizing and post-processing the results both at individual and group levels. SimNIBS was first released in 2013 [7], had a major update in 2015, with the release of version 2 [2], and more recently another major update with the release of version 2.1, described in the current work. SimNIBS 2.1 is a free software, distributed under a GPL 3 license, and runs on all major operating systems (Windows, Linux and MacOS). In this tutorial, we will concentrate on **what** SimNIBS 2.1 can be used for and **how** the analyses are performed in practice with step-by-step examples. The chapter is structured as follows: First, we give a general overview of the simulation pipeline and of its building blocks. Next, we provide a step-by-step example of how to run a simulation in a single subject, and then we demonstrate a set of MATLAB tools developed for easy processing of multiple subjects. Finally, we conclude with an analysis of the accuracy of automated electrode positioning approaches. More information, as well as detailed tutorials and documentation can be found from the website www.simnibs.org.

1.2   Overview of the SimNIBS Workflow

Figure 1.1 shows an overview of the SimNIBS workflow for an individualized electric field simulation. The workflow starts with the subject's anatomical MRI images, and optionally diffusion-weighted MRI images. These images are segmented into major head tissues (white and grey matter, cerebrospinal fluid, skull and scalp). From the segmentations, a volume conductor model is created, and used for performing the electric field simulations. The simulations can be set up in a graphical user interface (GUI) or by scripting. Finally, the results can be mapped into standard spaces, such as the Montreal Neurological Institute (MNI) space or FreeSurfer's FsAverage.

1.2.1   Structural Magnetic Resonance Imaging Scans

The minimum requirement for running an individualized SimNIBS simulation is a T1-weighted structural scan of a subject's head anatomy. Although SimNIBS will run on almost all types of T1-weighted scans, we have found that setting the readout
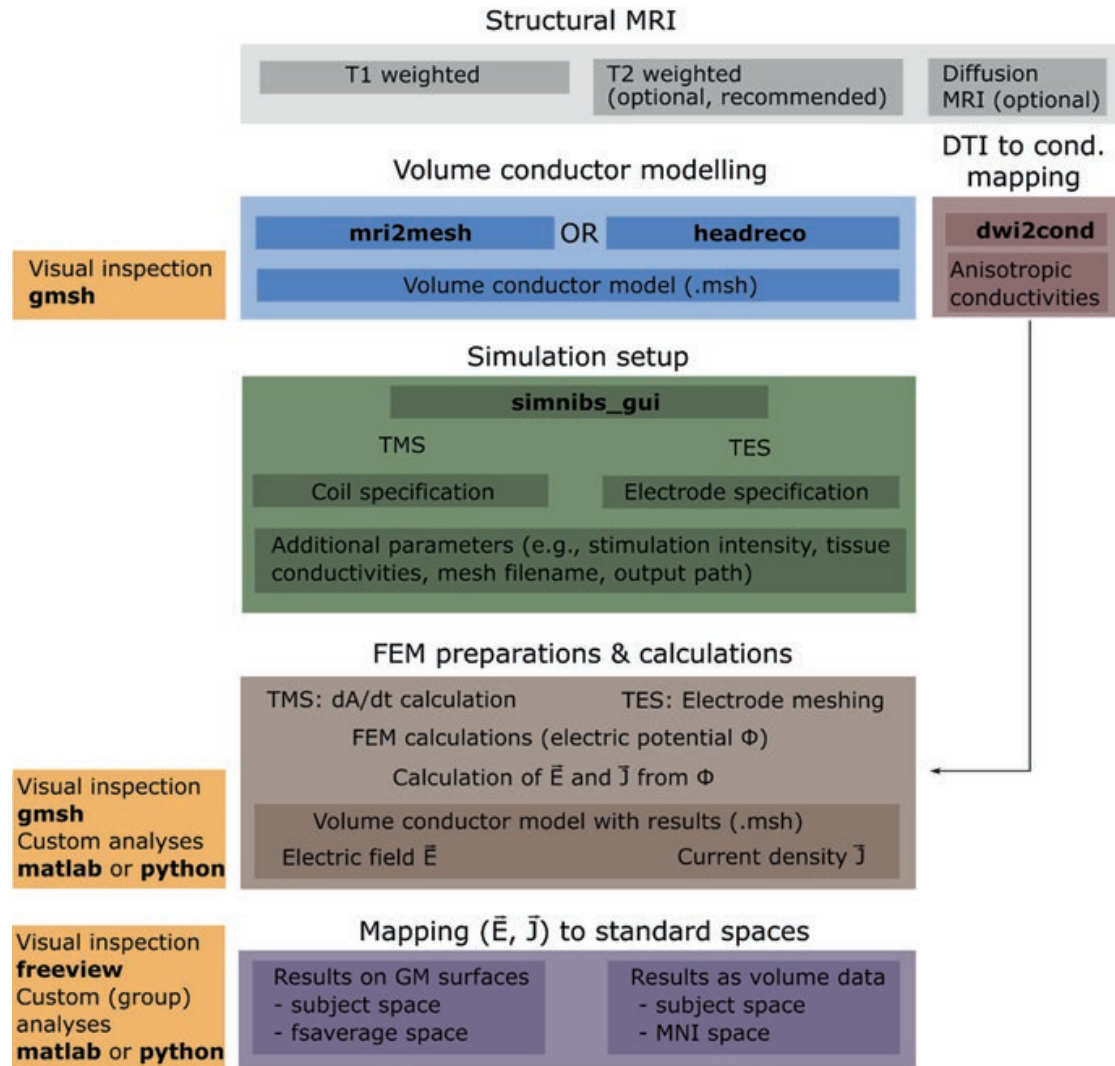
Fig. 1.1 Overview of the SimNIBS workflow

bandwidth low to ensure a good signal-to-noise ratio in the brain region and using a fat suppression method, such as selective water excitation, to minimize the signal from spongy bone, typically ensure a high quality of the resulting head models. See Fig. 1.2 for an example of good quality scans we found to work well with SimNIBS and [8] for the details of the sequences.

Including a T2-weighted scan is optional, but highly recommended as it facilitates accurate segmentation of the border between skull and cerebrospinal fluid (CSF). Both skull and CSF appear dark in T1-weighted scans, whereas in T2-weighted scans the CSF lights up, thus guiding the separation between the tissues. Skull has a low electric conductivity, while CSF is highly conducting, meaning that any segmentation errors in these two compartments can have a large effect on the resulting electric field distribution inside the head, especially when TES is applied [8]. If you are interested in modelling the neck region in detail, we recommend using neck coils if these are available at the imaging site.
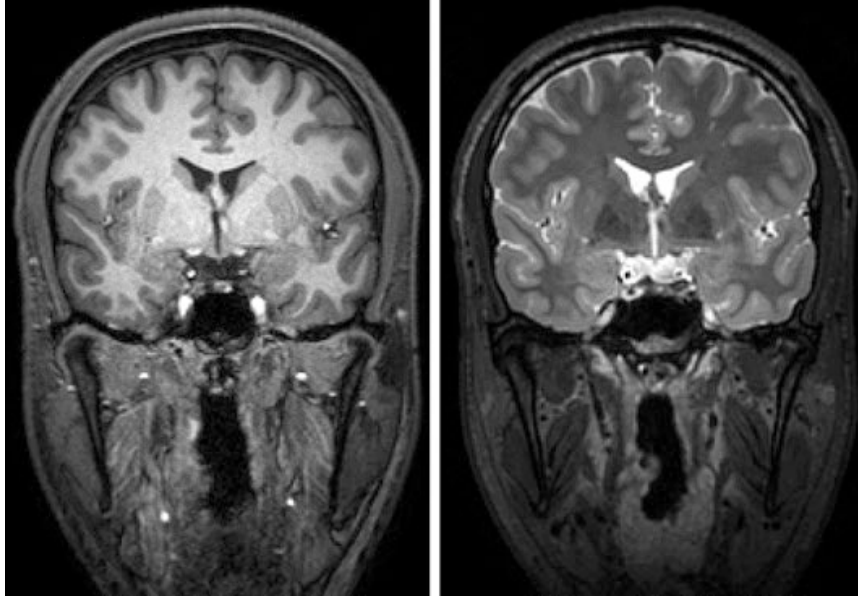
Fig. 1.2 Example of high-quality T1- and T2-weighted scans likely to work well with SimNIBS. Note that in the T1-weighted scan, the skull appears dark due to the fat suppression

Optionally, SimNIBS also supports modelling of anisotropic conductivities for grey (GM) and white matter (WM), which requires a diffusion-weighted MRI scan (dMRI). Only single shell data (i.e. with a single b-value in addition to some b = 0 images) with a single phase encoding direction for the echo planar imaging (EPI) readout is supported.

1.2.2   Volume Conductor Modelling

The first step in the pipeline is the generation of a volume conductor model of the head, which is needed for simulating the induced electric fields. In order to create this finite element (FEM) mesh, we need to assign each voxel in the MRI scan(s) to a specific tissue class, i.e. to segment the scan into the different head tissues. Currently, SimNIBS offers two options for segmentation: **mri2mesh** [7] and **head-reco** [8].

mri2mesh combines FSL [9] (version 5.0.5 or newer) and FreeSurfer [10] (version 5.3.0 or newer) to segment the head tissues. FSL is used to segment the extra-cerebral tissues, while FreeSurfer is used to segment the brain and to generate accurate surface reconstructions of the grey matter sheet. Note that **mri2mesh** is restricted only to the head and does not create models of the neck region.

headreco uses the SPM12 [11] toolbox for segmenting the MRI scan, and is now the recommended option in SimNIBS. It has been shown to be more accurate in segmenting the extra-cerebral structures, especially the skull, compared to **mri2mesh** [8], while also providing accurate segmentations of the brain tissues. The computational anatomy toolbox (CAT12, recommended) [12] provided with

SPM can be used to create surface reconstructions of the grey matter sheet which are on par with the accuracy of those generated by FreeSurfer [12]. In addition, **headreco** has an extended field of view, also modelling the neck region. For ease of use, both SPM12 and CAT12 are distributed together with SimNIBS.

Once the segmentation by either method has finished successfully, the tissue maps are cleaned by applying simple morphological operations, and used to create surface reconstructions. As a final step, the FEM mesh is generated by filling in tetrahedrons between the tissue surfaces using Gmsh [13].

Neither **mri2mesh** nor **headreco** have off-the-shelf support for pathologies such as tumours or lesions. These can however be included into the head models by manually editing the segmentation masks generated by the methods. When using **mri2mesh**, please consult the FreeSurfer website (https://surfer.nmr.mgh.harvard.edu/fswiki/FsTutorial/WhiteMatterEdits_freeview) on how to handle scans with pathologies. Manual edits using **headreco** should be done on the output segmentation masks in the *mask_prep* folder located within the *m2m_{subID}* folder. Once corrections have been made, the surface meshing step ("**headreco surfacemesh subID"**) and volume meshing step (**"headreco volumemesh subID"**) should be re-run to generate the edited head model. Note that when creating head models from scans with pathologies, the CAT12 toolbox should *not* be used.

dwi2cond (optional) uses FSL (version 5.0.5 or newer) to prepare diffusion tensors for GM and WM from dMRI data. The tensors are used by SimNIBS to estimate anisotropic conductivities in WM and GM during the FEM calculations.

1.2.3 Simulation Setup

Simulations can be set up using the graphical user interface (GUI), which provides an interactive view of the head model. This allows users to easily select parameters such as coil positions, electrode positions and shapes, as well as more advanced settings such as tissue conductivities and post-processing options.

It might also be of interest to do simulations of one or a few different setups across a group of subjects. With this in mind, version 2.1.1 introduced a new interface for setting up simulations using MATLAB or Python scripts.

The GUI as well as the scripts will be described in more detail in Sect. 1.3, as well as on the website www.simnibs.org.

1.2.4 Finite Element Method Calculations

Transcranial direct current stimulation (tDCS) simulations begin by adding electrodes to the head model. In this step, nodes in the skin surface are shifted to form the shape of the electrode, while keeping good quality elements. Afterwards, the body of the electrodes is constructed by filling in tetrahedra. As this step does

not require re-meshing the entire head, it can be done much more efficiently compared to other methods that require re-meshing, especially when only a few electrodes are used.

TMS simulations start by calculating the change in the magnetic vector potential A, that is the dA/dt field in the elements of the volume conductor mesh for the appropriate coil model, position and current. There are currently two types of coil models:

.ccd files: Created from geometric models of the coil and represented as a set of magnetic dipoles from which we can calculate the dA/dt field using a simple formula [14].

.nii files: Created either from geometric models of the coils or direct measurement of the magnetic field [15]. Here, the dA/dt field is defined over a large volume, and the calculation of the dA/dt at the mesh elements is done via interpolation. This allows for faster simulation setup at little to no cost in simulation accuracy.

Both simulation problems are solved using the FEM with linear basis functions. This consists of constructing and solving a linear system of the type $Mu = b$, where M is a large (in SimNIBS typically $\sim 10^6 \times 10^6$) but sparse matrix, called the "stiffness matrix", u are the electric potentials at the nodes and the right-hand side b contains information about boundary conditions (such as potentials in electrode surfaces in tDCS simulations), and source terms (such as the dA/dt field in TMS simulations). SimNIBS solves the linear system using an iterative preconditioned conjugate gradient method [16]. SimNIBS 2.1 uses GetDP [17] to form the linear system, which in turn calls PETSc [18] to solve it.

TDCS simulations can also be easily extended to simulations of transcranial alternating current stimulation (tACS). In the frequency ranges used in tACS, a quasi-static approximation holds [19]. In the quasi-static approximation, the relationship between input currents $I(t)$ and the electric field at the positions x, $E(x)$ is linear:

$$E(x,t) = \alpha(x)I(t)$$

where $\alpha(x)$ is a proportionality constant, meaning that it does not vary during the oscillation. This constant can be obtained simply by running a simulation where we set the input current to unity. $I(t)$ is the input current. For example, a sinusoidal current input can be written as

$$I(t) = I_o \sin\left(2\pi\, t/f + \phi\right)$$

where f is the stimulator frequency, ϕ the stimulator phase and I_o the stimulator amplitude, which corresponds to half of the peak-to-peak current. Usually, we would visualize the electric field at the maximum or minimum of $I(t)$, which

corresponds to $\pm I_o$. In case several stimulators are used at different frequencies of phases, we have several pairs $(\alpha_i(x)I_i(t))$, one for each stimulator, and the total electric field at a given time point is given by the sum of their individual contributions

$$E(x,t) = \sum_{i=1}^{n} \alpha_i(x) I_i(t)$$

1.2.5 Mapping Fields

The result of the FEM calculation is the electric field at each tetrahedral element of the subject's head mesh. However, visualization is often easier using cortical surfaces or NifTI volumes. Therefore, SimNIBS 2.1 can transform fields from the native mesh format to these formats via interpolation. Our interpolation algorithm is based on the superconvergent patch recovery method [20], which ensures interpolated electric field values that are consistent with tissue boundaries.

When performing simulations on multiple subjects, we often want to be able to directly compare the electric field across subjects to, for example, correlate the electric field with behavioural or physiological data on the stimulation effects [21]. For this purpose, SimNIBS can also transform simulation results to the MNI template, using linear and non-linear co-registrations, as well as to the FreeSurfer's FsAverage surface.

1.3 Practical Examples and Use Cases

1.3.1 Hello SimNIBS: How to Process a Single Subject

Here we describe how to run a TMS and a tDCS simulation on a single example subject. The example subject "Ernie" can be downloaded from the SimNIBS website, and the steps below can be reproduced step by step to get familiar with SimNIBS.

Generating the Volume Conductor Model

Open a terminal and go to the directory "ernie" to access the example data set. Copy the content of the "org"-subfolder to another location in order to not overwrite the files of the original example dataset. Next, go to the folder where you copied the data, and call headreco to generate the volume conductor model:

headreco all --cat ernie ernie_T1.nii.gz ernie_T2.nii.gz

In the command, the first argument, "**all**", tells headreco to run all reconstruction steps including: segmentation, clean-up of tissue maps, surface meshing, and volume meshing. The second argument, "**--cat**" is a flag for using the CAT12 toolbox for accurate reconstruction of the cortical surface. The third argument, "**ernie**", is a subject identifier (subID), which is used to name generated folders, e.g. m2m_ernie, and output files, e.g. ernie.msh. The two final arguments are the paths to the T1- and T2-weighted structural scans.

A few extra input options are useful to know:

-d no-conform Adding this option will prevent headreco from modifying, i.e. transforming and resampling, the original MRI scan. This might be desirable when a one-to-one correspondence between the head model coordinates and the neural navigation system coordinates is required.

-v < density > This option allows you to set the resolution, or vertex density (nodes per mm^2), of the FEM mesh surfaces. By default, SimNIBS uses 0.5 nodes/mm^2 as the **<density >** value.

In general, we recommend using the **--cat** option; however, the execution time will be longer compared to omitting the option. In addition, if you want to process scans with pathologies, you should not use CAT12, as the cortical reconstruction is not designed to work with pathologies.

After **headreco** has finished, please check the quality of the head model by calling:

headreco check ernie

If needed, open a new terminal for this operation and go into the folder in which you started headreco the first time. For our example case, the subject identifier is "ernie", but please replace this one with whichever subID was used in the first call to **headreco**. Note that we recommend that you have installed freeview (provided by FreeSurfer, available on Linux and Mac OS X platforms) to visualize the results. The **check** function displays two windows for inspecting the output. The first window shows the T1-weighted scan with the segmentation and structure borders overlaid (Fig. 1.3, left). We recommend de-selecting the segmentation (**ernie_final_contr. nii**) in freeview, and checking that the segmentation borders follow the intensity gradients of different tissues (Fig. 1.3, middle). Fig. 1.4 shows the second freeview window, which displays the T1-weighted scan co-registered to the MNI template. We recommend checking if the T1-weighted scan overlaps well with the MNI template by de-selecting the T1-weighted scan (**T1fs_nu_nonlin_MNI.nii**) in freeview (Fig. 1.4, right). Figure 1.5 shows an example of a segmentation error where the skull is erroneously labelled as skin. This can be seen in the front of the head, where the skin label protrudes into the skull. This example emphasizes the need for fat-suppressed data when only a T1-weighted scan is used. In the scan shown in Fig. 1.5, spongy bone is bright with intensities comparable to those of scalp, causing the segmentation method to mis-classify it as extra-cerebral soft tissue. Small segmen-
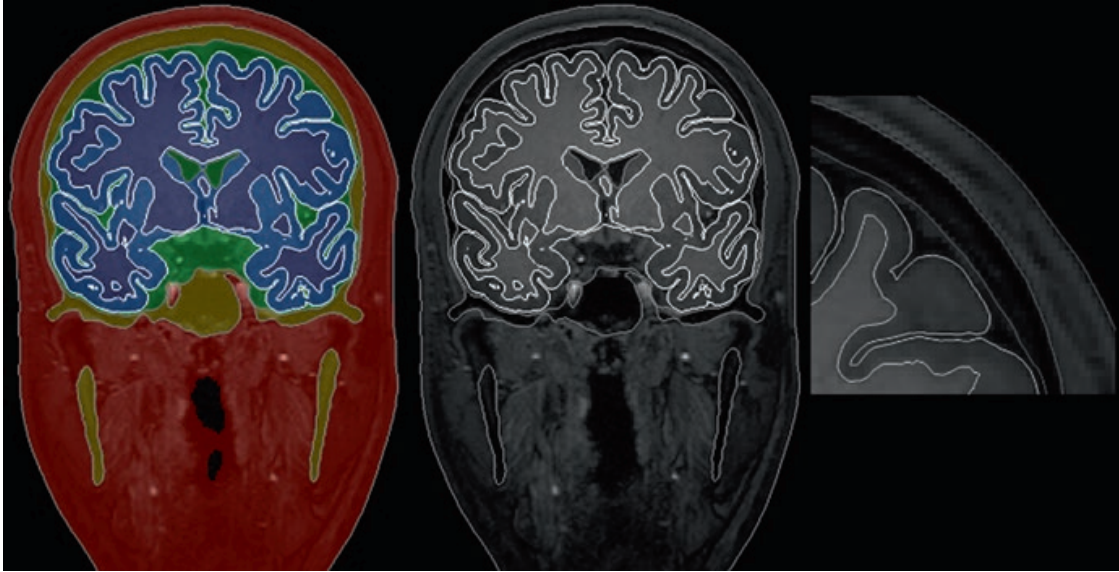
Fig. 1.3 Data displayed after calling the **check** option. Left: T1-weighted scan with the segmentation and structure borders overlaid. Middle: structure borders overlaid on the T1-weighted scan after de-selecting the segmentation in freeview. Right: zoom-in of the cortex. Note that the segmentation borders nicely follow the intensity borders between the tissues
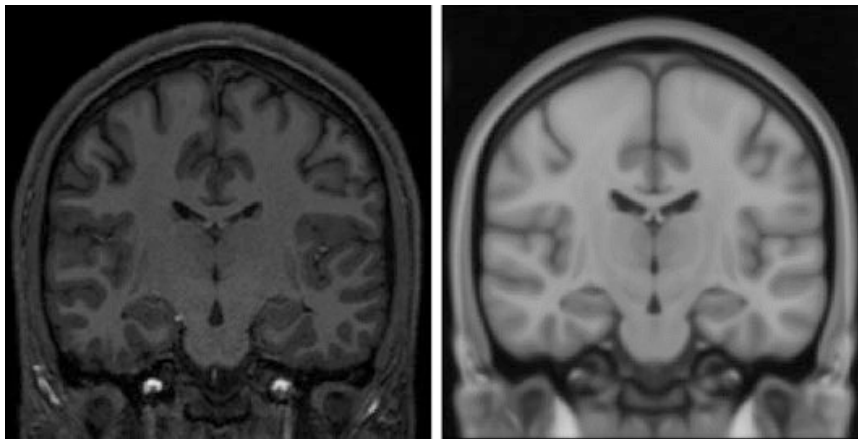

Fig. 1.4 Data displayed after calling the **check** option. Left: T1-weighted scan co-registered to the MNI template. Right: MNI template shown after de-selecting the T1-weighted scan in freeview. Note that the scans seem to be well registered

tation errors like this can be corrected by manually re-labelling the segmentation masks in the "*mask_prep*" folder located in the *m2m_{subID}* folder, and re-running the surface and volume meshing steps. If you are not familiar with using freeview, please refer to the tutorial on the SimNIBS website (*http://www.simnibs.org/_media/ docu2.1.1/tutorial_2.1.pdf*). If you do not have access to freeview, the visualizations will be displayed using SPM. However, these are very primitive and are not recommended for checking the output from **headreco**.
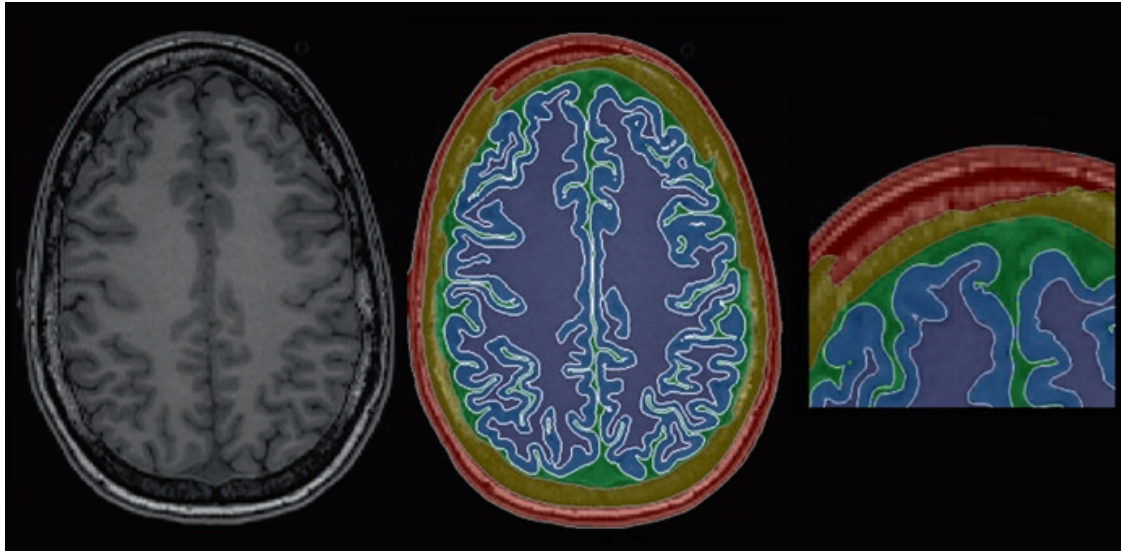
Fig. 1.5 Example of a segmentation error after headreco processing. The spongy bone is errone-ously labelled as skin. This example emphasizes the need for fat-suppression when using only a T1-weighted scan

Finally, you should inspect the volume conductor mesh for any obvious errors. This can be done by calling:
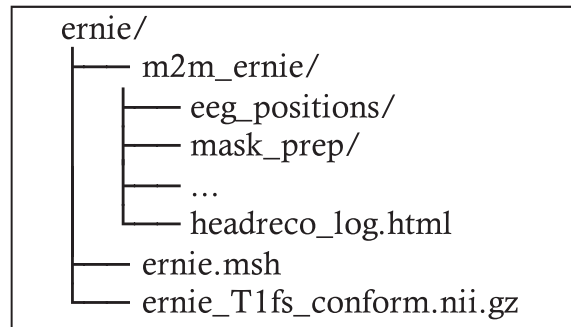
<div align="center">**gmsh ernie.msh**</div>

in the subject folder. This call opens a gmsh window displaying the generated head model; please see the tutorial on the website if you are not familiar with gmsh (*http://www.simnibs.org/_media/docu2.1.1/tutorial_2.1.pdf*).

The folder structure and most important files are shown in Table 1.1.

- *eeg_positions/* Folder containing the 10-10 electrode positions for the subject both as a ".*csv*", used for acquiring electrode positions, and a ".*geo*" file, used for visualization of the positions in Gmsh. If you have custom electrode positions, they should be added here as a .csv file.
- *mask_prep/* Folder containing the cleaned tissue maps along with the white mat-ter and pial surface files if CAT12 was used. In case there are errors in the seg-mentation, the masks can be manually corrected and a new head model can subsequently be generated. Note that the CAT12 WM and GM surfaces can cur-rently not be modified.
- *headreco_log.html*, a log-file with output from the **headreco** run. If something goes wrong, the log-file helps with troubleshooting, and should be sent as an attachment when contacting the SimNIBS support email list (support@simnibs. org).
- *ernie.msh*, the FEM head model used for the simulations.
- *ernie_T1fs_conform.nii.gz*, the input scan in the conform space defined by the –d option. This scan has the same millimetre space as the head model, and can be used to annotate landmarks which can then be directly transformed onto the head model.

Table 1.1 The folder structure after **headreco** has finished. In this table, only the most important folders and files are listed

```
ernie/
├── m2m_ernie/
│     ├── eeg_positions/
│     ├── mask_prep/
│     ├── …
│     └── headreco_log.html
├── ernie.msh
└── ernie_T1fs_conform.nii.gz
```

Setting Up a Simulation

Once the head model is ready, we can set up tDCS and TMS simulations interactively using the GUI. The GUI can be started on the command line by calling:

simnibs_gui

In the GUI, the user can:

- Visualize and interact with head models.
- Define electrode and coil positions by clicking in the model or selecting a position from the EEG 10-10 system.
- Visually define electrode shapes and sizes.
- Select from the available coil models.
- Change tissue conductivity parameters and set up simulations with anisotropic conductivity distributions.
- Run simulations.

In the GUI, there are two types of tabs, one for tDCS simulations, and another for TMS simulations, shown respectively in the top and bottom of Fig. 1.6. The tDCS tabs define a single tDCS field simulation with an arbitrary number of electrodes. On the other hand, TMS tabs can define several TMS field simulations using the same coil. For this example, we will set up a tDCS simulation with a 5 × 5 cm anode placed over C3 and a 7 × 5 cm cathode placed over AF4, and a TMS simulation with the coil placed over the motor cortex, pointing posteriorly. Details on how to use the graphical interface can be found on the website (*http://www.simnibs.org/_media/ docu2.1.1/tutorial_2.1.pdf*).

After the simulation setup, click on the **Run** button to start the simulations. Running both simulations takes 10–15 minutes, depending on the computer, and uses around 6 GB of memory. As a note, before starting the simulations, you can set additional options (in the menu Edit➜Simulation Options) to let SimNIBS write out the results as surface data or NifTI volume data. This is not further covered in this basic example, but the output files created in these cases are described in the next example. The results of the simulation will be written in the output folder specified in the GUI, in this case "*simnibs_simulation/*". The folder has the files shown below in Table 1.2.

Fig. 1.6 Set-up of a tDCS (top) and a TMS (bottom) simulation in the graphical user interface
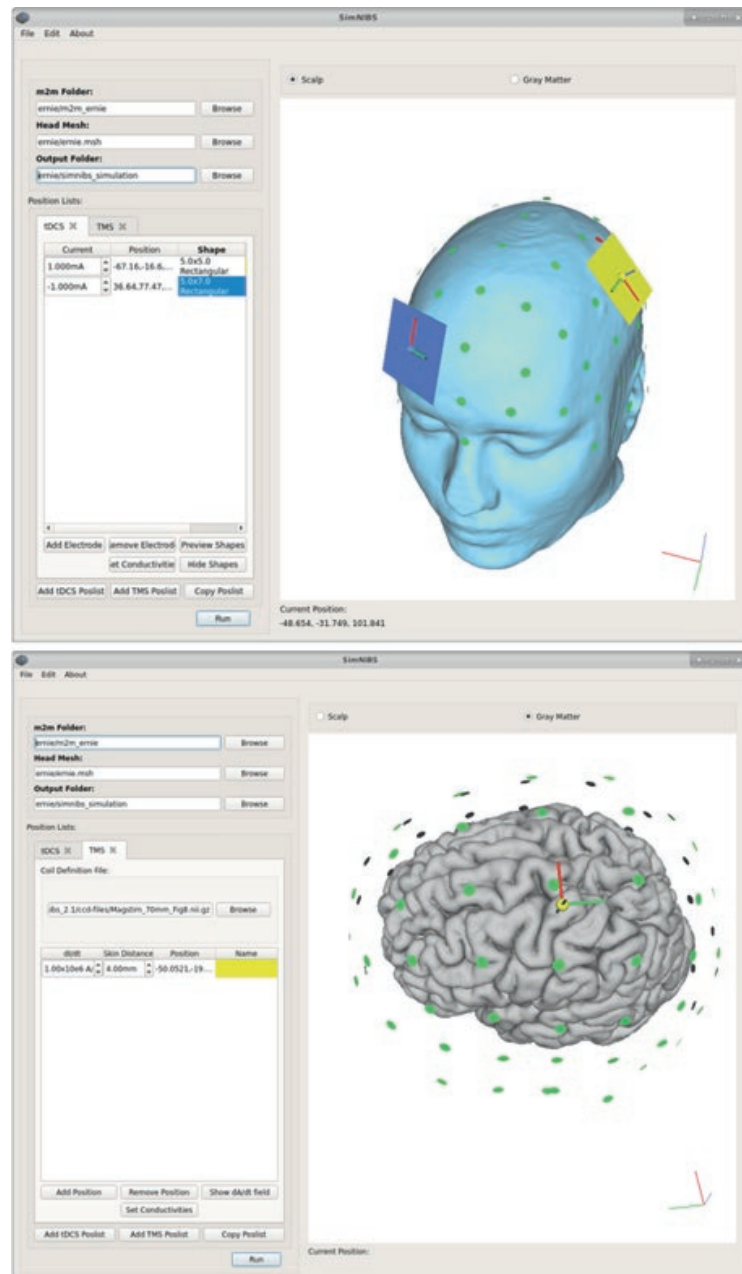

Table 1.2 The output folder of a simple tDCS and TMS simulation

```
simnibs_simulation/
    ├── ernie_TDCS_1_scalar.msh
    ├── ernie_TMS_2-0001_Magstim_70mm_Fig8_nii_scalar.msh
    ├── ernie_TMS_2-0001_Magstim_70mm_Fig8_nii_coil_pos.geo
    ├── simnibs_simulation_20180920-130401.log
    └── simnibs_simulation_20180920-130401.mat
```

- "*ernie_TDCS_1_scalar.msh*" is the output from the tDCS simulation, in Gmsh ".*msh*" format. The first part of the file name, "*ernie*", is the subID. The second part, "*TDCS*", informs us that this is a tDCS simulation. The third part, "*1*", denotes that this was the first simulation we have defined in the GUI, and finally, "*scalar*" tells us have used scalar (as opposed to anisotropic) conductivities for the simulations.
- "*ernie_TMS_2-0001_Magstim_70mm_Fig8_nii_scalar.msh*" is the output of the second simulation, also in gmsh ".*msh*" format. As is the case for the tDCS output, the first part of the file name is the subID, and the second is the number of the simulation in the simulation list. We next see the number of the TMS position, as it might happen that several TMS positions are defined in a single TMS list. Following this, "*Magstim_40mm_Fig8_nii*" gives us the name of the coil used for the simulation, and "*scalar*" the type of conductivity.
- "*ernie_TMS_2-0001_Magstim_70mm_Fig8_nii_coil_pos.geo*" is a Gmsh ".*geo*" file which shows the coil position for the corresponding simulation.
- "*simnibs_simulation_20180920-13041.log*" is a text file with a detailed log of the simulation steps. This file can be used for troubleshooting. Here, the second part of the file is date and time information of when the simulation started.
- "*simnibs_simulation_20180920-13041.mat*" is a MATLAB data file with the simulation setups. This file can be loaded into the GUI or MATLAB at a later time to check the simulation parameters, or to change them and re-run the simulation.

Visualizing Fields

The electric field **E** is a vector field meaning that the electric field has both a norm (i.e. vector length or magnitude) and a direction in space, as shown in Fig. 1.7. As visualizations of the entire vector are challenging and often unclear, in SimNIBS we
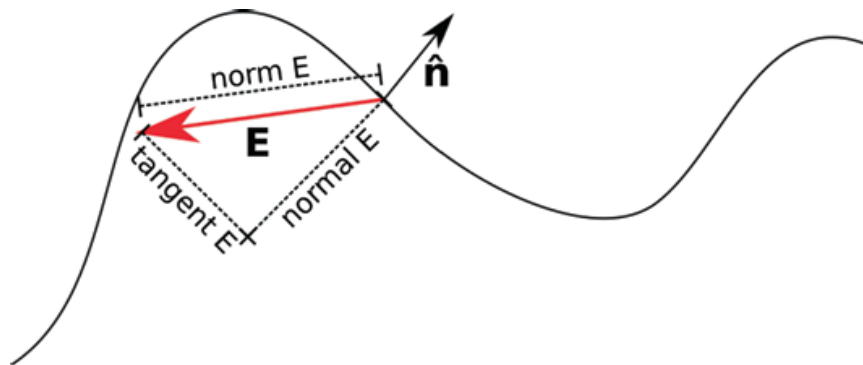

Fig. 1.7 Decomposition of a vector **E** in relation to a surface. The norm corresponds to the length of the vector. At each point, the surface defines a normal vector **n̂ ,** and this vector is perpendicular to the tangent plane to the surface at that point. Given the normal vector, we can decompose the vector **E** into normal and tangent components. The normal component is the part of **E** in the same line as the normal vector, and the tangent component is perpendicular to it. The normal component also has a sign, indicating if the field is entering or leaving the surface. In SimNIBS, a positive normal indicates that the field is entering the surface, and a negative normal indicate the field is leaving the surface

usually visualize the **norm** (or strength) of the electric field instead. The norm of the electric field corresponds to the size of the electric field vector, and therefore is always positive and does not contain any information about the direction of the electric field.

One way we can quickly visualize the simulation results is to use the **mesh_ show_results** MATLAB function. This function comes as a part of SimNIBS version 2.1.2, and provides visualizations of the output fields using MATLAB plotting tools, as well as some summary values for the field strength and focality. For example, when running the function on the output tDCS mesh, we obtain the plot shown in Fig. 1.8a, and the values below in Table 1.3.

The first lines in Table 1.3 show that the displayed data is the field "norm E", that is the norm or strength of the electric field, calculated in the region number 2, which corresponds to the GM volume. Afterwards, we have information on the peak electric fields. We see that the value of 0.161 V/m corresponds to the 95th percentile of the norm of the electric field, the value of 0.201 V/m to the 99th percentile and 0.249 to the 99.9th percentile. We also have information about the focality of the
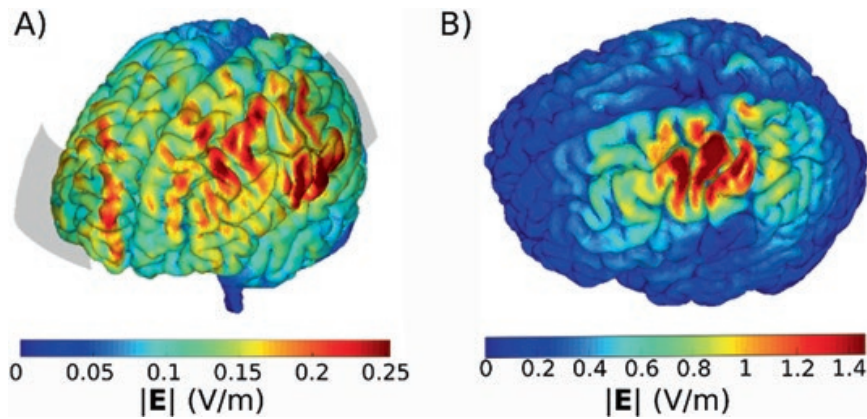

Fig. 1.8 Visualization of (**a**) tDCS and (**b**) TMS electric field norms in MATLAB

Table 1.3 Output of **mesh_show_results** for the tDCS simulation

```
----------------------------------------------
SUMMARY
field name: normE
region indices: 2

peak fields
percentiles:     95        99      99.9
values:         0.161     0.201     0.249  (in [V/m])

focality
cutoffs:         50       75 (in % of 99.9 percentile)
values:        1.4e+05   1.29e+04  (in cubic mm)
----------------------------------------------
```

electric field. Here, focality is measured as the GM volume with an electric field greater or equal to 50% or 75% of the peak value. To avoid the effect of outliers, the peak value is defined as the 99.9th percentile.

Running the same function on the TMS result file, we obtain the plot shown in Fig. 1.8b, as well as the peak fields and focality measures shown below in Table 1.4.

We can see that the peak fields for TMS are much higher than for tDCS, even though we simulated with a current of 10^6 A/s, very low for TMS. In the focality measures, we see that the TMS electric fields are much more focal than the tDCS electric fields, with around five times less GM volume exceeding 75% of the peak value than tDCS.

Additionally, the "*.msh*" files can be opened with the Gmsh viewer, producing 3D visualizations as shown in Fig. 1.9. Gmsh has a vast range of functionalities, such as clipping planes, but can be harder to use than **mesh_show_results**.

Table 1.4 Output of **mesh_show_results** for the TMS simulation

```
-----------------------------------------
SUMMARY
field name: normE
region indices: 2

peak fields
percentiles:    95      99      99.9
values:        0.446   0.849    1.41  (in [V/m])

focality
cutoffs:       50      75  (in % of 99.9 percentile)
values:       1.28e+04  3.32e+03  (in cubic mm)
-----------------------------------------
```
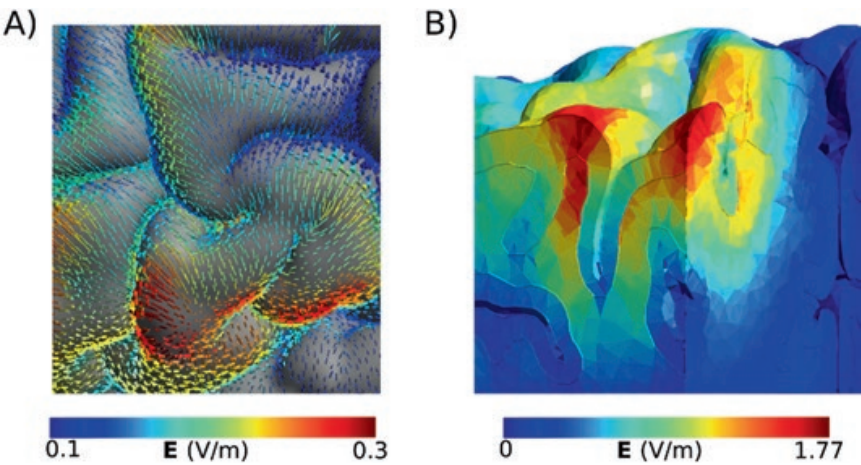

Fig. 1.9 Visualization in Gmsh of (**a**) electric field vectors around central gyrus for the tDCS simulation and (**b**) TMS electric field depth profile in the hotspot

1.3.2   Advanced Usage: Group Analysis

Now, we want to simulate one tDCS montage, with a 5 × 5 cm electrode over C3 and a 5 × 7 cm electrode over AF4 in five subjects, called "sub01", "sub09", "sub10", "sub12", "sub15" and visualize the results in a common space, namely the FsAverage surface. The subjects and example scripts can be downloaded from: https://osf.io/ah5eu/

Head Meshing

For each subject, follow the steps in section "Generating the Volume Conductor Model".

Write a Python or MATLAB Script

We can set up the simulation of each subject using the GUI, as described in the first example. However, when working with multiple subjects, it can be advantageous to script the simulations for efficiency. SimNIBS provides both MATLAB and Python interfaces to set up simulations. Script 1.1 shows how to set up and run a simulation with a 5 × 5cm anode placed over C3 and a 7 × 5cm cathode placed over AF4 for all subjects. The output of Script 1.1 for sub01 is shown in Table 1.5.
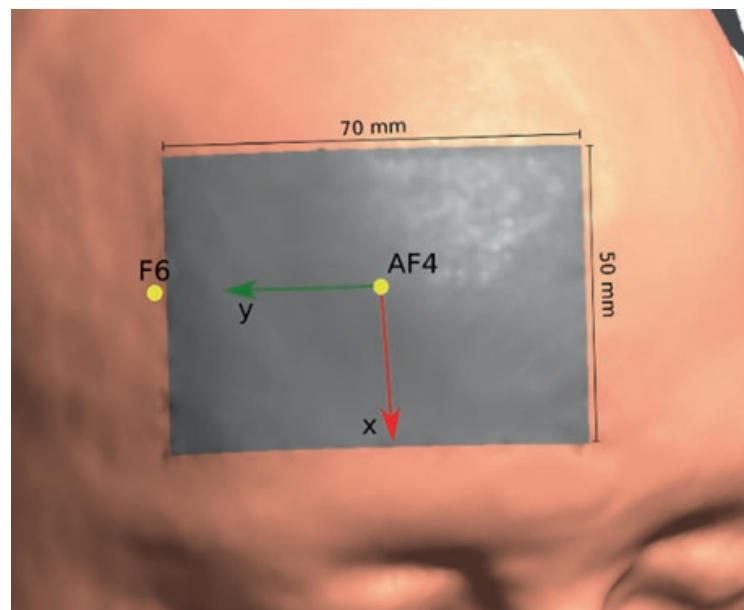
To define the rectangular electrodes, we need two coordinates. The "*centre*" defines where the electrode will be centred, and "*pos_ydir*" how the electrode will be rotated. More precisely, the electrode's "y" axis is defined as a unit vector starting at "centre" and pointing towards "*pos_ydir*". Fig. 1.10 shows one of the cathodes (return electrode) defined using the script above, with the coordinate system and EEG positions overlaid. We can see that the electrode is centred in AF4, and its Y axis points towards F6. "*pos_ydir*" does not need to be set when the electrodes are round.

When the *map_to_fsavg* option is set to *true*, SimNIBS computes the electric fields in a surface located in the middle of the GM layer. This cortical surface, along with the norm, normal and tangent components of the electric field at the cortical surface and the angle between the electric field and the cortical surface can found in the *subject_overlays* folder, for both the left hemisphere (*lh*) and for the right hemisphere (*rh*) as shown in Table 1.5. Afterwards, these quantities are transformed into the FsAverage space. The transformed quantities can be found in the *fsavg_overlays* folder, as shown in Table 1.5. Additionally, we have the electric field and its norm in MNI space in the *mni_volumes* folder.

Table 1.5 Output files and folders of Script 1 for sub01. The ".angle", ".norm",.. files are FreeSurfer overlay files and the ".central" files are FreeSurfer surface files

```
bipolar/
├── fsavg_overlays
│       ├── lh.sub01_TDCS_scalar.fsavg.E.angle
│       ├── lh.sub01_TDCS_scalar.fsavg.E.norm
│       ├── lh.sub01_TDCS_scalar.fsavg.E.normal
│       ├── lh.sub01_TDCS_scalar.fsavg.E.tangent
│       ├── rh.sub01_TDCS_scalar.fsavg.E.angle
│       └── …
├── mni_volumes
│       ├── sub01_TDCS_scalar_MNI_E.nii.gz
│       └── sub01_TDCS_scalar_MNI_normE.nii.gz
├── simnibs_simulation_20181019-100530.log
├── simnibs_simulation_20181019-100530.mat
└── subject_overlays
        ├── lh.central
        ├── lh.sub01_TDCS_scalar.central.E.angle
        ├── lh.sub01_TDCS_scalar.central.E.norm
        ├── lh.sub01_TDCS_scalar.central.E.normal
        ├── …
        ├── rh.central
        ├── rh.sub01_TDCS_scalar.fsavg.E.angle
        └── …
```


Fig. 1.10 50 × 70 mm electrode defined with a "centre" in AF4 and a "pos_ydir" in F6

```matlab
path_to_headmodels = "/path/to/head/models/";
subjects = ["sub01", "sub09", "sub10", "sub12", "sub15"];
results_folder = "bipolar/fsavg_overlays";

normals = {};
for i = 1:length(subjects)
    sub = subjects(i);
    % Load normal field data
    normal_surf = sprintf('lh.%s_TDCS_1_scalar.fsavg.E.normal', sub);
    m = mesh_load_fsresults(char(...
        fullfile(path_to_headmodels, sub, results_folder, normal_surf)));
    % Add to cell
    normals{i} = m.node_data{1}.data;
end
% Calculate average and standard deviation of the normal at each node
normals = cell2mat(normals);
avg_normal = mean(normals, 2);
std_normal = std(normals, 0, 2);
% Place the fields in the mesh structure
m.node_data{1}.data = avg_normal;
m.node_data{1}.name = 'E.normal.avg';
m.node_data{2}.data = std_normal;
m.node_data{2}.name = 'E.normal.std';
% Plot the fields
mesh_show_surface(m, 'field_idx', 'E.normal.avg')
mesh_show_surface(m, 'field_idx', 'E.normal.std')
```

Script 1.1 Script for running a tDCS simulations with an anode over C3 and a cathode over AF4 in five subjects and transforming the results to FSAverage and MNI spaces.

```matlab
path_to_headmodels =  "/path/to/head/models/" ;
subjects = ["sub01", "sub09", "sub10", "sub12", "sub15"];
results_folder =  "bipolar/fsavg_overlays" ;

normals = {};
for i = 1:length(subjects)
    sub = subjects(i);
    % Load normal field data
    normal_surf = sprintf( 'lh.%s_TDCS_1_scalar.fsavg.E.normal' , sub);
    m = mesh_load_fsresults(char( ...
        fullfile(path_to_headmodels, sub, results_folder, normal_surf)));
    % Add to cell
    normals{i} = m.node_data{1}.data;
end
% Calculate average and standard deviation of the normal at each node
normals = cell2mat(normals);
avg_normal = mean(normals, 2);
std_normal = std(normals, 0, 2);
% Place the fields in the mesh structure
m.node_data{1}.data = avg_normal;
m.node_data{1}.name =  'E.normal.avg' ;
m.node_data{2}.data = std_normal;
m.node_data{2}.name =  'E.normal.std' ;
% Plot the fields
mesh_show_surface(m,  'field_idx' , 'E.normal.avg' )
mesh_show_surface(m,  'field_idx' , 'E.normal.std' )
```

Script 1.2 Analysis of simulation results in FSAverage space.

Visualizing Results

We can also make use of the MATLAB library within SimNIBS to analyze the results from the simulations. Here, we are interested in the average and standard deviation of the normal component of the electric field in the cortex. The normal component, as shown in Fig. 1.7, is the part of the electric field which is either entering or leaving the cortex.

Script 1.2 loads the normal field component data for each subject and calculates the mean and the standard deviation across subjects at each position of the FsAverage template. The fields are then visualized using MATLAB visualization tools. The results are shown in Fig. 1.11. We can, for example, see strong current in-flow in the central gyrus, and large variations in the normal component in frontal regions.

1.4   The Accuracy of Automatic EEG Positioning

Here, we compare EEG 10-10 positions obtained either from:

A. Transforming EEG 10-10 electrode positions defined in MNI space to the subject space using a non-linear transform, and then projecting the positions to the scalp. This is done for both **mri2mesh** and **headreco** head models.
B. Manually locating the fiducials: left pre-auricular point (LPA), right pre-auricular point (RPA), nasion (Nz) and inion (Iz) on MRI images, and afterwards calculating the EEG positions using the definitions in [22].

Calculations using method A require no user input and are automatically performed in both **mri2mesh** and **headreco** head modelling pipelines, while calculations using method B require the user to manually select the fiducial positions.
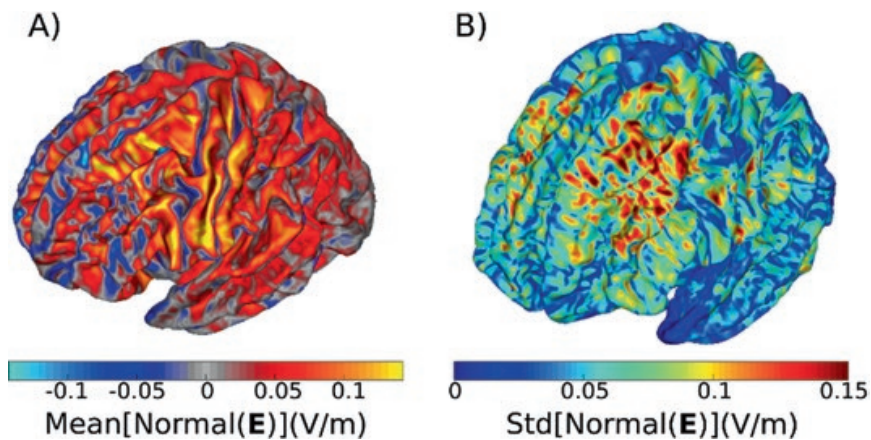

Fig. 1.11 (**a**) Mean and (**b**) Standard deviation of the normal field component across 5 subjects. The fields were caused by tDCS with an anode over C3 and a cathode over AF4. Positive values in (**a**) denote inflowing currents, and negative values outflowing currents

To compare the methods A and B to position the electrodes, we calculated the EEG 10-10 positions using both ways for MR data of 17 subjects. The data was acquired as part of a larger study. The subjects gave written informed consent before the scan, and the study was approved by the local ethics committee of the University of Greifswald (Germany). The 17 datasets were acquired on a 3-Tesla Siemens Verio scanner (Siemens Healthcare, Erlangen, Germany) using a 32-channel head coil (T1: $1 \times 1 \times 1$ mm^3, TR 2300 ms, TE 900 ms, flip angle 9°, with selective water excitation for fat suppression; T2: $1 \times 1 \times 1$ mm^3, TR 12770 ms, TE 86 ms, flip angle 111°). For method B, the fiducials were manually located for each subject by a trained investigator on the T1- and T2-weighted images. The later had no knowledge of the automatically determined positions. The fiducials Nz, Iz, LPA and RPA were set in freeview, following the procedure described in [22] and additionally verified using the SimNIBS GUI. The subject-specific coordinates of the fiducials were extracted, and these manually set positions were then compared with those calculated by the automatic algorithm in each individual.

Table 1.6 shows the maximal distance across all subjects between the fiducials obtained using method A and manually selected fiducials (B). We see that Nz is the most consistent fiducial, where we have the least deviation, whereas Iz is where we have the highest deviation. Also, the maximal difference in position across the two methods is ~1 cm, indicating that method A works well to approximate the positions of the fiducials.

Furthermore, in Fig. 1.12, we compare the two methods for all electrode positions in the EEG 10-10 system. The deviation in positioning each electrode was calculated as the mean of the distance between the positions obtained with either headreco or mri2mesh to the manually located fiducial positions, across all 17 subjects and for each electrode.

The errors for all electrodes are below 1 cm, indicating that the two algorithms for placing EEG electrodes are in agreement. We can also see that the errors in the EEG positions obtained from **headreco** are on average lower than the ones obtained from **mri2mesh**. It also seems that the anterior electrodes have less errors than the posterior electrodes. Interestingly, the location of the errors is different across the two pipelines, with **mri2mesh** being more inaccurate in superior regions and **headreco** more inaccurate in posterior regions. This might be caused by differences in the way FSL (**mri2mesh**) and SPM (**headreco**) calculate non-linear MNI transfor-

Table 1.6 Maximum and mean distance between the fiducial positions selected by hand and obtained from the MNI transformations across 17 subjects, for the two head modelling pipelines

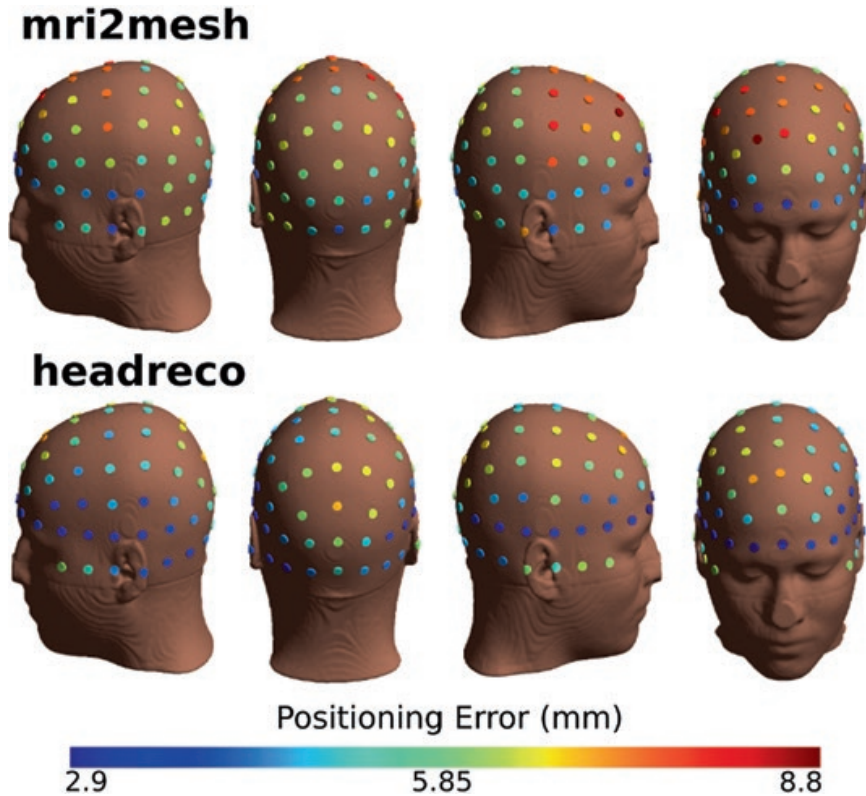| Fiducial	mri2mesh		headreco	
	Max distance (mm)	Mean distance ± standard deviation (mm)	Max distance (mm)	Mean distance ± standard deviation (mm)
LPA	6.4	3.2 ± 1.5	8.7	5.4 ± 2.0
RPA	8.9	3.0 ± 1.6	10.6	5.9 ± 1.7
Nz	3.9	2.1 ± 1.0	6.0	3.9 ± 1.6
Iz	14.3	4.0 ± 3.5	13.2	5.2 ± 3.3

Fig. 1.12 Positioning error for electrodes in the EEG 10-10 system. The error is calculated by comparing the positions calculated based on manually selected fiducials to positions calculated based on non-linear MNI transformations

mations is different. The average error across all positions was 5.6 mm for **mri2mesh** head models and 4.9 mm for **headreco** head models indicating good accuracy.

1.5   Conclusion

We presented SimNIBS 2.1 (www.simnibs.org), a software for individualized modelling of electric fields caused by non-invasive brain stimulation. SimNIBS is free software and avaliable for all major platforms. SimNIBS does not require the installation of any additional software in order to run simulations on the example dataset. To construct head models, SimNIBS relies either on MATLAB, SPM12 and CAT12 (**headreco**) or on FSL and FreeSurfer (**mri2mesh**).

We also presented two examples of workflows in SimNIBS. In the first example, we started by using **headreco** to construct a head model. Following this, we used the GUI to set up a tDCS and a TMS simulation in an interactive way, and finally visualized the results. In the second example, we constructed several head models and used a MATLAB script to run simulations for each subject. We then calculated the mean and the stardard deviation of the electric field norm across all subjects, using the FreeSurfer's FsAverage brain template. Finally, we show results validating our automatic procedure to obtain electrode positions for the EEG 10-10 system.

SimNIBS is still being actively developed, and we expect further updates to be implemented in the future.

References

1. Fregni, F., & Pascual-Leone, A. (2007). Technology insight: Noninvasive brain stimulation in neurology – Perspectives on the therapeutic potential of rTMS and tDCS. *Nature Clinical Practice Neurology, 3*(7): 282–393

2. Thielscher, A., Antunes, A., and Saturnino, G. B.. (2015). Field modeling for transcranial magnetic stimulation: A useful tool to understand the physiological effects of TMS? In *Proc. Annu. Int. Conf. IEEE Eng. Med. Biol. Soc. EMBS* (pp. 222–225).

3. Guerra, A., López-Alonso, V., Cheeran, B., & Suppa, A. (2018). Solutions for managing variability in non-invasive brain stimulation studies. *Neuroscience Letters*.

4. Li, L. M., Uehara, K., & Hanakawa, T. (2015). The contribution of interindividual factors to variability of response in transcranial direct current stimulation studies. *Frontiers in Cellular Neuroscience, 9*, 181.

5. Kubis, N. (2016). Non-invasive brain stimulation to enhance post-stroke recovery. *Front. Neural Circuits, 10*, 56.

6. Morishita, T., & Hummel, F. C. (2017). Non-invasive Brain Stimulation (NIBS) in motor recovery after stroke: Concepts to increase efficacy. *Curr. Behav. Neurosci. Reports, 4*(3), 280–289.

7. Windhoff, M., Opitz, A., & Thielscher, A. (2013). Electric field calculations in brain stimulation based on finite elements: An optimized processing pipeline for the generation and usage of accurate individual head models. *Human Brain Mapping, 34*(4), 923–935.

8. Nielsen, J. D., Madsen, K. H., Puonti, O., Siebner, H. R., Bauer, C., Madsen, C. G., Saturnino, G. B., & Thielscher, A. (2018). Automatic skull segmentation from MR images for realistic volume conductor models of the head: Assessment of the state-of-the-art. *NeuroImage, 174*, 587–598.

9. Smith, S. M., Jenkinson, M., Woolrich, M. W., Beckmann, C. F., Behrens, T. E. J., Johansen-Berg, H., Bannister, P. R., De Luca, M., Drobnjak, I., Flitney, D. E., Niazy, R. K., Saunders, J., Vickers, J., Zhang, Y., De Stefano, N., Brady, J. M., & Matthews, P. M. (2004). Advances in functional and structural MR image analysis and implementation as FSL. *NeuroImage, 23*, S208–S219.

10. Fischl, B. (2012). FreeSurfer. *NeuroImage, 62*(2), 774–781.

11. W. Penny, K. Friston, J. Ashburner, S. Kiebel, and T. Nichols, Statistical parametric mapping: The analysis of functional brain images. 2007. Elsevier; London, UK.

12. Dahnke, R., Yotter, R. A., & Gaser, C. (2013). Cortical thickness and central surface estimation. *NeuroImage, 65*, 336–348.

13. Geuzaine, C., & Remacle, J.-F. (2009). Gmsh: A three-dimensional finite element mesh generator with built-in pre-and post-processing facilities. *International Journal for Numerical Methods in Engineering, 79*(11), 1309–1331.

14. Thielscher, A., & Kammer, T. (2004). Electric field properties of two commercial figure-8 coils in TMS: Calculation of focality and efficiency. *Clinical Neurophysiology, 115*(7), 1697–1708.

15. Madsen, K. H., Ewald, L., Siebner, H. R., & Thielscher, A. (2015). Transcranial magnetic stimulation: An automated procedure to obtain coil-specific models for field calculations. *Brain Stimulation 8*(6), 1205–1208.
16. Saad, Y. (2003). *Iterative methods for sparse linear systems* (2nd ed.). SIAM. Philadelphia, PA, USA.
17. Geuzaine, C. (2007). GetDP: A general finite-element solver for the de Rham complex. *PAMM, 7*(1), 1010603–1010604.
18. Balay, S., Abhyankar, S., Adams, M., Brown, J., Brune, P., Buschelman, K., Dalcin, L., Eijkhout, V., Gropp, W., Kaushik, D., Knepley, M., May, D., McInnes, L. C., Mills, R. T., Munson, T., Rupp, K., Sanan, P., Smith, B., Zampini, S., Zhang, H., and Zhang, H. (2018). {PETS}c {W}eb page.
19. Opitz, A., Falchier, A., Yan, C. G., Yeagle, E. M., Linn, G. S., Megevand, P., Thielscher, A., Deborah, R. A., Milham, M. P., Mehta, A. D., & Schroeder, C. E. (2016). Spatiotemporal structure of intracranial electric fields induced by transcranial electric stimulation in humans and nonhuman primates. *Scientific Reports, 6*, 1–11.
20. Zienkiewicz, O. C., & Zhu, J. Z. (1992). The superconvergent patch recovery and a posteriori error estimates. Part 1: The recovery technique. *International Journal for Numerical Methods in Engineering, 33*(7), 1331–1364.
21. Bungert, A., Antunes, A., Espenhahn, S., & Thielscher, A. (2017). Where does TMS stimulate the motor cortex? Combining electrophysiological measurements and realistic field estimates to reveal the affected cortex position. *Cerebral Cortex, 27*(11), 5083–5094.
22. Jurcak, V., Tsuzuki, D., & Dan, I. (2007). 10/20, 10/10, and 10/5 systems revisited: Their validity as relative head-surface-based positioning systems. *NeuroImage, 34*(4), 1600–1611.